UNIVERSITY OF
LIVERPOOL

IC Engine Control by Ionization Current Sensing

Thesis submitted in accordance with the requirements of the
University *of* Liverpool for the
Degree of Doctor in Philosophy

by

Nick Rivara

March 2009

Acknowledgments

Throughout the undertaking of this work I have been surrounded by exceptional people; Paul, Chris, Georgios, Jack and Rebecca, without whom I would have given up and found a job long ago.

I thank my supervisor Tom Shenton for his guidance, Derek Neary for his ability and the EPSRC for the funding.

Statement of Originality

This thesis is submitted for the degree of Doctor in Philosophy in the Faculty of Engineering at the University of Liverpool. The research project reported herein was carried out, unless otherwise stated, by the author in the Department of Engineering at the University of Liverpool between September 2005 and March 2009.

No part of this thesis has been submitted in support of an application for a degree or qualification of this or any other University or educational establishment. However, some parts of this thesis have been published, or submitted for publication, in the following papers:

- N. Rivara, P. Dickinson and A. T. Shenton, Constrained Variance Control of Peak Pressure Position by Spark Ionization Feedback, Inaugural Automotive Researchers Conference, Huddersfield, 2008
- N. Rivara, P. Dickinson and A. T. Shenton, Constrained Variance Control of Peak Pressure Position by Spark Ionization Feedback, UKACC, Manchester, 2008.
- N. Rivara, P. Dickinson and A. T. Shenton, An Implementation of Peak Pressure Position Control by Spark Ionization Feedback, ASME, Journal of Dynamic Systems, Measurement and Control, DS-08-1011, 2009
- N. Rivara, P. Dickinson and A. T. Shenton, A Transient Virtual-AFR Sensor using the In-Cylinder Ion Current Signal, Mechanical Systems and Signal Processing, 2009.01.004
- N. Rivara, P. Dickinson and A. T. Shenton, Peak Pressure Position Control of Four Cylinders through the Ion Current Method, SAE Technical Paper, 2009-01-0235, 2009
- N. Rivara, P. Dickinson and A. T. Shenton, Constrained Variance Control of Peak Pressure Position by Spark Ionization Feedback Leading to Multi-Cylinder Control, IJAMechS, 08039, 2009

N. Rivara
4th March 2009

Abstract

Vehicles powered by internal combustion (IC) engines produce harmful emissions and are a significant cause of greenhouse effects and environmental pollution. The need for less polluting cars is driven by new legislation requiring manufacturers to reduce their vehicles' emissions and increase fuel economy. The need to control various parameters in the engine is the key to reduction in emissions, currently done through open loop control with an engine management system operating variables at mapped set points. To produce a map for the engine management system is a time-consuming task, with calibration for parameters such as spark advance, fuel pulse width or EGR required to be set for every conceivable load or throttle value. These maps do not take into account driver variability leading to changing wear rates between engines.

Ion current sensing is a cost effective way to obtain in-cylinder combustion information that can be used in feedback control loops.

This thesis describes the implementation of ion current sensing techniques to predict the air-fuel ratio and peak pressure position on an internal combustion engine. Firstly, spark advance is controlled through the prediction of peak pressure position from the ion current technique, initially on a single cylinder, and then on all four cylinders. This is done through a feedback control loop of an ARX model encompassing a neural network estimation of peak pressure position. The control, via minimum variance techniques, is seen to have no adverse affect on cycle to cycle variations in combustion or torque output of the engine, not only in steady state but also across transient ranges. Secondly, air-fuel ratio is predicted with the ion current sensing system in a similar neural network manner. Fuelling is controlled through a neural network feed-forward technique, with the air-fuel ratio regulated through a loop shaping control technique. Results show that a wide-band oxygen sensor signal can be replicated with the ion current technique whilst time delays involved with classical air-fuel ratio control with an oxygen sensor are reduced.

Contents

List of Figures

Nomenclature

$P\hat{P}P$ Estimated Peak Pressure Position

ABV Air Bleed Valve

AFR Air-Fuel Ratio

ARMAX AutoRegressive with Moving Average and eXogeneous input

ARX AutoRegressive with eXogeneous input

ATDC After Top Dead Centre

BTDC Before Top Dead Centre

CA Crank Angle

CCV Cycle to Cycle Variations

COV Coefficient of Variation

CV Constrained Variance

DOHC Double Overhead Camshaft

DWT Discrete Wavelet Transform

EGR Exhaust Gas Recirculation

EMS Engine Management System

HEGO Heated Exhaust Gas Oxygen

IC Internal Combustion

IMV Integrated Minimum Variance

IP Integrated Pressure

MAP Manifold Absolute Pressure

MBT Maximum Brake Torque

MFB Mass Fraction Burned

MIMO Multiple Input Multiple Output

MISO Multiple Input Single Output

MV Minimum Variance

N Engine Speed

NMSE Normalised Mean Squared Error

NN Neural Network

NOx Nitrous Oxides

PCA Principal Component Analysis

PFI Port Fuel Injection

PI Proportional-Integral

PPP Peak Pressure Position

SA Spark Advance

SI Spark Ignition

TDC Top Dead Centre

TDL Tapped Delay Line

UEGO Universal Exhaust Gas Oxygen

Chapter 1

Introduction

1.1 Engine Control Requirements

It is a stark reality that oil prices will probably continue to increase for the foreseeable future. With over 70% of households currently owning at least one car in the UK [1], it is of major interest to car manufacturers to show their cars have excellent fuel economy and it is a major benefit to consumers that their vehicles perform with excellent fuel economy. Considerable development has been undertaken to increase efficiency and power output per unit volume of cylinder capacity on the internal combustion engine since its conception over 100 years ago. Legislation is driving a reduction in exhaust pipe emissions as the requirements are becoming more stringent. The US is the world's largest market for cars and in December 2007 George W. Bush signed a new US bill into law to demand an increase in the fuel efficiency of cars and light trucks in the US by 40%, to an average of 35 miles per US gallon, the first increase since 1975. In Europe a typical, mid-sized, modern car manages about 38 miles per US gallon already. Over half of the vehicles sold in the US were SUVs and pickups, experiencing a 150% growth in sales between 1992 and 2001 [2]. This has subsequently changed in dramatic fashion since mid 2008 as sales of larger SUVs drop. The owners of these powerful vehicles are being hit hard by the cost of fuel so naturally, an increase in efficiency would be a solution. This will not only cause reductions to a consumer's fuel bill at the pump but has implications on exhaust emissions that are just as important. Without a sacrifice in output power of an engine, technology research is required to increase the efficiency and reduce emissions and this has posed a dilemma to the vehicle manufacturer when considering the end consumer; people have only been willing to pay for more power [3]. This means that any emissions reductions and fuel efficiency increases on a vehicle's engine must have little or no cost implications to the consumer.

Doubling a car's efficiency will effectively halve its CO_2 emissions. During the 1990's, the compulsory introduction of the catalytic converter along with the removal of leaded petrol

from garage forecourts helped reduce emissions dramatically.

Further reduction in emissions and fuel efficiency rises can be experienced through precise control of an engine's operating parameters. Currently car engine management systems (EMS) control a number of operating parameters in an open loop manner. These parameters are chosen by mapped set points within the management system. This map is calibrated by the manufacturers on a single engine before being replicated in production engine management systems. To produce a map for the engine management system is a time-consuming task, with calibration for numerous parameters such as spark advance, fuel pulse width or exhaust gas recirculation (EGR) required to be set for every conceivable load or throttle value. These maps do not take into account driver variability leading to changing wear rates between engines since operating in an open loop manner.

To overcome this expensive set-up constraint, feedback control could be employed to determine parameter set-points rather than follow predetermined maps. Feedback control requires sensors and actuators to read in-cylinder and exhaust phenomena and problems arise due to capital cost and installation of such sensors in production engines.

The amount of fuel entering the engine and the ignition timing or spark advance (SA) are the two most important parameters that influence the fuel consumption in addition to the emission of pollutants [4]. There is a trade off between emissions and fuel consumption when setting the SA; minimising the emissions through retarded SA causes an increase in fuel consumption, as illustrated in fig. 1.1 [4].

1.1.1 The Need for Spark Advance Control and Minimal Advance for Best Torque

Correct SA over the entire engine operating range is very important as it has a major impact on fuel consumption as well as emission rates [4]. Previous engine control research has demonstrated that the use of in-cylinder pressure as a feedback control variable could someday remove the requirement for the laborious task of ignition timing mapping [5, 6, 7]. Further advantages of the use of feedback in SA control include the automatic compensation for varying environmental conditions, engine wear and fuel characteristics, and the potential for reduced lean-limit operation by reduction in cycle-to-cycle combustion variation.

The cycle-to-cycle combustion process within a spark ignition (SI) combustion engine cylinder is subject to variability, not only through the alteration of key parameters such as SA but also through the natural inconsistency of turbulent flame propagation. This manifests as noise in the peak pressure position (PPP) output and is an indicator of the cycle-to-cycle variations (CCV) when spark timing is fixed [8]. Variability in the PPP is a highly useful measure of CCV of combustion since it may be determined directly and so can be used in

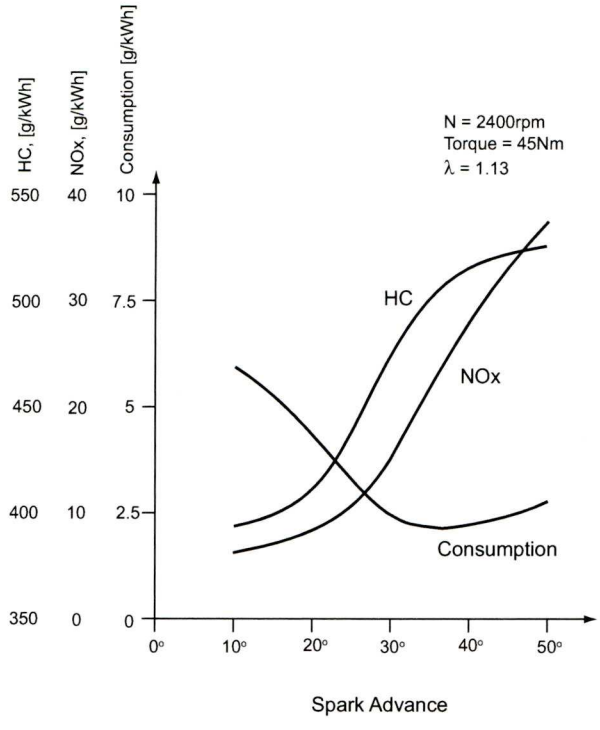

Figure 1.1: Fuel Consumption and emission levels over SA

feedback control. Adjusting SA directly affects the combustion initiation process and thus will alter the PPP. By controlling the SA, and hence the PPP, the desired amount of torque output can be achieved whilst minimizing losses. By advancing the SA at a fixed speed and inlet manifold condition, the produced torque curve illustrates the importance of accurate spark advance control.

If the SA is advanced (occurs at an increasing crank angle before TDC) the combustion is initiated earlier into the piston compression stroke. This implies that the work transferred from the rising piston into the propagating mixture expansion is increased, consequently the maximum burn rate and maximum work rate transferred from the gases to the piston on the expansion stroke, and hence the PPP, occurs earlier.

Conversely, if the SA is retarded (occurs at a decreasing crank angle before TDC) the PPP occurs later in the expansion stroke. There is a SA setting that will give a maximum torque output, called the maximum brake torque timing. Advancing or retarding the SA from maximum brake torque timing results in lower produced torque. The SA setting that can achieve maximum brake torque timing is not a single crank angle degree setting, but is a narrow range of SA settings over a few crank angle degrees. In recent years the acronym MBT has changed to refer to minimal advance for best torque (MBT), the minimal or most advanced SA that will achieve maximum best torque. In this manner, the SA can be retarded on demand to maintain the maximum best torque when required.

Another factor determining the importance of SA is that flame development and propagation varies cycle by cycle since the flame growth depends on local mixture motion and composition. These quantities vary in successive cycles in any given cylinder and may vary cylinder to cylinder. These cylinder to cylinder and cycle to cycle variations limit the operating regime of the engine and spark timing is set for 'average' cycles. Faster burning combustion cycles in extremely advanced SA will result in engine knock and the slower burning combustion cycles in an extremely retarded SA will cause incomplete burn setting the practical lean limit of the engine [9].

The engine knock phenomenon is a crucial limiting factor in SA control; not fully understood, knocking is unwanted self ignition or pre-ignition that can damage engine pistons due to localised high pressures [9, 10]. During operation, the SA angle is computed from pre-calibrated EMS look-up tables, depending on the speed and load, to obtain MBT and simultaneously avoid knock and observe emissions requirements. The EMS look-up table is optimal for the engine in a static manner only during calibration of the EMS [10]. Feedback control would allow incorporation of sensor signals, such as knock or pressure sensors, to compute optimal SA irrespective of engine wear, driver style or environmental conditions.

Controlling SA to achieve MBT is desirable during normal engine operation, but the ability to regulate or track the SA to other desired crank angle positions should not be overlooked. Upon cold start-up the catalytic converter must reach operating temperatures of around $300°C$ as rapidly as possible since at lower temperatures, the chemical reaction in the catalyst is reduced and exhaust emissions are higher. More rapid heating of the catalyst can be obtained by retarding SA so that the cylinder combustion is occurring when the exhaust valves have already opened [4]. Air-fuel ratio control requirements are detailed in the next section.

1.1.2 The Need for Air-Fuel Ratio Control

The control of air-fuel ratio (AFR) currently achieved in gasoline engines is acceptable at tracking stoichiometry at steady state operating conditions [11]. Stoichiometry is the theoretical ideal for complete combustion of the air-fuel mixture within an engine cylinder and is a mass ratio of $14.7:1$ [9, 12, 4] (a volumetric ratio would be around 9500 litres of air per litre of fuel). Load and speed transients introduce excursions from the stoichiometric levels. For a three way catalytic (TWC) converter to perform optimally, the AFR has to be kept within a window as small as 0.1% around the stoichiometric level [10, 4] during steady state operation, often expressed in terms of maintaining the *lambda* coefficient at unity where:

$$\lambda = \frac{AFR_{\text{measured}}}{AFR_{\text{stoic}}}$$

Interestingly, as the engine operates in a lean condition, the TWC efficiency drops dramatically and the NOx emission reductions are minimal. This is explained by the resultant abundance of oxygen from lean operation in the exhaust gas, which in turn oxidises unburned hydrocarbons [10]. A change in λ of 0.1% around $\lambda = 1$ would double the emissions rate although across transients of engine speed and torque, deviations of 2 to 3% around $\lambda = 1$ over short periods of time are acceptable [4, 11]. Figure 1.2 illustrates the optimum air-fuel ratio for the operation of a TWC.

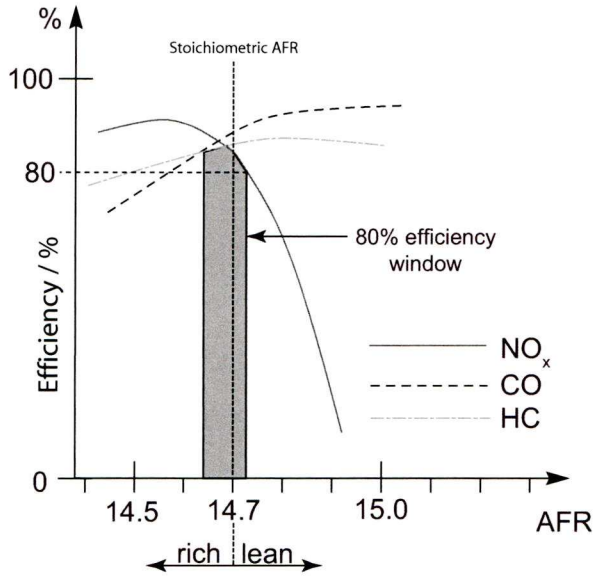

Figure 1.2: Efficiency window of a TWC

Optimization of the fuel control system to reduce emission levels requires accurate measurement of the post-combustion exhaust gases. Most production vehicles are fitted with a single oxygen sensor downstream of the confluence point on the exhaust system and is used for feedback for the control of the fuel injectors. A significant problem associated with this configuration is the difficulty of isolating individual cylinder behaviour. In general a single oxygen sensor is used in production vehicles for two main reasons; the cost of installing multiple sensors (one for each of the exhaust runners) is too high and secondly, installing such sensors close to the exhaust ports to minimise time delays and mixing effects exposes the sensor to much greater exhaust temperatures that significantly reduce the longevity of the sensors. The sensor is thus traditionally fitted at the confluence point on the exhaust system but gases become mixed making it difficult to detect which cylinders are operating away from stoichiometry, since individual cylinders may be operated rich or lean of $\lambda = 1$ due to mismatches in injectors and unbalanced airflow [13]. Mixing of exhaust gases can occur not only between cylinders at the confluence point of the exhaust stream but also between an individual cylinder's current and previous exhaust cycle. This occurs because before it can be detected, the gas emerging from an exhaust port must first displace the exhaust gas from

a previous cycle past the sensor [14].

In general, the type of AFR sensor fitted to vehicles is a nonlinear heated exhaust gas oxygen (HEGO) sensor. This is often referred to as a 'switching type' sensor since the output is one of two levels depending on which side of stoichiometry the engine is operating. Robust feedback techniques can not easily be applied to nonlinear systems and the severity of this nonlinearity makes it challenging for linear approximations.

A significant proportion of hydrocarbon emissions occur during engine start up, in part due to a lack of sensing for feedback control during this period [15]. Oxygen sensors are incapable of measuring AFR from an engine cold start-up due to their time to 'light-off', a duration required for the sensor to reach an elevated operating temperature [9]. During this period the engine is operated open-loop.

Further difficulties in AFR feedback control are associated with time delays. The most significant is due to the transportation of the exhaust gases following the combustion event to the detection at the oxygen sensor downstream. Additionally, the sensor is often considered to behave as a 1st order lag which acts to filter the signal [10].

1.2 Measuring and Controlling Peak Pressure Position and Air-Fuel Ratio

1.2.1 Peak Pressure Position

The following parameters in various combinations have been stated as being used as parameters in populated look-up tables or maps to control the ignition [4]:

- Manifold Air Pressure (MAP)
- Mass Air Flow (MAF)
- Engine Speed (N)
- Throttle Angle
- Air-Fuel Ratio (AFR)
- Crank angle and top dead centre (TDC)
- Ambient Air Temperature
- Engine Temperature
- Battery Voltage

As these parameters change, they have an effect on the engine operation and hence the SA would be adjusted accordingly to ensure smooth engine operation.

Conventionally in-cylinder pressure is measured with pressure sensors. This requires the pressure sensor to be inserted into a precision machined hole in the cylinder head so that the pressure sensor face is exposed to the piston chamber. The pressure sensor is then connected to a signal amplifier to produce meaningful pressure outputs after being calibrated appropriately. This is prohibitively expensive for production vehicles and their reliability is questionable over long periods (thousands of combustion cycles). However, the obtained signals from the pressure sensor apparatus is useful for in-cylinder information. Algorithms can efficiently determine the peak pressure position of a combustion cycle in real time. A series of papers involving Powell and colleagues published from 1976 begin to use the peak pressure position (PPP) as a feedback variable for control of ignition [5, 16, 17, 18, 19].

In [5] the use of a pure integral controller is recommended as a suitable method for maintaining the maximum cylinder pressure at a desired crank angle. Non-linear parametric models were used in [6] at the University of Liverpool to model SA to PPP relationships for control using in-cylinder pressure sensors. This equipment was used again for more advanced control algorithms for PPP regulation [7, 8].

In-cylinder pressure can also be measured via non-intrusive pressure sensors as in [20]. Cylinder pressure readings were taken at a minimum of 4 sample points and pressure ratios calculated with an estimate of a motored cylinder pressure. These pressure ratios were used to control combustion phasing for spark control, using a parameter based on the pressure ratios with cylinder pressures measured at 10° ATDC and 55° ATDC.

Ion current sensing is a method of obtaining the in-cylinder pressure information in a low cost, non-intrusive manner. In this scheme an electric potential is applied across the plug electrodes producing an electrical field during the period of non-sparking and hence ion species, produced during combustion, generate a current as they move between these electrodes. Using a simple electrical circuit, the voltage across a resistor is measured and the resulting signal is rich in combustion information.

1.2.2 Air-Fuel Ratio

Production vehicles use an oxygen sensor to determine the air-fuel ratio (AFR) in the gas exhaust stream whereby a voltage signal dependent on the oxygen concentration is generated. This signal is used in feedback systems to control the fuel volume in the intake. The standard switching heated exhaust gas oxygen (HEGO) sensor is the most common since it is relatively cheap, but is highly non-linear in output voltage: high voltage for rich mixtures and low

voltage for lean mixtures with a steep transition of voltage around stoichiometry, see fig. 1.3. Feedback control utilises this rapid transition to set-up a limit-cycle of the air-fuel ratio around stoichiometry.

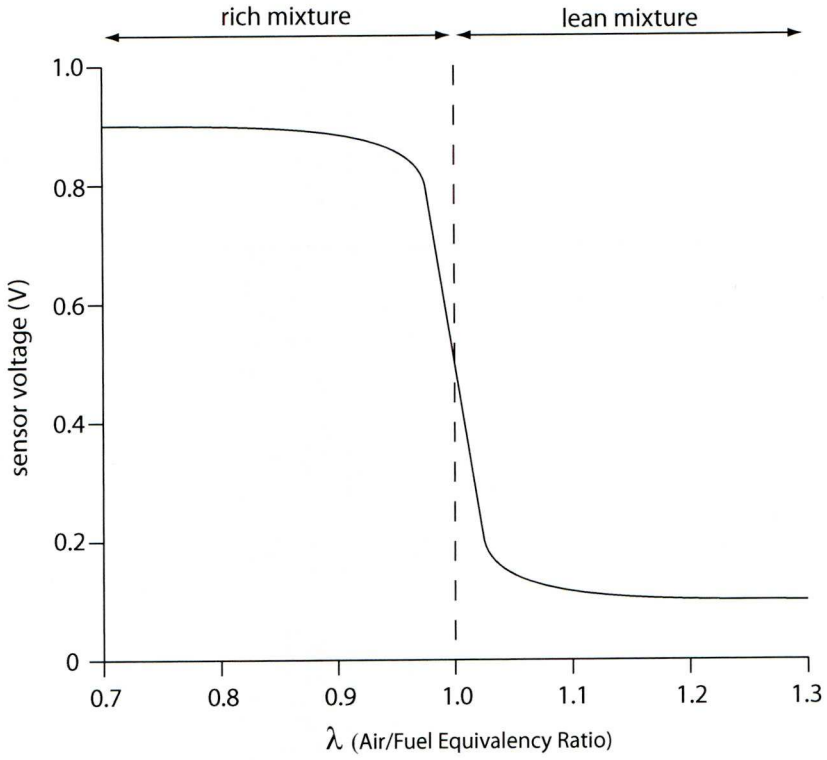

Figure 1.3: Output Characteristics of a HEGO sensor

Succeeding the standard switching HEGO sensors are universal exhaust gas oxygen (UEGO) sensors. Known as Lambda sensors their voltage output is proportional to the air-fuel ratio (AFR) or lambda level and can give both useful and accurate readings of exhaust gases. Problems arising from the use of such sensors are the cost, currently only one is normally fitted at the exhaust confluence point, taking average exhaust readings across all cylinders. Further problems for feedback are the inherent delays with such a sensor; exhaust gas from a particular combustion event must reach the sensor a distance along the exhaust pipe before the AFR can be measured and used for feedback.

To address some of the problems associated with oxygen sensors for feedback control a significant amount of research has focused on estimation using diverse combustion sensors including pressure sensors, optical sensors, hot-wire sensors and infrared sensors. The spark plug with appropriate diagnostic circuitry has also been extensively investigated for possible use in the measurement of in-cylinder combustion variables and as a 'virtual' lambda sensor [21].

Spark plug voltage analysis, more specifically, the voltage decay time can be used to study

AFR [22]. The principle is that the spark discharge time is related to the number of ions in the flame and, hence, the quality of combustion. It was found that this discharge time was only sensitive to the AFR in lean mixtures. Spark voltage characterization (SVC) is another similar method [21, 23, 24]. It involves analysis of the time-varying spark voltage vectors and a lambda accuracy has been achieved to within ± 0.1 in about 95% of the time over its identified operating range [21].

It is well established that the ion current sensing method can obtain in-cylinder combustion information including AFR in a low cost, non-intrusive manner by utilizing the existing spark plugs on a spark ignition (SI) IC engine [25]. Whilst SVC analyses the actual sparking event from a spark plug to estimated AFR, ion current sensing involves analysing ionization of combustion gases after the sparking event.

1.3 Overview of Thesis

Following on from the engine control requirements, the remainder of the thesis is sectioned into appropriate parts and these are detailed here.

Chapter 2 - Ion Current Sensing

Ion current sensing is the main concentration of this research for estimation and control of in-cylinder air-fuel ratio and peak pressure position. Ion current sensing is reviewed extensively starting with an explanation of the technique and methodology. Previous research in a range of applications that the ion current sensing method has been applied to has been reviewed showing the depth of information that is available from a typical ion current signal. Obtaining an ion current signal is perhaps trivial in comparison to obtaining combustion information from the signal and so methods of feature extraction have been reviewed. Principal component analysis is presented as a more robust method of feature extraction from a cycle by cycle varying stochastic signal. Methods of modelling are discussed concentrating on neural networks; network structures are discussed along with possible training algorithms.

Chapter 3 - Experimental Set Up

A detailed explanation of the available facilities at the University of Liverpool powertrain control laboratory is given, describing the engine and dynamometer set up with all additional sensors, actuators and software employed in the research for air-fuel ratio and peak pressure position control. The ion current sensing device that was built in-house is detailed with accurate circuit diagrams, including any novel components integrated in the device. The extension of this device to a four cylinder version is also detailed.

Chapter 4 - Single Cylinder PPP Estimation and Control

This chapter describes the theory and reasoning behind the acquisition of data for the identification process of producing models to predict the peak pressure position from a single cylinder. Principal component analysis is described as a method of data reduction and feature extraction from the ion current signal. After data acquisition and signal processing, modelling of the system can begin. Neural networks are employed and a detailed explanation is given in this chapter. The process of implementation of the identified neural networks to predict the PPP is explained before control feedback is incorporated. Minimum variance and a constrained variance technique are compared as a method of regulating the stochastic nature of peak pressure position on a single cylinder. All techniques are validated experimentally on the powertrain control group engine and dynamometer.

Chapter 5 - Four Cylinder PPP Estimation, Control and Cylinder Balancing

Extending the single cylinder PPP estimation and control detailed in chapter 4 is not a straightforward process. This chapter explains the need for solving crank angle phasing from the angle encoder, before describing the process to balance the cylinders when individual controllers are implemented on each cylinder. Indicated mean effective pressure is a measure used to determine improvements in the balance of the cylinders and control is done with a constrained variance technique as used in chapter 4. Again, techniques are demonstrated experimentally.

Chapter 6 - Single Cylinder AFR Estimation

This chapter describes the theory and reasoning behind the acquisition of data for the identification process of producing models to predict the air-fuel ratio of a single cylinder. Principal component analysis is described as a method of data reduction and feature extraction from the ion current signal. After data acquisition and signal processing, modelling of the system can begin. Neural networks are employed and a detailed explanation of the specific networks is given in this chapter. The process of implementation of the identified neural networks to predict the AFR from a single cylinder is explained. The process is demonstrated experimentally. Control of the AFR is undertaken in the next chapter. An estimation of average torque is also presented through the conversion of the MISO network used in this chapter to a MIMO network. Torque is presented as a second target output dataset and initial training proves the ability of the network to predict both AFR data and average torque.

Chapter 7 - Single Cylinder AFR Control

Following on from estimation of AFR on a single cylinder, this chapter introduces AFR control of a single cylinder by first covering simple feedforward fuelling without feedback. Then this feedforward controller is enhanced using the UEGO signal as feedback to show improved fuelling. The UEGO feedback signal is then substituted for the ion current signal as a feedback signal to show similar measures of performance but with reduced time delays due to the advantageous location and operation of the ion current system. This process involves generating two neural networks for a single cylinder, with loop shaping controllers implemented into a feedback system. The techniques are validated experimentally.

Chapter 8 - Conclusions and Recommendations for Further Work

The thesis is concluded in this chapter summarising the outcomes of the research work with the advantages and disadvantages of the ion current technique for powertrain control. Limitations of the ion current and modelling techniques are presented and suggestions for further improvement are made.

1.4 Contribution of Thesis

Previous ion current work has mainly concentrated on the estimation and rudimentary control of powertrain variables. In this thesis, emphasis is placed not only on accurate estimation of air-fuel ratio and peak pressure position but on modern, powerful control techniques and the practical issues of applying these. The elements of the thesis believed to be novel are detailed here:

- Identifying a linear parametric model around the neural network so that classical control techniques can be applied easily has not been undertaken previously. The neural network model, whilst implemented online, works in the background to estimate desired parameters whilst the parametric model identified around the neural network has feedback loops applied directly.
- The level of accuracy achieved with the technique presented appears to surpass previously presented results.
- In chapters 6 and 7 loop shaping is used control the feedback of the air-fuel ratio around a neural network.
- Constrained variance control used in conjunction with the ion current sensing technique to regulate PPP is novel.

- Balancing using constrained variance across all cylinders through PPP control with the ion current technique has not been presented previously.
- In chapter 7, a feedforward neural network is used to control the fuelling of the engine combined with a second NARX neural network that predicts λ.

Chapter 2

Ion Current Sensing Preliminary Research

2.1 Introduction

Ion current sensing has been chosen as a candidate for an alternative method to determine in cylinder peak pressure position and air-fuel ratio. It provides an information rich signal at a low-cost, non-intrusive manner but requires processing to obtain valuable in-cylinder information. This chapter details the basis of the ion current sensing technique in depth and the applications that are feasible by using the technique. Previous research undertaken using the ion current technique in numerous applications are detailed.

Together with the various applications, typical ion current processing techniques are explored; Principal Component Analysis is highlighted as an effective method of feature extraction from the ion current signal.

This chapter continues with an overview of neural networks for modelling, covering the network structure composing of neurons and layers. Possible training algorithms are discussed for the purposes of estimating peak pressure position and air-fuel ratio and the chapter finishes by describing the disadvantages of neural networks.

2.2 What is Ion Current Sensing?

The concept of ion production in flames has been known for nearly two hundred years, attempts to understand the physics of the flame and the burned gas have been undertaken since the first half of the 20^{th} century [26] with studies of engine in-cylinder flame propagations dating back to 1934 [27, 28]. First attempts to utilise the ion production phenomenon in automotive applications also started later that century [29, 30].

The 'ionization current technique', also known as the 'ion current technique', 'ion sensing' or 'spark ionization sensing', is undertaken by applying a DC bias voltage across a spark-plug during the period of non-sparking. Upon combustion in the cylinder, ion species and free electrons are produced at the flame front. High temperatures within the cylinder then cause re-ionization of gases behind the flame front. The DC bias voltage applied across the spark plug generates an electrical field that causes the produced ionic species and electrons to move within the cylinder, hence producing an electrical current between the two electrodes of the spark-plug. In this manner the spark-plug is utilised as the sensor for this produced current and using a simple circuit, a voltage across a resistor is measured. It is proposed that the ionization current is representative of a number of combustion event parameters and from a typical generated output waveform of the ionization current, a number of these important parameters can be measured.

The species of gases and their reactions during the combustion flame front itself are numerous and complex. Fortunately most of the species in the burned gases, in the 'post flame' zone, have reached equilibrium and analysis of the chemistry is then simpler [31]. Saitzkoff *et al* first modelled the ionization equilibrium in the 'post flame' zone [32] and determined that the main carrier of the current is electrons rather than ions, also stated in [33], due to the smaller mass of the particles and hence higher drift velocities. This was realised after an analysis of 64 species of gases and 268 reactions that occur in the cylinder upon combustion [31]. The chemical reaction leading to the final species from the initial species are detailed here:

$$C_8H_{18} + \frac{27}{2}O_2 \rightarrow 8CO_2 + 9H_2O$$

but these do not indicate the intermediate reactions that result in electron production:

$$\begin{aligned} CH + O &\rightarrow CHO^+ + e^- \\ CHO^+ + H_2O &\rightarrow H_3O^+ + CO \\ CH + C_2H_2 &\rightarrow C_3H_3^+ + e^- \end{aligned}$$

The ionization current signal is indeed complex but is information rich. The produced current is dependent on the density of the ions which is affected by pressure in the cylinder [25], temperature and fuel additives [31].

2.2.1 The Ion Current Signal

The ions are formed during and after the combustion and the type and amount depend on the combustion characteristics. The more ions and electrons produced, the higher the produced current and hence the better the ionization current signal.

The ionization signal has been accepted to have two [34] or three [32, 31, 25, 35, 36, 37, 38, 39] main phases, depending on the research one reads:

- 1st phase relating to ignition or spark event, ionization here is from the flame kernel that initiates at the spark plug electrode gap. Some researchers do not consider this a phase of the ionization signal.
- 2nd phase relating to ions through flame development and propagation. This phase (and first peak of the ionization signal) represents the flame kernel growth as the fuel reacts with oxygen and is also known as the chemical phase. It is during this phase of the ionization current signal in which information relating to the AFR is contained.
- 3rd phase called the 'post flame phase' or 'the thermal phase' in which re-ionization of the gases occurs due to rising in-cylinder temperatures. The 'second peak' occurs within this phase and is believed to relate to the PPP since pressure and temperature are closely related. If the in-cylinder temperatures do not reach a threshold for re-ionization, this 'second peak' may disappear [40].

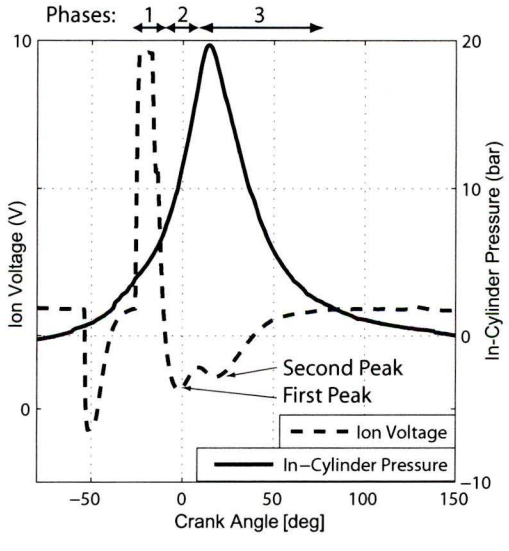

Figure 2.1: Actual cylinder pressure and a typical ionization current signal from a non-averaged combustion cycle

The basic cycle of a single cylinder in a spark ignition combustion event is detailed here to indicate the timing of the resulting ionization. The following relates to $-30°$ BTDC ignition timing, wide open throttle at a speed of 1044 rev/min [9]. Initially the fuel and air mixture are inducted through the intake valve to the cylinder from the intake system and then during the compression stroke all inlet and exhaust valves are closed. Mixing with residual gas from the previous combustion event occurs. The temperature of the charge is below that of the

cylinder walls upon intake but during compression, the temperature of the charge rises above the cylinder wall temperature.

- At $-30°$ crank angle relative to top dead centre: The single compression stroke of a piston within a cylinder occurs over $180°$ and the spark plug ignition occurs towards the end of this stroke though the precise timing is subject to control and can be varied to affect the PPP. The spark plug plasma kernel develops into a flame front that radiates outwards. Pressure within the cylinder is at around 5 bar and rising at this crank angle as the piston reduces the volume of the mixture in the cylinder. The temperature of the mixture rises rapidly and the heat transfer into the cylinder walls approaches maximum. Ionization is during the 2nd phase as listed above, through flame development and propagation.

- At $0°$ crank angle relative to top dead centre: This is TDC. The piston has reached the extreme of the compression stroke, pressure can be between 13 and 20 bar depending on the spark ignition timing relative to crank angle. At this point the surface area of the cylinder wall exposed to mixture is at a minimum. The heat release of the mixture is at a maximum and the temperature at the flame front is around $2500°C$ [29]. Re-ionization of the gases is beginning during the 'thermal phase'.

- At $+15°$ crank angle relative to top dead centre: The flame reaches the cylinder wall, farthest from the initial spark plug ignition kernel. Quenching of the flame begins but combustion will still occur for another $10°$. Pressure within the cylinder is between 20 and 30 bar depending on the spark ignition timing relative to crank angle.

- At $+16°$ crank angle relative to top dead centre: This is stated [9] as being the crank angle to ideally locate PPP (although others have stated between $+12°$ and $+20°$)[16][17]. Reionization of the gases during the 'thermal phase' is at a maximum at the PPP before decreasing. Pressure within the cylinder is about 30 bar but the temperature of the gases are reducing as the gases expand.

- At $+25°$ crank angle relative to top dead centre: Combustion has now ceased. Pressure is between 25 and 30 bar and is decreasing. The burned gases are still at a temperature of $2000°C$ and will be until around $+30°$ to $+40°$crank angle relative to top dead centre [29].

The ionization current signal is subject to large cycle to cycle variations since there are many influencing parameters. Localised temperatures, composition differences driven by internal aerodynamics and air-fuel ratio inhomogeneity. With this in mind, the ion current cannot be easily calibrated in an 'absolute' manner [34].

2.2.2 Methodology

The numerous methods for measuring the ionic signal all follow the same basic principals but differ in the use of physical equipment used in the signal's capture. Previous research undertaken at various institutions use the following set-ups:

1. The use of the existing spark plug to capture the ion current in conjunction with the existing ignition system [41, 34]. A series of papers detail the use of a Saab 9000, equipped with a 2.3 litre low pressure turbo engine [25, 36, 35, 42, 43, 44, 45, 46] that uses the existing ion current equipment.

2. The use of the existing spark plug to capture the ion current with the use of additional circuitry [47, 31, 48, 49, 50, 38, 51, 52, 53, 54, 55, 56].

3. A system completely separate from the ignition system, that uses a second electrode in a modified spark plug [34].

4. A system that uses additional spark plugs or ion probes that can be located anywhere in the combustion chamber [57, 34, 58, 59].

5. A single cylinder test engine not intended for production vehicle use with a production ion sensing system [37, 22, 24, 39, 60, 61, 62].

Circuitry

A popular method such as in scheme 2 above is as follows: A 300V power supply is required for the ionization sensing circuit and is completely separate from the ignition spark circuit. A 0.1mm gap [29] is used to separate the spark generating secondary coil from the bias DC supply.

This does however require access to the spark side of the secondary coil plus the use of a 300 volt power supply. The voltage across a resistor is measured on the low voltage side of the ignition coil and the current can then be deduced. Figure 2.2 shows a basic spark ionization circuit. Voltages above 500V should be avoided to prevent spurious sparking [63] but voltages of 150V have been quoted [50].

Electrodes

As well as the electronic circuit design, electrode design and geometry can influence the ionic signal too. Greater signal to noise ratios are achieved with a larger surface geometry [34] of the electrodes. The ion current amplitude and timing is also dependent on the location of the

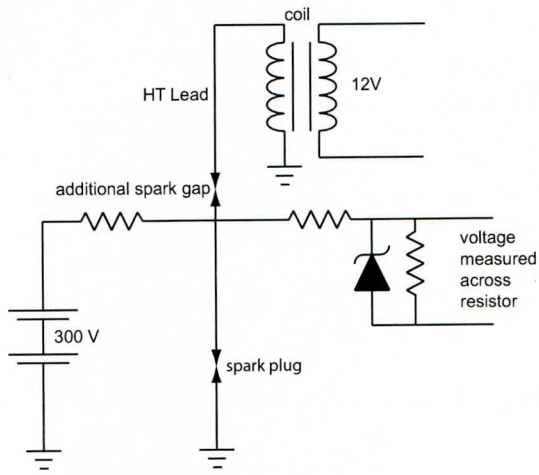

Figure 2.2: Basic Spark Ionization Current Sensing Circuit

spark plug probe within the cylinder [50] due to the ions being produced locally in the flame front region. Timing is reported to vary by up to 2° throughout the cylinder and is linked with the cylinder wall temperature [59]. Many studies, when using a standard spark plug as the ion probe, state it is best to use the centre electrode of the spark plug as the positive electrode due to it having a larger surface area [33, 41, 22, 58]. The reasons for this is that the main carrier of the current are electrons [32] that will be attracted by the positive electrode. Although the positive ions still carry current it is important that the electron mobility is greater than the positive ion mobility [64]. This is contrary to that in Kienke and Nielsen [4], where it is stated that the smaller electrode should be positive and the larger electrode negative; this is recommended so that the same number of lighter, faster moving electrons reach the small positive electrode as the slower, heavier positive H_3O ions that reach the large negative electrode.

Gazis *et al* [57] explored the use of additional dedicated ion probes in addition to the existing spark plug in an attempt to produce a less noisy signal. Examples of ion current signals are presented that show a significantly higher produced voltage and clearly defined curves on the chemical and thermal phases from a separate ion probe as opposed to the curve from the single spark plug ion probe. This does mean that a cylinder head would have to be modified accordingly to accommodate the ion probe.

Modern coil systems that are appearing utilise one coil per plug, in which each spark plug is powered by an individual ignition coil. Zhao *et al* [63] developed an ion current sensing system based on this type of coil although a system based on these individual coils is also mentioned in [65]. Ohashi *et al* [48] claim to develop a system that can be fitted into mass production vehicles or even retro fitted into existing ignition systems. This consists of simple modification of the coil and circuitry for detection of the ion signal, but this system is only

for misfire and knock control.

2.3 Influence of Additives and Fuel Composition

Fuel compositions and fuel additives are reported to give high variations in the ionization current [66, 50, 34].

In [34], the ion current signal has been compared with six fuel types and one additive. It was reported that cylinder pressure was not influenced but the ionization level was, in that it was altered in amplitude. The greatest difference was between unleaded and leaded fuel which has metallic particles that improve conductivity between electrodes. The amplitude of the ionization current was increased significantly with leaded fuel. Between unleaded RON 98, unleaded RON 95, propane gas and an additive (INJEXION 5) there was little difference in the ionization signals reported.

Reinmann *et al* [66] explains any differences in the shape and amplitude of the ion signals at a chemical level. The first peak (the chemical phase) is sensitive to the carbon-hydrogen ratio of the fuel due to the carbon-hydrogen radical that is formed and required for the chemi-ionization process. The second peak of the ion current signal (thermal phase), governed by thermal dynamical conditions, is related to thermal ionization of nitrous oxide and electronegative species.

Förster *et al* [50] conclude that additives Methylcyclopentadienyl Manganese Tricarbonyl (MMT) and Methyl Tert-Butyl Ether (MBTE) only increase the amplitude of the ion current over 3000 rpm. Sodium and potassium have low thermal ionization energies and so when used as fuel additives, they not only increase the absolute signal level during the thermal phase but reduce the main frequency of the ion current[66]. This has the effect of perturbing an ideal two-peak signal to yield a single peak.

2.4 Influence of Atmospheric Humidity

Humidity affects the burn rate which can delay the peak pressure position (PPP) by several crank angle degrees [5, 45]. Hellring and Holmberg [45] state that the ion current can reflect this lower burn rate induced by high humidity and that soft sensors (using the ion current) show the same performance for normal and higher humidities. Eriksson [67] performed an experiment whereby he used an adapted paint sprayer to atomize water as it is spayed toward a throttle plate, thereby adjusting the apparent humidity experienced by an engine. The ion current sensor was deemed able to control the engine SA to compensate for the changes in humidity.

Humidity is not usually measured in a production engine and is not normally compensated for.

2.5 Influence of Applied Voltage

Laboratory tests demonstrate the effect of applied voltage to the ion current signal. Figure 2.2 shows an applied voltage of $300V$. Basic voltage adjustments on an ionization current sensing circuit have been undertaken at the University of Liverpool. Although, the voltage output from a DC/DC converter within the circuit allows up to 500V, a theoretical maximum can be calculated at about 414 volts before zener diodes that protect the dSPACE equipment cap the output voltage at 10V (see section 3.5.1). An engine and dynamometer set-up was run at a constant speed, load and SA setting. The effect of adjusting the applied voltages on the acquired signal waveform is shown in fig 2.3.

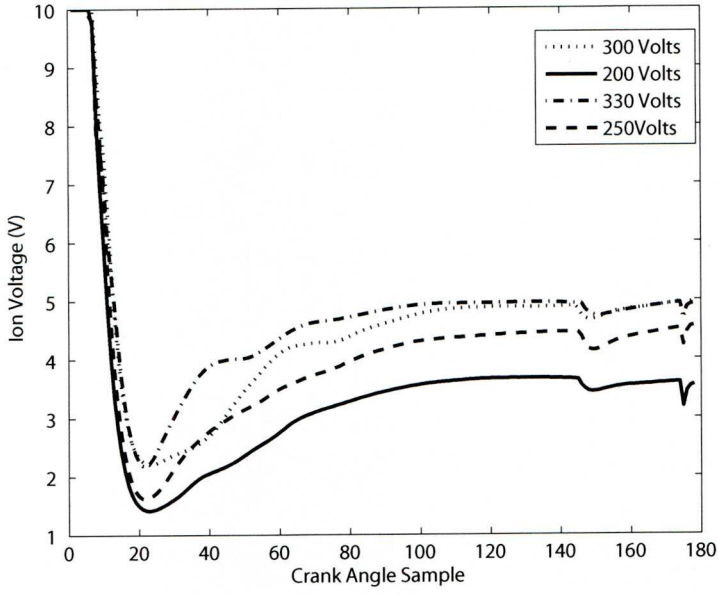

Figure 2.3: Effect on Ionization Waveform with Varying Voltages

By varying the applied DC voltage, the resulting base ionization voltage varies and this can be seen in the plot after 100 crank angle samples whereby there is no ionization occurring. This resulting base voltage is explained in detail in section 3.5.1.

2.6 Applications

The ion current signal is rich in combustion information. Efforts to exploit this signal in a multitude of methods for a multitude of applications have been researched since the technique was developed. The following section details these efforts.

2.6.1 Mass Fraction Burned

Mass fraction burned (MFB) is a parameter that relates to engine design and performance, it indicates the percentage of fuel consumed versus crank angle during an engine cycle and can give insight into the combustion process.

The best results for the mass fraction burned for a spark ignition engine are commonly calculated using the Rassweiler-Withrow method from 1938, although the accuracy is limited by pressure sensors, crank angle phasing and compression ratio. This method uses the cylinder volume at the instance of ignition and calculates the pressure increase for each angle of the combustion process, then normalises the pressure by the maximum pressure increase at the end of the combustion. The percentage of MFB is signified by each percentage of pressure increase at the corresponding angle [28]. Attard and Micallef [68] integrate the ionization signal and determine 50% of its final value correlates to within 0.1° to the 50% MFB. In [69], 50% MFB location can be used in closed loop control as MBT timing criteria since it is between 8° and 10° ATDC.

In [47, 31, 40], MFB is proposed using spark ionization. Daniels *et al* [47] compares this MFB from the ionization current to the curves obtained from the pressure sensors. Often, mass fraction burned at a crank angle θ, x_b, is described using the Weibe function, (equation 2.1), whereby the measurements of the crank angle, start and end of combustion can be used along with the form factor, m, and efficiency parameter, a. In this ionization current method, the start of combustion, θ_0 is determined from the ignition timing, the duration of combustion $\Delta\theta$ can be calculated from the ion current peak in the 'thermal' phase since this is related to PPP and $\Delta\theta/2$. A typical MFB curve is shown in fig. 2.4.

$$x_b = 1 - exp\left[-a\left(\frac{\theta - \theta_0}{\Delta\theta}\right)^{m+1}\right] \tag{2.1}$$

These combustion measurements can be easily obtained from the spark ionization signal and the whole mass fraction burned curve described. Comparison of this method and the standard pressure sensor method show similar results.

The estimated MFB curve can be used to calculate pressure within the cylinder with the

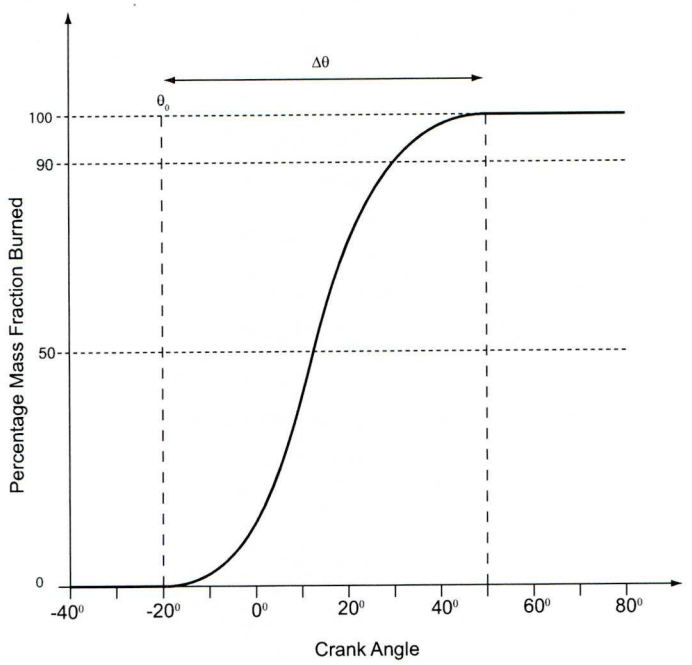

Figure 2.4: Typical Mass Fraction Burned Curve

reverse Rassweiler-Withrow method [47]. Again comparable results are obtained against a standard pressure sensor.

The point of 50 percent MFB, i.e the point of inflection of the MFB curve, can be found through a differentiation of the ionization signal, then a peak algorithm can be implemented since it correlates to an inflection point of the rise of the ion current during the second peak [54, 40, 55]. This generally occurs between 8° and 10° ATDC when MBT is achieved [40]. Zhu *et al* also relate other points on the ion current signal to the MFB curve [40]. A first inflection point on the fall of the first peak of the ion current can be correlated to the maximum acceleration point of the net pressure increase during combustion. This is normally between 10% and 15% MFB.

2.6.2 Knocking Detection

The earliest practical, implemented use of the ion current phenomenon in an SI IC engine was knock and misfire prediction. Early work determined that the ion current signal contained useful combustion information. Rado and Johnson [29] noticed that the ionization signal is very different when no combustion occurs and so designed a circuit that could be implemented with any vehicle engine for misfire detection. From this initial work in the mid 1970's, numerous studies have occurred on misfire and knock detection by various teams [63, 22, 50, 48, 60, 52, 54].

Knocking combustion is a phenomenon that affects the performance and efficiency of a spark ignition engine. It is regarded as the resonant sound of the combustion gases, caused by auto ignition of the mixture [9]. At low engine speeds an unpleasant sound is emitted by the engine block with no damage, at higher speeds the knock becomes inaudible but severe engine damage can occur [70]. At the onset of engine knock conditions, the conventional approach to eliminating the knock is to immediately retard and then to gradually advance the spark advance (SA) back to the desired set point until knock is again detected [4]. SA of an engine is thus often limited by knocking in the advanced position but the ability to operate the engine timing at the borderline knock spark limit is a key to improving output power and fuel economy [54]. Improved detection of combustion knock and pre-ignition enables safe operation closer to MBT spark advance [20, 41, 48].

The spark ionization method can realise knock detection due to the remarkable differences in output ionization signal under these events compared to non-knocking events [60]. The ionization current is suited to knock events because it responds to combustion phenomena, normal or abnormal [34]. The higher frequency constituent of the ion current corresponds to the knocking level. These higher frequencies are caused by the ion density changing with coarseness and minuteness of the pressure wave [58] from the knocking. The processed signals can be compared with predetermined reference signal values to evaluate a knocking event [48, 50].

The advantages of using the spark plug as a knock sensor over a vibration type sensor are the ease of installation due to engine vibrations not affecting the spark plug and the relatively high signal to noise ratios. The spark plug is also cost effective as it is already installed in production engines. The Saab Motor Company have been using their Trionic^{TM} ionization current system for a number of years in their production vehicles as knock sensors; the ionization current method is currently also employed in high-end vehicles with gasoline engines such as Mercedes-Benz, Maybach and BMW [68].

2.6.3 Misfire Detection

The spark ionization method can realise misfire detection due to the significant differences in output ionization signal under these events compared to non-misfire events [60]. The detection of misfire using ion current sensing may be very simple since if no combustion occurs, no ions are produced, hence no ionic current is produced. Integration of the ionization signal should reveal misfire occurrence [34]. In [48, 50], the ion current signal is filtered to remove high frequencies since combustion information is reported to lie in the low frequency part of the signal. The processed signals can be compared with predetermined reference signal values to evaluate a misfire event.

2.6.4 Spark Advance

Spark advance (SA), or spark ignition timing, is used to position the in-cylinder peak pressure position (PPP) relative to the top dead centre (TDC) in the crank angle domain in addition to enabling knock and misfire control in the operational extremes of advance and retard. Research has shown that the position for the peak pressure is almost constant at optimal SA [9, 5] but installation of accurate pressure sensors is expensive and not viable yet in production engines. SA is paramount for good operation of the engine, and affects several outputs directly. Currently, the SA is achieved from a map, within the engine EMS, to position the pressure curve to give the maximum engine torque output at a fixed speed, load, fuel and air flow rate. This is referred to as minimal advance for best torque (MBT) timing. Work is lost to compression and heat transfer if SA is too early and through expansion if SA is too late. There is as yet no on-line feedback control scheme in production engines for SA to achieve this required PPP for MBT.

With optimum SA, the maximum pressure occurs around 16° ATDC [5, 9, 19] but varies slightly with with engine speed, load and AFR (±4°).

Using the spark plug with the ion current technique as a pressure sensor, a feedback scheme can be used to perform this operation without the use of costly pressure sensors. The spark plug, when implemented as a sensor, is a fast, direct measurement, unlike exhaust sensors which have a significant transport delay, and can be used on each cylinder individually so the positive implications for control are evident.

When the SA hardware is implemented, the ion current signal is easily obtained but through cycle to cycle variations, extracting repeatable, useful and accurate information from this signal proves to be the difficult part. To estimate absolute pressure with the ion current signal technique is not easy and would need excessive calibration. In [31], an achieved accuracy of between 10% to 15% between absolute values of the predicted and measured pressure using a spark ionization technique is achieved. A correlation of 0.8 was obtained for the ion current peak (in time) to the PPP when measured and an algorithm for calculating the PPP was by a simple addition to the measured data. Then the duration of combustion, $\Delta\theta$, could be calculated in the MFB curve and used in pressure calculations.

The pressure has most influence on the post flame (or thermal) phase, but a simple peak search cannot be executed due to several spurious peaks within the spark ionization signal per cycle, and often the post flame phase appears with no peak. With this in mind, analysis to obtain this 'pressure' information is ongoing. Concentrated efforts emerged from a group at the Lund Institute of Technology, Sweden and Linköping University, Sweden.

Initial work proposed that the 'flame front phase' and 'pressure' indicating section of

the spark ionization signal have shapes close to Gaussian curve functions and parameterized functions can be used to describe the relevant sections of the ion current signal [25, 36, 35, 42]. An idealized model of the ionization current (consisting of two Gaussian curves) was fitted in the least-squares sense to the measured ionization current. This work was undertaken and validated on a SAAB 2.3l production engine. Closed loop control is demonstrated in [36] through a PI like feedback control law with an heuristically tuned gain although a step response of 30 cycles is reported. Although no control is proposed in [31], the relation of PPP to the ion current is recognized and used for pressure calculations. Problems arise with these curve fitting methods in that the ionization current is variable under different load and speed conditions. The required Gaussian curve shapes occur at higher loads whereas at lower loads, the phenomenon is different. At higher speeds the curves of the chemical and thermal phase become merged.

The use of neural networks (NN) with the ion current technique as a system identification procedure began in the mid 1990's for work with PPP and AFR estimation and is still ongoing [71, 37, 49, 44, 43, 72, 53, 46, 57]. Following on from two-stroke AFR estimation, [71], Wickström *et al* applied similar techniques to PPP estimation and AFR estimation on a 1.6l Opel engine. For PPP estimation a window of the ionization current was sampled every degree from 6° ATDC to 35° ATDC. Instead of curve fitting or parameterization, principal component analysis is used to extract information from the ion current signal and reduce this data to a significantly less number of PCA variables per cycle [71, 37, 44, 43, 46, 51, 53]. Details of PCA theory can be found in [73] and later in this thesis in section 2.8.3. Speed, torque, ignition (assumed to be crank angle degrees but not stated explicitly) and the 7 PCA variables are used as training inputs to the non-linear feedforward NN with PPP as a training output. Training was done using the 'resilient backpropagation with early stopping' algorithm. The NN results are compared with a linear model and seem to be favourable although these results are from validation data and the method was not implemented on an engine.

Subsequent work involved processing of the pressure related section of the ion current curve with principal component analysis in a similar manner but the inclusion of not only speed and ignition timing but manifold air pressure (MAP) as inputs to an NN [44]. This was later concluded to be sensitive to disturbances and humidity so networks were trained from PCA results from the ion current signal exclusively to estimate the peak pressure position [46]. Again with promising results from validation data, no engine implementation occurs. In [57] the neural network is aimed to be trained in only seventy cycles per one operating condition (out of five based on throttle, speed, load, AFR and SA) to reduce computation expense. This implies a knowledge of AFR and SA is required and these five inputs are used in addition to another thirteen 'measurants' of the ion current signal with four pressure

'measurants' as target output. Results are claimed to be at an accuracy of 2.55° of CA when sampled once per 2° of CA although these results are again from validation data sets, not from engine implementation.

In [74], a peak finding algorithm for PPP estimation is attempted. This employs a quadratic function for successive local fits of the ion current signal operating in a crank angle window of 0° to 35° ATDC. Reported to be computationally inexpensive, it requires around twice the computation of the neural network method but a fraction of the memory storage.

Hellring and Holmberg [45] further reviewed three PPP estimation algorithms (N.B. specifically work from their own research team):

1. The Gaussian curve fit approach
2. The neural network approach
3. The peak finding approach

They conclude that the early Gaussian curve method is poor below engine loads of 30% maximum (the second peak of the thermal phase does not occur) and the computational complexity implies implemenation in real time on an EMS is a drawback. The NN approach is deemed positive being easy to implement but has too narrow an operational range. The peakfinding approach appeared the most promising meeting performance requirements and being easily implementable.

In [51] a method of indirect PPP information extraction from the ionization signal is investigated. A PPP estimator is extracted using high dimensional data analysis and is theoretically determined to be robust at various operating points. Rather than finding a correlated relationship between SA and PPP, a different measure of dependence is maximized to detect a relevant structure in the data. This theoretical technique was applied to engine data, whereby a pressure sensor was used, simultaneously with the ion current, to obtain the actual PPP reference measurement. A parameterized family of functions was obtained that relate to model parameters and engine parameters; spark advance, engine speed, first PCA variable of ion current signal, ion current signal integral and signal mass centre, etc. From candidate functions they are optimized in the sense of maximizing the quality of the PPP estimate. Although no engine implementation is undertaken, the technique is claimed to be of low complexity (after variable selection and calibration) and good theoretical results are achieved.

Delphi Corporation have also subsequently been experimenting with ion current sensing technology. In [53] and although unfairly critical of the efforts at Lund Institute of Technology,

PPP estimation was done using a neural network preceded by a PCA algorithm such as in [44]. This work concentrates, along with other authors [57], on technique simplicity. Using CPU hardware that is realistically implementable in vehicle production, Malaczynski *et al* note the computation in the PCA vector matrix multiplication as being 'more expensive' than the ANN computation. It should be noted that in the example used for this comparison, the ion current signal was sampled every 1/2 degree over 60° giving a vector input before PCA of 120 samples in addition to N, MAP and SA. Stated limitations of the PCA process are that all possible variations of combustion events must be utilised in the training data otherwise the PCA matrix multiplication output becomes non-representational and the system fails. A high correlation of results is reported but due to the cycle to cycle variability in the ion sense signal, a running average between three to ten cycles is used as a compromise between accuracy and response. The interesting technique of wavelet theory is also applied to AFR estimation and is covered in section 2.8.4.

Visteon corporation have produced a number of publications involving the ion current technique [52, 75, 40, 54, 55, 56, 62]. Inaudible knock detection methods are compared in [52]. Ionization signals are found to detect the knock phenomenon across the full range of engine operational conditions where the others sensors failed to. Standard knock sensors and in-cylinder pressure sensors were used as the comparison. From SA control through knock sensing, SA control from PPP estimation was attempted. Haskara *et al* [75] process the ionization signals to derive a metric for combustion quality in reference to partial burn/misfire limits. Implemented for cold start up strategies, this reduces the initial HC emissions as it reduces the warm-up time period for the catalysts by delaying the ignition timing to avoid misfires. Next, MBT timing was controlled using a PI type controller on an algorithm scheme calculating metrics from the ion current relating to the MFB curve [40]. Using the ionization current as a feedback signal closed loop control is achieved whilst reducing the cycle to cycle combustion variations. A metric for combustion stability is again used in [54, 55]. This is obtained from the integral of the ionization current signal during a specific crank angle domain 'window' (the 'chemical' and 'thermal' phases). A parameter is obtained from the crank angle at which the integral reaches, for example, 90% of the total window area. Stochastic feedback control is implemented through three methods; regulating a stochastic parameter to a mean value, adaptive feedback by using an error in a confidence level for a mean target then adjusting the mean target for the regulation controller appropriately and thirdly, with a PI controller and look up table.

Fuzzy logic is applied to PPP control in [76]. Following on from extensive earlier work by the same authors to determine the PPP from a dynamical model that assumes the 'thermal' phase of the ion current signal produces a peak that matches the peak on the actual pressure curve, fuzzy logic is applied as feedback control for the PPP. Good results are presented but

again, only from simulation.

2.6.5 Air-Fuel Ratio

To optimize the performance and reduce emission levels, measurements of the quality of combustion are required. Along with peak pressure position, air-fuel ratio (AFR) can be used in feedback control as a measure of combustion quality. For a three way catalytic converter to perform optimally, the AFR has to be kept within a window as small as 0.1 air-fuel ratios around the stoichiometric level [9]. It has been stated that an 80% catalyst efficiency window for the three emmission constituents (see fig. 1.1) corresponds to $\lambda = 1.0000 \pm 0.005$ [43]. Obviously this is a high degree of precision for a cycle by cycle basis so any sensors would need to operate accurately and continuously. Traditionally an engine management system (EMS) is employed to control the fuel and air for any speed and load through the use of the engine map; the design of this map being an intensive and expensive task. Feedback control is a method of overcoming this. A universal exhaust gas oxygen sensor (UEGO) is too expensive for production car use and being situated in the exhaust leads to slow sensor dynamics. A UEGO sensor also has a period of around 30 seconds in which it does not operate from being switched on until it has reached operating temperature. This period of cold start-up for an IC engine produces heavy exhaust emissions and pollutants.

It has been reported from various researchers e.g. [77, 78, 79, 34] that the air-fuel ratio has an effect on and can be estimated by the ion current produced during combustion. AFR information is present mainly during the chemical ionization phase section of the ionization current [49, 43], and as AFR becomes richer more ionization occurs which manifests as more pronounced peaks during the chemical phase of the ionization signal. By using ion current sensing to determine the AFR in each cylinder and then employing feedback control, 24% NOx reduction and a 4.4% drop in specific fuel consumption are claimed [41]. In [43], it is notable that during the thermal ionization phase portion of the ionization current signal, changes in AFR also produces similar changes to that experienced in the chemical phase. Peron *et al* [34] indicate that the entire window of ionization signal from near spark ignition to around 45° ATDC experiences a variation as AFR changes; richer mixtures producing a higher ionization level.

Spark plug voltage analysis, more specifically, the voltage decay time can be used to study AFR [65, 22] and should be mentioned due to its similarity in set-up and technique to the ion current method. The principle is that the spark discharge time is related to the number of ions in the flame and, hence, the quality of combustion. It was found that this discharge time was only sensitive to the AFR in lean mixtures.

Linde *et al* [71] determined the AFR using neural networks in combination with the spark

ionization signal on a two stroke engine. Three static λ target values were used, $\lambda = 0.6$, $\lambda = 1$ and $\lambda = 1.1$. Principal component analysis was undertaken on the ion current signal window for data reduction with a 'Sanger' network giving the backpropagation network inputs. Speed was also used as an input. Various back propagation networks were tested and the results demonstrate that the technique proved promising and was able to predict the static λ values with validation data.

Using PCA on this 'window' of the spark ionization signal can give inputs for a neural network that can predict averaged values of the AFR [37, 49, 43]. Using the ion current signal, the period between 10° ATDC to 20° ATDC (the flame front phase) was used to relate to AFR [49]. Along with the PCA variables, N, Torque and ignition timing were used with λ used as an output training variable. Trained using the 'resilient backpropagation with early stopping' algorithm, the ANN results are compared with a linear model and are an order of magnitude better. The results are from validation data and unfortunately the method was not implemented on an engine.

Further work using this methodology has seen the the inputs to the neural network increase in number to include engine speed, manifold air pressure and spark advance along with the PCA scores to predict the air-fuel ratio [43]. Results show a robust air-fuel ratio sensor to within 1.2 percent of the correct value, validated by data from a UEGO sensor though this work was then not implemented experimentally but demonstrated from hold-out data. The advantage of the ionization current method in this application is the ability to control each cylinder independently. The use of neural nets for AFR prediction is becoming commonplace in recent research [80, 24, 43]. Networks sizes and complexities have been determined through trial and error and estimation errors as low as 2 percent for 90 percent of test transients have been achieved [81].

Simultaneously to the research occurring in Sweden, the Centre for Automotive Research and Intelligent Transportation, Ohio State University were working on ion-current sensing technologies [37, 79, 39]. Early work from this team used PCA to extract features from the ion current before being processed with a neural network. Data was taken from a single-cylinder methane fueled test engine and a combustion bomb. Very high accuracy of AFR prediction using the ion-current signal is claimed in [39] using stochastic estimation methodology. Various parameters, representative of the ion current signal, are taken from averaged cycles and a model is used for the AFR values. The model polynomials are fitted in a least squares method and errors (averaged over 60 cycles) are below 0.5%.

As an alternative to the common spark ionization method, spark voltage characterization (SVC) offers similar advantages. This involves analysis of the time-varying spark voltage vectors and again, these vectors have been used with neural networks. It shares common

characteristics with the ion current method though SVC involves no bias voltage supply. A lambda accuracy has been achieved to within +/- 0.1 of λ in about 95 percent of all cases [21, 24] though the sampling rate to characterize the spark voltage during the few milliseconds before combustion requires advanced hardware.

2.6.6 Ionization Current Relationship to Emissions

To measure the level of unburnt hydrocarbons in an engine exhaust, a flame ionization detector (FID) is used in [82]. Unlike the ionization current method, the FID uses a bias voltage electrode immersed in a hydrogen/air flame into which the exhaust sample is supplied. The current flow to the electrode is virtually proportional to the rate of supply of carbon atoms in a hydrocarbon form [83] and therefore the method allows hydrocarbon measurements of the exhaust gas. The equipment is not for production use but does occur in real time.

The combustion temperature has a correlation with the NOx formation; higher combustion temperatures produce higher NOx concentrations. But NOx is formed primarily as a result of the oxidation of Nitrogen in the environment established by combustion in the cylinder, not the combustion itself [32]. Naoumov *et al*, presented models that could predict small concentrations of ions and electrons in combustion events from the chemical reactions of hydrocarbons and air. This model would be able to predict the peaks seen in the ionization current signal (thermal and chemical phases) in natural gas engines [84, 85]. It was claimed that the ion current peak during the thermal phase correlates with NO formation concentration, also found in [32]. 50% MFB was found to be correlated to 50% of the final value of the integral of the ionization signal and is used as a relative measure of the NOx formation; 50% MFB occuring later in the combustion cycle indicates lower NOx values since the temperature of combustion is lower [68].

EGR Dilution Limit Control

Exhaust gas recirculation (EGR) is a process of recirculating a certain volume of exhaust gas back into the cylinder through the inlet manifold or controlled valve timing; this practice can improve fuel economy and reduce NOx emissions by reducing the temperature of combustion (in gasoline engines and diesel engines) [86]. The effect of EGR on the ion current is similar in effect to reducing the air-fuel ratio. The amplitude of the chemical phase of the signal is weaker. The thermal phase of the signal is also reduced, more oscillatory and the duration is extended [50]. Obviously, there is an EGR dilution limit whereby exceeding this limit would deteriorate combustion quality [56].

This phenomenon can be utilised in the control of EGR operation rather than relying

on extensive pre-calibrated EMS look-up tables. Combustion is a stochastic process and the stability is often measured by the indicated mean effective pressure (IMEP), which would imply the necessity for an in-cylinder pressure sensor. The interpretation of the ionization signal has been exploited as an alternative for use in the calculation of IMEP. Haskara *et al* state that the use of the integral of the ionization signal is a satisfactory method of assessing the combustion duration [75]. The covariance and the coefficient of variation (COV) of the integral of the ionization signal were correlated with the covariance of IMEP in [87] and found to be good at lower load conditions. In [56], the integral of ionization is used to obtain a measure of 90% combustion duration under varying EGR conditions. A standard deviation of this duration is used in feedback control to adjust the EGR amount.

2.7 Ion Current Experimental Implementation and Feedback Control

It is accepted that knock and misfire events manifest in ion current signals differently to a normal combustion event. It is also accepted that there is a variation in ion current signal due to changing air-fuel ratio or peak pressure position. Much research has been done using the ion current technique or spark plug voltage characterization to demonstrate these differences online [60, 63, 22, 61, 59, 62]. Research has been done to exploit these differences and extensive publications demonstrate its effectiveness theoretically but although data is collected from actual experimental engine apparatus, the presented algorithms are not usually implemented back on the engine for online estimation or control, as in the following publications: [35, 37, 42, 49, 24, 43, 74, 38, 23, 51, 45, 53, 57]. Obtaining an ion current signal is a straightforward matter (after obtaining the necessary hardware) of attaching the ion current sensing equipment between the coil pack and the spark plug of an engine and reading an output voltage. The difficulty in the ion current technique is using the obtained signal effectively; feature extraction is challenging and implementing any algorithms back onto an engine for real time estimation requires fast data acquisition hardware. The publications that demonstrate the technique experimentally, implementing parameter estimation algorithms online, are in the minority [50, 54, 21]. Discounting knock control, there are few examples where estimation and feedback control of air-fuel ratio or peak pressure position implementations have been demonstrated [36, 48, 44, 41, 40, 46] whether successful or not. In [76], no experimental apparatus was used and so the research was purely theoretical.

2.8 Signal Processing Techniques

The resulting ion current signal varies significantly depending on many parameters. The ideal signal shows two peaks, as in fig. 2.1, which are rich in combustion information. This would allow simple algorithms to locate the peaks to extract information but unfortunately this 'double bump' curve occurs at a small operating range of engine parameters, that is higher loads, lower speed and lower throttle positions. As engine speed increases, these two peaks can merge. At lower loads, the second peak can disappear. Feature extraction proves to be the most difficult step in implementing the ion current technique successfully. This section explores the methods that have been used in attempts to extract useful information from the ion current signal.

2.8.1 The Gaussian Curve Fitting Technique

A series of papers, [25, 36, 35, 42, 38], attempted feature extraction from the ion current signal using Gaussian curve functions and parameterized functions to describe the relevant sections of the ion current signal. The analytical expression for the ionization current is [35]:

$$\frac{I}{I_m} = \frac{1}{(\frac{p}{p_m})^{\frac{1}{2}-\frac{3}{4}\frac{\gamma-1}{\gamma}}} e^{-\frac{E_i}{2kT_m}\left[(\frac{p}{pm})^{-\frac{\gamma-1}{\gamma}}-1\right]} \tag{2.2}$$

where the variables are: I, ionization current; I_m, maximum ionization current; p, cylinder pressure; p_m, maximum cylinder pressure; T_m, maximum temperature; γ, specific heat ratio; k, Boltzmann's constant; E_i, ionization energy.

It is assumed that the pressure relating phase of the ionization current is close to a Gaussian function and a second Gaussian function added to this model to represent the flame front section of the signal. The combined Gaussian model of the ionization current becomes:

$$I(\theta) = \alpha_1 e^{-\frac{1}{\alpha_2}(\theta-\alpha_s)^2} + \beta_1 e^{-\frac{1}{\beta_2}(\theta-\beta_s)^2} \tag{2.3}$$

where θ denotes the crank angle.

However, the extreme variability of ionization current across different engine operating regions gives noisy signal forms with numerous peaks and shapes. These signals cannot be modeled accurately by Gaussian curves therefore this method is severely limited for feature extraction.

2.8.2 Peak Finding Algorithms

In [74], an algorithm termed the 'peakfinder' is attempted, which is again later reviewed in [45]. The peakfinder uses a quadratic function for successive local fits to a specific window of interest (0 to 35° ATDC) of the ion current signal. The second derivative gives information as to the change in the slope; a negative indicates a maximum and a positive indicates a minimum. A backwards sliding window of 5° is used and the algorithm stops when the window ends or the peak of the thermal phase is found. One parameter, a threshold for the local curvature of the signal, is used to locate the peak. This gives a maximum of thirty calculations. The authors state that this method uses half of the iterations or calculations that the neural network approach uses. Again, peak finding algorithms would not work to locate the peak pressure position if the peak of the thermal phase did not exist.

2.8.3 Feature Extraction with Principal Component Analysis

PCA is a multivariate statistical process that can be used to significantly reduce sample data sizes by obtaining the most significant characteristics in the data set and thus reduce data sample sizes. This simplification is done by generating a new set of variables, the 'principal components', from an original data set. The full set of principal components is as large as the original set of variables but it is usual for the sum of the variances of the first few principal components to have a substantial amount of the total variance of the original data, hence the few most 'principal' component scores will effectively represent the original data set [73]. This technique has been used to extract combustion information from a window of a cycle by cycle varying ion current signal quite effectively [71, 37, 44, 43, 46, 51, 53] and also reduces the volume of data per combustion cycle for the interpretation.

A summarised method is as follows:

- The mean of the data set is removed and the data is normalised
- A covariance matrix is calculated
- The eigenvector-eigenvalue pairs are found
- The eigenvectors with the highest corresponding eigenvalues are selected
- These eigenvectors are multiplied by the original data set to produce the new reduced data set.

The initial data set consists of vectors of data in rows to form the data matrix, each row is an observation, and each column is a variable. The data is normalised and considered to be vectors X_1 to X_p where p is the number of variables. The covariance matrix is calculated, which is a $p \times p$ matrix, i.e. this is a matrix whose individual elements are the variance between one row or vector and another, the main diagonal of the matrix contains elements that are the variance of that row or vector and itself. The matrix is also symmetrical about the main diagonal.

If Σ is the covariance matrix of the vector $X' = [X_1, X_2, \ldots, X_p]$, it has eigenvalue-eigenvector pairs (σ_1, e_1) to (σ_p, e_p) where $\sigma_1 \geq \sigma_2 \geq \cdots \sigma_p \geq 0$. The i^{th} principal component is given by $Y_i = e_i'X = e_{1i}X_1 + e_{2i}X_2 +, \ldots, e_{pi}X_p$ where $i = 1, 2, \ldots, p$

The percentage that each score contributes to the total population variance can be calculated. Let $Y_1 = e_1'X, Y_2 = e_2'X, \ldots, Y_p = e_p'X$ be the principal components. Then

$$\sigma_1 + \sigma_2 +, \ldots, \sigma_p = \sum_{i=1}^{p} Var(Y_i)$$

so the proportion of total variance explained by the i^{th} principal component is :

$$\frac{\sigma_i}{\sigma_1 + \sigma_2 +, \ldots, \sigma_n}$$

where n is the size of the covariance vector.

2.8.4 Feature Extraction using Wavelets

Wavelets are a relatively new field in signal processing which allows analysis of signals. Wavelet analysis is developed from Fourier analysis (or Fourier series for discrete signals),

which breaks down a signal into constituent sinusoids of different frequencies. This can be useful for examining the important frequency content of a signal but the Fourier Analysis technique has shortcomings when analysing transient or non-periodic signals because time domain information is lost in the transformation. Most real world signals such as speech, intermittent vibrations or music contain valuable time information such as drift, beginnings and ends of events or abrupt changes. Hence, Short-time Fourier Transforms (or Windowed Fourier Transforms) were developed to provide localised time and frequency approximate information. STFTs transform signals into a two dimensional function of time and frequency but accuracy is determined by the size of the window and once the size of the time window is determined, it cannot be changed for different frequencies. This is an obvious disadvantage when processing signals with a time dependent spectrum, such as a chirp signal [88, 89].

From STFT, wavelet analysis was developed, allowing variable sized time windows. It allows the study of both high and low frequency information using relatively shorter and longer time windows respectively. Wavelet analysis breaks down a signal using finite time, irregular signals (wavelets) instead of a continuous smooth sinusoid as in Fourier methods. This allows better analysis of signals with squarer edges or with local phenomenon.

A signal, S, is decomposed with a combination of filters; a low pass filter applied to S will extract low frequency components of the signal whilst high pass filters extract high frequency components. The resulting two signals are effectively downsampled so that the combined data size of the two signals is not greater than the original signal. The data in the downsampled resulting signals are discrete wavelet transform (DWT) coefficients; the resulting coefficients from the low pass filter are referred to as approximation coefficients, cA, whilst the resulting coefficients from the high pass filter are referred to as detail coefficients, cD, [88]. Filters used are commonly derived from the Daubechies family of wavelets.

Figure 2.5 illustrates a three level decomposition in this manner, whereby the low pass and high pass filters are applied to the preceding approximation coefficients to further extract approximation and detail coefficients.

The signal can then be reconstructed as an approximation or a detailed reproduction of the original signal using inverse DWT.

Wavelet analysis has been applied to the ion current in [53]. Wavelet analysis was used in a three level decomposition, as per fig. 2.5, of the ion current signal. The signal was then reconstructed as an approximation of the original signal before feature extraction was applied to the reproduced signal. The type of filter used in the decomposition is undisclosed and it is reported that this method is more efficient at reducing data sizes than the PCA method (achieving $\frac{1}{8}^{th}$ of the original data in the signal approximation). This does not take into account the selection of the few most principal components as a data reduction

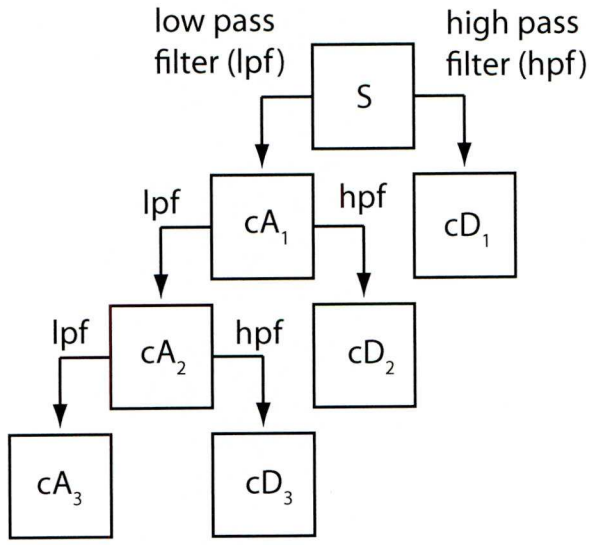

Figure 2.5: A Three Level Wavelet Decomposition

method in PCA which can also achieve $\frac{1}{8}^{th}$ of the original size of data. In addition, the signal reconstruction used in the wavelet analysis method is a further computation in addition to an undisclosed feature extraction process as another computation.

2.8.5 Identification of Combustion Measurants and Metrics

Predicting PPP and AFR from the shape or peaks of the ionization signal directly has been discussed. Research has also been attempted to extract some other measure of combustion quality or combustion duration from the ionization signal to relate to the SA. Attard and Micallef [68] state 50% MFB was found to be correlated to 50% of the final value of the integral of the ionization signal at an accuracy of 99.7%. In [75] the use of the integral of the ionization signal is stated as a satisfactory method of assessing the combustion duration and this is used to limit the SA retard in closed loop control. The integral is used in a further study to obtain a measure of 90% combustion duration [56]. Gazis *et al* suggest the ability to extract up to 13 measurants from the ionization signal to relate with a neural network to pressure information [57]. These are the crank angles of the start of the ion signal, first peak and second peak; magnitudes of the two peaks; slopes of four locations of the curves; areas under three sections of the signal and finally the crank angle location of the end of the signal. These would be extremely dependent on the shape of the ionization signal and would be computationally expensive to determine in real time. Building on their previous work [69], the concept of these measurants is explored in [40, 62] where by inflection points and peaks of the ionization current are used to relate to MBT, illustrated in the fig. 2.6, which is an idealised ionization current curve. The first inflection point after the first peak relates to the maximum acceleration of net pressure (10% to 15% MFB), The inflection point after

the second peak is 50% MFB. These points along with the second peak are used for MBT timing, but again depend on the shape of the obtained ionization signal.

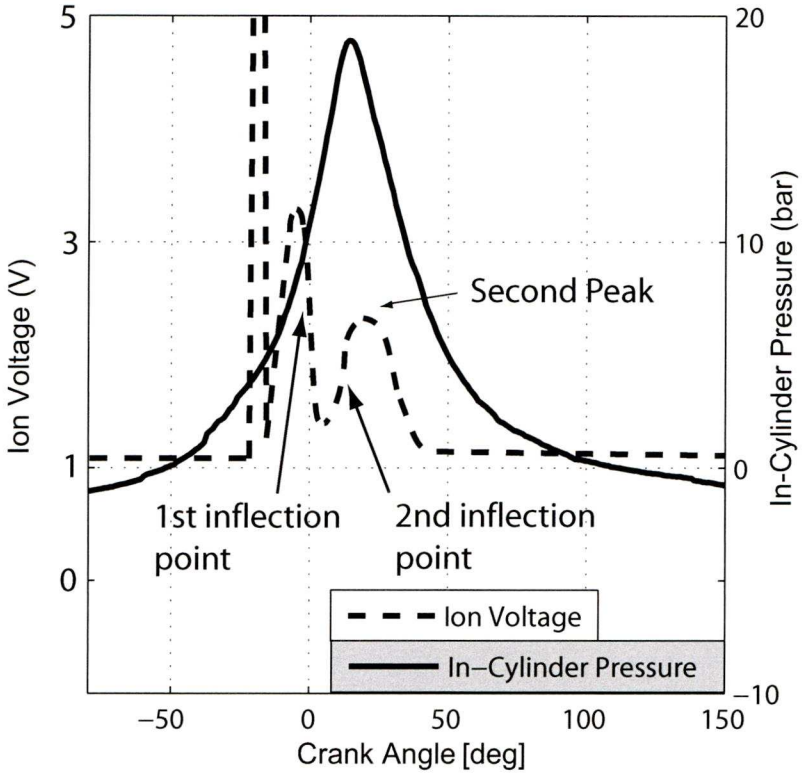

Figure 2.6: An Ideal Ionization Curve

2.9 Neural Networks

2.9.1 Overview of Neural Networks

Neural networks (NN) have been used for over five decades but only within the last twenty years have there been solid and suitable applications, this field is still developing rapidly. Neural networks have been successfully applied in pattern or handwriting recognition, speech, vision and control systems and, more relevantly, in identification.

The application of NN in automotive sectors is of major interest currently. Powertrain problems are well suited to the modelling abilities of the NN and various attempts have been undertaken at modelling engine operating conditions. In [90], the dynamic modelling of the manifold pressure and mass flow processes were done with recurrent networks. In-cylinder pressure work and AFR estimation has been discussed extensively [91, 92, 72, 81, 93, 94, 95, 96].

Hanzevack *et al* [91] used various available engine variables to predict AFR, emissions, power output and fuel pressure in a general aviation aircraft SI engine with three neural networks. Good prediction accuracy was achieved in steady state (±3% to ±6%) dropping over transients (±4% to ±11%). In [72], a feedforward neural network is used to predict the location of peak pressure using five samples of voltage from in-cylinder pressure sensors. The estimated PPP is then used as an index for combustion phasing.

Arsie *et al* initially modeled and then controlled the AFR of SI engines in a series of papers using neural networks [97, 98, 81, 99, 96]. The papers model wall wetting dynamics in SI engines using recurrent NN. Multi input-single output structures involving injected fuel, manifold pressure and engine speed as inputs; the AFR at the exhaust gas oxygen sensor location has been considered as an output. Control is implemented in an inverse identification of the NN using the same identification data for the original NN [96].

Similar work with the use of neural networks with the added complexity of the ion current method for PPP estimation and AFR estimation has also been attempted [37, 49, 43, 24, 53, 21, 57].

2.9.2 Network Structures

Neural networks are composed of simple small elements, or neurons, and have their origins developed from the human brain. It is the inter connection of these neurons in parallel that give the neural networks their ability to compute and defines their specific function. This network of neurons is adjusted or trained so that a particular input will lead to a particular output. The adjustment or training arises from differences in a comparison of a target output from an actual output and this training continues to reduce this difference so that the actual output matches the target output. This section establishes the notation used, details neural networks in their composition, format and training styles and from this emerges techniques applicable to engine identification and control.

The Basics

The small component element, the neuron, is the building block of a neural network. There are three basic elements of the neuron.

- A set of synapses or connecting links
- An adder
- An activation function

The neuron can be fed with multiple inputs $x_1, x_2, \ldots, x_R$ giving the input vector x of size R. The neuron transmits the input elements through a connecting link (or synapse) that multiplies its strength by a scalar weight, $w1, w2 \ldots, w_R$ to form a product $x_R w_R$. These products are then summed using the adder with a bias b to generate the net input to the neuron, n, (or axon's signal) as in equation 2.4. The input n is the input to the neuron activation function, f, which then gives the neuron output y. See fig. 2.7 for a basic model of an artificial neural network neuron.

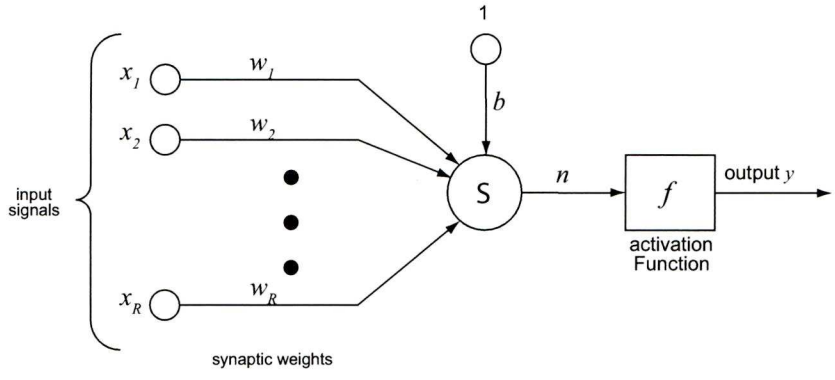

Figure 2.7: Schematic of a Neuron

$$n = \sum_{i=1}^{R} (w_i x_i) + b \tag{2.4}$$

The output of this neuron thus corresponds to equation 2.5:

$$y = f(n) \tag{2.5}$$

There are numerous activation functions that can be implemented in the neuron. The Matlab NN toolbox currently has 13 activation functions. Although the choice of activation function determines the kind of neuron model and how the neuron behaves given input data, it is the weights and biases that are the adjusted parameters of the neuron through training.

Activation functions

An overview of the 13 activation functions of the Matlab NN toolbox are presented in table 2.1 [100].

Table 2.1: Neural Network Activation or Transfer Functions

Function Name	Plot of Function
Competitive	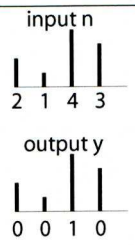
Hard Limit	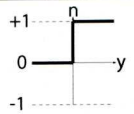
Symmetrical Hard Limit	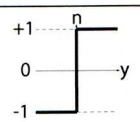
Log Sigmoid	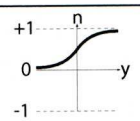
Positive Linear	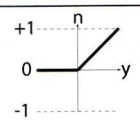
Linear	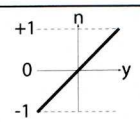
Radial Basis	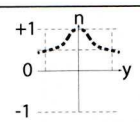
Saturating Linear	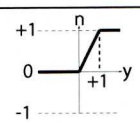
Symmetrical Saturating Linear	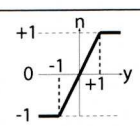
Soft Max	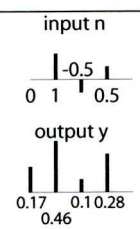
Hyberbolic Tangent-Sigmoid	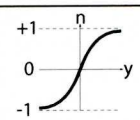
Triangular Basis	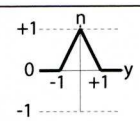
Inverse	N/A

Layers

A single neuron is capable of very little computationally, however many neurons can be combined to create a layer. A network can consist of a single layer or multiple layers can be combined to create a larger network. The layer that produces the output is termed the output layer, all others are considered the 'hidden' layers. Figure 2.8 illustrates a non-abbreviated layer with R input elements and S neurons.

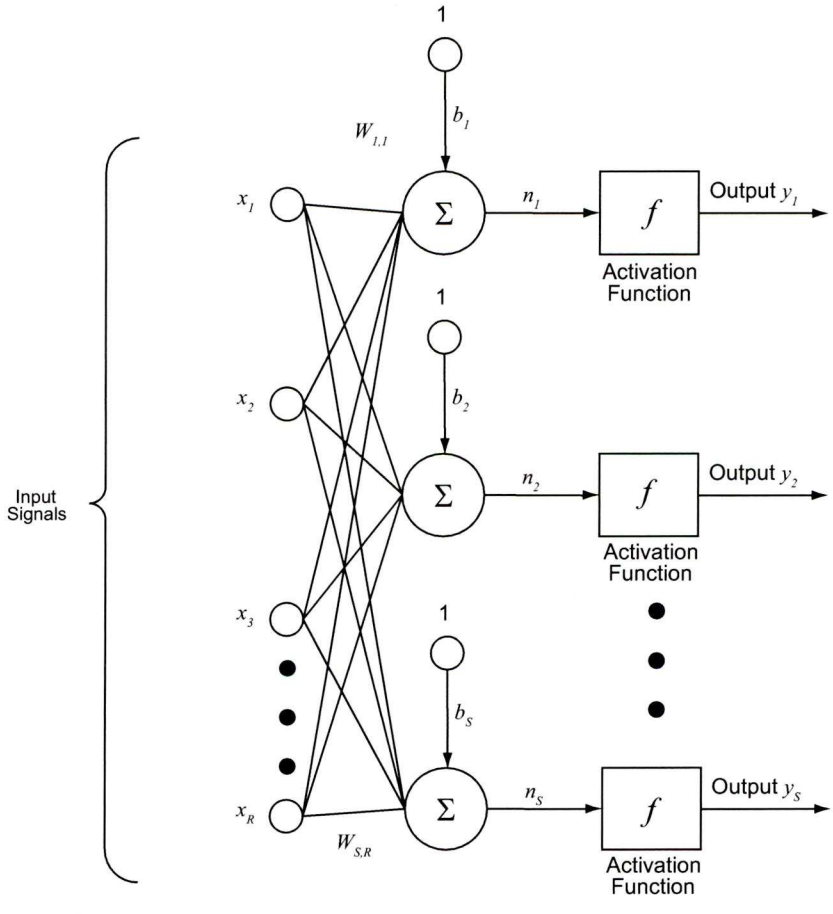

Figure 2.8: Schematic of a Single Layer

This schematic can be abbreviated as in fig. 2.9 and this notation will be used throughout. Again R denotes the number of elements in the input vector, S denotes the number of neurons in the layer, hence b is an S length vector and x denotes an input vector of length R. It should be noted that W is the S x R weight matrix through which the input vector enters the network.

$$W = \begin{bmatrix} w_{1,1} & w_{1,2} & \dots & w_{1,R} \\ w_{2,1} & w_{2,2} & \dots & w_{2,R} \\ \vdots & & & \vdots \\ w_{S,1} & w_{S,2} & \dots & w_{S,R} \end{bmatrix}$$

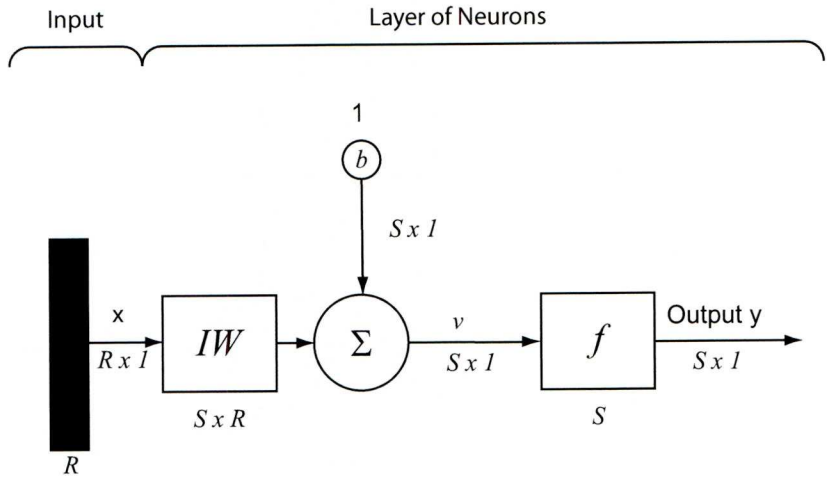

Figure 2.9: Schematic of an Abbreviated Single Layer

The output, y, of this single layer is a S length vector and thus corresponds simply to equation 2.6:

$$y = f(Wx + b) \tag{2.6}$$

Now if two layers together are joined together sequentially, there would be one output layer and one hidden layer. The input layer weight matrix (in this case the hidden layer) is denoted IW and other Layer weight matrices are denoted LW. See fig. 2.10.

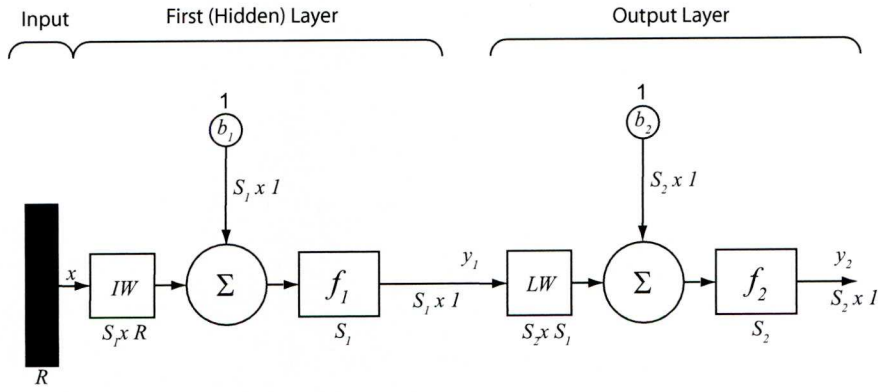

Figure 2.10: Schematic of a Two Layer Network

Hence the output y of this network corresponds to equation 2.7:

$$y = f_2(LWf_1(IWx + b_1) + b_2) \tag{2.7}$$

Types of Neural Network

Three common types of neural network have been identified; multi layer perceptrons (MLP), recurrent networks [101] and radial-basis function networks [100].

The single layer feedforward network is the simplest form of a layered network consisting of inputs that are projected through a single layer of neurons (essentially the output layer of neurons). They are called feedforward networks because connecting synapses only pass data forwards, there are no feedback loops. The single layer may have numerous neurons but they are suited to very simple applications. An MLP is a multilayer feedforward network and is an expansion of the single layer but contains one or more hidden layers. This becomes a more complex neural network and can thus fit higher order or more complex functions. The neurons in each layer have as their input the output from the neurons in the preceding layer only. Hidden layer activation functions are of tan-sigmoid type with the final layer containing the linear activation function. These types of networks are suited to, or indeed limited to, speech analysis or simple pattern recognition.

The recurrent neural network is distinguished because it contains feedback loops and tapped delay lines, which allow the network to behave dynamically and work with delays. This then is referred to as a dynamic network whereas networks with no feedback or delays are referred to as static networks. It is the dynamic recurrent neural network that is of interest to this work because of their ability to identify delays. For example, this would be especially useful in the case of identifying an air-fuel ratio model where any perturbation in the volume of fuel injected in a particular engine cycle causes a fluctuation of the λ ratio measured downstream by a UEGO wideband oxygen sensor that is delayed due to fuel puddling and exhaust gas flow.

The radial-basis function (RBF) neural network consists of a slightly different structure to that of a perceptron based network and is trained in a different way. A perceptron based network uses statistical approximation in its training algorithm, an RBF network is considered as a curve-fitting problem in multi-dimensional space so the training of which involves finding a surface in multidimensional space that best fits the training data [101].

2.9.3 Network Size

A few basic rules can be observed to determine network size but the size is application specific. Training is fundamental to determining if a network structure is appropriate. After network

training, the network will either work satisfactorily or not. If the network generalizes well then the network is large enough and step reductions in the size of the network can be undertaken, again with retraining at each size reduction. Upon reducing the number of parameters, a minimum network size will be obtained that will still achieve the required performance error.

2.9.4 Training

A neural network derives its computing power through its massively parallel distributed structure and secondly, its ability to learn and therefore generalize [101]. Generalization refers to the neural network producing reasonable outputs from inputs not encountered during training. It is this training that allows the neural network weights and biases to adjust through repetitive iterations so the network becomes more knowledgeable about its environment.

There is more than one method of training a neural network, some methods are more suited to a particular network structure than others and they differ in the way that they allow the synaptic weight to update or adjust with each iteration. Indeed, the manner in which the neurons of a neural network are structured is intimately linked with the algorithm used to train that network [101]. For this reason, the training algorithms and rules covered here are limited to those appropriate for dynamic recurrent neural networks.

Fundamentally, the identification data that is available for training determines the training algorithm style. *Supervised* (also known as 'training with a teacher' and 'teacher forcing') is used when the output (or target) data is available for the training algorithm. The training algorithm updates the weights and bias values of the neurons with a cost function, usually *mean-square error* that compares the desired target output and the actual network output. *Unsupervised* training (also known as 'training without a teacher'), as expected, refers to training a network without target or output data.

With these two training styles established, there are also two basic concepts of presenting the identification data to networks in training; incremental training or batch training. In incremental training the weights and biases of the network are updated each time an individual input is presented to the network. In batch training the weights and biases are only updated after all the inputs are presented [100], referred to as an 'epoch'. There are two passes to the training during an epoch; the forward pass, where the identification data is presented to the network and a backward pass, during which the weights and biases are updated. As stated, these updates are made according to a cost function, the aim being to minimise the cost function. Following is an account of the most basic of training functions and its evolution to faster training functions that require less computation.

A dynamic recurrent neural network is an extension of a multi-layered feedforward net-

work but with feedback loops. The most basic training algorithm for multi-layered feedforward networks is standard backpropagation (SBP). Backpropagation, a *supervised* training algorithm in batch mode, is a gradient descent technique, in which the network weights are moved along the negative of the gradient of the cost function [100], that is, the direction in which the cost function is decreasing most rapidly.

In general terms, the error signal at the output of neuron j at iteration n is defined as

$$e_j(n) = d_j(n) - y_j(n) \tag{2.8}$$

where $d_j(n)$ refers to the desired response or target for neuron j for iteration n and $y_j(n)$ refers to the function signal or actual output of neuron j for iteration n. If the instantaneous value of the error energy for neuron j is defined as $\frac{1}{2}e_j^2(n)$, then the instantaneous value of the total error energy, $\xi(n)$ is obtained by summing the error energy over all of the neurons in the output layer. Errors can only be calculated directly from these output neurons as the outputs from these neurons are compared to the target identification data.

$$\xi(n) = \frac{1}{2}\sum_{j \in C} e_j^2(n) \tag{2.9}$$

where C includes the neurons in the output layer.

The aim of the training algorithm is to minimise this cost function by applying a correction to the synaptic weights. Consider the values of a synaptic weight $w_j(n)$ at iteration (n), then the correction $\Delta w_j(n)$ applied to the synaptic weight, according to the delta rule, is proportional to the partial derivative $\frac{\partial \xi(n)}{\partial w_j(n)}$.

$$\Delta w_j(n) = -\eta \frac{\partial \xi(n)}{\partial w_j(n)} \tag{2.10}$$

where η is the learning rate and being negative indicates the gradient descent. Hence one iteration of this algorithm in sequential training can be written:

$$w_j(n+1) = w_j(n) + \Delta w_j(n) \tag{2.11}$$

When considering batch training of the back propagation algorithm, weights are updated after all of the training data has been presented, this constituting an epoch. The cost function is now defined as the averaged squared error across all time steps, ξ_{av}, where n, the training example is now an epoch:

$$\xi_{av}(n) = \frac{1}{2N} \sum_{n=1}^{N} \sum_{j \in C} e_j^2(n) \tag{2.12}$$

where $e_j^2(n)$ is the error at output neuron j at epoch n and N is the number of training data samples. The adjustment to the weight, according to the delta rule, now becomes:

$$\Delta w_j = -\eta \frac{\partial \xi_{av}}{\partial w_j} \tag{2.13}$$

and

$$w(n+1) = w(n) + \Delta w(n) \tag{2.14}$$

This is the standard backpropagation algorithm [101, 100, 102] but has the problem of being slow to converge so variations on the standard backpropagation are used. Faster training rates can be achieved through allowing variable learning rates. If the learning rate is set too high, the algorithm can oscillate and become unstable but if the learning rate is too small, the algorithm takes too long to converge. An adaptive learning rate attempts to keep the learning step size as large as possible while keeping learning stable.

Multilayer networks and dynamic recurrent neural networks often use sigmoid transfer functions in the hidden layers, see table 2.1. These functions compress an input range into a finite output range, hence saturation of the output occurs from the neuron. The gradient approaches zero as the input becomes large. When using a steepest descent algorithm this causes a problem due to the gradient being very small therefore causing small changes in the weights and biases, even though the weights and biases are far from their optimal values [101].

An extension to the simple back-propagation technique is to use Levenberg-Marquardt (LM) algorithms to update the weights. First reported in [103], it was then adopted for neural network training algorithms [104]. An evolution of the Gauss-Newton method, it is a second order training algorithm that can attain second order convergence speeds. First order training algorithms use only the first order derivatives (Jacobian matrix) of the cost function (errors) whilst second order training algorithms use the Hessian matrix (second order derivatives of the cost function) to introduce curvature information to the weight update and speed up training. The Newton method requires a full calculation of the Hessian matrix for the incremental update of weights, $\Delta w(n)$:

$$\Delta w(n) = H^{-1}(n) g(n) \tag{2.15}$$

where $H^{-1}(n)$ is the inverse Hessian matrix and g(n) the gradient vector of the average cost function. The Levenberg-Marquardt overcomes this expensive computation by approximating the Hessian matrix from the Jacobian Matrix:

$$H = J^T J \tag{2.16}$$

where J denotes the Jacobian matrix. The gradient can be calculated from:

$$g = J^T e \tag{2.17}$$

where e is the vector of errors in the network. The weights are thus incrementally updated:

$$\Delta w(n) = -[J^T J + \mu I]^{-1} J^T e \tag{2.18}$$

where μ is a scalar value that can be known as the learning rate. When μ is zero, the algorithm equates to the Newton's method but using the approximate Hessian matrix. When μ is large, the weight update becomes gradient descent with a small step size. μ is set during the training. The goal is to have μ as small as possible so as to shift toward Newton's method as quickly as possible since it is faster and more accurate near an error minimum. Training commences with a small value for μ and the error of the weight vectors examined for an increase or decrease. If the next weight vector produces a smaller error, this is a successful step and μ is decreased. If the next weight vector produces a larger error, μ is increased, the weight revert to their previous value and the step is repeated [100, 105, 101].

2.9.5 Stopping Criteria

Training can be stopped upon reaching predefined stopping criteria, such as reaching a limit on training iterations or epochs, or when a particular network error has been reached. These methods produce little insight into the quality of the training or the resulting performance achieved by the training [106].

Early stopping is a useful technique that can automatically stop training at an optimum epoch to prevent over-training of the data. As per identification theory, the available data set is divided into more than one subset for validation purposes; one set for estimation and a second set for validation. The first set, for estimation and training, is used for computing the gradient, updating the network weights and biases and obtaining the sum of squared errors. After each pass or epoch of the first estimation set, the second validation set is employed as the error on the validation set is monitored, though the weights and biases are not updated

from this validation set error. After each epoch the errors on the validation set and the training set decrease. However, over-training occurs when when the neural network begins to overfit to the estimation data; the error on the validation set typically begins to rise. This means that the training has reached the optimum epoch and training should stop.

2.9.6 Drawbacks of Neural Networks

Neural networks would appear to be a universal solution to modelling. A multilayer perceptron network is reported to be have the ability to identify any linear or nonlinear relationship [105].

Neural networks have the limitation of only being able to predict an output from inputs that are within the ranges of the identification data ranges. This is due jointly to the method of processing input signals and the inherent nature of the tansigmoid activation. The estimation inputs, according to neural network theory, are processed by mapping or normalising them to a maximum of 1 and a minimum of -1. The tangsigmoid functions are then trained within these normalised signal bounds. Hence when inputs of values outside of the mapped estimation data are experienced by the network, there is saturation at the limits of the tansigmoid functions hence the output of the network has finite bounds. This results in the network being unable to predict outputs outside of the estimation training data range.

2.10 Control Methods

Feedback control theory has progressed as practical problems that needed to be solved have presented themselves. The first rigorous mathematical analysis of feedback control systems was written in 1868 by J. C. Maxwell [107], who analyzed the stability of a well documented early feedback system: Watt's flyball governor for speed regulation of a steam engine. The period proceeding this until the early 1900's is known as the primitive period of automative control, from then until around 1960 is known as the period of classical control and subsequently from around 1960 until present is known as the period of modern control [108].

2.10.1 Feed-forward and Feedback Control

Feed-forward control is effective only when the model of the system is well understood. It uses measurable, available system inputs to provide measurable known responses. The disadvantage is that feed-forward does not take into account unknown or unpredictable external inputs that can cause errors to the output. A feedback signal could compensate for any experienced errors.

Feed-forward control is implemented in an engine management systems (EMS) for fuelling by using estimates of the air entering the cylinders from manifold absolute pressure (MAP) or mass air flow (MAF) sensors and manifold wall wetting dynamics to determine the correct fuel pulse width (FPW) [109]. The FPW is determined from mapped EMS look-up tables in the static sense where dynamics are not addressed. Additional disadvantages of using this feed-forward control means that the resulting look-up tables require extensive modification for environmental effects such as temperature or humidity [12]. Due to transport delays of fuel within the engine intake manifold, fast feed-forward control is required [10]. The requirements for a feedback controller is primarily to compensate for any error in the feedforward controller due to modelling deficiencies, manufacturing tolerances, mechanical wear or environmental effects. The feedback signal in a fuelling system would arrive from an UEGO (universal exhaust gas oxygen) sensor.

2.10.2 Stochastic Control

Stochastic control is an optimisation method that aims to minimise the effects of random noise disturbances to a model. Random signals cannot be described as deterministic, only the average properties are known. The development of minimum variance (MV) control to deal with such systems can be attributed to Astrom [110]. The optimal MV regulator to achieve the lowest output variance was intended only for zero mean disturbances and therefore could not reject non-zero mean disturbances and was unable to allow tracking to specific set-points. Subsequent developments included non-zero tracking regulation with integrated minimum variance (IMV) and de-tuned MV which limited the control effort [111].

Minimum variance control of peak pressure position (PPP) through spark advance (SA) regulation on a single cylinder of a multi-cylinder engine was presented in [8] using pressure directly measured using an in-cylinder pressure sensor. This was revisited and expanded to cover all cylinders in [112] with the same equipment.

2.10.3 Robust Control

In stochastic control, uncertainties in the system are modelled as probability distributions combined to yield a control law which deals with the expected values of inputs and control. Unexpected or abnormal situations may arise that allow the system to experience inputs that are not necessarily close to the expected value; optimal control algorithms are not always tolerant to changes in the control system or the environment. This may not be acceptable for control systems that have safety critical implications such as flight dynamnics or avionics.

If system gains or other parameters are not precisely known this leads to model un-

certainty and can arise from a number of sources; uncertainty in the model of the plant, disturbances that occur in the plant system and noise which is read on the sensor inputs. Each of these uncertainties can have an additive or multiplicative component [113]. Robust control is an approach to controller design that can explicity deal with this uncertainty and some performance of the controller may be sacrificed in a trade-off to ensuring the system requirements or robustness. It is especially useful in the case of multivariable MIMO models that can have multiple control loops within the closed loop, whereby the robustness of each individual control loop cannot be simultaneously maximised.

A popular field with regard to robust control is H_∞ theory which is conceptually concerned with bounding the values of a given closed loop transfer function of interest. Consider a closed-loop transfer function, often referred to as a sensitivity function F(s), where the H_∞ norm is concerned with bounding the peak of the frequency response across all frequencies.

Loop shaping is a robust control method published in [114] for shaping the open loop system $L = GK$ by tuning the controller K. Many of the constraints for the desired closed loop shapes can readily be translated into similar open loop requirements.

2.10.4 Predictive Control

Model predictive control relies on a dynamic model of a process, that is to be controlled, defined by system identification [115]. Again, as an optimization control method, it aims to minimise a cost function using a history of past control actuations. Although a well established control approach, its application to time critical systems requiring fast feedback is a major computational challenge [116], such as in automotive applications. Ferreau *et al*, [116], aim at tracking a desired torque profile of a gasoline engine without increasing the emissions, using the throttle and the exhaust gas recirculation valve as manipulated variables. They report that it was possible to reduce the torque error considerably compared to controls taken from an optimal static map although no experimental results were presented. In [117], and air-fuel ratio control scheme was devised using generalised predictive control consisting of two feedback systems; one on an engine model and a second on the catalyst system. An ARX model was used for the engine and catalyst, around which the controller was implemented. Again, experimental results were not presented.

2.11 Conclusions

Fixing peak pressure position to a predetermined crank angle value through the control of spark advance is a desirable requirement but the cost of in-cylinder pressure sensors effectively rule out direct PPP measurement in production engines. Similarly prediction and control of

AFR is expensive with UEGO sensors, especially if individual cylinder AFR is required. The ion current signal technique can offer a low cost solution to both applications. Careful processing and feature extraction of selective regions of the ion current signal, using techniques such as principal component analysis or wavelet analysis, can offer insightful information relating to combustion. Of the numerous applications which are feasible, PPP and AFR estimation are of interest in this work. It will be ion current sensing that is employed in this research for estimation and control of both applications since it can be implemented with no additional engine modifications or expensive machining processes.

Feature extraction is the most difficult step in implementing the ion current method. The correct window of the signal needs to be accessed depending on the desired estimated variable and furthermore obtaining the correct information from this window is not trivial. Principal component analysis has been repeatedly used and appears to work as a feature extraction method.

Modelling of the systems for predicting air-fuel ratio or peak pressure position by a neural network is a popular method and will also be adopted in this research. Although parameter estimation has been undertaken extensively, details of closed loop control using the ion current method is limited within the literature due to its challenging nature.

Optimisation control, specifically minimum variance techniques, are suitable for PPP regulation due to the inherent stochastic nature of combustion. Minimum variance control is explained in greater detail in chapter 4. Robust control techniques will be attempted on air-fuel ratio control and details of loop shaping are detailed in chapter 7.

Chapter 3

Experimental Set up

3.1 Introduction

This chapter provides an overview of the equipment used during the experimental work in this thesis. Estimation and control of the various engine parameters have been undertaken on the engine and dynamometer facilities in the IC laboratory at the University of Liverpool. Originally built for idle speed control work, the engine has been modified to allow switchable control of ABV, spark advance, fuel pulse width whilst a desired, moderate load can be applied through the low inertia DC dynamometer setup. In addition, various sensors have been installed on the engine to allow monitoring using a standard desktop PC running appropriate software. Speed, in-cylinder pressure, MAF, MAP and crank angle can be measured along with the ion current through the ion current sensing box. Figure 3.1 shows the setup of the engine with the sensors used for control and estimation of various operating parameters.

3.2 Engine and Dynamometer Specification

The experimental engine used is a spark-ignited, Ford Zetec 1.6l, 16 valve, four-stroke, four-cylinder, double overhead cam, water cooled, multi-point fuel injected IC engine. Each of the four cylinders, which are inline, have two inlet valves and two exhaust valves. The fuel is delivered via the electronic port fuel injectors. Table 3.1 denotes the engine statistics.

The dynamometer, essentially a DC motor, is a 7.5 kW unit. This is bolted directly to the crankshaft via a universal joint and so can simulate loading on the engine via a braking force or can assist the forward rotation. Controlled through a secondary dSPACE unit, the dynamometer was installed originally for idle speed control work so is limited in a rotational speed of 3000 RPM maximum and has a maximum rated torque of 80NM at 1000 RPM.

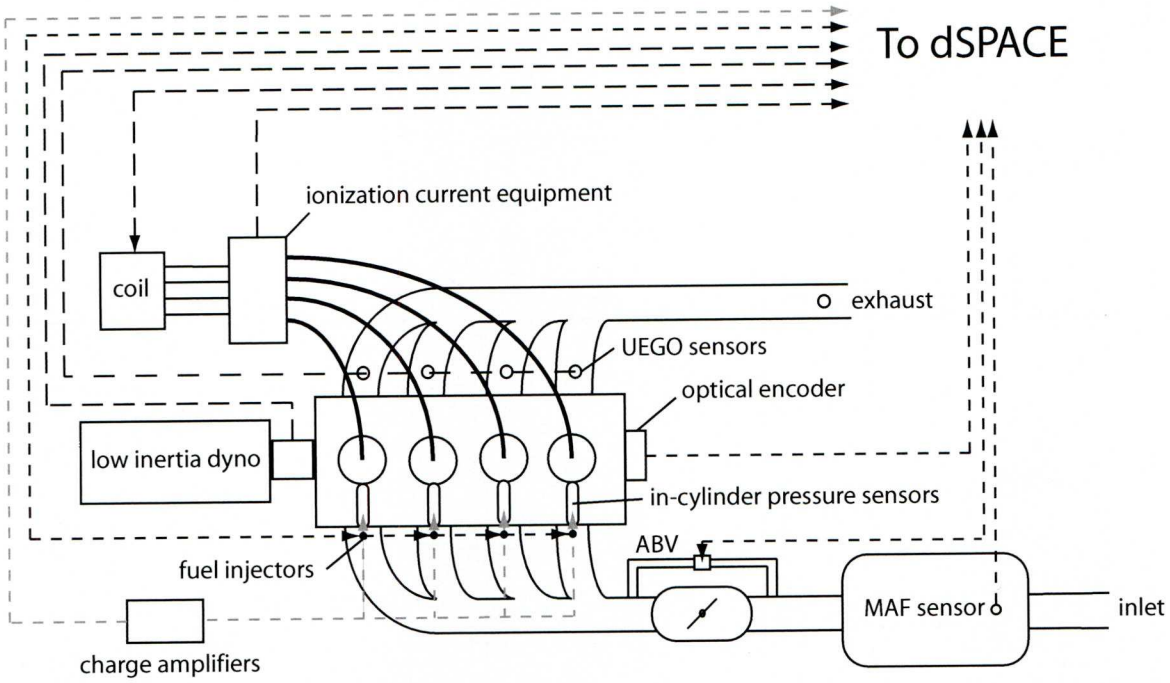

Figure 3.1: Engine Setup showing Sensors

Table 3.1: Engine Specifications

Cylinder Bore	76.0 mm
Connecting Rod Length	136.2 mm
Compression Ratio	10.3:1
Cubic Displacement	$1597cm^3$
Stroke Length	88 mm
Firing Order	1-3-4-2
Exhaust Valve Opens	64° B.B.D.C.
Exhaust Valve Closes	12° A.T.D.C.
Inlet Valve Opens	22° B.T.D.C.
Inlet Valve Closes	12° A.T.D.C.
Maximum Torque	138 Nm at 3500 rpm
Maximum Power	90 PS
Idle speed	880 rpm
Fuel	Unleaded RON 95 petrol

Table 3.2: dSPACE Card Specifications

Board	Function	Specification	Interfacing Apparatus
DS1005	Processor Board	PowerPC 750GX running at 1 GHz	Engine
DS2003	Analogue Input Board	32 Channel ADC Board (16 bit)	Engine
DS4001	Digital IO	Timing and DIO	Engine
DS4002	Digital IO	DIO including PWM generation	Engine
DS2103	Analogue Output Board	32 Channel DAC Board (16 bit)	Dynamometer

3.3 Interfacing Hardware

Figure 3.2 shows the general orientation of the engine with the interfaced hardware. Apart from the additional sensors and the removal of EGR capability for this work, the engine operates under its original configuration. The engine is controlled through a Ford production EEC IV EMS with a 58KB microprocessor where control of the SA, fuel pulse width and air bleed value (ABV) can be switched to operate from a powerstage unit connected to dSPACE.

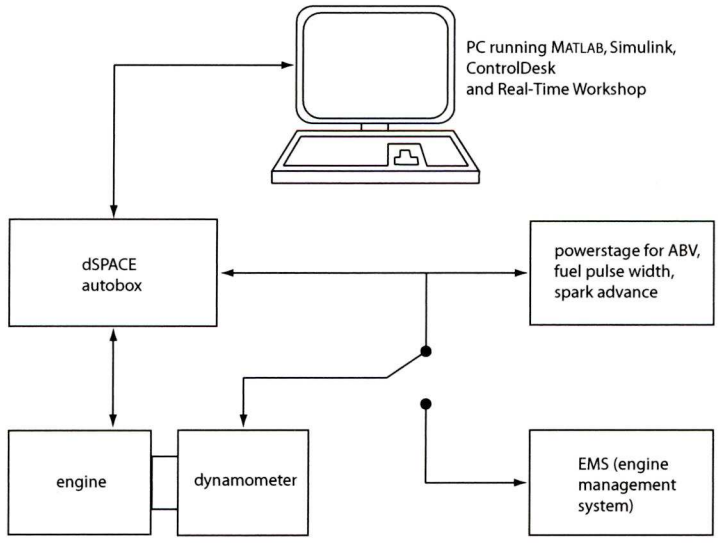

Figure 3.2: Hardware Setup

Table 3.2 details the specification of the cards in the dSPACE unit interfaced with the engine.

3.4 Software

All implemented algorithms are run on the PC using the following software: MATLAB, SIMULINK, Control Desk and Real-time Workshop. MATLAB and SIMULINK are used for all estimation processes, principal component analysis, generation of all neural networks and calculation and implementation of the control schemes.

In producing a neural network that will eventually be impelemented to run on the engine, first the acquired training data in processed within MATLAB to be useable for training a neural network. The network is constructed offline within a MATLAB program and subsequently generated into a SIMULINK model offline. Similarly for all other signal processing that is executed offline with MATLAB program files; this processing must be replicated into SIMULINK models offline.

Control Desk is a user interface that allows control of the hardware through a desktop PC and Real-time Worshop is software that allows the SIMULINK models that have been developed to be compiled onto and used with the dSPACE hardware.

3.5 Sensors and Actuator Specification

3.5.1 The Ion Current Sensing System

The ionization current sensing systems were built in-house. Initially a device suitable for single cylinder work was constructed prior to building a second device capable of four cylinder work. The basic circuit was detailed in section 2.2.2 but after initial experimentation, this was concluded to need additional circuit design.

The single cylinder version is spliced between the coil and the spark plug and connects them with standard HT lead fittings.

The additional spark gap that is designed to isolate the existing coil and spark plug circuit from the ion current sensing circuit is substituted for a gas discharge tube (GDT) for practical and safety reasons. When the coil is actuated, the voltage is sufficient to break down the insulating gas in the GDT and allow the spark plug to deliver a spark to the cylinder. Figure 3.3 illustrates the circuit in more detail. 12 Volts AC is supplied from a power supply, that is transformed to DC voltage. A DC to DC converter ramps up this voltage to 300 Volts. This is in effect protected by a $470k\Omega$ resistor and zener diode 1. Zener diodes 2 and 3 are in place to limit the output voltage from $-10V$ to $+10V$, which prevents damage to dSPACE which is connected to the ionization output point by a BNC connection. The circuit is then a potential divider and there are three periods of operation:

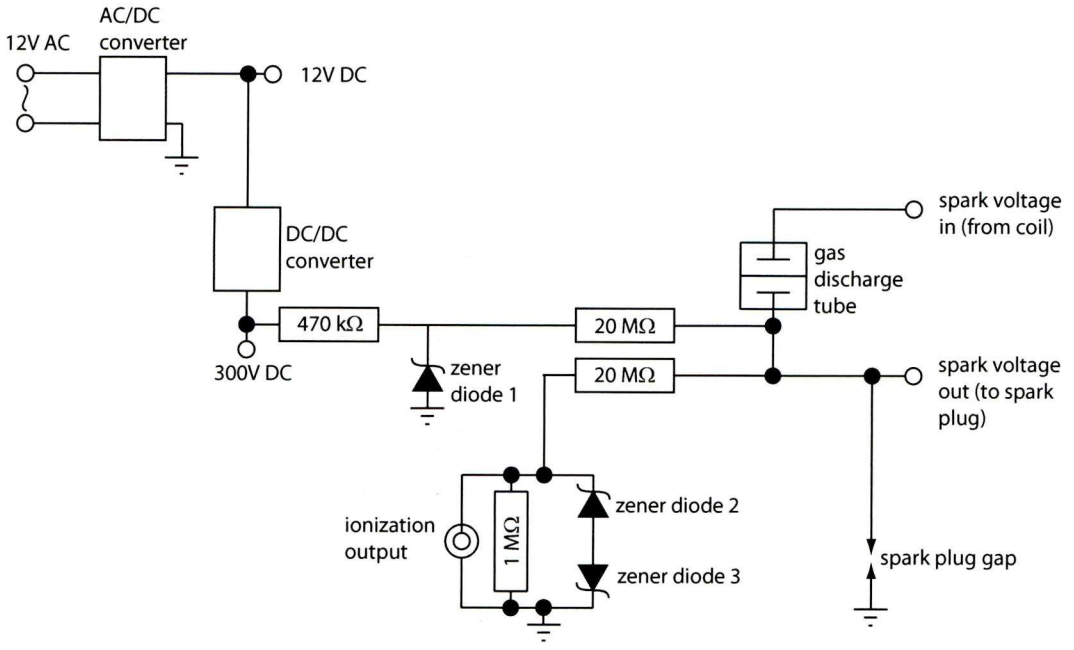

Figure 3.3: Single Cylinder Ionization Current Sensing Circuit

1. No sparking event and no ionization: The GDT isolates the engine coil from the ionization circuit. $300V$ bias DC is being supplied across the series of resistors to ground. The current through this circuit is then:

$$\begin{aligned} i &= \frac{300V}{41.47M\Omega} \\ &= 7.2\mu A \end{aligned}$$

and the voltage being read at dSPACE during this period is a bias voltage of:

$$\begin{aligned} V_{dSPACE} &= 7.2\mu A \times 1M\Omega \\ &= 7.2V \end{aligned}$$

2. A sparking event upon the coil discharging through the spark plug: The voltage, around $20kV$, is enough to break down the gas in the GDT to produce a sparking event at the spark plug. The current through the circuit is then:

$$\begin{aligned} i &= \frac{20000V}{21M\Omega} \\ &= 0.952\mu A \end{aligned}$$

and the voltage being read at dSPACE during this period is a bias voltage of:

$$\begin{aligned} V_{dSPACE} &= 0.952\mu A \times 1M\Omega \\ &= 952V \end{aligned}$$

Depending on the cylinder, the polarity of this voltage can be positive or negative, hence the zener diodes 2 and 3 limit this voltage to $-10V$ or $+10V$. These ignition sparking events can be seen in the ion current signal waveform immediately preceding the ionization window, see phase 1 in fig. 2.1.

3. Ionization event immediately following the ignition sparking event: The circuit would be the same configuration as in case 1 but with the addition of electron flow between the spark plug electrodes. The electrons produced during the in-cylinder ionization flow to the anode and hence the bias DC voltage to dSPACE of $7.2V$ is lowered. This is the reason the 'peaks' in the ideal ionization waveform are inverted; the bias DC voltage is being reduced due to the ionization. The actual voltage reduction due to the ionization is only a few volts.

The output of the DC/DC converter is adjusted to $300V$ for experimentation in this research but a maximum of $500V$ can be selected, though this can produce spurious sparking [63]. The zener diodes cap the output voltage to dSPACE at $-10V$ or $+10V$ so a theoretical maximum DC bias voltage in the circuit can be calculated. The current in the circuit is:

$$\begin{aligned} i &= \frac{V_{dSPACE}}{1M\Omega} \\ &= \frac{10V}{1M\Omega} \\ &= 10\mu A \end{aligned}$$

and so the maximum voltage in the circuit is:

$$\begin{aligned} V_{in} &= 10\mu A \times 41.47M\Omega \\ &= 414.7V \end{aligned}$$

The four cylinder version (fig. 3.4) [118] is fundamentally similar although it shares the voltage transformer between all four cylinders.

Noteworthy is the voltage that is occurring within this four cylinder ion current sensing box. For a single spark plug, the voltage is reaching $20kV$ for the ignition spark event. The standard coil pack is divided into two sections that are each responsible for firing two spark plugs simultaneously, meaning that each cylinder experiences a redundant spark event 360° out of phase which the combustion igniting spark event. The charging of these events between cylinders is an opposing polarity and this has serious implications on the voltages inside the ion current sensing box; a potential difference approaching $40kV$ is experienced. Care was taken to allow the voltage paths within the box carrying these opposing voltages to be a distance far enough apart to prevent spurious arcing. The dielectric breakdown voltage for air is approximately 3KV/mm [119] so voltage paths were designed to be at least 13.3mm apart.

3.5.2 Pressure Sensors

In the cylinder head, below the inlet orifices at the air/fuel intake side are four cylinder pressure sensors, one per cylinder. These Kistler type 6123 transducers are piezo electric devices and are compression fitted into the head so that the 'pressure sensing' surface is facing into the cylinder cavity. The piezo electric device outputs a reading which is proportional to a change in pressure, this reading is first passed through a Kistler model 2004 charge amplifier before being read into the dSPACE DS2003 A/D converter card sampled every 1° of crank angle.

The pressure sensors are not calibrated for absolute pressure values. Since this work requires only the peak pressure position as in-cylinder pressure information then this can be calculated using appropriate algorithms [6].

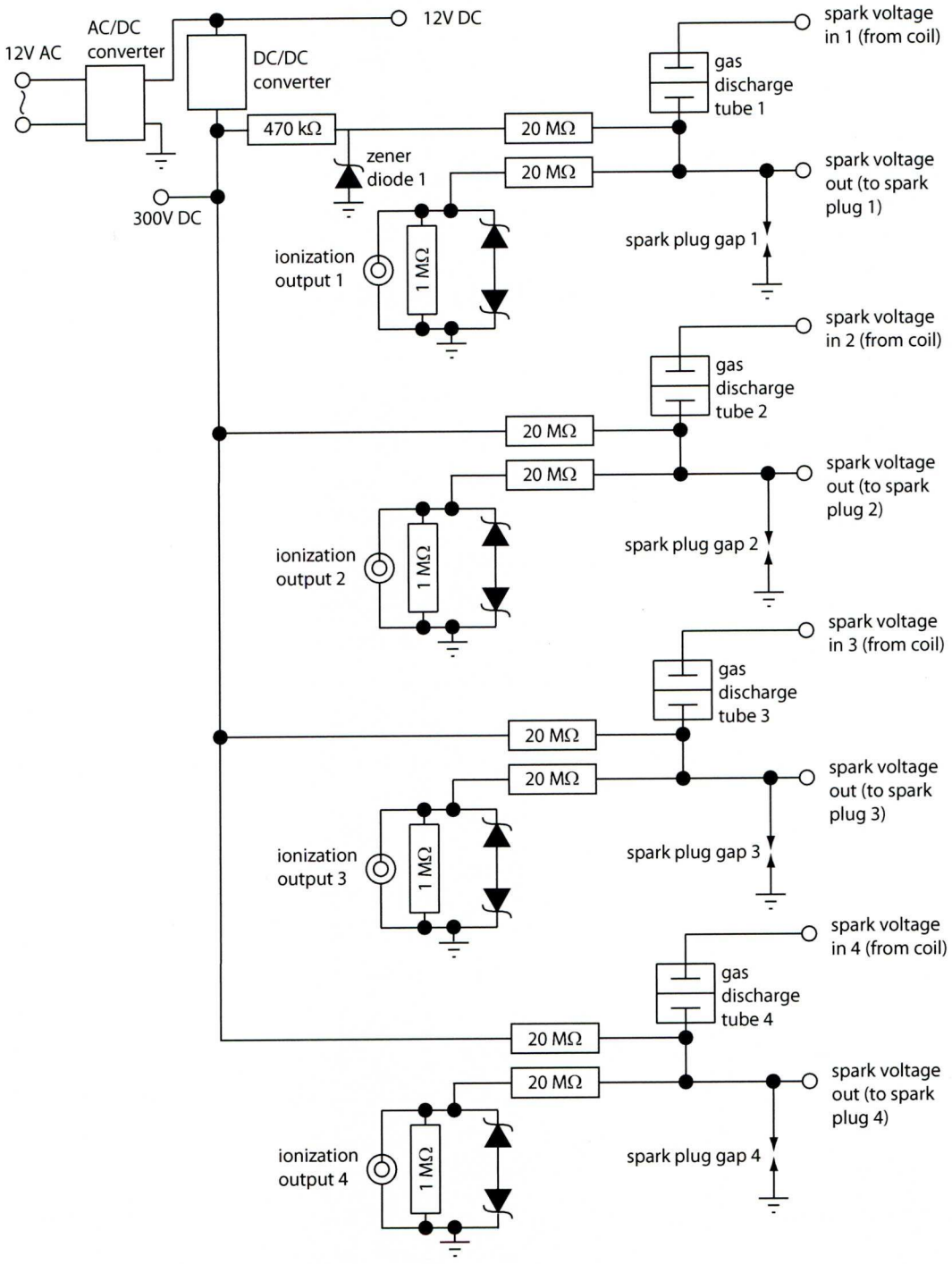

Figure 3.4: Four Cylinder Ionization Current Sensing Circuit

3.5.3 Oxygen Sensors

The engine uses, as standard, a heated exhaust gas oxygen sensor (HEGO) that is installed in the front exhaust pipe section at a confluence point. This switching sensor provides a high voltage if the exhaust gas in rich of stoichiometry and a low voltage if the exhaust gas is lean of stoichiometry. This is used for emission control for the EEC IV module. Additional universal exhaust gas oxygen (UEGO) sensors have been installed and are employed to determine a more accurate air-fuel ratio (AFR) than the HEGO sensor. Also known as wideband sensors or lambda sensors, these are heated devices that measure the oxygen content in the exhaust gas stream. The engine itself, in addition to a UEGO sensor at the standard confluence point, has the capability of additional oxygen exhaust sensors near the four exhaust ports in the exhaust manifold. The four sensors, being so close to the exhaust ports, not only remove any transport delays on AFR readings normally taken at the confluence point but also allow the monitoring of AFR of each of the individual cylinders. It is these four UEGO sensors positioned near the cylinder outlet ports that are used in the research. This is essential for comparison with any ion current AFR data from each individual cylinder that may be used for AFR prediction.

The sensors used are Bosch wideband O_2 sensors that give an output voltage proportional to the oxygen content and input to dSPACE. The engine used, when running at stoichiometric conditions, has the air to fuel (by mass) ratio of 14.7:1. This ratio of air to fuel can also be represented by lambda, λ, where the stoichiometric AFR has a λ value of 1. λ is the ratio of measured AFR relative to stoichiometric AFR:

$$\lambda = \frac{AFR_{measured}}{AFR_{stoichiometric}} \tag{3.1}$$

3.5.4 Angle Encoder

The determination of crank angle is important in this research since the algorithms and models created in SIMULINK are event based and not time based. This means that the models are synchronised and triggered relative to a particular rotational crank angle relative to a piston TDC. In addition, numerous signals are sampled every degree. An angle encoder is mounted directly onto the crank shaft and outputs two signals; one pulse per 1° and one pulse per 360°. The 1° pulses are transmitted to a hardware interrupt function on the DS4001 card that synchronises the timing between the engine and dSPACE. The latter 360° pulse acts as a TDC synchronisation pulse of cylinder 1, checking if any 1° pulses have been missed and resetting TDC in dSPACE if a discrepancy occurs.

3.5.5 MAP and MAF Sensors

The manifold absolute pressure (MAP) sensor provides instantaneous manifold pressure information, traditionally for the engine management system but also for dSPACE in this set-up. It is plumbed into a low pressure (less than 1 bar atmospheric) hose on the inlet manifold and determines the air mass flow rate, which in turn is used to meter the appropriate fuel flow since the amount of fuel required is directly related to the mass of air entering the engine.

The MAP signal holds a high correlation with the load placed on the engine since the pressure is related to the load level. The low pressure (between 0 and 1 bar atmospheric) drops when the engine is under load or at wide open throttle and the low pressure increases at low load or smaller throttle angle settings. For identification, the MAP signal integrated over 180° was used as a measure of load which correlated better than the simple MAP signal.

A mass airflow (MAF) sensor is used to determine the mass of air entering the engine upstream of the throttle. This is a hot wire type MAF sensor, used in conjunction with an inlet air temperature sensor, where its resistance drops proportionally to the amount of air flowing past.

3.5.6 Engine Speed and Torque Estimation

Although there is more than one way to calculate speed on the engine set-up (e.g. with the angle encoder or the EMS) the best results are from an in-line Torque Vibrometer (Torquemaster TM112 200Nm rating). This is mounted on the engine/dynamometer coupling. The vibrometer provides analogue speed and torque outputs that are logged into the dSPACE DS2003 ADC card.

3.5.7 Air Bleed Valve

Engine speed is controlled throughout this work, not by the throttle, but by the air bleed valve (ABV). The engine does indeed have a throttle but it is cable driven. The ABV is a throttle bypass valve that is used during engine idle, it acts in a similar manner to the throttle in controlling the volumes of air that pass into the inlet manifold. The ABV is electronic and can be controlled externally by the engine management unit or more crucially Control Desk and Real Rime Workshop via dSPACE. This means that an electronic input to the ABV can in effect allow a change in engine speed.

3.5.8 Fuel Injection

The engine is a port fueled injection (PFI) type. This means that are are four electronic injector valves (one per cylinder) connected by a single fuel rail. Supplied from a lateral fuel supply, the fuel is sprayed from the injector toward the inlet port where it is mixed with the air. The amount of fuel that is sprayed is determined electronically by the time period that the injector sprays, the fuel pulse width (FPW). This fuel pulse width is controlled by the EMS or by dSPACE sending electronic signals to the individual injector devices. It is these actuators that will be used for determination and control of the AFR by monitoring and varying the FPW. Each fuel pulse (or charge) that is injected toward the inlet port does not entirely enter the cylinder instantly since it is sprayed before the inlet valve opens. This causes a puddle of fuel to form on the inlet runner, some of which evaporates immediately, from the heat and air, and is then induced into the cylinder with the air flow. This phenomena causes interesting dynamics and fuel delays that should be accounted for in fuelling strategies.

3.6 Conclusions

Using the equipment, the ion current sensing technique will be applied to the engine/dynamometer setup with the aim of predicting and controlling both the AFR and PPP. Actuators will be used to perturb engine variables necessary to excite dynamics that can be monitored using the sensors and recorded with dSPACE.

Available signals that can be manipulated using the dSPACE and actuators with software are listed as follows:

- Air bleed valve (ABV)
- Spark advance or spark ignition timing (SA)
- Load (through the dynamometer)
- Fuel pulse width (FPW)
- Exhaust gas recirculation (EGR)

Available signals that can be recorded using the apparatus with software are listed as follows:

- Air bleed valve (ABV)
- Engine speed, N.

- Spark advance or spark ignition timing (SA)
- Cylinder pressure and pressure related variables
- Load (through the dynamometer)
- Fuel pulse width (FPW) and timing
- Air-fuel ratio (AFR) of each cylinder
- Manifold absolute pressure (MAP)
- Coolant Temperature
- Ion current signal on all cylinders
- Torque

Using these recorded signals enables manipulation for training neural networks within MATLAB and subsequent generation of SIMULINK models that can be compiled into dSPACE with Real-time Workshop.

Chapter 4

Single Cylinder PPP Estimation and Control

4.1 Introduction

Spark advance (SA) is one of the most important key parameters in efficient engine operation, usually determined open loop by an EMS dependent on speed or load to achieve a desired peak pressure position (PPP). To regulate the PPP to a desired crank angle in a closed loop feedback manner, SA will be controlled from an estimated PPP. This chapter describes the process undertaken for the identification process of producing models to predict the peak pressure position (PPP) in a single cylinder using available engine signals and the ion current method. The theory and reasoning behind the selection of signals and the acquisition of data is first explained in section 4.2. Principal component analysis is described as a method of data reduction and feature extraction from the ion current signal in section 4.4. It should be noted that the raw data is acquired from the engine dynamometer set up and then initially processed offline to produce the identification data. This identification data is then used to create a model of the engine with a neural network (NN) for the purpose of predicting the PPP in section 4.6, again created and trained offline with initial network validation being done offline. Only when a satisfactory, offline, simulated prediction is achieved is the model then implemented onto the engine/dynamometer set up and online validation achieved in section 4.8. When satisfactory online model validation occurs, control loops can be implemented and the PPP can be set through control of spark advance in section 4.9.2.

The graphic figure 4.1 displays the location of the in-cylinder pressure sensor machined into the cylinder head near the inlet port along with the spark plug used for ionization current sensing located in the top of the combustion chamber.

Figure 4.2 illustrates the concept of the system; a neural network is trained to predict

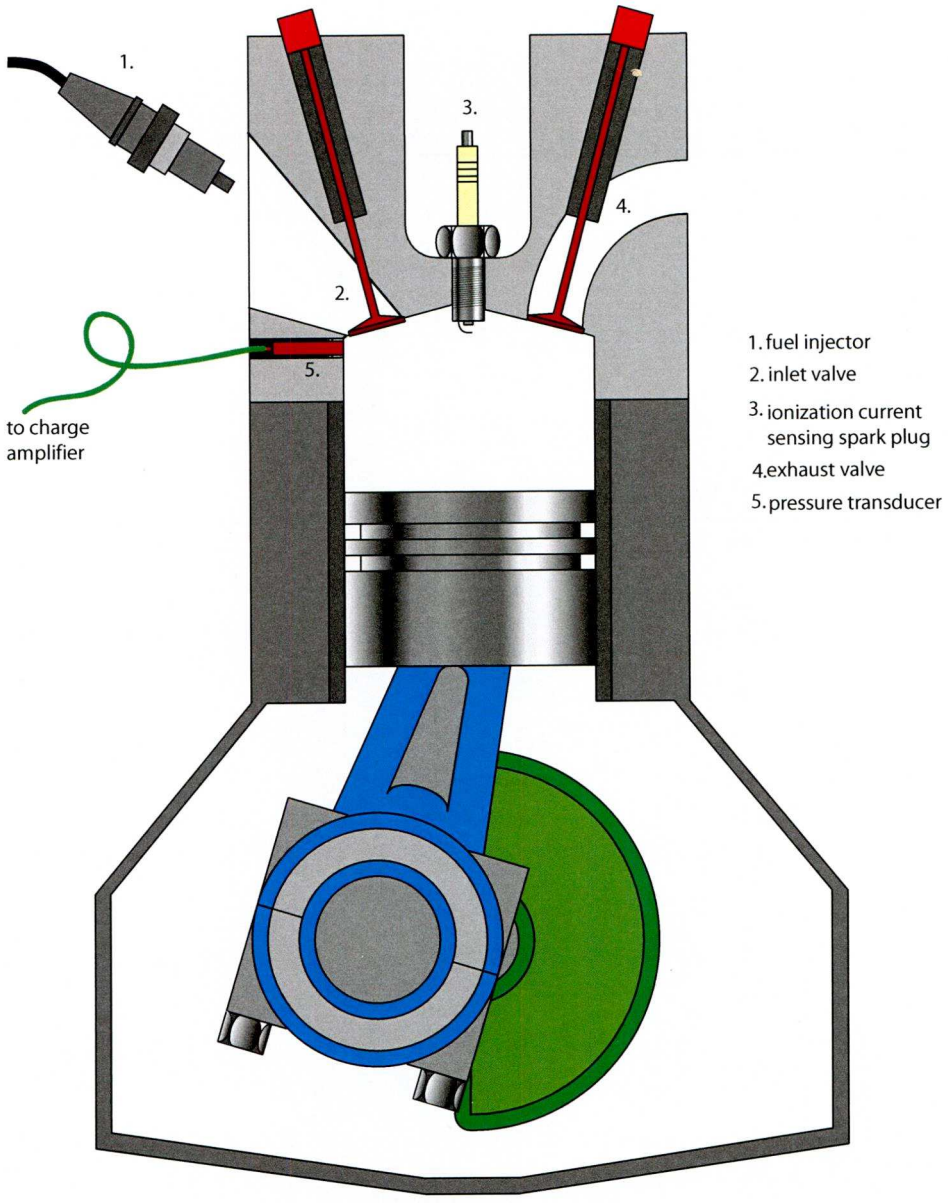

Figure 4.1: Location of Ion Current Sensor and Pressure Sensor

peak pressure position and then an ARMAX model will be identified around this network and the plant (enclosed by the dashed line) so that feedback control can be applied to regulate the peak pressure position to a desired crank angle robust to changes in speed and load.

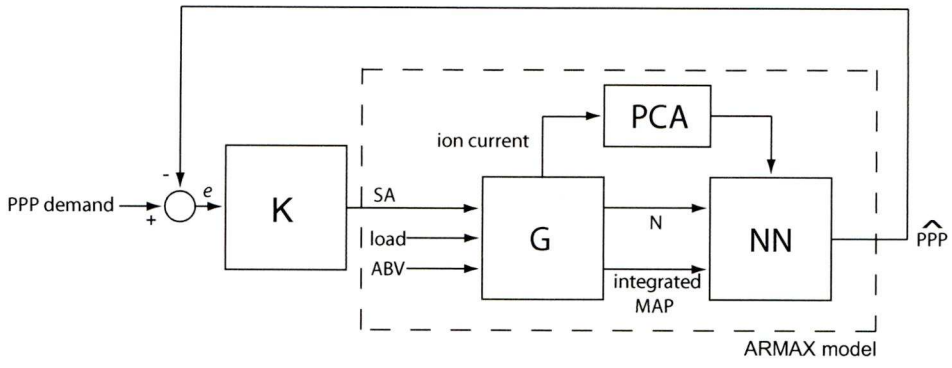

Figure 4.2: Single Cylinder PPP Control System Concept

4.2 Signal Selection and Excitation

In trying to ascertain a relationship between input and output signals a model is established. A model has to be constructed from observed data, recorded during specifically designed identification experiments [120] . In trying to establish models that can predict PPP from identification data, the acquired signals must be sufficiently representative of a system. The models are required to predict not only in steady state but in transients also. Sufficient and suitable excitation of input signals and the resulting causal output signals expose the dynamics of a system and these can be used to produce a model. Neural networks (NN) have been chosen as a suitable model foundation.

It is established that the SA has a direct correlation with PPP [9]. In this research, although in-cylinder pressure information is measured directly with a Kistler pressure sensor for comparison, it is hoped that the ion current can establish cylinder pressure information within its output signal.

PPP is subject to changes in speed and load therefore any identified models should be able to accurately predict PPP whilst the cylinder experiences changes in speed and load and therefore speed and an integrated MAP signal[1] are used in creating models. Load is not measured directly in production vehicles but MAP correlates very highly with engine load and is a signal available in production engines so this is a valid model component signal to incorporate. To obtain identification data, perturbed input signals are excited simultaneously by scaled, biased random numbers over a range as indicated in table 4.1. The effect of these perturbed signals fluctuates the engine speed between 800rpm to 2200rpm

[1]Integrated over 180° prior to sampling

Table 4.1: Perturbed signals for Identification

Signal	Range	Perturbation Period
ABV [$\%_{duty}$]	49 to 59	0.7 s
Load [V]	-0.10 to -0.18	0.8 s
SA [° BTDC]	26 to 36	0.4 s

whilst the integrated MAP fluctuates between 55 and 110 bar^2. The perturbation period for each input signal is chosen to be low enough to allow any dynamic response of the output signal to be fulfilled but still be high enough to allow rapid representative transient output responses. This will ensure the identification will accurately predict both steady state and transient behaviour by experiencing these dynamics. A significant advantage of using this signal perturbation method over datasets consisting of multiple static set-points is that fewer samples are required to train the network from this dataset; 3000 training samples cover the entire identification range with 1000 of these samples for the training, 1000 for validation and 1000 for 'hold-out' unseen data. In this manner, the time to obtain the training data is vastly reduced compared to multiple set point tests.

Input and output data is collected over 3000 combustion cycles from the engine and dynamometer set-up. All signals are sampled online once per degree and so over 3000 combustion cycles would give 2160000 samples per signal channel. This resolution of information is unnecessary in identifying this model; PPP is a value that remains constant over a complete combustion cycle of 720° and so only one sample is required per combustion cycle. Likewise, although N and MAP change by a relatively small amount over the course of a combustion cycle, just one sample per cycle is deemed sufficient. Hence for N, MAP and PPP 3000 samples each for 3000 combustion cycles are used in the identification process.

These 3000 cycles are split equally, after processing, into three parts; 1000 cycles for identification (network training), 1000 cycles for validation and the final 1000 cycles as a 'hold-out' data set for proving of the neural network before engine implementation occurs [101].

The identification input data consists of 1000 cycles of the ionization current signal, integrated MAP signal (that correlates well to the load) and the engine speed, N. The identification output data are the corresponding PPP measured from the in-cylinder pressure sensors obtained over the 1000 cycles. The entire datasets are displayed in fig. 4.3 including the target PPP dataset. The processing of the ion current to create suitable identification data is described in the next section.

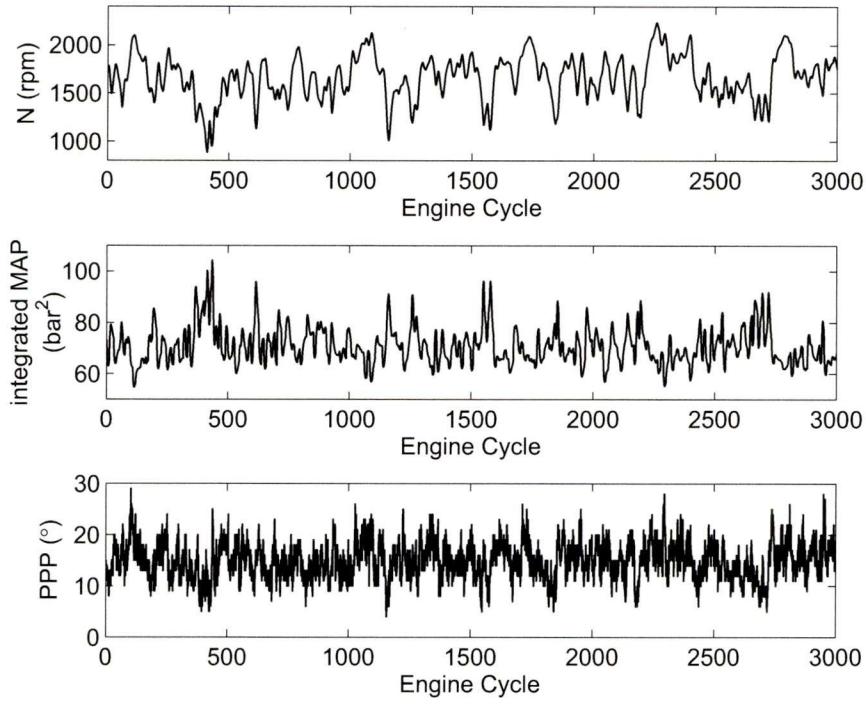

Figure 4.3: 3000 cycles of Engine Speed and Integrated MAP Identification data

4.3 Ion Current Signal Processing

To relate the ion current 'window' to the PPP incurs an increase in complexity when compared to MAP and N. Integrated MAP and N are sampled every crank angle degree by the data acquisition hardware and software but only one sample per combustion cycle is used in the model identification as explained in the previous section. The ion current signal is again sampled once per degree but a 'window' of samples per combustion cycle is used for the model. Various lengths of window have been used in previous research to relate the ion current to the PPP; in [49] a window of between 6° to 35° ATDC was used, in [46] it is 5° to 35° ATDC and in [45] the peak finding algorithm operates between 0° to 35° ATDC. A window of 60° is mentioned in [53], sampled at half a degree, to predict the AFR and PPP.

Other authors in previous research have chosen to determine the ion current window in reference to TDC whereas is this work, the window has been chosen in reference to the spark ignition event. This effectively allows the extraction of ion current features independent of the SA for a particular cycle since the same window is sampled for any SA setting. During this work, the observed 'windows' of the ion current signal are sampled once per degree over 30° of crank angle for PPP estimation. This would effectively give 30 samples to relate to the PPP per combustion cycle. The window of the ion current signal chosen to relate to the PPP

is the 'thermal phase', where re-ionization of the gases occurs due to rising temperatures in the cylinder and believed to correlate to the pressure, as in fig. 4.4.

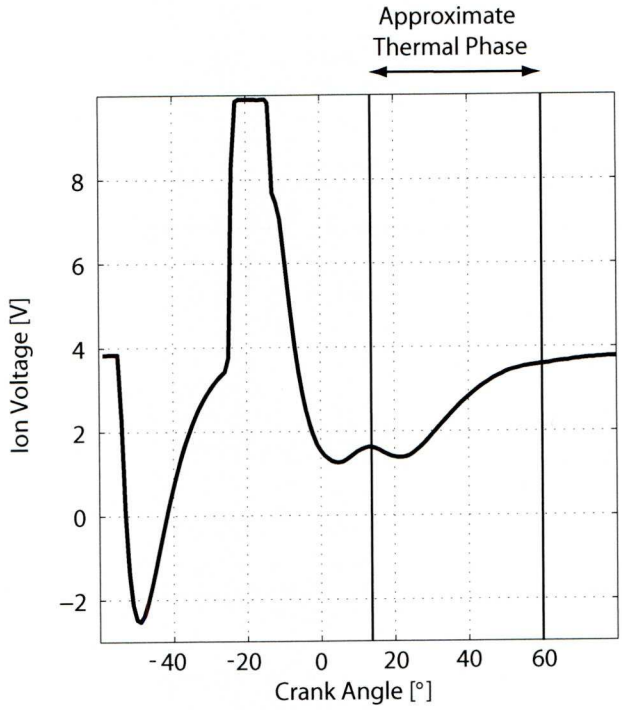

Figure 4.4: A window of a typical ion current curve

This phase, appearing as a peak in the signal at higher loads and lower engine speeds that is not apparent at lower loads and higher speeds, occurs around 25° after ignition for around 20° to 40°. 30° is chosen as a window large enough to capture most of the pressure related information and small enough to not be too computationally heavy since any signal processing done at 'leisure' offline still has to be repeated in SIMULINK and used online for model proving.

Early ionization current signal to peak pressure position identification worked on the principle of curve fitting [25] or the assumption that the post flame phase of the ionization current signal was present and clearly defined. Later work has acknowledged that this is not the case [44], usually in low load situations or when engine speed is high causing the separate phases of the ionization current signal to merge. Principal component analysis (PCA) is proposed to acquire important characteristics from the ionization current signal even when the desired waveform does not occur. By effectively determining the 'principal' characteristic of the signal window, it also reduces data sizes so that the ionization current signal to PPP relationship can be identified using significantly less data.

4.4 Principal Component Analysis

4.4.1 The Ion Current Signal

PCA is applied to a specific window of the ionization current signal, which is believed to contain information relating to the PPP. The ionization current signal is sampled every degree and a complete cycle is 720°. The window that contains the PPP information is calculated to be through 30° of crank angle, between 25° and 55° after spark ignition. This would imply that initially 30 sample points are used, one per degree indicating a specific ionization voltage. From these 'windows' of sample points, PCA obtains the 'principal components'. Figure 4.5 shows the variability in overlayed plots of 20 random typical windows of the ion current signal. In practice, 3000 cycles are used for PCA but for illustrative purposes, only 20 cycles are shown.

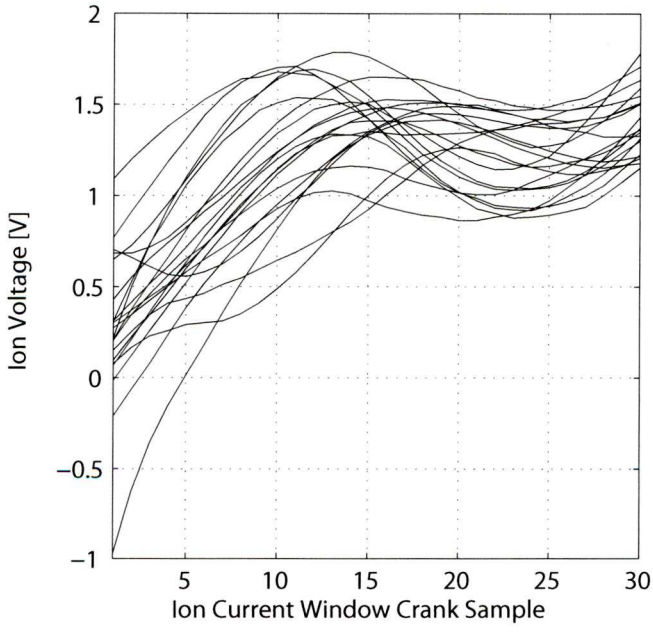

Figure 4.5: A window of a typical ion current curve

4.4.2 PCA Applied to the Ion Current Signal for PPP Estimation

The following procedure is observed to initially produce the PCA scores for the identification data. Using the 30 degrees of window of the ion current signal, PCA is to be applied to reduce these 30 samples per cycle to a smaller dataset.

1. The ion current signal is sampled online every degree of crankshaft rotation and a complete cycle is 720°.

2. Offline, a window of the ion current signal is selected; the 'thermal phase' of the ion current signal, which is calculated to be through 30° of crank angle, between 25° and 55° after the spark event. This would imply that initially 30 sample points per cycle are used, one per degree indicating a specific ionization voltage. If each 'window' of each cycle contains 30 sample points over 3000 combustion cycles, this presents a 30×3000 matrix, each row is an observation or cycle, and each column is a crank angle position.

3. The 30 rows of data are normalised and are considered to be vectors X_1 to X_{30}. The covariance matrix is calculated offline. This results in 30×30 matrix.

4. If Σ is the covariance matrix of the vector $X' = [X_1, X_2, \ldots, X_{30}]$, it has eigenvalue-eigenvector pairs (σ_1, e_1) to (σ_{30}, e_{30}) where $\sigma_1 \geq \sigma_2 \geq \cdots \sigma_{30} \geq 0$. The 30^{th} principal component is given by $Y_{30} = e_i'X = e_{1i}X_1 + e_{2i}X_2 +, \ldots, e_{30i}X_{30}$ where $i = 1, 2, \ldots, 30$. The full resulting data set would contain 30 PCA scores. The percentage that each score contributes to the total population variance can be calculated and hence most scores can be 'discarded'. In this case $Y_1 = e_1'X, Y_2 = e_2'X, \ldots, Y_{30} = e_{30}'X$ are the principal components. Then

$$\sigma_1 + \sigma_2 +, \ldots, \sigma_{30} = \sum_{i=1}^{p} Var(Y_i)$$

so the proportion of total variance explained by the i^{th} principal component is :

$$\frac{\sigma_i}{\sigma_1 + \sigma_2 +, \ldots, \sigma_{30}}$$

The eigenvector with the highest corresponding eigenvalue is the principal component. The 5 eigenvectors with the highest corresponding eigenvalues are chosen since they contain over 99% of the total signal variance. This results in a reduced 30×5 matrix. This matrix is stored and is used for all offline and online reduced dataset computations. For reference, this matrix shall be refered to as the 'FeatureVector' matrix.

5. The original ion current data is projected onto the 30×5 'FeatureVector' matrix to produce a reduced identification dataset of 5 samples over 3000 cycles for offline identification.

Hence the new sample set is reduced from 30 principal components per cycle to 5 principal components per cycle and therefore the computational complexity is significantly lowered.

Table 4.2 displays the first 30 principal components and the proportion of total variance explained by them. It can be clearly seen that beyond the first 15 or so principal components, the variance explained is negligible.

Table 4.2: First 30 principal components from a window of a ionization current signal and the proportion of total variance explained by them

Principal Component	Proportion of Total Variance	Accumulated Percentage
1^{st}	86.245306	86.245306
2^{nd}	9.027634	95.272940
3^{rd}	3.204490	98.477429
4^{th}	1.152524	99.629954
5^{th}	0.290061	99.920014
6^{th}	0.046533	99.966547
7^{th}	0.017786	99.984332
8^{th}	0.007501	99.991833
9^{th}	0.002816	99.994649
10^{th}	0.001444	99.996093
11^{th}	0.000765	99.996858
12^{th}	0.000387	99.997245
13^{th}	0.000300	99.997545
14^{th}	0.000260	99.997805
15^{th}	0.000212	99.998017
16^{th}	0.000169	99.998187
17^{th}	0.000158	99.998344
18^{th}	0.000147	99.998492
19^{th}	0.000136	99.998627
20^{th}	0.000129	99.998756
21^{st}	0.000124	99.998881
22^{nd}	0.000124	99.999005
23^{rd}	0.000122	99.999127
24^{th}	0.000119	99.999245
25^{th}	0.000115	99.999360
26^{th}	0.000114	99.999475
27^{th}	0.000110	99.999584
28^{th}	0.000108	99.999692
29^{th}	0.000105	99.999799
30^{th}	0.000103	100.000000

If the plot of the 1^{st} principal component is visually compared to a plot of PPP, it can be seen that they have a high correlation. This implies that a large amount of the information relating to the PPP is contained within the 1^{st} principal component, and this first principal component (by definition) contains a high percentage of the total variance of the ion current. If a larger or different ion current window is used that encompasses a more complex waveform with more features, then it would be expected the percentage of total variance captured by the 1^{st} principal component would drop and the secondary principal components would contribute a higher percentage of the total proportion of variance as these extra features are introduced. It is hoped that by allowing up to five principal components in the identification will be sufficient to capture significantly differing features in a signal that is varying cycle by cycle.

The separate principal components are displayed in fig. 4.6.

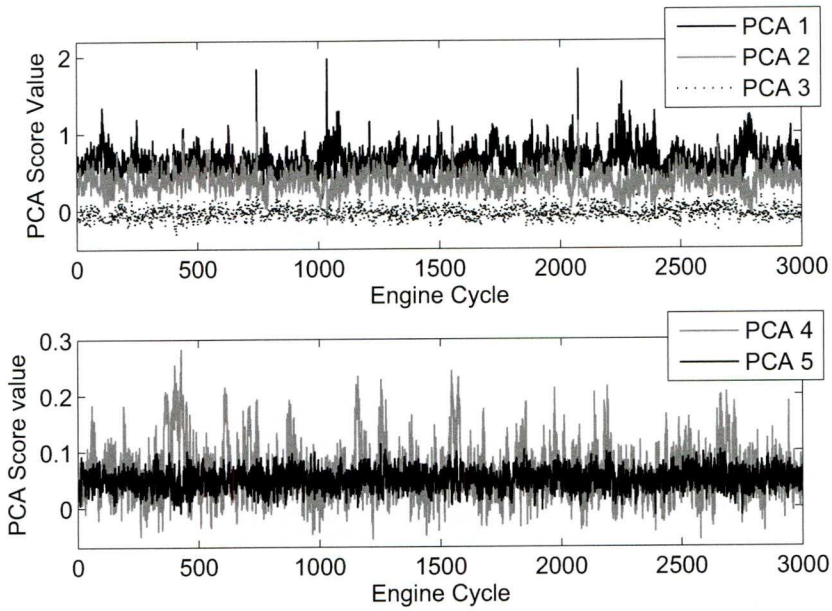

Figure 4.6: 3000 Cycles of 5 Principal Components of the Identification Data

Using a statistical analysis technique the matrix of the correlation coefficients between the principal components and the PPP was calculated, see table 4.3. The correlation coefficient matrix represents the normalised measure of the strength of linear relationship between variables. The coefficients can range from -1 to 1, where values close to 1 suggest that there is a positive linear relationship between the data columns. Values close to -1 suggest that one column of data has a negative linear relationship to another column of data. Values close to or equal to 0 suggest there is no linear relationship between the data columns [121]. The correlation between principal components themselves is not included since it is unimportant in this work. Interestingly, principal component 4 has a higher correlation to the PPP than

principal component 3. This is a linear indication and since neural networks are to be used in identifying the relationships and are of a non-linear method, then all of the first five principal components will be used rather than disregarding the principal components with lower correlations.

Table 4.3: Correlation Coefficient Matrix between PCA and PPP

-	PPP	PCA1	PCA2	PCA3	PCA4	PCA5
PPP	1	-0.452	-0.372	0.0756	0.222	-0.027

4.5 Applying Wavelet Analysis to the Ionization Current Signal

An alternative to PCA in reducing data sizes is to apply wavelet theory as discussed in chapter 2, section 2.8.4.

Wavelets can potentially be used in the following ways in this work:

- Decompose the 'window' of spark ionization signal for data reduction, reconstruct the signal and then use pattern recognition as in [53] for system identification (e.g. neural network inputs)
- Decompose the 'window' of spark ionization signal for data reduction, use the coefficients for system identification.
- Use Wavelets for non-linear system identification of the spark advance to PPP relationship. This application implies a new method, disregarding the neural networks methods already worked on.
- System identification with Wavelet networks.

The first two items will be explored whereas the latter two are expansive areas of research beyond the scope of this work.

4.5.1 Signal Decomposition

For PPP prediction, the window of ionization current data contains 30 samples per combustion cycle. Using PCA, this was reduced to just 5 samples per combustion cycle. Wavelet analysis was used in a three level decomposition, as per fig. 4.7, of the ion current signal before an approximation of the signal was reproduced for feature extraction purposes. The

filters used were a second order Daubechies family wavelet. Assuming a 3 level decomposition and using the approximation coefficients, data sizes can be reduced to potentially around $\frac{1}{8}^{th}$ thus giving 4 data samples per combustion cycle.

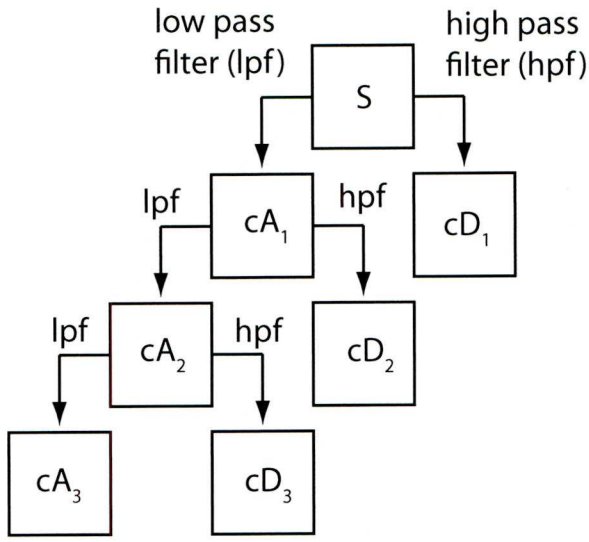

Figure 4.7: A Three Level Wavelet Decomposition

Figure 4.8 illustrates the original window of five combustion cycles of the ionization current, whilst various stages of the decomposition of each of the five cycles are illustrated in fig. 4.9.

Note that because the plots in fig. 4.9 illustrate the coefficients, the number of samples per plot are reduced in comparison to the original signal window.

A three level decomposition reduced the dataset of each combustion cycle to just 4 samples. These coefficients could be used as inputs to a neural network where as the PCA technique used 5 principal components per combustion cycle.

The signal can be reconstructed from the decomposition approximation coefficients at each level to produce simplified signals. These are shown in fig. 4.10. The number of samples of each reconstruction matches the original signal. In [53], the third level reconstruction was then used for an undisclosed pattern recognition technique.

Using this technique for an initial multi level decomposition of the signal, then a low level reconstruction before a pattern extraction technique adds additional complexity levels into the feature extraction process over the PCA technique. PCA will therefore be used for a chosen feature extraction technique over wavelet decomposition throughout this thesis.

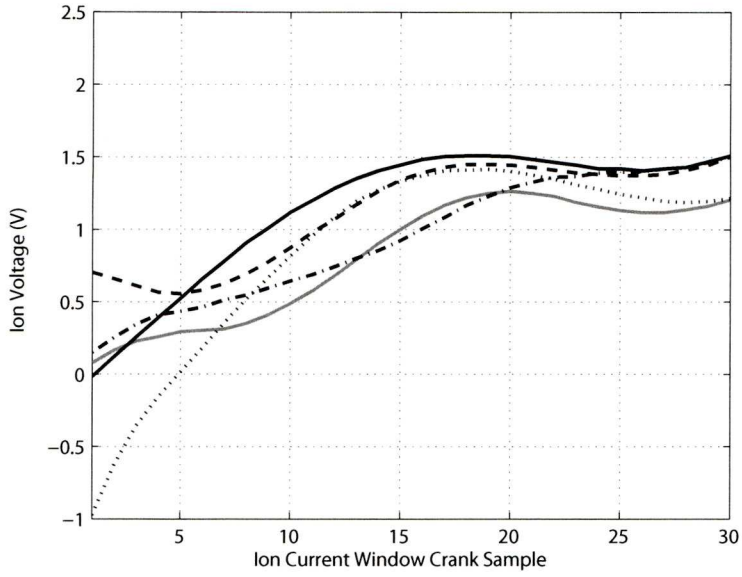

Figure 4.8: A typical window of the Ionization Current Curve

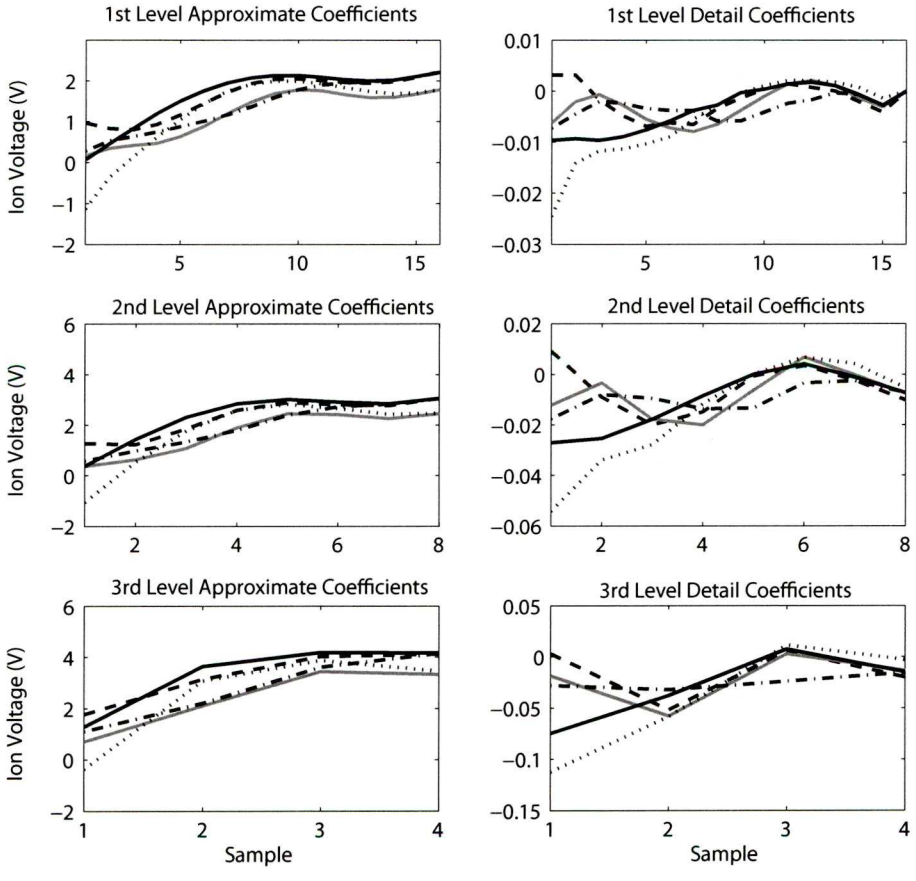

Figure 4.9: Multi Level Wavelet Decomposition of Ionization Current

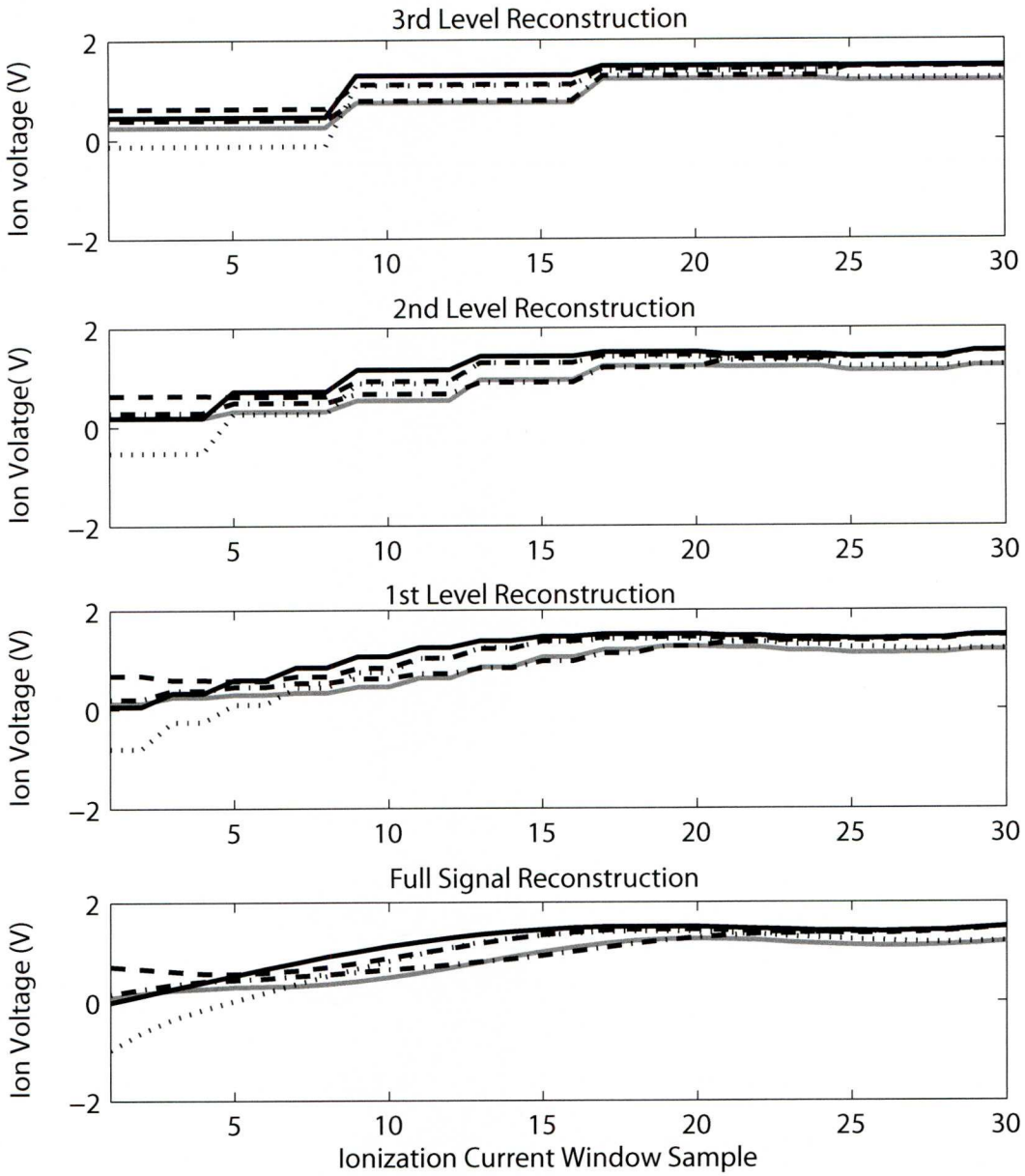

Figure 4.10: Multi Level Wavelet Reconstruction of Ionization Current

4.6 Neural Networks for Ion Current Sensing

The data relationship being used, spark timing to peak pressure position, involves time delays and so the identification of any model would involve these dynamic time delays, i.e. the current output signal is dependent on the current input and previous input signals. For this reason any neural network that would be constructed to predict the peak pressure position must be able to handle delays and thus a dynamic recurrent neural network is the obvious choice. Initial work with SA to PPP models has identified relationships through the use of autoregressive with exogenous inputs (ARX) models. A neural network that is based on the linear ARX model is the NARX (non-linear autoregressive with exogenous inputs) neural network. This NARX network is commonly used in time series modelling. The defining equation for a NARX model is as equation 4.1. Although SA to PPP is a nominally linear relationship, an advantage of the non-linear properties inherent in a NARX neural network would be the ability to recognise any non-linear phenomena that occur, specifically misfires.

$$y(t) = f(y(t-1), y(t-2), \ldots, y(t-n_y), u(t), u(t-1), u(t-2), \ldots, u(t-n_u)) \tag{4.1}$$

To choose a specific network, the input and output training data must be taken into consideration. Following principal component analysis there will be 5 PCA scores per cycle that will act as inputs to the network along with N and integrated MAP whilst the target data will be a single PPP per cycle. This constitutes a MISO network which will be able to, after training, predict an estimated PPP ($P\hat{P}P$) from the 5 PCA scores, N and integrated MAP.

Through a size reduction technique, large network structures are initially tested followed by smaller structures and a performance comparison made. Smaller networks that can match the larger networks for accuracy and performance are preferable. Ultimately this leads to a two layer NARX network which has a compromise between model prediction accuracy, complexity and computational processing speed. Table 4.4 shows the network structure sizes trialled using identical datasets before a minimum structure being decided upon. Achieved r^2 values (equation 5.4) and the number of effective parameters compared to number of available parameters are used as a justification for the choice of network [101]. Each network was trained twice and an average of the r^2 values taken, since the networks are initially seeded with random numbers [100] giving slightly differing training results. In table 4.4, SSE (Est) denotes the resulting sum of squared errors over the estimation training data and SSE (Valid) denotes the resulting sum of squared errors over the validation training data.

Figure 4.11 shows the chosen 2 layer NARX network where the input layer weight matrix is denoted IW and other layer weight matrices are denoted LW. f_1 activation function is

Table 4.4: Trialled Neural Network Structures

No. Layers	Neurons in Layer	Total No. Params	Effective No. Params	No. Epochs	SSE (Est)	SSE (Valid)	r^2
3	20 20 1	781	82.1	42	16.66	17.87	83.45
3	20 10 1	561	78.8	23	15.32	17.72	82.27
3	10 10 1	291	75.6	22	16.98	18.64	81.55
3	10 5 1	231	64.8	25	15.38	17.52	83.61
3	5 5 1	121	88.7	33	16.27	17.55	82.50
2	20 1	361	65.8	26	15.99	17.93	82.41
2	10 1	181	77.9	27	15.08	18.21	82.30
2	5 1	91	76.1	23	20.42	19.65	74.55

tansigmoid functions while f_2 is a pure linear activation function. Layer 1 contains 10 neurons whilst layer 2 contains 1 neuron. The network has a single feedback loop from the final layer to the first layer through a tapped delay line (TDL) to instigate the delays present in the data; $y(t-1), y(t-2)$. The 7 inputs pass through a specific TDL where the output of this is a vector made up of the input signals at the current time and the previous input signals; $u(t), u(t-1)$. The bias values for each layer are denoted b_1 and b_2, k is algebraically the number of neurons per layer and $R = 7$ represents the number of input vectors at time (t). If the last layer of a multilayer network has sigmoid neurons, then the outputs of the network are limited to a small range. If linear output neurons are used the network outputs can take on any value [100].

The defining equation of this NARX network is as equation 4.2.

$$y(t) = f(y(t-1), y(t-2), u(t), u(t-1)) \tag{4.2}$$

The input training data consist of the 5 rows of 1000 cycles obtained from PCA representing the ionization current signal, integrated MAP signal (that correlates well to the load) and the engine speed. The output training data are the corresponding PPP measured from the in-cylinder pressure sensors obtained over the 1000 cycles. All datasets have mean values removed and are normalised so that they have maximum and minimum values of 1 and -1 according to neural network theory for training rapidness and network adaptivity ease [101]. Scaling the inputs in this manner results in the NN output also being scaled between 1 and -1. For the output of the NN (predicted PPP) to represent realistic values of PPP, it is upscaled in a reverse procedure to that in which the target data (measured PPP) was downscaled.

Using these 7 input data sets and 1 target data set, the network is trained using 'Bayesian-Regularisation backpropagation with early stopping', which prevents over-training. The val-

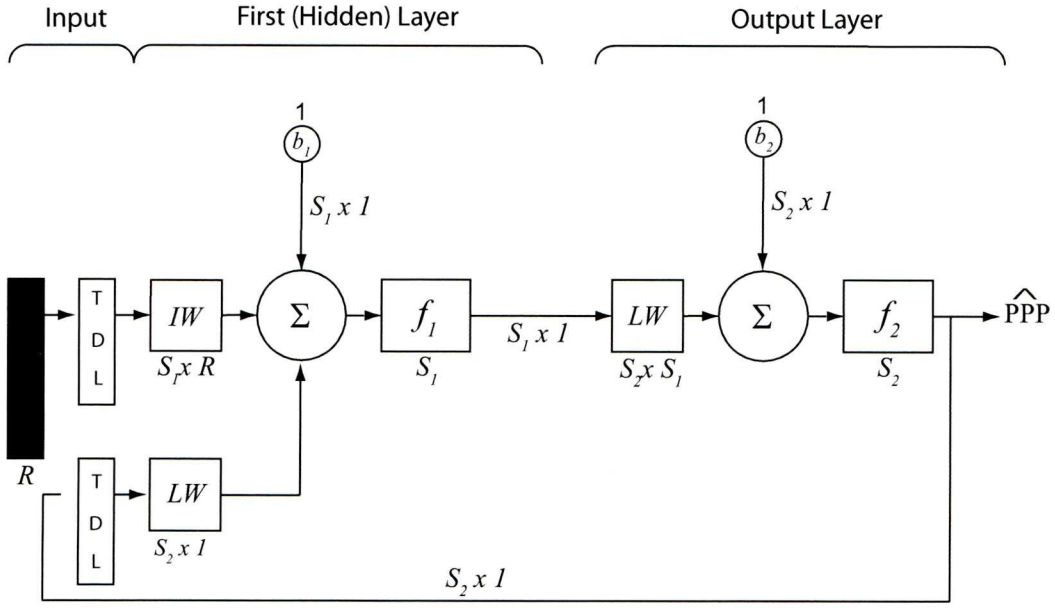

Figure 4.11: Schematic of a Two Layer NARX Network

idation dataset of 1000 cycles is employed here after each training epoch through being presented to the network. Early stopping occurs when the mean squared error of the validation dataset begins to increase indicating the optimal training epoch for that network has been reached.

4.7 Offline Neural Network Proving

After offline training, the 'hold-out' dataset of 1000 cycles is used to prove the network is predicting the PPP accurately offline. A sample of the comparison of actual PPP to predicted PPP over 1000 cycles is shown in fig. 4.12.

The offline correlation of the predicted PPP and actual PPP over 1000 cycles of 'hold-out' data can be seen in fig. 4.13. To quantify the accuracy of the neural network predictions on this 'hold-out' dataset, two measures of performance are used; Normalised Mean Square Error (NMSE) and R^2, which is the coefficient of determination where 1 is a maximum [122, 123, 120].

$$NMSE = \frac{1}{N\sigma_t^2} \sum_{n=1}^{N} [y(n) - t(n)]^2$$

where $y(n)$ is the predicted PPP in cycle n, $t(n)$ is the target value of PPP, σ_t^2 is the variance of the target and N is the number of engine cycles.

$$R^2 = 1 - \frac{\sigma_\epsilon^2}{\sigma_y^2}$$

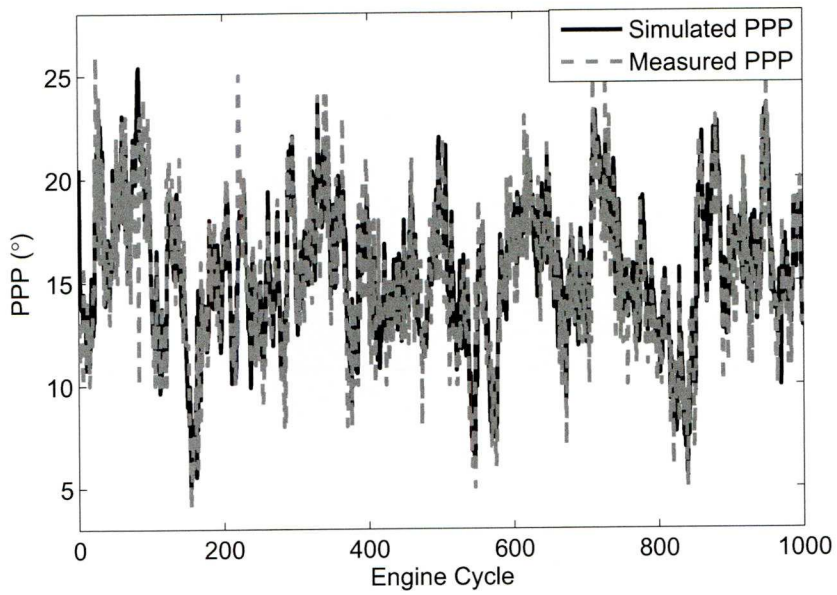

Figure 4.12: Predicted PPP and Actual PPP over 1000 cycles

where σ_ϵ^2 indicates the variance of the model residuals and σ_y^2 is the variance of the system output. Over the 1000 cycles of 'holdout' data:

$$\begin{aligned} NMSE &= 0.0162 \\ R^2 &= 0.7671 \end{aligned}$$

indicating over 75% of the variance in the PPP is explained by the estimated PPP based on the ionization signal. Figure 4.13 also shows the predicted PPP against the measured PPP as datapoints, clearly showing a definite correlation.

This correlation of 'hold-out' data implies good offline accuracy of the neural network at predicting PPP. This network was then implemented onto the engine to predict PPP in real time with a visual on-line measurement of actual PPP from the in-cylinder Kistler pressure sensor.

4.8 Online Neural Network Proving

Online network proving involves predicting PPP in real time as the engine is running with input signals streaming into the network. To emulate the offline simulation online, all signal processing that was done offline has to be undertaken online on the engine/dynamometer. This is done with SIMULINK and Real Time Workshop and the advantages of simplifying the offline computation becomes apparent.

Whilst the engine is running, the following must be occurring:

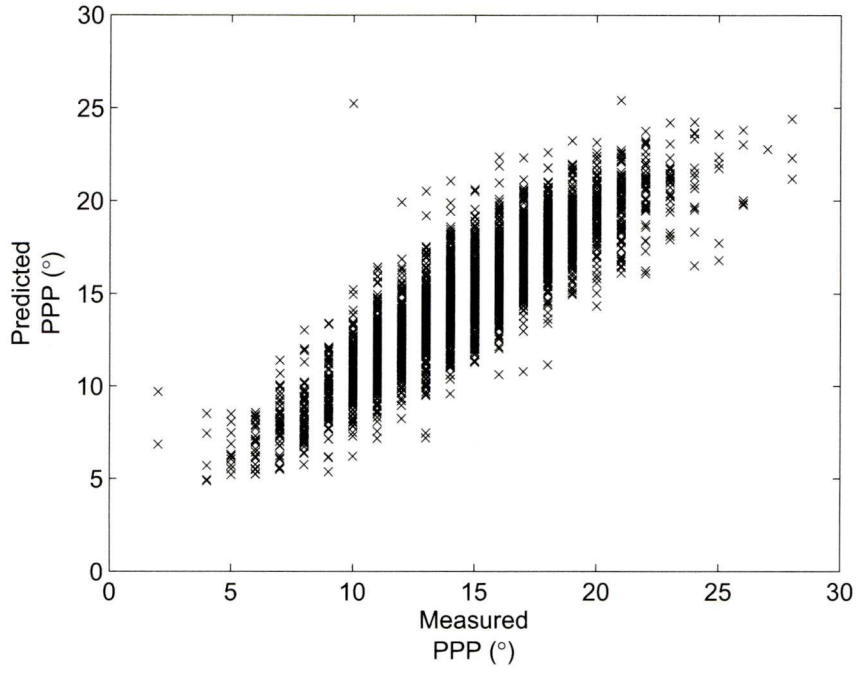

Figure 4.13: Correlation of Normalised and Scaled Predicted PPP and Normalised and Scaled Actual PPP over 1000 cycles

- N and integrated MAP are to be sampled once per 720° at a specific crank angle, matching the angle chosen for offline computation.
- From 25° until 55° after SA occurs, the ion current signal is sampled and stored into memory. This vector of 30 samples per combustion cycle is used for PCA.
- PCA reduces the 30 samples of ion current data to just 5 per combustion cycle. When executing PCA online the 30 samples of ion current data per combustion cycle are projected onto the previously calculated 'FeatureVector' matrix, which is stored in memory. This means that eigenvector-eigenvalue computations are not necessary online, only a simple multiplication computation.
- N, integrated MAP and the 5 PCA score samples have mean values removed and are normalised using values obtained during offline training of the network.
- The normalised 5 PCA scores, N and integrated MAP scaled samples are input to the neural network and a predicted PPP value is output that is upscaled using values obtained in network training. A comparison of this predicted PPP from the network and measured PPP from the in-cylinder pressure sensors will visually show the validity of the neural network model online.

Engine variables (load, ABV and SA ranges) were brought in line with the ranges used for

identification data acquisition (a must) and these were step-changed individually to illustrate robustness of the network at predicting PPP. The resulting predicted PPP and actual PPP are presented in the figs. 4.14, 4.15 and 4.16.

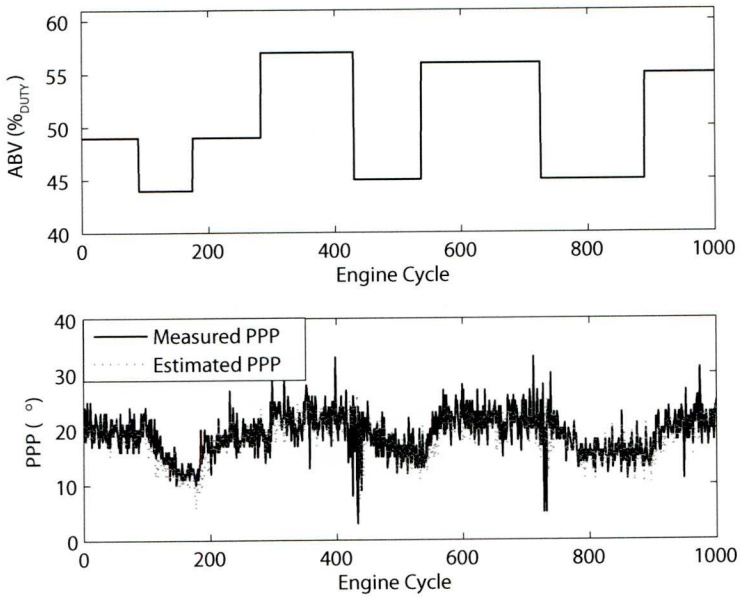

Figure 4.14: Correlation of Predicted PPP and Actual PPP over 1000 cycles due to step changes in ABV

4.9 Control Techniques

The good online correlation of actual PPP to predicted PPP from the ionization current signal indicates a successful neural network predictor. Accordingly to utilise this signal a feedback scheme which controls the ignition timing to maintain the PPP at a desired set-point of 16° for MBT is suggested. Since the PPP signal is affected by combustion variability, stochastic flame propagation and sensor noise the feedback scheme should be of a minimum variance type [8].

The feedback controllers were design on an identified model of the system from the inputs of the neural network to estimated PPP. A SISO linear Auto Regressive and Moving Average eXogenous (ARMAX) model was obtained by perturbing the SA and measuring the predicted PPP. The load and ABV were fixed around the mid-point of the intended neural network operating range. A summary of the excitation signals is detailed in table 4.5. The ARMAX model was thus represented as

$$y(z) = z^{-n_k}\frac{B(z)}{A(z)}u(z) + \frac{C(z)}{A(z)}e(z) \tag{4.3}$$

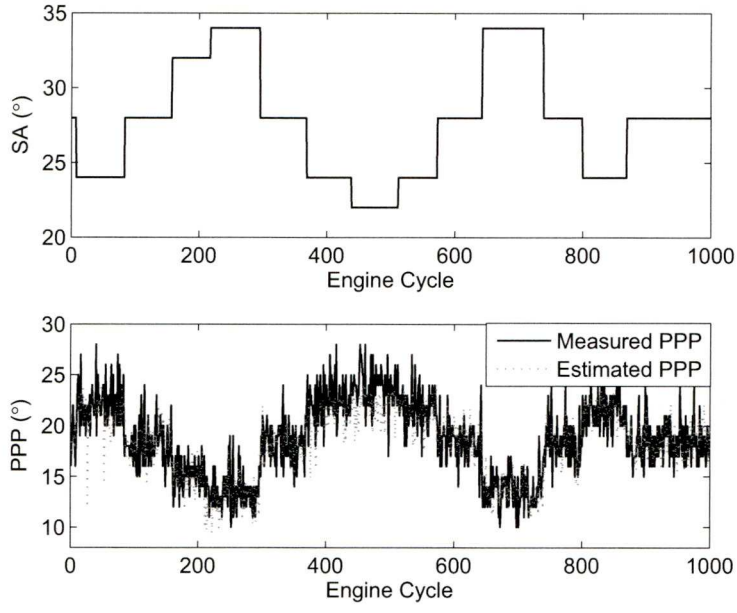

Figure 4.15: Correlation of Predicted PPP and Actual PPP over 1000 cycles due to step changes in Spark Ignition Timing

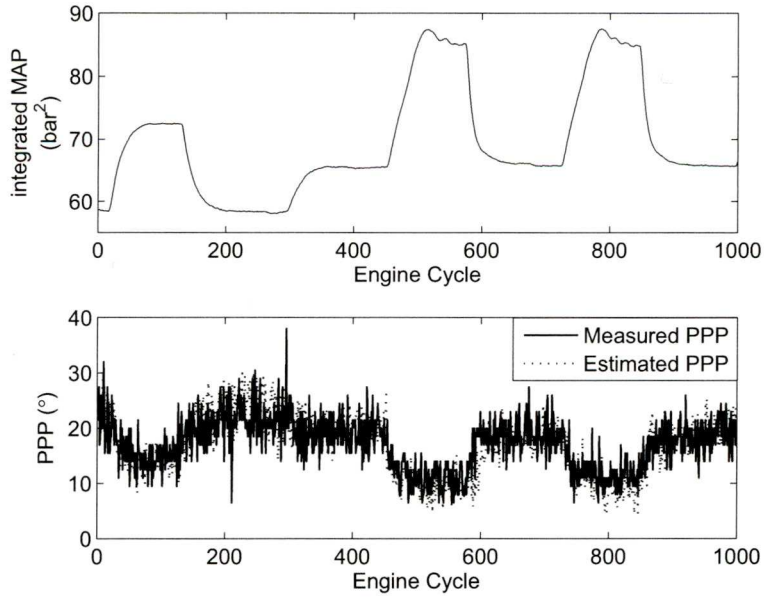

Figure 4.16: Correlation of Predicted PPP and Actual PPP over 1000 cycles due to step changes in Applied Load

Table 4.5: Perturbed signals used to generate ARMAX model of estimated PPP

Signal	Range	Perturbation Period
ABV [$\%_{duty}$]	Steady state 51	N/A
Load [V]	Steady state -0.10	N/A
SA [° BTDC]	24 to 34	0.4 s

where $y(z)$ represents the PPP output, e is the white noise assumed to be driving the coloring filter G_c (see fig. 4.17) acting on the PPP output and u is the SA input . A, B , and C are polynomials of the form

$$\begin{aligned} A(z) &= 1 + a_1 z^{-1} + \ldots + a_{na} z^{-n_a} \\ B(z) &= b_0 + b_1 z^{-1} + \ldots + b_{nb} z^{-n_b} \\ C(z) &= 1 + c_1 z^{-1} + \ldots + c_{nc} z^{-n_c} \end{aligned}$$

In this case the model orders n_a, n_b, n_c and the discrete time delay order, n_k were found to be 2, 1, 2, 1 respectively.

The identified parameters lead to the following transfer functions

$$\begin{aligned} G_b = z^{-n_k}\frac{B(z)}{A(z)} &= \frac{b_0 z^{-1} + b_1 z^{-2}}{1 + a_1 z^{-1} + a_2 z^{-2}} \\ &= \frac{-0.7398 z^{-1} + 0.3287 z^{-2}}{1 - 0.3952 z^{-1} - 0.04656 z^{-2}} \qquad (4.4) \\ G_c = \frac{C(z)}{A(z)} &= \frac{1 + c_1 z^{-1} + c_2 z^{-2}}{1 + a_1 z^{-1} + a_2 z^{-2}} \\ &= \frac{1 - 0.3738 z^{-1} - 0.03667 z^{-2}}{1 - 0.3952 z^{-1} - 0.04656 z^{-2}} \qquad (4.5) \end{aligned}$$

4.9.1 Types of Controllers

Four controllers were designed and evaluated for suitability to the problem in simulation; a standard minimum variance (MV) controller, a minimum variance with tracking (IMV) controller, a constrained variance (CV) controller and a pure integral controller. Minimum variance type controllers are suited to systems subject to persistent type noises since their aim is to minimize the output variance [111]. Using the determined zero mean ARMAX model, different control strategies were applied and evaluated in simulation. The resulting controllers were used with a negative feedback control scheme as illustrated in fig. 4.17, where G_c represents the coloring filter transfer function, G_b being the plant model, K the controller. The disturbance input, assumed to be of unit variance white noise, is denoted by e, the tracking command reference by u and the output by y.

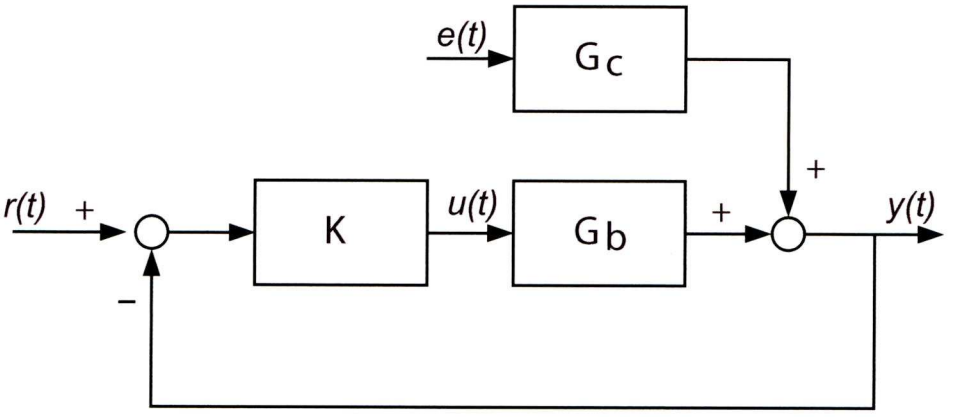

Figure 4.17: Implemented Closed Loop Feedback Control

Since all controllers are designed for zero mean models, an average of 16° of crank angle is to be removed from the predicted PPP output of the NN to achieve a zero mean signal and then this 16° is to be added to the controller output.

Minimum Variance Controller, MV

Minimum variance control has been implemented in peak pressure position control successfully [7, 8, 124, 125]. Minimum Variance (MV) controllers regulate outputs of closed loop stochastic systems to a constant set point by seeking a control signal $u(t)$ that will minimise the following performance or cost function:

$$J = E[y^2(t+k)] \tag{4.6}$$

where k is the time delay [111]. J involves the time delay, k, because $u(t)$ will only affect the output after $t+k$ delays. Minimum variance control is applied to the identified ARMAX structure for the strictly proper plant ($k > 0$) where A,B and C are polynomials in $z-1$ and k is the system delay:

$$y(t+k) = \frac{B(q)}{A(q)}u(t) + \frac{C(q)}{A(q)}e(t+k) \tag{4.7}$$

or

$$Ay(t) = z^{-k}Bu(t) + Ce(t) \tag{4.8}$$

where $e(t)$ is a random zero mean sequence (or white noise) with a finite variance σ^2. That is:

$$E[e(t)] = 0; E[e(t)^2] = \sigma^2 \tag{4.9}$$

The key point now is that no control action $u(t)$ may affect the output variance until time $t = t + k$ and this will reflect in the search for the optimal control action $u(t)$.

The effects of the disturbance input (characterised by $\frac{C}{A}$) $e(t)$, are separated into the polynomials F(of order k) and G. F characterises the noise dynamics not affected by the control input, G is associated with the remaining noise dynamics affected by the control action [8].

These polynomials are defined:

$$\begin{aligned} F &= 1 + f_1 z^{-1} + \ldots + f_{k-1} z^{-(k-1)} \\ G &= g_0 + g_1 z^{-1} + \ldots + g_{n_g} z^{-n_g} \\ n_g &= max(n_a - 1, n_c - k) \\ n_f &= k - 1 \end{aligned}$$

so that they satisfy the polynomial

$$C = AF + z^{-k} G \tag{4.10}$$

or

$$\frac{C}{A} = F + z^{-k} \frac{G}{A} \tag{4.11}$$

From equation 4.7, it follows that the system can be expressed as:

$$y(t + k) = \left[\frac{B}{A} u(t) + \frac{G}{A} e(t) \right] + F e(t + k) \tag{4.12}$$

By inverting 4.8, $e(t)$ can be expressed in terms of causal signals available when deciding the control action, y(t) and u(t). This is necessary since t is the current time sample and so terms will involve $e(t), e(t-1), \ldots,$:

$$e(t) = \frac{A}{C} y(t) - z^{-k} \frac{B}{C} u(t) \tag{4.13}$$

Now $e(t)$ can theoretically be determined from the measurable input $u(t)$ and output $y(t)$. This equation for determining $e(t)$ can be substituted into 4.12 to give:

$$y(t+k) = \left[\frac{B}{A}u(t) + \frac{G}{C}y(t) - z^{-k}\frac{BG}{AC}u(t)\right] + Fe(t+k) \tag{4.14}$$

which can be simplified using 4.10 to give:

$$y(t+k) = \left[\frac{BF}{C}u(t) + \frac{G}{C}y(t)\right] + Fe(t+k) \tag{4.15}$$

Clearly $\frac{BF}{C}u(t)$ and $\frac{G}{C}y(t)$ are dependent on inputs up to sample time t so the best prediction of $y(t+k)$, $\hat{y}(t+k)$, up to time t is:

$$\hat{y}(t+k|t) = \left[\frac{BF}{C}u(t) + \frac{G}{C}y(t)\right] \tag{4.16}$$

and hence $Fe(t+k)$ is the output prediction arising from uncontrollable noise sources $e(t+1), \ldots, e(t+k)$.

Equations 4.15 and 4.16 can be substituted into the cost function to be expressed as:

$$J = E\left[y^2(t+k)\right] = E\left[\hat{y}(t+k|t) + Fe(t+k)\right]^2 \tag{4.17}$$

J, the variance, is minimised by setting the predicted output, $\hat{y}(t+k|t)$, to zero. This gives the control law [111]:

$$BFu(t) + Gy(t) = 0 \tag{4.18}$$

or

$$u(t) = -\frac{G}{BF}y(t) \tag{4.19}$$

Figure 4.18 illustrates the minimum variance control strategy.

This theory was applied to the identified ARMAX model of transfer functions for the plant 4.4 and the noise 4.5. This ARMAX model has the structure: $n_a = 2$, $n_b = 1$, $n_c = 2$, $n_k = 1$. The following polynomials can be defined for $k = 1$:

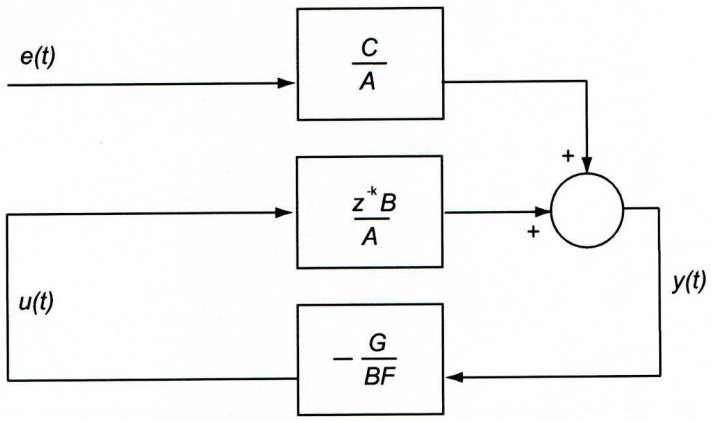

Figure 4.18: Implemented Minimum Variance Closed Loop Feedback Control

$$\begin{aligned} F &= 1 \\ n_g &= 1 \\ G &= g_0 + g_1 z^{-1} \\ n_f &= 0 \end{aligned}$$

for the polynomial:

$$C = AF + z^{-k}G \tag{4.20}$$

From the ARMAX model (4.4 and 4.5), polynomials A, B and C are defined as:

$$\begin{aligned} A(z) &= 1 - 0.3952z^{-1} - 0.04656z^{-2} \\ Bz^{-1}(z) &= z^{-1}\left[-0.7398 + 0.3287z^{-1}\right] \\ C(z) &= 1 - 0.3738z^{-1} - 0.03667z^{-2} \end{aligned}$$

and so substituting into 4.10 and solving for coefficients of z terms:

$$\begin{aligned} g_0 &= 0.0214 \\ g_1 &= 0.099 \\ G &= 0.0214 + 0.099z^{-1} \end{aligned}$$

G, B and F can be substituted into the control law 4.19 to give

$$K = -\left[\frac{0.0214 + 0.099z^{-1}}{-0.7398 + 0.03287z^{-1}}\right]$$

The output variance is theoretically reduced to 1 deg^2. However, one limitation of this controller is that it is designed to regulate the output $y(t)$ about zero; it does not contain integral action required for non-zero mean disturbances or tracking demand changes. This can be seen in fig. 4.21 where by the minimum variance controller has little response to a step disturbance.

Integrated Minimum Variance Controller, IMV

Minimum variance control can be adapted to allow non-zero mean tracking which is applicable in this application. The standard minimum variance control, as described for the ARMAX model 4.4 and 4.5 regulates the peak pressure position variance to 16° ATDC from steady state input signals. Incorporating integral action in the controller would allow peak pressure position to be regulated at alternative desired settings. Figure 4.19 illustrates the minimum variance control strategy with the integrator to provide tracking.

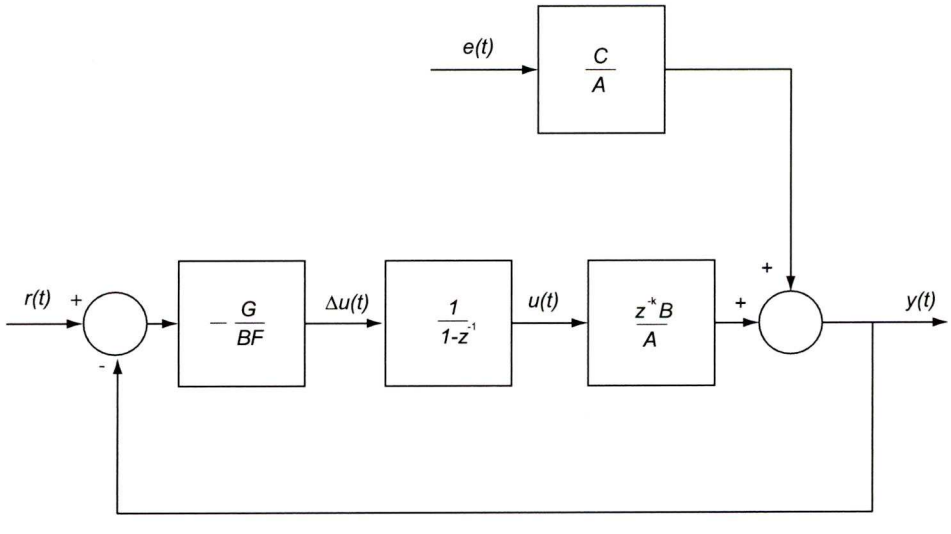

Figure 4.19: Implemented Minimum Variance Closed Loop Feedback Control

The minimum variance regulator $\frac{G}{BF}$ provides the control increment $\Delta u(t)$ whilst $u(t)$, the input to the plant, is provided by the integrator. The non-zero set point $r(t)$ has been included and so the minimum variance regulator is now applied to $y(t) - r(t)$. The cost function now becomes:

$$J = E[y(t+k) - r(t+k)]^2 \tag{4.21}$$

where k is the time delay.

The polynomials can be solved:

$$\begin{aligned} F &= 1 + f_1 z^{-1} + \ldots + f_{k-1} z^{-(k-1)} \\ G &= g_0 + g_1 z^{-1} + \ldots + g_{n_g} z^{-n_g} \\ n_g &= max(n_a, n_c - k) \\ n_f &= k - 1 \end{aligned}$$

to satisfy the modified identity:

$$C = \Delta AF + z^{-k} G \tag{4.22}$$

The control law is thus:

$$\Delta u(t) = \frac{G}{BF}(r(t) - y(t)) \tag{4.23}$$

which following the discrete integrator gives the controlled input:

$$u(t) = \Delta u(t) + u(t-1) \tag{4.24}$$

The standard MV controller is hence designed for the system augmented with an integrator so therefore the output variance is increased.

This theory was applied to the identified ARMAX model of transfer functions for the plant (eqn. 4.4) and the noise (eqn. 4.5). This ARMAX model has the structure: $n_a = 2$, $n_b = 1$, $n_c = 2$, $n_k = 1$. The following polynomials can be defined for $k = 1$:

$$\begin{aligned} F &= 1 \\ n_g &= 2 \\ G &= g_0 + g_1 z^{-1} + g_2 z^{-2} \\ n_f &= 0 \end{aligned}$$

for the identity 4.22. G has increased by 1 order from standard minimum variance resulting from the multiplication by the integrator.

From the ARMAX model (4.4 and 4.5), polynomials A, B and C are defined as:

$$\begin{aligned} A(z) &= 1 - 0.3952z^{-1} - 0.04656z^{-2} \\ Bz^{-1}(z) &= z^{-1}\left[-0.7398 + 0.3287z^{-1}\right] \\ C(z) &= 1 - 0.3738z^{-1} - 0.03667z^{-2} \end{aligned}$$

and so substituting into 4.22 and solving for coefficients of z terms:

$$\begin{aligned} g_0 &= 1.0214 \\ g_1 &= -0.3853 \\ g_2 &= -0.04656 \\ G &= 1.0214 - 0.3853z^{-1} - 0.04656z^{-2} \end{aligned}$$

G, B and F can be substituted into the control law, equation 4.23, to give

$$K = \left[\frac{1.0214 - 0.3853z^{-1} - 0.04656z^{-2}}{-0.7398 + 0.3287z^{-1}}\right]\left[\frac{1}{1 - z^{-1}}\right]$$

Simulation of the controller demonstrated a fast response time, however it also revealed overshoot and excessive control effort as shown in fig. 4.21.

Constrained Variance Controller, CV

To achieve a good compromise between tracking and low output variance, a constrained variance technique was applied to the problem. For the closed loop system the transmission from the noise input e to the output y, is given by:

$$P_e^y(z) = \frac{y(z)}{e(z)} = \frac{G_c(z)}{1 + K(z)G_b(z)} \tag{4.25}$$

The output variance σ_y for the system determined by (4.25) is given (see [126, 127]) as:

$$\sigma_y^2 = \frac{1}{2\pi j}\oint_{c_1} P_e^y(z^{-1})P_e^y(z)\frac{dz}{z} \tag{4.26}$$

where c_1 denotes a contour on the unit circle and the system is assumed to be stable. Since the controller is required to provide tracking a proportional-integral (PI) controller

$\frac{(k_p+k_i)z-k_p}{z-1}$ is considered. For the system of Eqn. (4.3), the closed loop transfer function of Eqn. (4.25) can be expressed as:

$$P_e^y(z) = \frac{(z^2 + c_1 z + c_2)(z-1)}{(z^2 + a_1 z + a_2)(z-1) + ((k_p + k_i)z - k_p)(b_0 z + b_1)}$$

For a specified output variance, parameterized solutions of k_p and k_i for the definite integral of equation (4.26) can readily be obtained. The MV designed with an integrator for tracking revealed an output variance of 2 deg^2 which is significantly higher than the MV design with an output variance of 1 deg^2. A compromise of both low variance and tracking can be achieved by constraining the output variance between these values. Several fixed variance values were trialled in the design of the constrained variance controller to obtain the best trade-off between tracking and output variance. Simulation revealed an output variance of 1.1 deg^2 was sufficient to provide adequate tracking and non-zero mean disturbance rejection whilst retaining a low level of output variance. Accordingly, a symbolic solution for k_i and k_p to the definite integral of Eqn. (4.26) for the closed loop system was obtained and loci of possible controller gains with the desired output variance plotted as can be seen in fig. 4.20.

$$\begin{aligned} k_p &= -0.0480 \\ k_i &= 0.2740 \end{aligned}$$

resulting in the constrained variance PI controller:

$$K(z) = \frac{0.2260z + 0.0480}{z - 1}$$

Integral Controller, I

A pure integral controller that has no variance minimizing action was also implemented in a negative feedback scheme to provide a bench mark for tracking. Instead of an heuristically tuned controller, the choice of the integral value was chosen in a methodical manner; from the same variance loci as in fig. 4.20. This choice gives a lower integral, hence a slower controller, than the CV controller at the same variance constraint.

$$K = -\frac{0.2684}{1 - Z^{-1}}$$

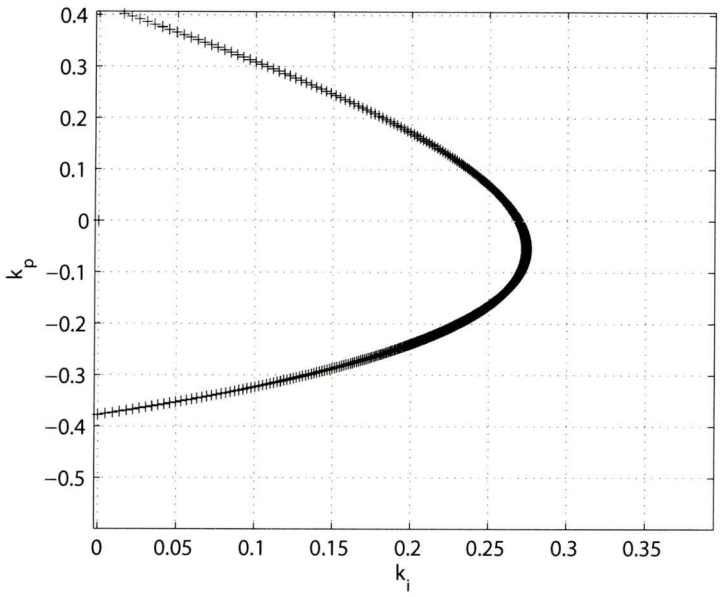

Figure 4.20: Loci of Possible Controller Gains for $\sigma_y^2 = 1.1deg^2$

Table 4.6: Comparison of Stability Margins for the Four Controllers

Control	Gain Margin	Delay Margin
MV	24.8dB	∞
IMV	5.95dB	4.87
CV	23.03dB	23.8
I	19.47db	24.4

4.9.2 Validation of feedback scheme

Each controller was evaluated for tracking and variance reduction in a series of tests; the robustness of the four candidate controllers was evaluated and the gain and delay margins are detailed in table 4.6.

The four controllers were implemented onto the engine and closed loop variance of the estimated PPP was measured over 500 cycles when at steady state as in table 4.7. PPP was set to a demand of 16° ATDC with an ABV duty of 51% and a voltage of 0.10V through the dynamometer. Although it has no ability to track, MV control represents the benchmark for a reduction in the variance over the open loop variance. As integral action is added to create the IMV control, the variance increases. CV control shows a reduction in variance over the open loop PPP whilst I control shows an increase.

To evaluate the tracking ability of each controller, a step demand in SA of 7° was experimentally executed and shown in fig. 4.21. MV control has no tracking to the demand, IMV control tracks but has excessive variance in the PPP also. The I controller and the

Table 4.7: Comparison of Closed Loop PPP Variance for Controllers

Control	PPP Variance
MV	2.0646
IMV	3.4710
CV	2.4959
I	2.87
Open Loop	2.4784

CV controller perform in a similar manner since they were selected from the same loci of variance, though the CV controller is marginally quicker.

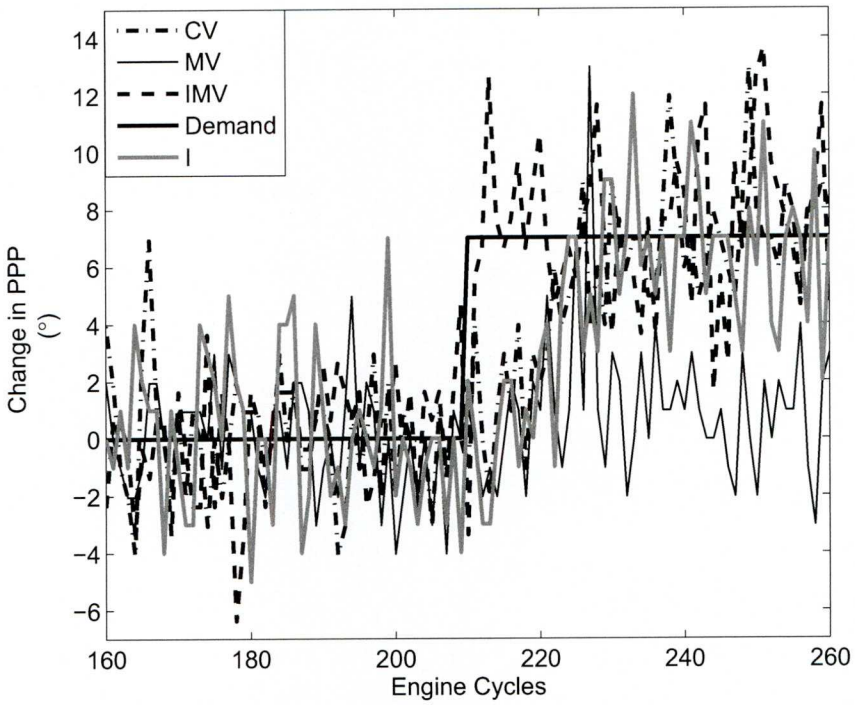

Figure 4.21: Step Response of Four Controllers

For tracking demands and for adequate rejection of non-zero mean disturbances it was necessary to consider the three techniques with integral action at the cost of the increases in output variance offered by the standard MV design.

Due to the lower robustness margins and excessive output variance observed in the IMV, this was not considered. The CV controller performs marginally better than the I controller in step response time. The value of the I controller was arrived at by following the CV methodology but then ignoring any desirable contribution to the controller other than the pure integral. The CV was thus deemed the most appropriate. The constrained variance type controller was implemented with the NN system in a feedback loop for control of PPP.

Robustness of the controller was examined by adding step disturbances to the control input signals. The controller was tested over a range of speed settings, by step changes in the ABV signal and by varying the applied load through the dynamometer. The closed loop system was found to be well behaved over a range within the ARMAX models identification data range. The system, through step input signal disturbances was able to track to a desired PPP value as illustrated in fig. 4.22. It can be seen that the mean of PPP and the mean of predicted PPP match the PPP tracking demand.

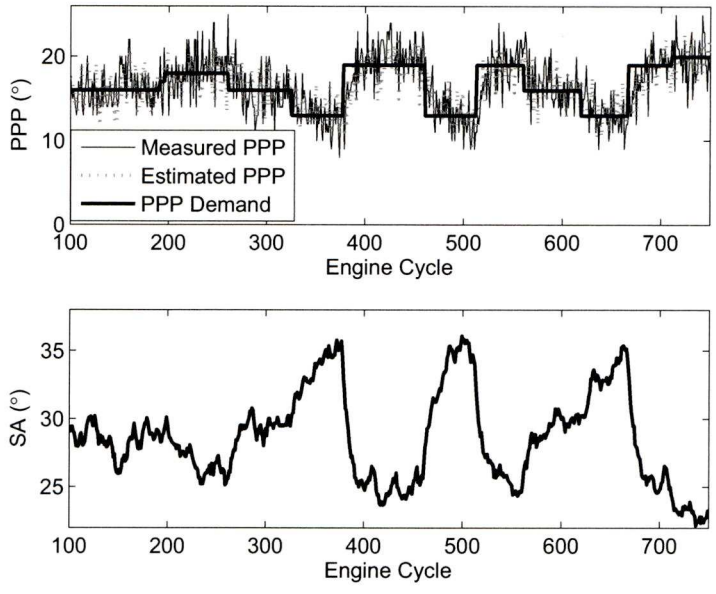

Figure 4.22: Predicted PPP and Actual PPP tracking to Demanded PPP and Required Spark Advance

Figure 4.23 illustrates the predicted PPP tracking to a demanded PPP whilst step disturbances are applied to the ABV, thus altering engine speed.

Figure 4.24 illustrates the predicted PPP tracking to a demanded PPP of 16° ATDC whilst step disturbances are applied to the load, thus altering engine speed and MAP.

The closed-loop system was intended to introduce the necessary tracking at the cost of increasing the output variance of the predicted PPP by 10% over the MV design. Furthermore, when changing the operating point away from the identified region the validity of the model reduces and the identification range is restricted by the equipment rather than the technique. Hence for effective control over the entire operating region of the PPP estimation algorithm it is suggested a series of scheduled linear CV controllers should be considered.

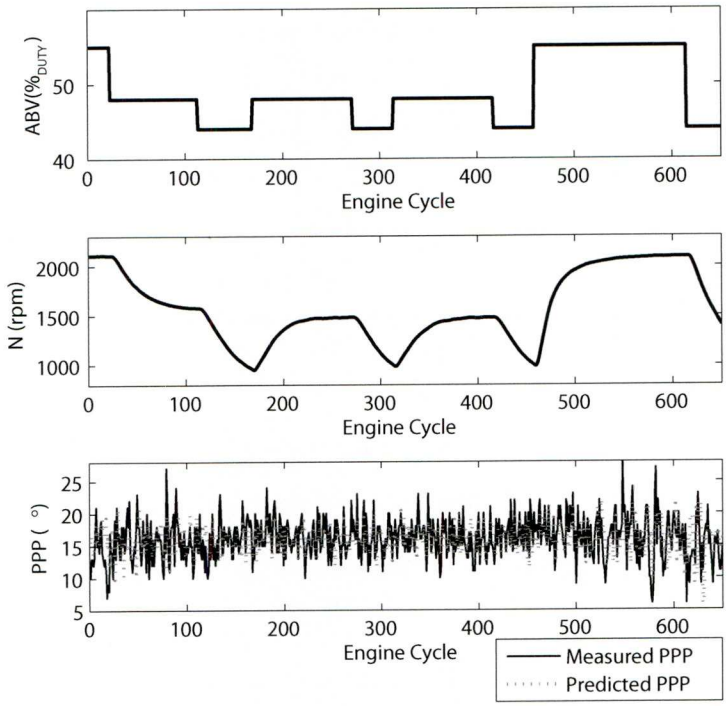

Figure 4.23: Predicted PPP and Actual PPP tracking to Demanded PPP with step disturbances to ABV

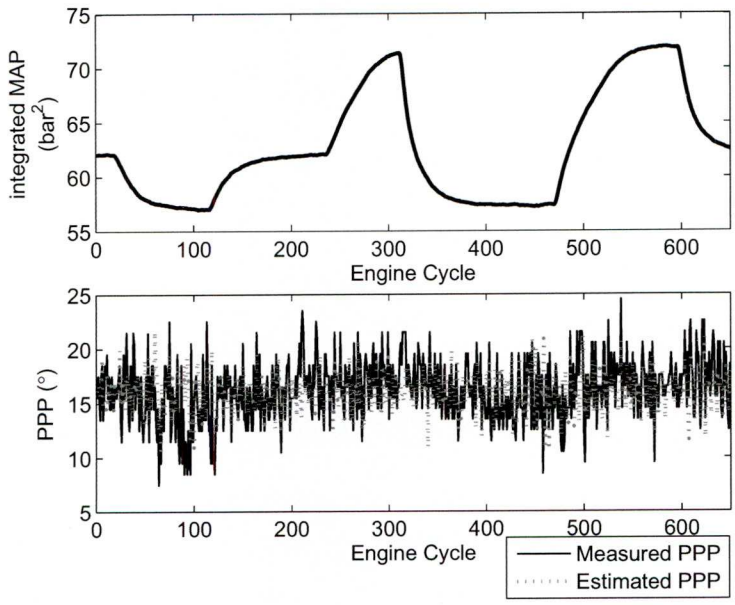

Figure 4.24: Predicted PPP and Actual PPP tracking to Demanded PPP with step disturbances to Load

4.10 Conclusions

A technique for on-line prediction of PPP from the ionization current signal is presented. The proposed method uses a NN scheme applied to dynamically changing data output from an on-line principal-component filter. Experimental results demonstrate that the network accurately predicts the PPP measured by a piezoelectric in-cylinder pressure sensor using charge amplifiers on-line across varying operating engine parameters. A constrained-variance, robust, low control-effort method for PPP regulation and tracking with near minimum variance control is described. It is shown experimentally on an engine dynamometer that with the proposed techniques the PPP in a single cylinder of a production four-cylinder PFI gasoline engine can be accurately controlled over the range of an identified model. The experimentally implemented control system is demonstrated to be robust to step disturbances of load and speed and to successfully track to a desired PPP setting.

Chapter 5

Four Cylinder PPP Control and Cylinder Balancing

5.1 Introduction

Flame development and propagation varies cycle by cycle since the flame growth depends on local mixture motion and composition. These quantities vary in successive cycles in any given cylinder and may vary between cylinders. These cylinder-to-cylinder variations are substantial; one or more cylinders may knock whilst others may not [9]. These cylinder-to-cylinder and cycle to cycle variations limit the operating regime of the engine, therefore it would be a natural progression of in-cylinder minimum variance control of peak pressure position (PPP) to be extended from a single cylinder to all four cylinders of the IC engine.

Chapter 4 described the procedure for estimation and control of PPP in a single cylinder of a four cylinder engine. The basic premise of establishing that technique on all four cylinders is to repeat the technique process steps on each individual cylinder; identifying a relationship between N, integrated MAP and the ion current signal to the PPP, creating a model for each cylinder and then ultimately implementing a control loop on each cylinder simultaneously. In this manner, the problem does not involve treating the engine as a single system to identify, model and control but constitutes the engine being treated as four individual systems identified into four individual models with four implemented control feedback loops.

Although demonstrated successfully on a single cylinder, progressing to four individual cylinders poses problems. The dSPACE hardware may 'struggle' to sample all information once per degree for each cylinder, before the PCA computation and feedback control and even more significantly: there is a difference between the cylinders as described in the section 5.3 whereby TDC occurs earlier than expected in two cylinders which is required to be accounted for in any four cylinder balancing control scheme.

Figure 5.1 illustrates the concept of the four cylinder system; neural networks are trained to predict peak pressure position on each cylinder and then ARMAX models will be identified around these individual networks and the plant (enclosed by the dashed lines) so that feedback control can be applied to regulate the peak pressure position to a desired crank angle on each cylinder.

After examining the differences between the cylinders, this chapter then describes the engine operation in an open loop manner with reference to spark advance and achieved indicated mean effective pressure (IMEP) in section 5.3.1. Through the techniques applied, the controlled cylinders will achieve these IMEP values whilst regulating the PPP on each cylinder across transients without an increase in the cycle to cycle variations in PPP. Section 5.4.1 describes the generation of the identification signals, which are processed in the same manner as chapter 4. The neural networks (NN) are described in section 5.5 before they are validated in section 5.6. Control is applied using the constrained variance technique in section 5.7 before the results are discussed in section 5.8.

5.2 Cylinder Balancing

Estimation and control of air-fuel ratio and peak pressure position on an individual cylinder would allow progression to individual control of all cylinders in an IC engine. This would allow attempts at the concept of cylinder balancing. Balancing of all cylinders ensures smoother engine operation which provides improved component life and driver perception of performance. The concept of cylinder balancing suggests an imbalance between the cylinders of an engine that, traditionally, refers to the air-fuel ratio differences across the cylinders and this can be caused by a multitude of geometric differences, injector differences or aging wear [128]. It is infact known that injector variability may cause cylinder-to-cylinder differences in the mixture composition of the order of 5% [9]. Solutions to this would be to adjust the fuel pulse width (FPW) for each cylinder individually to achieve a balance. Balancing in terms of peak pressure position for each cylinder to achieve MBT for each cylinder is also desirable. Allowing each cylinder to be controlled independently provides the opportunity for increased engine efficiency if the PPP is regulated to the optimum position on each cylinder.

Cylinder imbalance can be measured by numerous methods. Estimated crankshaft acceleration [128] is the least expensive in terms of cost. Since the rotational speed of a crankshaft can be reconstructed from a tooth wheel that generates pulses, the time between two teeth with respect to each cylinder can be found. If the teeth chosen are regarded to possess maximum crankshaft acceleration information, the passage times between the teeth can be calculated and any offsets in these passage times between cylinders are regarded as an imbalance.

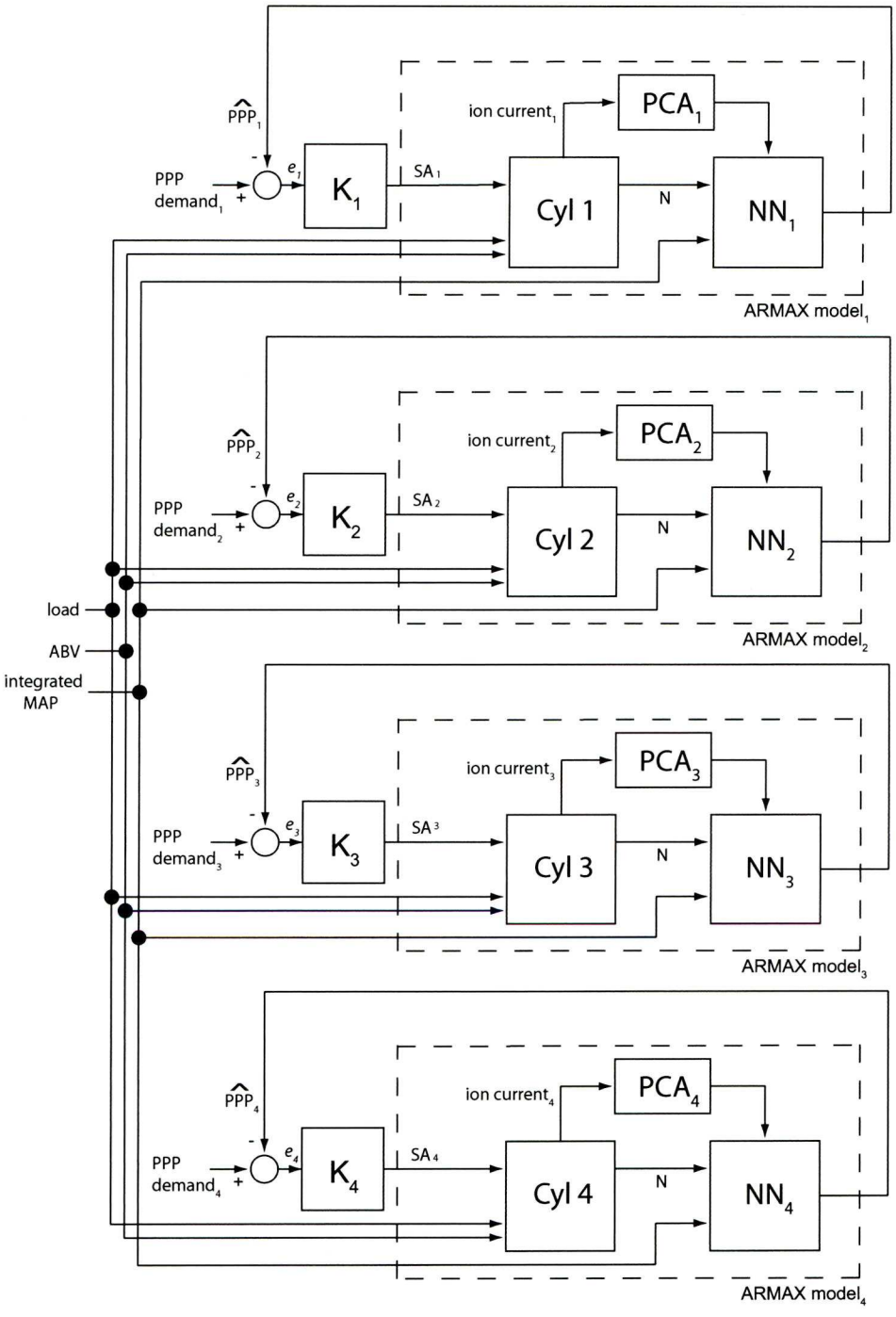

Figure 5.1: Four Cylinder PPP Control System Concept

In-cylinder pressure measurements and crank position can be used to calculate the cycle averaged torque for each cylinder [128]. Controllers can compensate for any torque imbalances between cylinders.

Exhaust manifold pressure can also be a measure of cylinder balance. The exhaust manifold pressure pulses due to an exhaust event for each individual cylinder are considered equal when cylinders are balanced [128]. Exhaust mounted UEGO sensors have been used in cylinder balancing to allow the individual tuning of the air-fuel ratio in closed loop strategies [13, 129, 130, 131, 124].

Benvenuti *et al* [131] propose a method for the estimation of each injector characteristics via measurements of the intake-manifold pressure, the crank-shaft speed, the throttle-valve plate angle, the injections on-time and the UEGO sensor reading from the exhaust.

In a series of papers Li *et al* [125, 124, 132] spark advance is used as an actuator for regulating peak pressure position. Progressively in [132] torque balancing is performed on a six-cylinder engine in a steady state operation using an index (deviation from an average torque value) for torque variation in each cylinder. ARMA models based on torque generation between cylinders in proposed and model predictive control is used. This work is only validated in statistical simulation with the author conceding that real-time control was a subject for future work.

5.3 Variation Between Cylinders

The experimental engine used in this work is a Ford Zetec $1.6l$ four-cylinder IC engine. Before crankshaft based (or crank angle domain) algorithms can be implemented on all four cylinders individually, the absolute TDC of each cylinder in relation to TDC of cylinder 1 must be checked. This would be due to the algorithms implemented being triggered at certain absolute crankshaft degrees relative to the encoder at cylinder 1. By rotating the crankshaft using the starter motor with the throttle wide open and measuring the in-cylinder pressure a non-motored curve is generated for each cylinder and shown in fig. 5.2. Expected maximum pressure for the non-motored curve is at TDC and for the four cylinder SI IC engine TDC for each cylinder as a position of the crank angle is displayed in table 5.1.

Expected TDC at these four angles is relative to Cylinder 1. On installation and set up of the engine/dynamometer apparatus at the University of Liverpool, TDC for cylinder 1 (or 0° crankangle) was determined via mechanical means [6] and the TDC for the other three cylinders was set at their respective expected TDC angles, as in table 5.1, relative to cylinder 1. Peak pressure for the non-motored curves for each cylinder are expected to occur very near to these TDC crank angles. Non-motored curves averaged for numerous cycles are shown in

Table 5.1: Expected TDC for Each Cylinder

Cylinder	TDC Location
Cylinder 1	0°
Cylinder 2	180°
Cylinder 3	540°
Cylinder 4	360°

fig. 5.2. The peak pressure may occur up to 1° of crank angle prior to the actual relative TDC due to the effects of heat transfer into the cylinder walls and gas blow by, known as the thermodynamic loss angle [9]. The thermodynamic loss angle would be consistent across all cylinders.

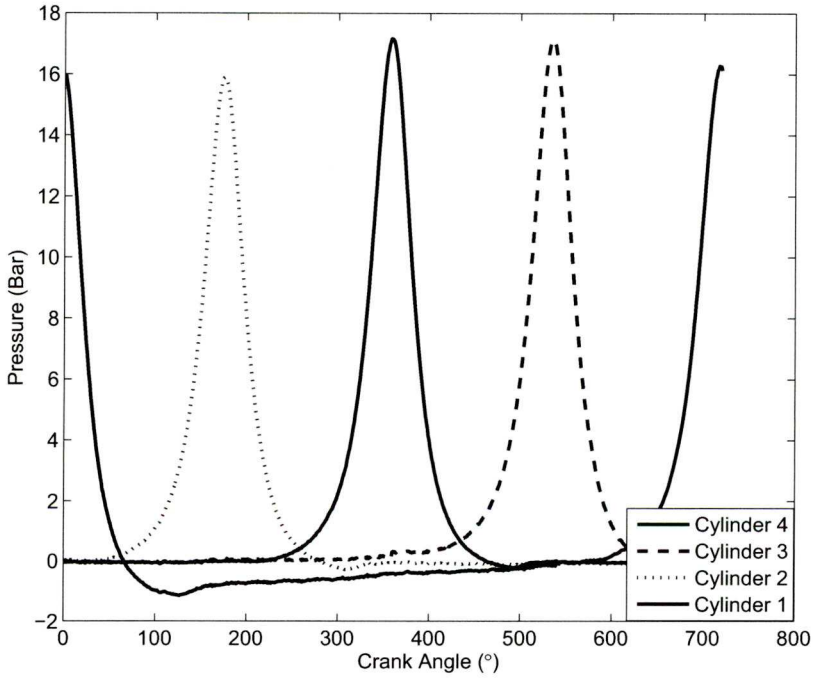

Figure 5.2: Pressure Plots of Non-Motored Cycles for Four Cylinders

However, after examination of the produced fig. 5.2, peak pressure for each cylinder occurs by a varying amount before the relative TDC for each cylinder. Table 5.2 displays the actual crank angle degree of rotation experienced that the peak pressure occurs relative to expected TDC for each cylinder.

Each cylinder experiences up to 1° of crankshaft rotation difference of measured PP to actual TDC explained by the thermodynamic loss angle but the explanation of the differences between cylinders 2,3 and 3,4 (3°) is a geometric design difference between the cylinders. This

Table 5.2: PP Angle Prior to TDC for Each Cylinder

Cylinder	Experienced PP Location	Angle of PP Relative to TDC
Cylinder 1	719°	−1°
Cylinder 2	176°	−4°
Cylinder 3	536°	−4°
Cylinder 4	359°	−1°

implies that cylinders 2 and 3 reach TDC 3° before expected. This has profound implications on any crank angle triggered control algorithms. If trying to control PPP for each cylinder to 16° ATDC by setting a SA at, say, 28° BTDC on each cylinder, SA and PPP are angular measurements relative to each individual cylinder TDC, which in turn is measured relative to the TDC of cylinder 1. This implies that control algorithms for cylinders 1 and 4 can be triggered directly from the crank angle encoder absolute values whereas control algorithms for cylinders 2 and 3 have to be triggered 3° early relative to the crank angle encoder.

If PPP is to be controlled on four cylinders and these cylinders are to be balanced, then this discrepancy between cylinders will have to be taken into account before cylinder balancing can begin.

Indicated mean effective pressure (IMEP) is the indicated work done by the gas on the piston, essentially a measure of the work output per swept volume and is independent of the size of the cylinder. The dynamic calculation of IMEP is highly sensitive to crank angle phasing errors [133], [134] and is calculated in real time using the following equation:

$$imep = \frac{\Delta i}{V_s} \sum_{i=0}^{719} p_i . \frac{dV_i}{di} \tag{5.1}$$

where V_s is the swept volume, V_i is the cylinder volume at crank angle i and p_i is the cylinder pressure at crank angle i.

The compression ratio of the engine used is 10.3 : 1. The cylinder bore diameter is $0.076m$ and the piston stroke length is $0.088m$. This gives a total swept volume ,V_s, of $3.9921\text{x}10^{-3}m^3$ with a clearance volume of $4.2926\text{x}10^{-5}m^3$.

This equation would give net IMEP values; the work delivered to the piston over 720° or crank angle (or four piston strokes). Gross IMEP, work delivered over the compression and expansion strokes only, can also be calculated by using the equation between 180° to 540° of crank angle ATDC. This gross IMEP is more commonly used than net IMEP due to it relating to the compression, combustion and expansion strokes and will be used in this work.

Table 5.3: Spark Advance and Resulting Averaged PPP across Four Cylinders

SA All Cylinders (° BTDC)	Average PPP for All Cylinders (° ATDC)
26	18.68
27	17.65
28	16.12
29	15.84
30	15.21
31	14.08
32	13.98
33	13.08
34	12.32

This susceptibility to phasing errors was evident after examining IMEP results for all cylinders in a steady state test with identical SA settings applied across all cylinders.

With this in mind for this work, the triggering of all algorithms for cylinders 2 and 3 will now be 3° earlier relative to expected TDC for that cylinder synchronised from cylinder 1. This 'removes' any geometric differences between all cylinders with respect to crank based triggered models and control algorithms and hence allows for real cylinder balancing as opposed to a perceived cylinder balancing from false TDC measurements. **Henceforth all crankshaft measurements detailed in the following have had these adjustments applied.**

5.3.1 Open Loop Spark Advance

EMS determined SA for an engine is not set individually for each cylinder but is the same across all cylinders. In this section the need for individual cylinder SA is highlighted by illustrating the differences in achieved PPP when SA is set equally for all cylinders. Each cylinder PPP characteristics are determined by running the engine in steady state open loop. It is accepted that a PPP of 16° ATDC will generally give MBT [9] and so a SA sweep was done to determine a universal SA that gives an average PPP of 16° ATDC across the cylinders. The single SA setting applied to all cylinders was retarded from 26° BTDC (for each respective cylinder) through to 34° in single crank angle degree increments. As an average across the cylinders, the SA setting was chosen that gave 16° PPP averaged across across all cylinders. Table 5.3 detail the engine parameters used to achieve the data where SA for each cylinder is in crank angle degrees BTDC of the respective cylinder. A constant ABV setting of $53\%_{duty}$ and an applied voltage load of $0.14V$ through the dynamometer is employed.

These results are plotted in fig. 5.3.

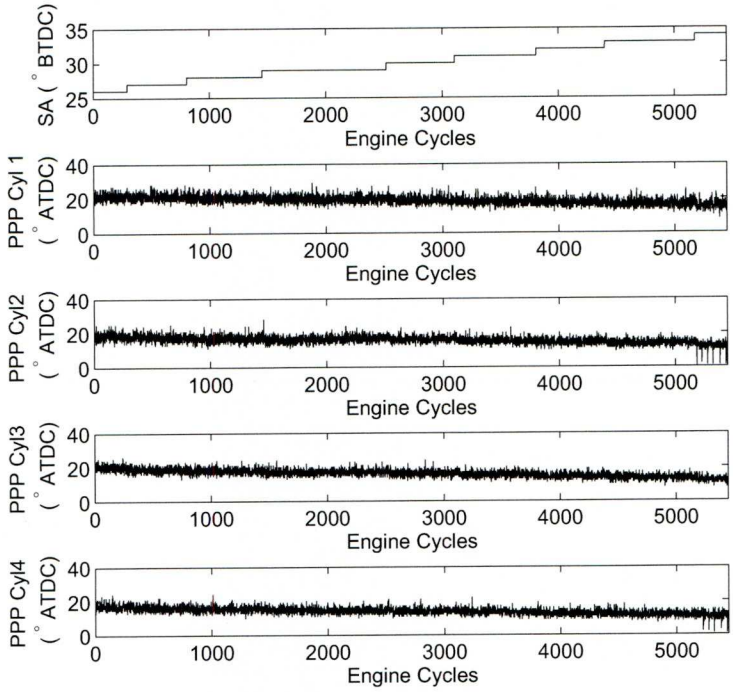

Figure 5.3: SA setting and resulting PPP plots for all cylinders

It can be seen that a universal SA setting of 28° BTDC across all cylinders gives an average PPP closest to 16° ATDC across all four cylinders. When the engine is run in the steady state at a common SA setting to achieve an average PPP of 16° ATDC across all cylinders, there is a variation of IMEP of 6.5% whilst the PPP between each cylinder varies as in table 5.4. The individual PPP and the variance in the achieved PPP for each cylinder are detailed in table 5.4. This highlights the variation between the cylinders and the need for cylinder balancing of SA settings.

Setting the SA for each cylinder individually may then allow MBT to be achieved more closely in each cylinder which should in effect allow smoother engine operation and an increase in the output torque. The steady state torque thus achieved is shown in Table 5.5.

The variation of IMEP across all cylinders at steady state operation is 1.3% which is less than that for a common SA. This is running in steady state conditions and the SA tuned manually for these conditions though. It is hoped that with four cylinder feedback control, the SA can be adjusted individually for each cylinder across a transient range of load and speed conditions.

Table 5.4: Variation in PPP between Cylinders for a Universal SA.

Engine Parameter/Variable	Achieved Value/Setting
ABV	$53\%_{duty}$
Applied Load Voltage	0.14 V
SA for all cylinders	28° BTDC
Mean Speed	1450 rpm
Mean Torque	69.01 Nm
Mean PPP cylinder 1	19°
Mean PPP cylinder 2	15°
Mean PPP cylinder 3	16.5°
Mean PPP cylinder 4	15°
Mean IMEP cylinder 1	3.61 bar
Mean IMEP cylinder 2	3.54 bar
Mean IMEP cylinder 3	3.64 bar
Mean IMEP cylinder 4	3.66 bar
Variance in PPP cylinder 1	5.59
Variance in PPP cylinder 2	2.47
Variance in PPP cylinder 3	3.34
Variance in PPP cylinder 4	4.02

Table 5.5: Achieving PPP of 16° on each cylinder by setting SA individually for each cylinder.

Engine Parameter/Variable	Achieved Value/Setting
ABV	$53\%_{duty}$
Applied Load Voltage	0.14 V
SA for cylinder 1	32° BTDC
SA for cylinder 2	29° BTDC
SA for cylinder 3	27° BTDC
SA for cylinder 4	29° BTDC
Mean Speed	1500 rpm
Mean Torque	69.98 Nm
Mean PPP cylinder 1	16.1°
Mean PPP cylinder 2	15.6°
Mean PPP cylinder 3	16.8°
Mean PPP cylinder 4	16.5°
Mean IMEP cylinder 1	3.64 bar
Mean IMEP cylinder 2	3.66 bar
Mean IMEP cylinder 3	3.65 bar
Mean IMEP cylinder 4	3.69 bar
Variance in PPP cylinder 1	4.61
Variance in PPP cylinder 2	2.43
Variance in PPP cylinder 3	3.08
Variance in PPP cylinder 4	2.90

Table 5.6: Perturbed signals for Identification

Signal	Range	Perturbation Period
ABV ($\%_{duty}$)	49 to 59	0.7 seconds
Load (V)	-0.1 to -0.18	0.8 seconds
Resulting Speed (rpm)	900 to 2100	N/A
Resulting MAP (bar)	0.3 to 1.2	N/A
Resulting Integrated MAP (bar)	55 to 120	N/A
SA cylinder 1	28° to 38° BTDC	0.4 seconds
SA cylinder 2	25° to 35° BTDC	0.4 seconds
SA cylinder 3	26° to 36° BTDC	0.4 seconds
SA cylinder 4	24° to 34° BTDC	0.4 seconds

5.4 Four Cylinder PPP Estimation

5.4.1 Signal Excitation

The engine speed (N) is influenced greatly by the air bleed valve (ABV); manifold absolute pressure (MAP) has a good correlation with the applied load. Both of these signals are common to all four cylinders and a step change in either cannot influence any one cylinder individually, but all four cylinders together. Conversely, spark advance (SA) can be set for each individual cylinder; a step change of SA in one cylinder will not affect the dynamics of the other three cylinders [8] unless the ignition is set to cause cylinder misfire, which would cause deceleration of the rotating crank and can affect the other cylinders. The ion current is also measured individually on each cylinder.

To identify the model of an individual cylinder for PPP estimation, SA for that individual cylinder is excited along with ABV and load (which affects all four cylinders). The other three cylinders have SA fixed at a mean value to achieve 16° PPP at steady state. The output signals N, integrated MAP and the ion current are measured for that individual cylinder. This process is repeated sequentially across the four cylinders so four NN models can be identified.

The input signals are excited simultaneously by scaled, biased random numbers over a range as indicated in table 5.6. The SA perturbed range was chosen individually for each cylinder so as to result in a mean PPP of 16° crank angle ATDC across the dataset since this is the desired PPP that the cylinders will be controlled to. The effect of these perturbed signals fluctuates the engine speed between 900rpm to 2100rpm whilst the integrated MAP fluctuates between 55 and 120 bar^2. This will ensure the identification will accurately predict both steady state and transient behaviour by experiencing these dynamics.

Datasets for each cylinder were collected in separate 'engine runs'; fig. 5.4 shows 1000 cycles of engine speed, integrated MAP and resulting PPP identification data for cylinder 1.

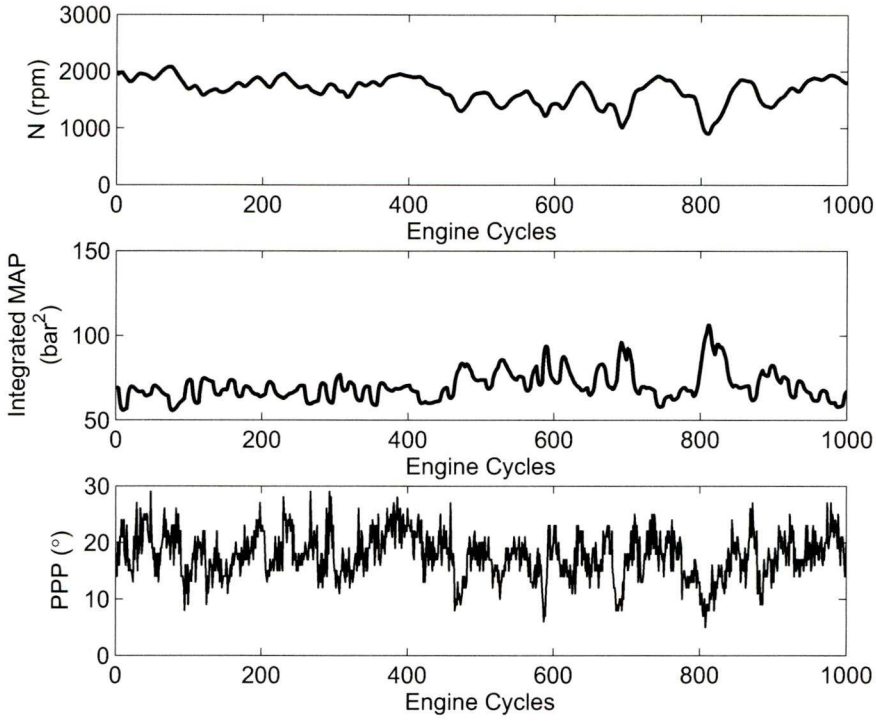

Figure 5.4: Identification Data for Cylinder 1

Differences in the choices for SA for each cylinder can be seen in table 5.6 which highlights the differences experienced for each cylinder of the engine and the need for balancing of these cylinders.

Input/output data is collected over 3000 combustion cycles from the engine/dynamometer set-up for each cylinder. All signals are sampled online once per degree, but down sampling is undertaken; just one sample per combustion cycle is deemed sufficient for N, MAP and PPP. Hence for these signals 3000 samples each for 3000 combustion cycles are used in the identification process.

These 3000 cycles from each cylinder are split equally, after processing, into three parts; 1000 cycles for identification (network training), 1000 cycles for validation and the final 1000 cycles as a 'hold-out' data set for proving of the network before engine implementation occurs [101].

The processing of the ion current to create suitable identification data is described in the next section.

5.4.2 Ion Current Signal Processing

The ion current signal processing is undertaken as per chapter 4. For each cylinder, the ion current signal is again sampled once per degree by dSPACE. A 'window' of 30° of crank angle of these samples per combustion cycle is used for the model for PPP estimation. The window of the ion current signal chosen to relate to the PPP is the 'thermal phase', between 25° to 55° after the spark ignition. 30° is chosen as window large enough to capture most of the pressure related information and small enough to not be too computationally heavy since any signal processing done offline still has to be repeated in SIMULINK and used online for model proving.

PCA will again be used to acquire important characteristics from the ionization current signal.

5.4.3 Principal Component Analysis Applied to the Ion Current Signal for PPP Estimation

PCA is applied to the 'thermal phase' of the ionization current signal, between 25° and 55° after spark ignition. From these 'windows' of sample points, PCA obtains the principal components relating to the most significant features.

The procedure is described in detail in chapter 4, and here, it is applied to produce the PCA scores for the identification data for each individual cylinder. Using the 30 degrees of window of the ion current signal from each cylinder, PCA is to be applied to reduce these 30 samples per cycle per cylinder to a smaller dataset.

The eigenvector with the highest corresponding eigenvalue is the principle component. For each cylinder, the 5 eigenvectors with the highest corresponding eigenvalues are chosen since they contain over 99% of the total signal variance for each cylinder. This results in four reduced 30×5 matrices, one per cylinder. These matrices are stored and used for all cylinder specific offline and online reduced dataset computations. For reference, the matrices shall be refered to as 'FeatureVector' matrices 1 to 4.

The original ion current data for each cylinder is projected onto the 30×5 'FeatureVector' matrix from that specific cylinder to produce a reduced identification dataset of 5 samples over 3000 cycles for offline identification, see fig. 5.5. Hence the new sample sets are reduced from 30 principal components per cycle per cylinder to 5 principal components per cycle per cylinder and therefore the computational complexity is significantly lowered. Figure 5.5 shows 1000 PCA score values for this dataset acquired from the appropriate windows of ion current signal. The 5 PCA scores have been separated onto two plots for clarity.

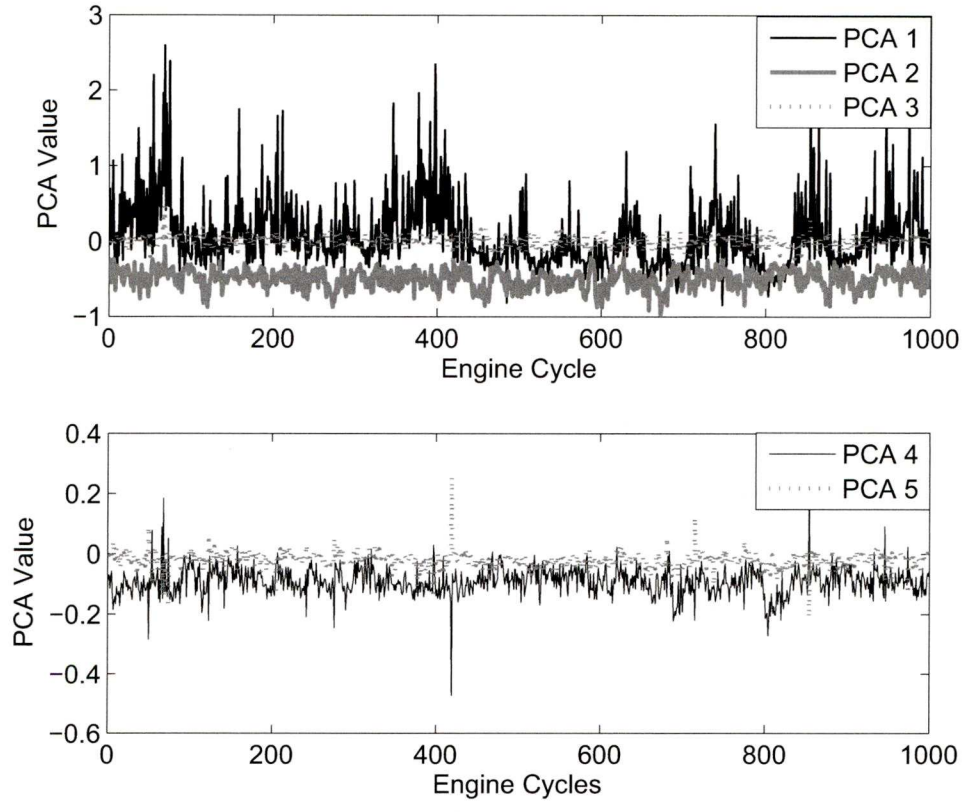

Figure 5.5: PCA Scores Acquired for Identification Data

5.5 Neural Networks for Ion Current Sensing

For PPP estimation of each cylinder four neural networks (NN) are developed, one for each cylinder. The experimental training data is collected and the NNs are trained offline and then implemented on the engine for online estimation and control. The NN for all cylinders will be identical in structure and applied training algorithm. Since the SA timing to PPP identification involves time delays, and the output signal is dependent on the input and previous input signals, a dynamic recurrent NN is again employed for each cylinder. A non-linear auto regressive with exogenous inputs (NARX) network is used for single cylinder PPP estimation and control and was demonstrated to function satisfactorily in chapter 4. The defining equation for a general NARX model is as equation 5.2.

$$y(t) = f(y(t-1), y(t-2), \ldots, y(t-n_y), u(t-1), u(t-2), \ldots, u(t-n_u)) \tag{5.2}$$

Figure 5.6 shows the chosen 2 layer NARX network that is implemented for each cylinder. The input layer weight matrix is denoted IW and other layer weight matrices are denoted LW. f_1 and f_2 activation functions are both tansigmoid functions while f_3 is a pure linear activation function. Layer 1 contains 10 neurons each whilst 2 contains 1 neuron (since the output of the network is a single value $P\hat{P}P$). TDL denotes a tapped delay line. The input are passed through a tapped delay line to instigate the delays present in the data. In this actual network, the 5 inputs pass through a specific tapped delay line where the output is a vector made up of the input signal at the current time and the previous input signal. The second tapped delay line is in the feedback loop, the output of which is the output of the network with one and two delays. If the last layer of a multilayer network has sigmoid neurons, then the outputs of the network are limited to a small range. If linear output neurons are used the network outputs can take on any value [100].

The defining equation of this NARX network is as equation 5.3.

$$y(t) = f(y(t-1), y(t-2), u(t), u(t-1)) \tag{5.3}$$

For each of the four individual NN, the input training data consist of the 5 rows of 1000 cycles obtained from PCA representing the ionization current signal for that specific cylinder, integrated MAP signal common to all four cylinders and the engine speed, which is also common to the four cylinders. The output training data are the corresponding PPP of each specific cylinder measured from each of the in-cylinder pressure sensors obtained over the 1000 cycles. All datasets have mean values removed and are normalised according to neural network theory for training rapidness and network adaptivity ease [101].

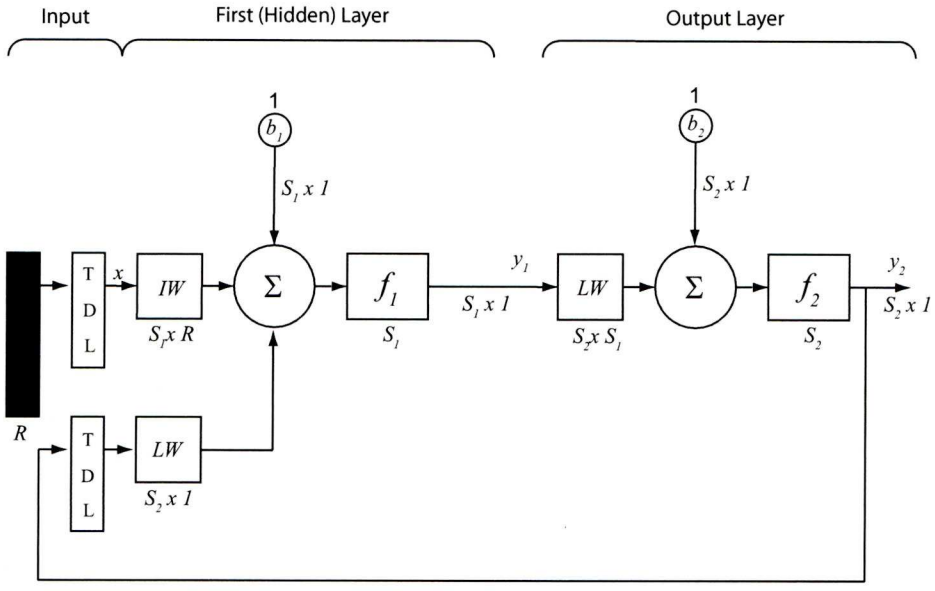

Figure 5.6: Schematic of a Two Layer NARX Network

Using these 7 input data sets and 1 target data set for each cylinder, the networks are trained individually using 'Bayesian-Regularisation backpropagation with early stopping', which prevents over-training. The validation datasets of 1000 cycles are employed here after each training epoch by being presented to the networks. Early stopping occurs when the mean squared error of the validation dataset begins to increase indicating the optimal training epoch for that network has been reached. Then, the 'hold-out' dataset is employed to check if the NN can generalise on unseen data.

The result is four NNs, one for each cylinder that can predict PPP for that specific cylinder. Again as in chapter 4, these networks will need to be proved to be satisfactory offline before online engine implementation occurs.

5.6 Neural Network Proving

To quantify the accuracy of the neural network predictions on the 'hold-out' dataset, R^2 is used as a measure of performance, which is the coefficient of determination where 1 is a maximum.

$$R^2 = 1 - \frac{\sigma_\epsilon^2}{\sigma_y^2} \tag{5.4}$$

where σ_ϵ^2 indicates the variance of the model residuals and σ_y^2 is the variance of the system

output. Over the 1000 cycles of 'holdout' for each cylinder data:

$$\begin{aligned} R^2_{Cyl1} &= 0.70 \\ R^2_{Cyl2} &= 0.74 \\ R^2_{Cyl3} &= 0.74 \\ R^2_{Cyl4} &= 0.76 \end{aligned}$$

indicating at least over 70% of the variance in the PPP for each cylinder is explained by the estimated PPP based on the ionization signal.

The high correlation deems the neural networks suitable for online proving before control techniques can be applied.

Online network proving involves predicting PPP in real time on each cylinder as the engine is running with input signals streaming into the network. All signal processing that was done offline to create the NN has to be undertaken online on the engine/dynamometer. This is done with SIMULINK and Real Time Workshop and the advantages of simplifying the offline computation becomes apparent.

Whilst the engine is running, the following must be occurring:

- N and integrated MAP are to be sampled once per 720° at a specific crank angle, matching the angle chosen for offline computation. N and MAP common inputs to the NN on each cylinder.
- From 25° until 55° after SA occurs on each cylinder, the ion current signal is sampled from each cylinder and stored into memory. These vectors of 30 samples per combustion cycle per cylinder are used for PCA
- PCA reduces the 30 samples of ion current data per combustion cycle per cylinder to just 5 per combustion cycle per cylinder. When executing PCA online the 30 samples of the ion current data per combustion cycle for each cylinder is projected onto the previously calculated 'FeatureVector' matrix respective for that cylinder, which is stored in memory. This means that eigenvector-eigenvalue computations are not necessary online, only a simple multiplication computation.
- The 5 PCA scores for an appropriate cylinder, common N and common integrated MAP samples are input to the neural networks and a predicted PPP value for that cylinder is output. A comparison of this predicted PPP from the networks and measured PPP from the in-cylinder pressure sensors will visually show the validity of the neural network models online.

Engine variables (load, ABV and spark advance ranges) were brought in line with the ranges used for the identification data acquisition (a must) and the load and ABV were step-changed individually to illustrate robustness of the networks to speed and load at predicting PPP for each cylinder. The resulting predicted PPP and actual PPP are presented in the figs. 5.7 and 5.8.

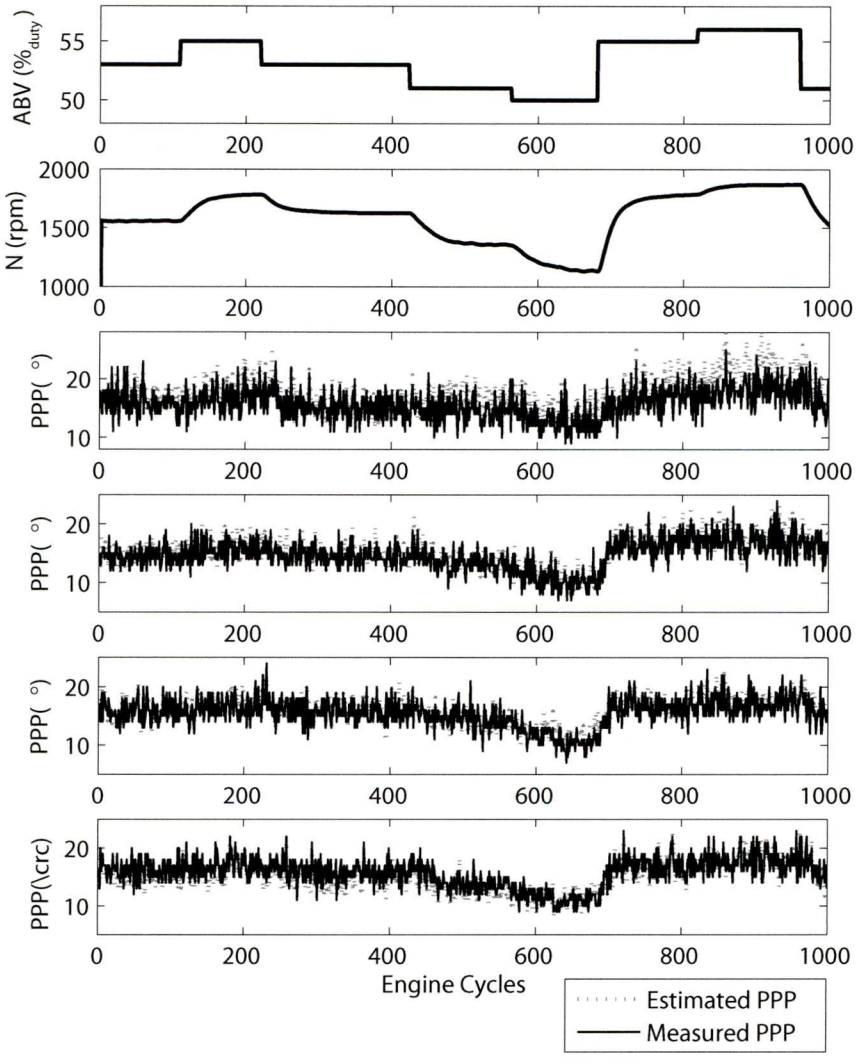

Figure 5.7: Correlation of Predicted PPP and Actual PPP over 1000 cycles due to step changes in ABV

5.7 Control Techniques

The good online correlation of actual PPP to estimated PPP from the ionization current signal for each individual cylinder indicates successful NN development. Accordingly feedback can

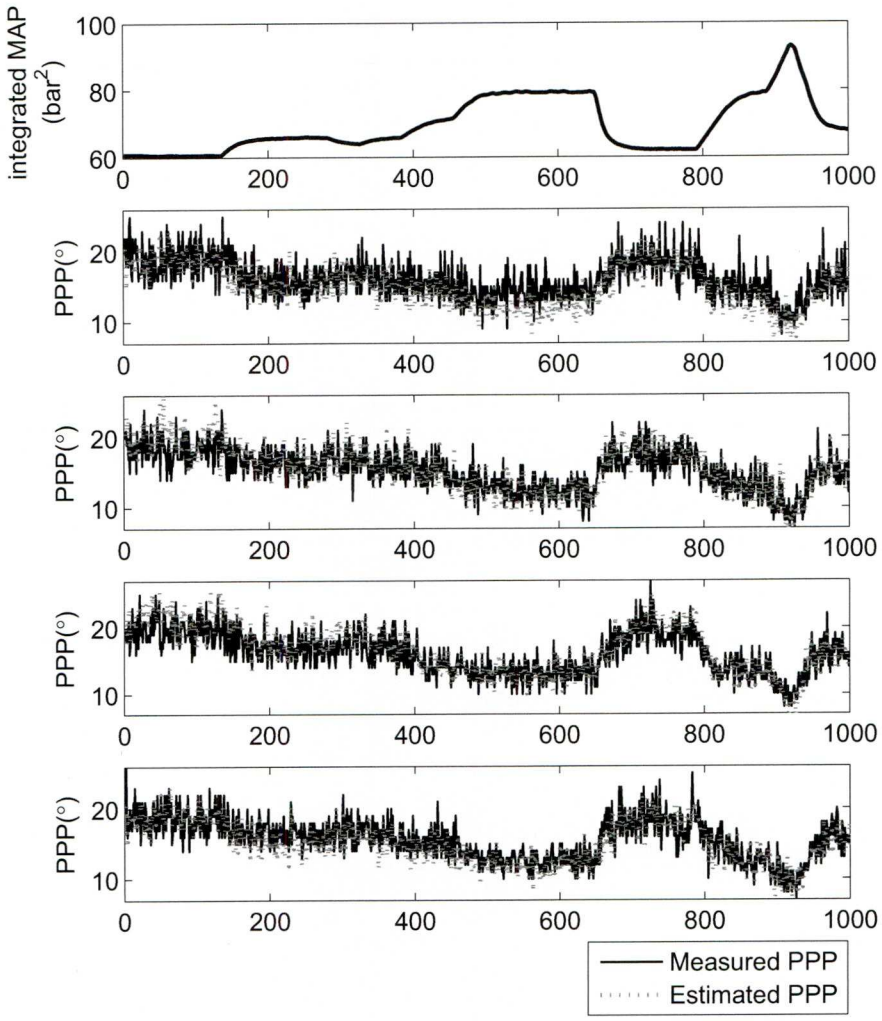

Figure 5.8: Correlation of Predicted PPP and Actual PPP over 1000 cycles due to step changes in Applied Load

Table 5.7: Perturbed signals used to generate ARMAX Models for all Cylinders

Signal	Range	Perturbation Period
ABV [$\%_{duty}$]	Steady state 54	N/A
Load [V]	Steady state -0.14	N/A
SA Timing Cyl1	28° to 38° BTDC	0.4 seconds
SA Timing Cyl2	25° to 35° BTDC	0.4 seconds
SA Timing Cyl3	27° to 37° BTDC	0.4 seconds
SA Timing Cyl4	25° to 35° BTDC	0.4 seconds

Table 5.8: Steady State SA used to Achieve 16° for Each Cylinder

Cylinder	Steady State SA to achieve 16° PPP
Cyl1	32°
Cyl2	28°
Cyl3	30°
Cyl4	28°

now utilise the estimated PPP from each cylinder, to control the ignition timing and so maintain the PPP of each cylinder at the assumed MBT desired set-point of 16° ADTC. Since the PPP signal is affected by combustion variability, stochastic flame propagation and sensor noise an appropriate feedback scheme is minimum variance control [8]. A constrained variance (CV) technique [112, 127] that was proved in chapter 4 to be most effective from a number of CV control techniques is employed.

The feedback controllers were designed using identified models of the system from the inputs of the neural network to estimated PPP for each cylinder giving four models. For each of the cylinders, a single input, single output (SISO) linear zero mean ARMAX model was obtained by perturbing the SA and measuring the predicted PPP. The load and ABV were fixed around the mid-point of the intended NN operating range. The excitation of the SA on each particular cylinder was done independently to the other three, that is, the other three cylinders had a fixed steady state SA set to achieve PPP at 16° ATDC 5.8 whilst the SA for the cylinder in question was perturbed as detailed in table 5.7. 1000 cycles of example identification data for cylinder 1 are given in fig. 5.9.

The general ARMAX model may be represented as

$$y(z) = z^{-n_k}\frac{B(z)}{A(z)}u(z) + \frac{C(z)}{A(z)}e(z) \tag{5.5}$$

where A, B and C are polynomials of the form

$$\begin{aligned} A(z) &= a_0 + a_1 z^{-1} + \ldots + a_{na} z^{-n_a} \\ B(z) &= b_0 + b_1 z^{-1} + \ldots + b_{nb} z^{-n_b} \\ C(z) &= c_0 + c_1 z^{-1} + \ldots + c_{nc} z^{-n_c} \end{aligned}$$

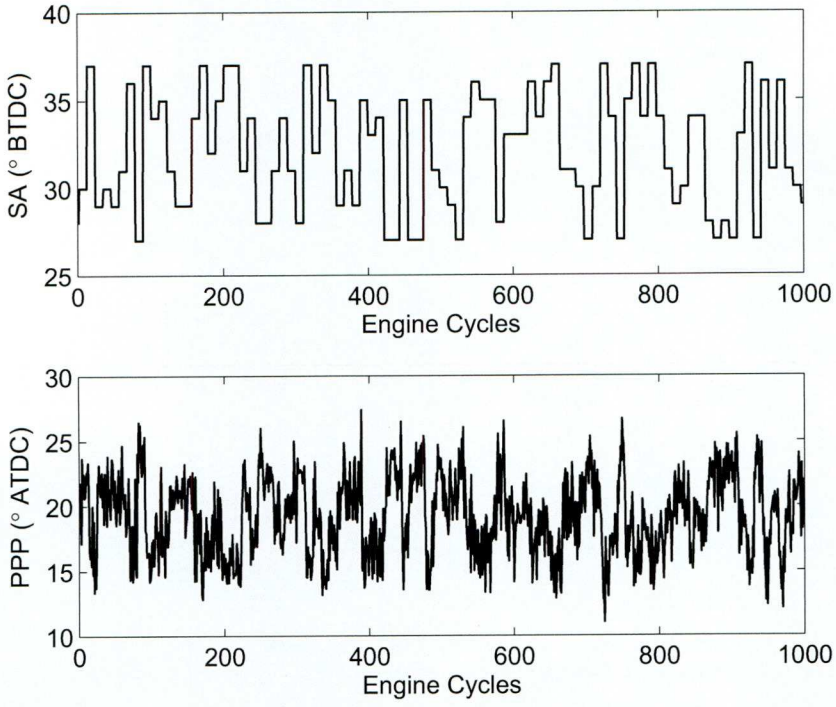

Figure 5.9: 1000 cycles of SA to estimated PPP data for cylinder 1

In this case the model orders *na*, *nb*, *nc* and the discrete time delay order, *nk* were taken to be 2, 1, 2, 1 respectively as determined in chapter 4.

The identified values of these parameters are detailed for each cylinder in table 5.9.

The negative feedback control scheme illustrated in fig. 5.10, is used where G_c represents the colouring filter transfer function, G_b being the plant model, K the controller where w denotes the disturbance input of unit variance white noise. The resulting individual controllers were thus applied independently on each cylinder.

Since the controllers are designed for zero mean ARMAX models, an average of 16° of

Table 5.9: Identified ARMAX parameters for each cylinder

Parameter	Cylinder 1	Cylinder 2	Cylinder 3	Cylinder 4
a_2	0.03326	0.009208	0.1463	-0.04656
a_1	0.1359	0.1038	-0.9986	-0.3952
a_0	1	1	1	1
b_1	-0.3043	-0.1156	0.5566	-0.3287
b_0	-0.521	-0.667	-0.6681	-0.7398
c_2	-0.1684	-0.01773	0.07371	-0.03667
c_1	0.2187	0.1416	-0.9346	-0.3738
c_0	1	1	1	1

crank angle is to be removed from the predicted PPP output of the NNs to achieve zero mean signals and then this 16° is to be added to the controller outputs.

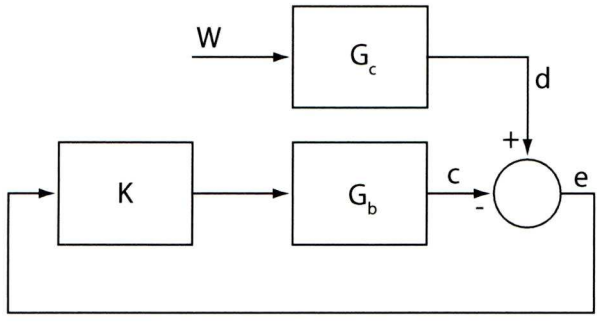

Figure 5.10: Implemented Closed Loop Feedback Control for an Individual Cylinder

For the closed loop system the transmission from the noise input to the output error w to e is given by

$$G_w^e(z) = \frac{e(z)}{w(z)} = \frac{G_c(z)}{1 + K(z)G_b(z)} \tag{5.6}$$

The output variance σ_e^2 for a system of 5.6 is given (see [127, 126]) as:

$$\sigma_e^2 = \frac{1}{2\pi j} \oint_{c1} G_w^e(z^{-1}) G_w^e(z) \frac{dz}{z} \tag{5.7}$$

Since the controller is required to provide tracking a proportional-integral (PI) controller $\frac{(k_p+k_i)z-kp}{z-1}$ is considered. For the system of Eqn. (5.5), the closed loop transfer function of Eqn. (5.6) can be expressed as

$$G_w^e(z) = \frac{(z^2 + c_1 z + c_2)(z-1)}{(z^2 + a_1 z + a_2 z)(z-1) + ((k_p + k_i)z - k_p)(b_0 z + b_1)}$$

5.8 Results

For a specified output variance, parameterized solutions of k_p and k_i for the definite integral of Eqn. (5.7) were obtained. A compromise of both low variance and tracking can be achieved by constraining the output variance between these values. An output variance of 1.05 deg^2 was sufficient to provide adequate tracking and non-zero mean disturbance rejection whilst retaining a low level of output variance for all four cylinders. Accordingly, a parametric solution for k_i and k_p for the closed loop system were obtained for each cylinder and loci of possible controller gains with the desired output variance plotted for each cylinder as can be seen in fig. 5.11. The plotted loci show the possible controller gains with the desired output variance from each cylinder. The maximum permitted integral gains were selected to

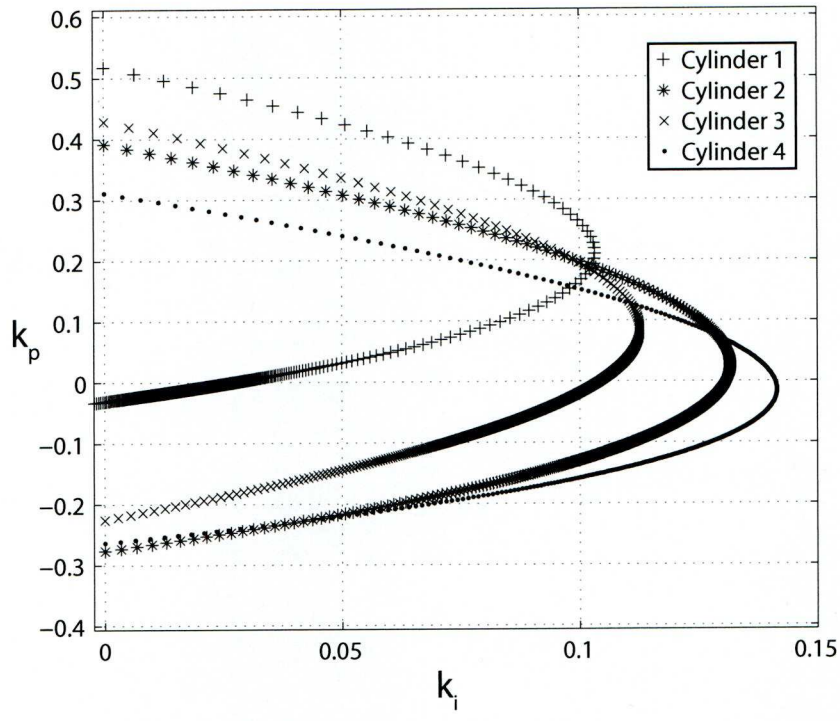

Figure 5.11: Plotted loci of controller gains at the desired output variance for each cylinder

Table 5.10: k_p and k_i values for all cylinders

Cylinder	k_p	k_i
1	0.2135	0.1037
2	0.0260	0.1320
3	0.0906	0.1129
4	-0.0121	0.1415

optimise the tracking performance and the selected values for k_p and k_i for each cylinder are detailed in table 5.10.

This results in the four constrained variance PI controllers:

$$K(z)_{cylinder1} = \frac{0.3172z - 0.1037}{z - 1} \tag{5.8}$$

$$K(z)_{cylinder2} = \frac{0.158z - 0.1320}{z - 1} \tag{5.9}$$

$$K(z)_{cylinder3} = \frac{0.2035z - 0.1129}{z - 1} \tag{5.10}$$

$$K(z)_{cylinder4} = \frac{0.1294z - 0.1415}{z - 1} \tag{5.11}$$

The constrained variance type controllers were implemented with the neural network systems in feedback loops for control of PPP on each cylinder.

In steady state operation, the controlled cylinders had mean IMEP values as in table 5.11. The range between the IMEP values across the cylinders has reduced (to 2.47%) under feedback control compared to universal SA across all cylinders. This is not as much of a reduction as when the SA was set individually across all cylinders open loop in steady state (table 5.5) but the feedback control allows operation over transient conditions.

Step changes were introduced to the load and ABV settings to induce transients whilst the PPP demand for each cylinder was set at a constant 16° ATDC. It can be seen in figs. 5.12 and 5.13 that the estimated PPP of each cylinder match the actual PPP measured by the pressure sensors and that they are maintained at the desired value. Figure 5.14 illustrates the estimated and actual PPP mean values tracking to a demand.

5.9 Conclusions

Four cylinder closed-loop feedback control of PPP has been demonstrated using an ion current technique. Estimation of PPP on each cylinder is achieved using the ion current signal and engine signals currently available to a production standard EMS. The signals are processed through NARX neural networks which are trained individually using pseudo binary random test signal data that gives network prediction accuracy, not only in steady state but

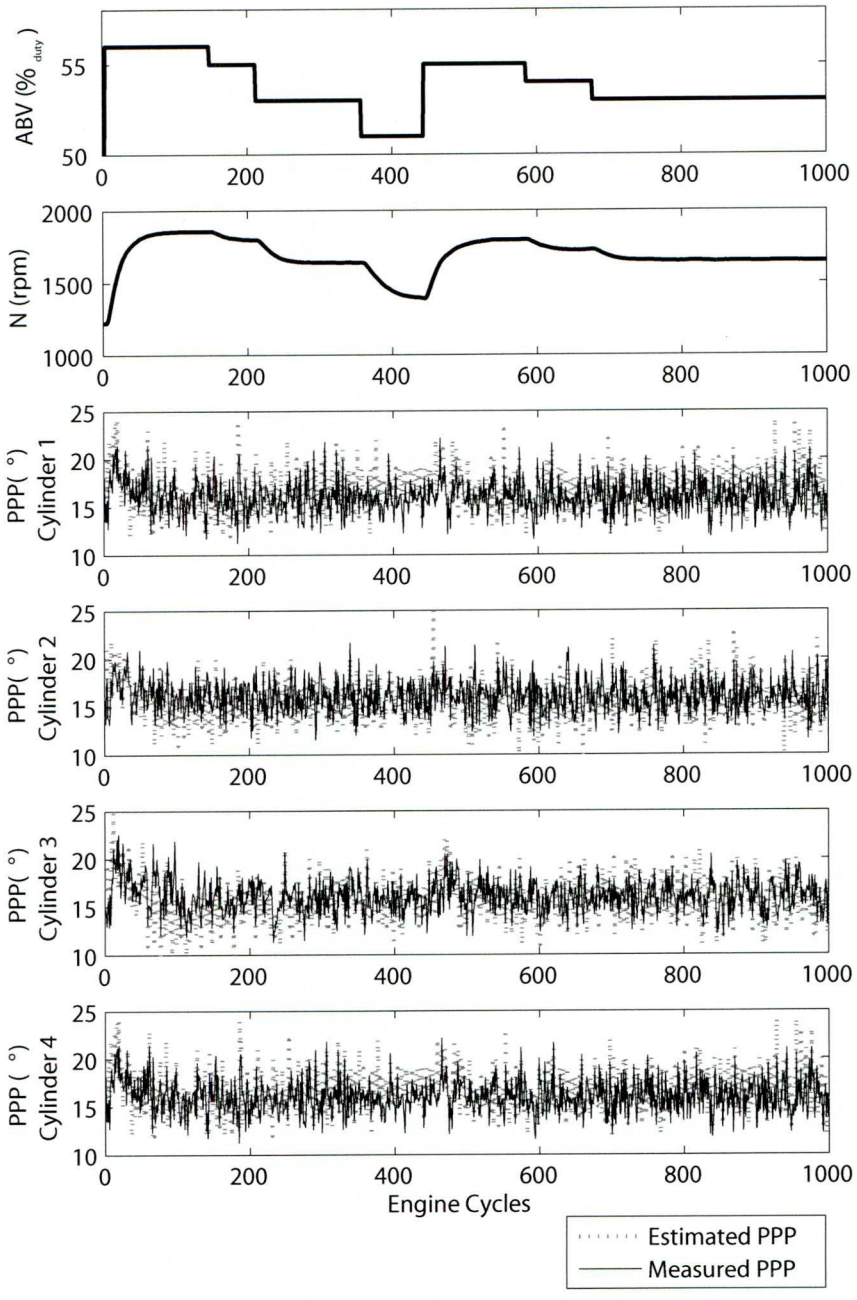

Figure 5.12: All cylinders maintaining 16° PPP through speed steps.

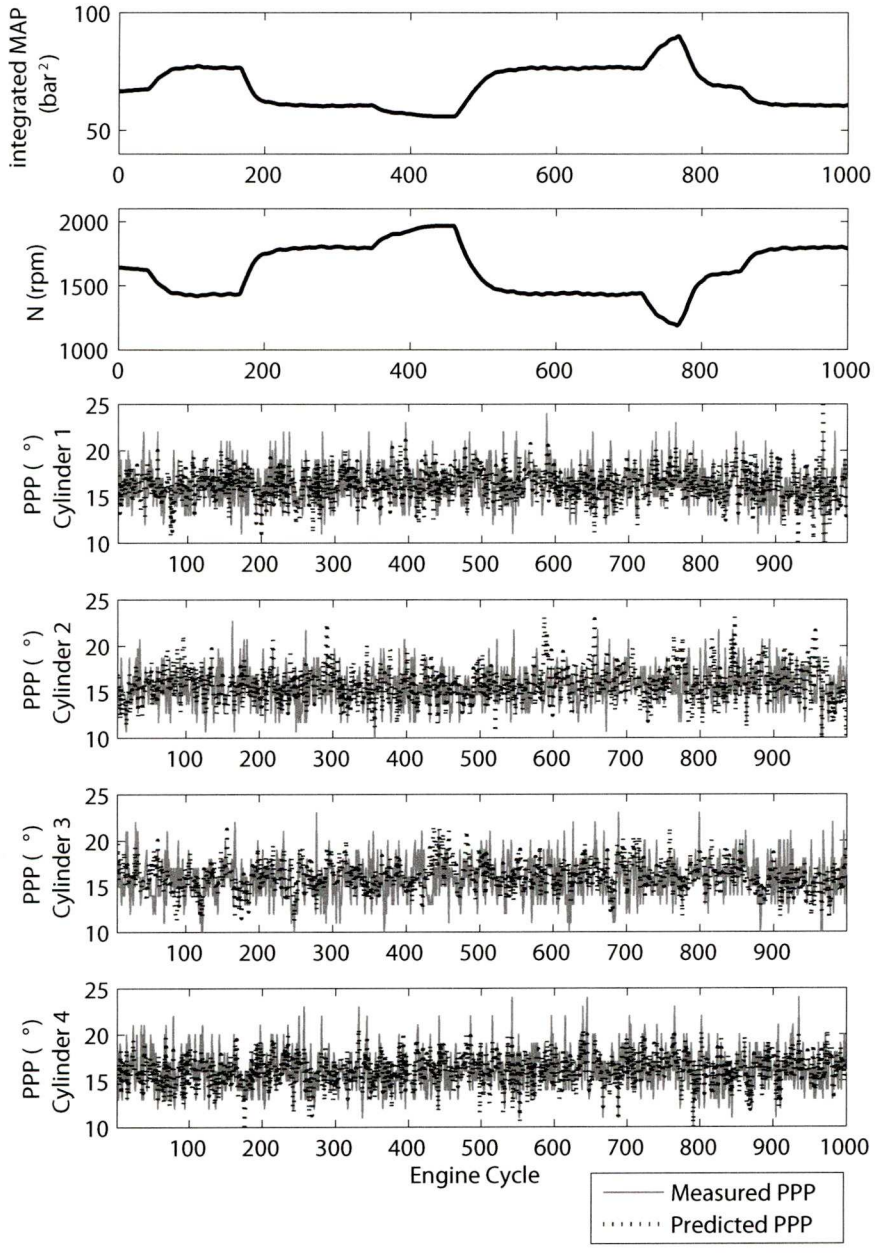

Figure 5.13: All cylinders maintaining 16° PPP through load steps.

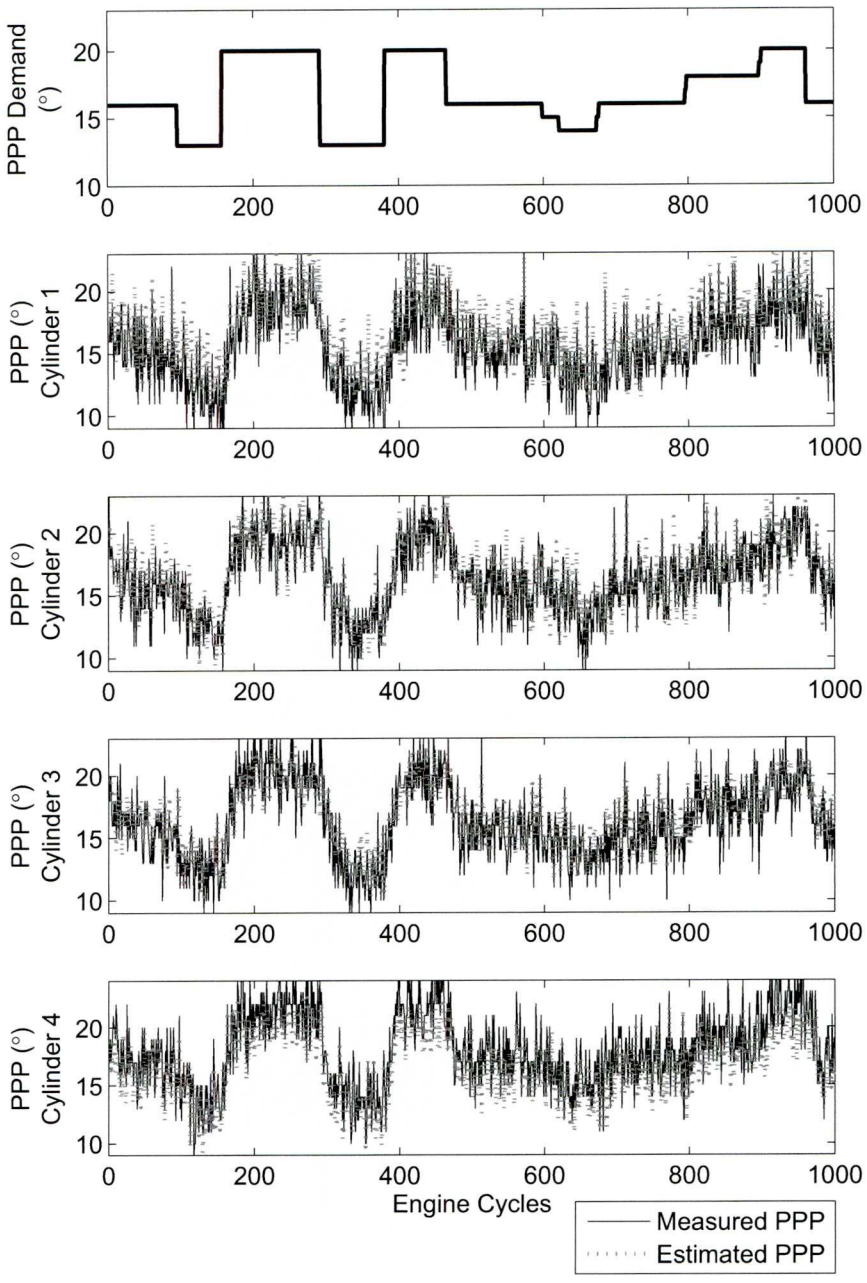

Figure 5.14: All cylinders tracking to random step demands of PPP in the range 12° to 20° ATDC

Table 5.11: Achieved IMEP and Variance on Each Cylinder under Steady State Feedback Control

Engine Parameter/Variable	Achieved Value/Setting
ABV	$53\%_{duty}$
Applied Load Voltage	0.14 V
Mean Speed	1500 rpm
Mean Torque	69.77 Nm
Mean IMEP cylinder 1	3.63 bar
Mean IMEP cylinder 2	3.54 bar
Mean IMEP cylinder 3	3.60 bar
Mean IMEP cylinder 4	3.58 bar
Variance in PPP cylinder 1	5.23
Variance in PPP cylinder 2	2.35
Variance in PPP cylinder 3	3.29
Variance in PPP cylinder 4	2.92

across transient ranges. An ARMAX model is identified around the neural network as a SA to PPP relationship, by again using randomly perturbed test signals. Accurate prediction of PPP on all cylinders has been demonstrated using the technique. The ARMAX models allow PID control to be applied. A form of robust minimum variance control was chosen as an appropriate control technique due to the stochastic nature of the PPP through combustion. The recently developed constrained variance controller design technique was applied. The resulting feedback control was shown to reduce the variance in the PPP whilst regulating it to a demanded value on each individual cylinder. Subject to the use of an appropriate PPP demand signal, MBT can thereby be achieved on each cylinder independently through the feedback scheme. The fundamental success in applying the technique is very much dependent on the use of the appropriate test signals used in training the neural networks and in identifying the ARMAX models. The technique can only reliably predict and control within the boundaries of the identification test data used.

Chapter 6

Single Cylinder Air-Fuel Ratio Estimation

6.1 Introduction

Production vehicles are as standard fitted with a switching heated exhaust gas oxygen (HEGO) sensor which provides a high voltage if the exhaust gas in rich of stoichiometry and a low voltage if the exhaust gas is lean of stoichiometry. This switching behavior of the HEGO sensor can be used in a feedback control system that is characterized by a limit cycle about stoichiometry. Stoichiometry is the theoretical ideal for complete combustion of the air-fuel mixture within an engine cylinder and is a mass ratio of 14.7 : 1 [9, 12, 4]. Succeeding these sensors are universal exhaust gas oxygen (UEGO) sensors. Known as Lambda sensors their voltage output is proportional to the air-fuel ratio (AFR) or lambda level and can give both useful and accurate readings of exhaust gases. Problems arising from the use of such sensors are the cost; currently (if present) only one is normally fitted at the exhaust confluence point, taking average exhaust readings across all cylinders. This chapter describes a technique using available engine signals and the ion current method to replicate the filtered output signal of a UEGO sensor and predict the air-fuel ratio (AFR) equivalence ratio (λ) in a single cylinder where:

$$\lambda = \frac{AFR_{\text{measured}}}{AFR_{\text{stoic}}}$$

The selection of signals and the acquisition of data for the identification process of producing models is discussed in section 6.3. This involves generating a fuel signal that follows a base manifold absolute pressure signal to ensure that the engine does not stall as it follows random input signals. Principal component analysis (PCA) is described as a method of data reduction and feature extraction from the ion current signal in section 6.6. Again as in

chapter 4, it should be noted that the raw data is acquired from the engine dynamometer set up and then initially processed offline to produce the identification data. This identification data is then used to create a model of the engine with a neural network (NN) in section 6.7 for the purpose of predicting the AFR, again created and trained offline with initial network validation being done offline, section 6.8. Only when a satisfactory, offline, simulated prediction is achieved is the model then implemented onto the engine/dynamometer set up and online validation achieved in section 6.9.

The graphic figure 6.1 displays the location of the UEGO sensor near the exhaust port in the exhaust manifold along with the spark plug used for ionization current sensing located in the combustion chamber.

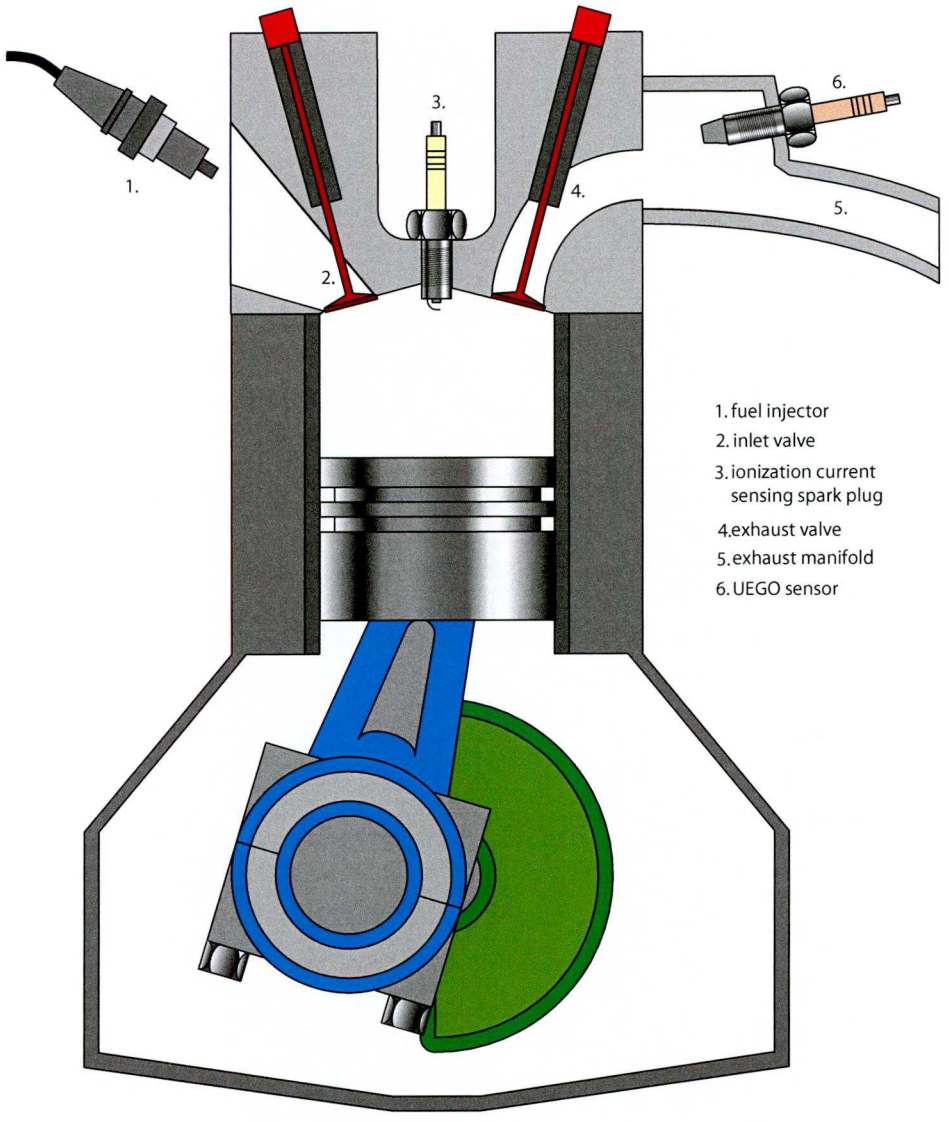

Figure 6.1: Location of Ion Current Sensor and UEGO Sensor

6.2 The Effect of Air-Fuel Ratio on the Ion Current Signal

It has been reported from various researchers e.g. [77, 78, 79, 34] that the air-fuel ratio has an effect on and can be estimated by the ion current produced during combustion. To determine if and what effect the AFR has on the ionization current signal using the equipment at the University of Liverpool, a simple test was undertaken whereby ionization curves were recorded from a single cylinder as the λ ratio was step traversed in that cylinder by altering the fuel pulse width (FPW) for that specific cylinder. The FPW was increased to achieve rich combustion operation and decreased to achieve lean combustion operation whilst the air bleed valve (ABV) and load were held at constant values. Ionization windows (between 1° to 100° after ignition) that corresponded to a particular range of λ are averaged to illustrate the AFR effect more clearly.

The following table 6.1 details the engine running parameters for the test.

Table 6.1: Engine Parameter for λ Sweep

Parameter	Value
ABV [$\%duty$]	44
Load [V]	0.05
Fuel Pulse [μs]	2500 to 3500

Figure 6.2 shows the achieved λ ratios as the ion current windows were recorded.

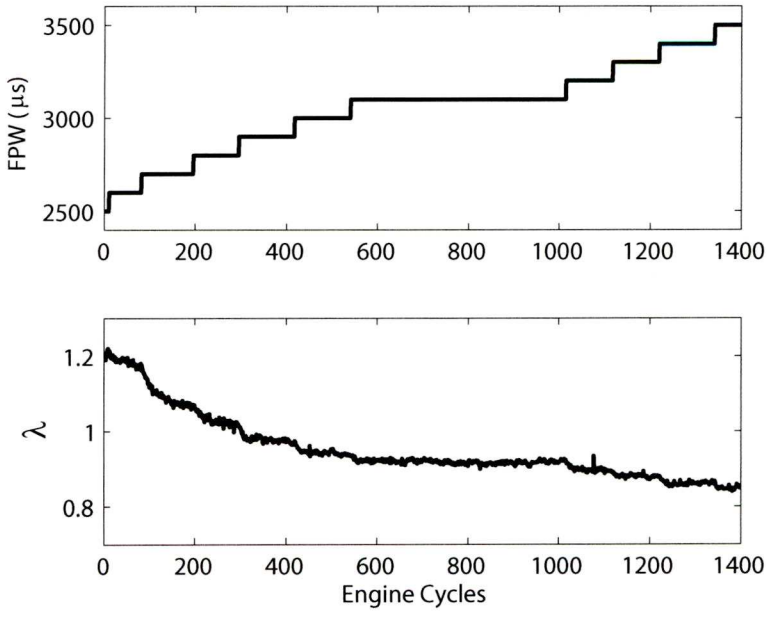

Figure 6.2: Achieved λ Ratios

Ionization curves are recorded at each combustion cycle. The ionization current windows (1° to 200° after ignition) for where the λ ratio falls into a specific range are then averaged and plotted in fig. 6.3.

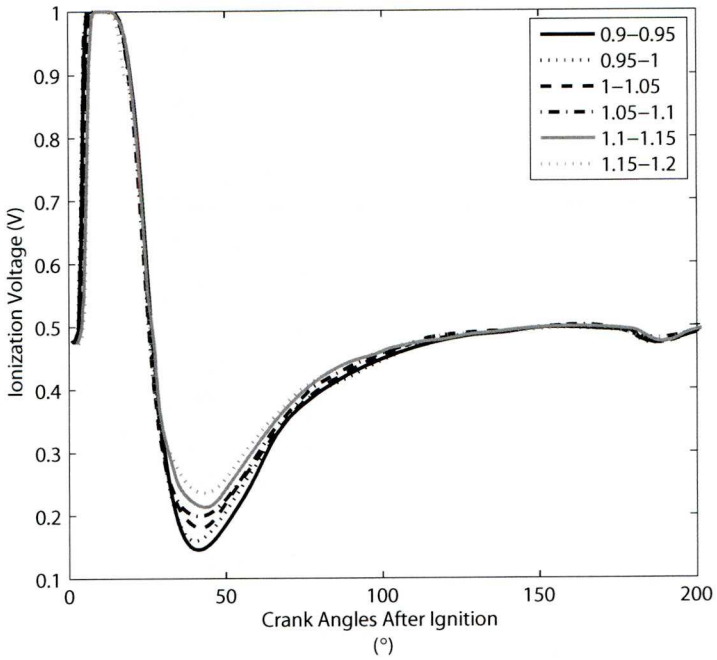

Figure 6.3: Averaged Ion Current Signals for Varying λ ratios

From this plot, it can be seen that the increase in λ from rich to lean does indeed have a subtle but meaningful effect on the ionization curve between 25° to around 70° after ignition. The first 'peak' of the ion voltage (relating to the chemical phase) becomes exaggerated as λ is decreased (becomes a richer mixture). This is as suspected from previous research in that there is more ionization occurring as the percentage of fuel per combustion charge increases.

6.3 Signal Selection and Excitation

Again, according to identification theory, in trying to ascertain a relationship between input and output signals a model has to be constructed from observed data, recorded during specifically designed identification experiments [120]. A model is required that can predict λ and to do so from identification data, the acquired signals must be sufficiently representative of a system, i.e. any input signals that are altered directly affect the AFR. The model is required to predict not only in steady state but in transients also. Sufficient and suitable excitation of input signals and the resulting causal output signals (in this case, λ) expose the dynamics of a system and these can be used to produce a model. The perturbation period for each input signal is chosen to be low enough to allow any dynamic response of the output

signal to be fulfilled but still be high enough to allow rapid representative transient output responses. This will ensure the identification will accurately predict both steady state and transient behaviour by experiencing these dynamics.

Figure 6.4 illustrates the concept of the system; a neural network (NN) is trained to predict λ using available engine signals including the actual λ value as a target, or output, dataset.

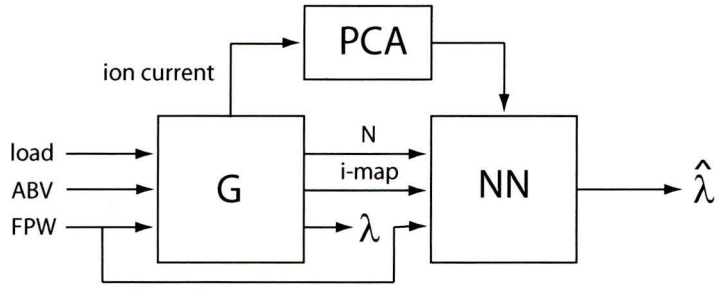

Figure 6.4: Single Cylinder λ Estimation Concept

The purpose of the identification in this application is to identify the relationship between the ion current, manifold absolute pressure (MAP), engine speed (N) and fuel pulse width (FPW) to the AFR. Suitable input and target training data must be obtained that will cause the identification to operate and predict λ over a desired range of speed, torque load and fuel settings in both steady state and in transients. A model must be able to take into account the inherent delays in the engine fuelling system; target data is sampled from a UEGO sensor signal that is placed at the output port of the cylinder and any measurements made by the sensor experience transport delays in the exhaust gas stream. Using the FPW signal incurs delays since the fuel is sprayed from the injector onto the closed inlet port prior to it opening to allow fuel evaporation before being inducted into the cylinder.

To determine which signals were to be chosen to relate to AFR from the range of available engine signals, actuators were perturbed randomly and all resulting signals were measured and recorded as in section 6.3.2. Signals measured were: AFR (air-fuel ratio), ABV (air bleed valve), i-MAP (integrated manifold absolute pressure), N (engine speed), FPW (fuel pulse width) and torque. Using a statistical analysis technique to calculate the correlation coefficient between the all recorded signals in a matrix, the appropriate signals became evident. The correlation coefficient matrix represents the normalised measure of the strength of linear relationship between variables. The coefficients can range from -1 to 1, where values close to 1 suggest that there is a positive linear relationship between the data columns. Values close to -1 suggest that one column of data has a negative linear relationship to another column of data. Values close to or equal to 0 suggest there is no linear relationship between the data columns [121].

Table 6.2 is the correlation coefficient matrix between all signals. The first row of data (or first column of data) is of most interest in this section since it displays the relationship of each signal to the AFR.

Table 6.2: Correlation Coefficient Matrix between Engine Signals

-	AFR	ABV	i-MAP	N	FPW	Torque
AFR	1	0.150	0.438	-0.317	0.153	0.440
ABV	0.150	1	0.264	0.493	0.272	0.032
i-MAP	0.438	0.265	1	-0.642	0.849	0.799
Speed	-0.317	0.493	-0.642	1	-0.46	-0.713
FPW	0.153	0.271	0.849	-0.466	1	0.594
Torque	0.440	0.032	0.799	-0.713	0.594	1

Ideally, signals to be used in a relationship to AFR would be resulting sensor signals that are available on a production engine so although torque has a high correlation with AFR, it was not used. Integrated MAP, N and FPW were used, along with the ionization current. The resulting correlation coefficient between the ionization current and the AFR is presented in section 6.6.

6.3.1 Load to Fuel Mapping

To obtain the identification data, perturbed input signals are excited simultaneously by scaled, biased, uniformly distributed random numbers. The dynamometer load applied to the crankshaft of the engine is perturbed, to vary the MAP, simultaneously with the FPW and ABV to excite dynamics of the speed and AFR.

During initial tests controlled engine signals occurred through perturbations by purely bias random numbers and as a result of the random signal generation, engine speed range was restricted due to engine stall, knocking and the requirement to prevent saturation of the λ signal ($0.5 < \lambda > 1.4$).

To overcome this issue, identification signal generation has to be rudimentarily mapped so as to not allow the engine to stall or knock, but to still be random to excite and expose the engine dynamics whilst preventing saturation of the λ signal from the UEGO sensor.

The solution is to regulate the FPW according to the applied load (or resulting MAP signal). As the load and ABV are perturbed in a random manner that traverses an adequate speed range, the FPW is set to follow the resulting MAP signal by a predefined relationship. This has the effect of ensuring that λ is kept close to 1, which in turn ensures that at higher loads and lower speeds, engine stall is prevented. Further minor perturbations using scaled,

biased, uniformly random numbers upon the FPW signals ensure minor deviations from stoichiometry that display the system dynamics.

To determine the required relationship between FPW and the MAP signal, the following systematic mapping procedure was done. An engine speed range roughly between 1000 rpm and 2000 rpm was chosen for the fuel mapping. The engine was set to run at the extremes of this speed range and a range of loads was applied by the dynamometer that ensured changes in the integrated MAP signal without engine stall. At these extremes, the fuelling was adjusted to bring the λ value to 1.

A plot of these test results in fig. 6.5 shows a linear relationship between the integrated MAP signal and FPW to give stoichiometry.

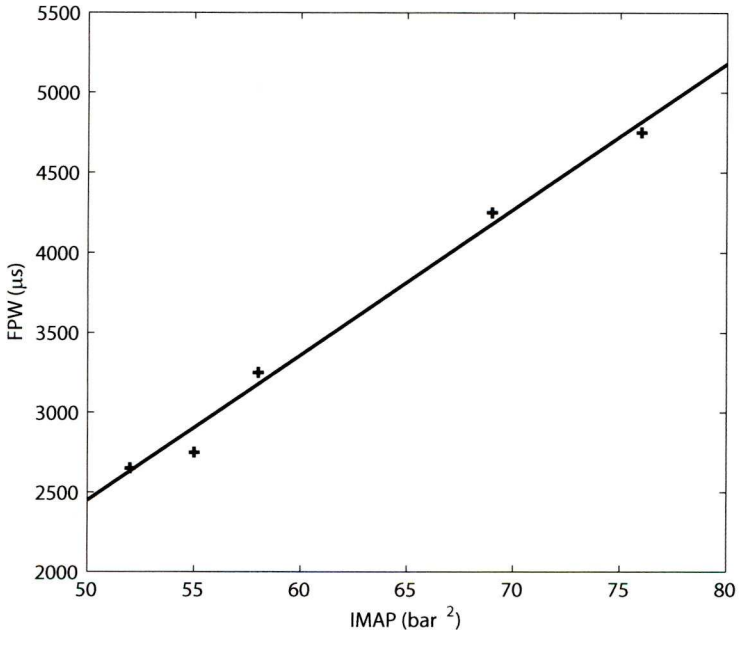

Figure 6.5: Relationship Between FPW and Integrated MAP to Give Stoichiometry

The equation of the straight line 6.1 gives the following relationship variables:

$$y = mx + c \tag{6.1}$$

where y would be the fuel pulse width, x is the integrated MAP signal and

$$\begin{aligned} m &= 91 \\ c &= 2100 \end{aligned}$$

Figure 6.6 illustrates the manipulation of the obtained integrated MAP signal to produce a FPW signal.

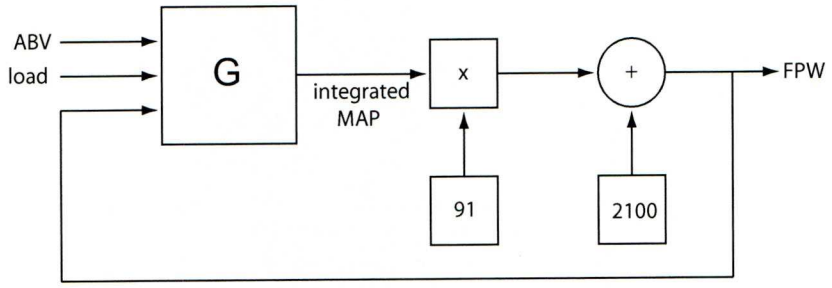

Figure 6.6: Manipulation of the obtained integrated MAP signal

6.3.2 Resulting Identification Signals

With this fuelling to load map in place, the dynamometer load applied to the crankshaft of the engine is perturbed, the FPW will 'follow' the resulting MAP signal with minor perturbations of the FPW signal added. The ABV signal is perturbed by scaled, biased, uniformly distributed random numbers. The effect of these perturbed signals fluctuates the engine speed between 800 rpm to 2000 rpm whilst the integrated MAP[1] fluctuates between 50 and 110 bar^2. The range of the engine signal values for the identification data are as indicated in the table 6.3.

Table 6.3: Perturbed Signals for AFR identification

Signal	Range	Period
ABV [$\%duty$]	44 to 54	1.2 s
Load [V]	0.07 to 0.13	2 s
Fuel Pulse [μs]	2200 to 8800	1.5 s

Again, as per PPP estimation, data is collected over 3000 combustion cycles. These 3000 cycles are split equally, after processing, into three parts; 1000 cycles for identification, 1000 cycles for validation and the final 1000 cycles as a 'hold-out' data set for proving of the identified model before engine implementation occurs [101].

The input data consists of cycles of the 6 PCA components representing the ion current signal, integrated MAP signal (known to correlate well to the load), N and FPW. The output data consists of the corresponding λ samples measured from the UEGO sensor in the exhaust manifold. The engine signal data for N, FPW and IMAP are displayed in fig. 6.7. The processing of the ion current to create suitable identification data is described in the next

[1]Integrated over 180° prior to sampling

section.

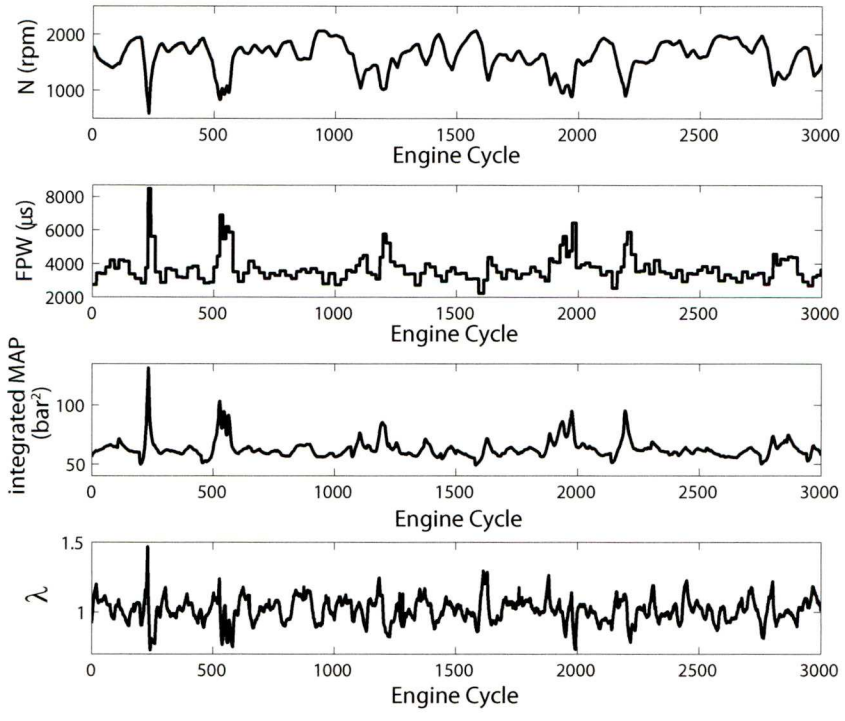

Figure 6.7: Identification Data: 1000 cycles of Speed (N), Fuel Pulse Width (FPW) & Integrated MAP (IMAP)

6.4 Ion Current Signal Processing

To relate the ion current 'window' to λ is not straightforward. IMAP, FPW and N are sampled every crank angle degree by the data acquisition hardware and software but only one sample per combustion cycle is used in the model identification. The ion current signal is again sampled once per degree but a 'window' of samples per combustion cycle is used for the model. The observed 'windows' of the ion current signal are sampled once per degree over 38° of crank angle for λ estimation. This would effectively give 38 samples to relate to λ per combustion cycle.

The window of the ion current signal chosen to relate to λ is the 'chemical phase', where the level of ionization of the gases represents the flame kernel growth as the fuel reacts with oxygen in the cylinder. This phase, ideally appearing as a peak in the signal occurring around

10° after ignition for around 30° to 40°, see fig. 6.8. Various lengths of window have been used in previous research to relate the ion current to the AFR; 10.5° to 32.5° after ignition is used in [49] and in [43], the window is chosen as 10.5° to 32.5° after ignition. A window of 60° is mentioned in [53], sampled at half a degree, to predict the AFR and PPP.

The window has been chosen in reference to the spark ignition event. 38° is chosen as a window large enough to capture all of the air-fuel ratio related information and small enough to not capture other phases of the signal that occur after the chemical phase (i.e. the 'chemical phase') which would increase variance in the secondary principal components unnecessarily.

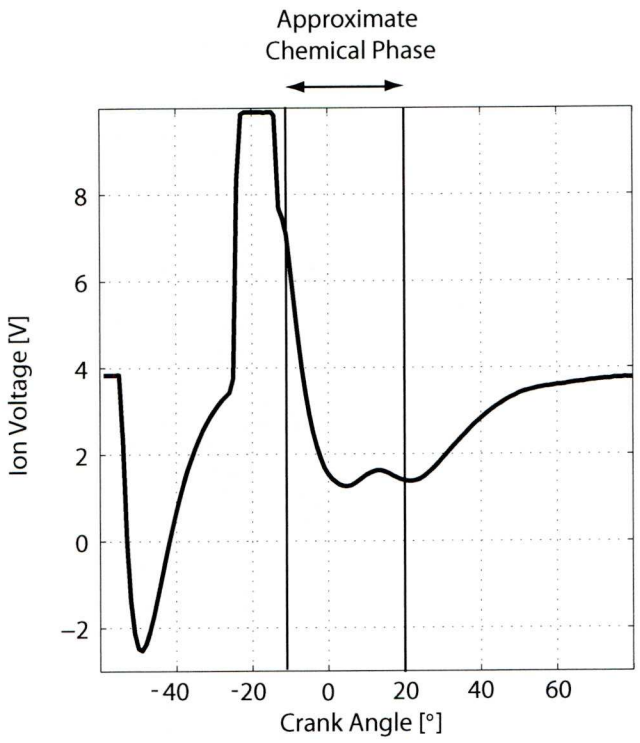

Figure 6.8: A window of a typical ion current curve

It should be noted that all signal processing computations undertaken offline to arrive at a model will subsequently need to be repeated online for validation.

6.5 Filtering λ

dSPACE is set to sample the air-fuel ratio every crank angle degree. This gives a signal displaying high frequency, stochastic dynamics with the low frequency air-fuel ratio reading. For the identification, the λ signal is filtered offline to effectively smooth this stochastic signal. Then as further processing is done to extract one sample per combustion cycle for NN training, the signal does not vary falsely as the high frequency component of the λ signal

has already been removed. This result of using this filtered signal for the NN training is that the output prediction will replicate this filtered signal also.

6.6 Principal Component Analysis

PCA is applied to a specific window of the ionization current signal, which is believed to contain information relating to the air-fuel ratio (AFR).

Figure 6.9 shows the variability in overlaid plots of 20 random typical windows of the ion current signal used for λ estimation. In practice, 3000 cycles are used for PCA but for illustrative purposes, only 20 cycles are shown. It can be seen that the variability in these different 'chemical phase' cycles is not as great as per the 'thermal phase' cycles shown in fig. 4.5.

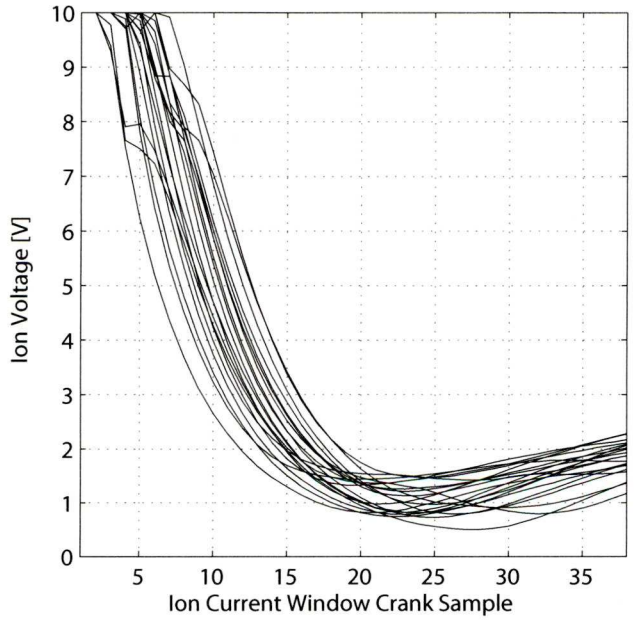

Figure 6.9: A window of a typical ion current curve

6.6.1 PCA Applied to the Ion Current Signal for λ Estimation

The following procedure is observed to initially produce the PCA scores for the identification data. Using the 38° of window of the ion current signal, PCA is to be applied to reduce these 38 samples per cycle to a smaller dataset.

1. The ion current signal is sampled online every degree of crankshaft rotation and a complete cycle is 720°.

2. Offline, a window of the ion current signal is selected; the 'chemical phase' of the ion current signal, which is calculated to be through 38° of crank angle, between 7° and 45° after the spark event. This would imply that initially 38 sample points per cycle are used, one per degree indicating a specific ionization voltage. If each 'window' of each cycle contains 38 sample points over 3000 combustion cycles, this presents a 38×3000 matrix, each row is an observation or cycle, and each column is a crank angle position.

3. The 38 rows of data are normalised and are considered to be vectors X_1 to X_{38}. The covariance matrix is calculated offline. This results in 38×38 matrix.

4. If Σ is the covariance matrix of the vector $X' = [X_1, X_2, \ldots, X_{38}]$, it has eigenvalue-eigenvector pairs (σ_1, e_1) to (σ_{38}, e_{38}) where $\sigma_1 \geq \sigma_2 \geq \cdots \sigma_{38} \geq 0$. The 38^{th} principal component is given by $Y_{38} = e_i'X = e_{1i}X_1 + e_{2i}X_2 +, \ldots, e_{38i}X_{38}$ where $i = 1, 2, \ldots, 38$. The full resulting data set would contain 38 PCA scores. The percentage that each score contributes to the total population variance can be calculated and hence most scores can be 'discarded'. In this case $Y_1 = e_1'X, Y_2 = e_2'X, \ldots, Y_{38} = e_{38}'X$ are the principal components. Then

$$\sigma_1 + \sigma_2 +, \ldots, \sigma_{38} = \sum_{i=1}^{p} Var(Y_i)$$

so the proportion of total variance explained by the 38^{th} principal component is :

$$\frac{\sigma_i}{\sigma_1 + \sigma_2 +, \ldots, \sigma_{38}}$$

The eigenvector with the highest corresponding eigenvalue is the principal component. The 6 eigenvectors with the highest corresponding eigenvalues are chosen since they contain around 99% of the total signal variance. This results in a reduced 38×6 matrix. This matrix is stored and is used for all offline and online reduced dataset computations. For reference, this matrix shall be refered to as the 'FeatureVector' matrix as in chapter 4.

5. The original ion current data is projected onto the 38×6 'FeatureVector' matrix to produce a reduced identification dataset of 6 samples over 3000 cycles for offline identification.

Hence the new sample set is reduced from 38 principal components per cycle to 6 principal components per cycle and therefore the computational complexity is significantly lowered.

Table 6.4 displays the entire 38 principal components and the proportion of total variance explained by them to six decimal places. It can be clearly seen that beyond the first 20 or so principal components, the variance explained is negligible.

Table 6.4: First 10 principal components from a window of a spark ionization signal and the proportion of total variance explained by them

Principal Component	Proportion of Total Variance	Accumulated Percentage
1^{th}	79.783383	79.783383
2^{th}	10.971967	90.755350
3^{th}	5.404370	96.159721
4^{th}	1.515168	97.674889
5^{th}	0.819616	98.494505
6^{th}	0.462819	98.957324
7^{th}	0.319574	99.276897
8^{th}	0.233889	99.510786
9^{th}	0.142990	99.653776
10^{th}	0.113175	99.766951
11^{th}	0.065364	99.832315
12^{th}	0.064166	99.896482
13^{th}	0.030527	99.927008
14^{th}	0.029481	99.956489
15^{th}	0.014433	99.970922
16^{th}	0.013358	99.984280
17^{th}	0.006251	99.990532
18^{th}	0.004422	99.994954
19^{th}	0.002452	99.997406
20^{th}	0.000976	99.998382
21^{th}	0.000464	99.998846
22^{th}	0.000250	99.999096
23^{th}	0.000214	99.999310
24^{th}	0.000155	99.999465
25^{th}	0.000108	99.999573
26^{th}	0.000090	99.999663
27^{th}	0.000075	99.999738
28^{th}	0.000052	99.999790
29^{th}	0.000038	99.999828
30^{th}	0.000035	99.999863
31^{th}	0.000029	99.999892
32^{th}	0.000024	99.999916
33^{th}	0.000022	99.999938
34^{th}	0.000021	99.999959
35^{th}	0.000021	99.999980
36^{th}	0.000020	99.999999
37^{th}	0.000001	100.000000
38^{th}	0.000000	100.000000

If a larger original data window is used that encompasses a more complex waveform with more features, then it would be expected the percentage of total variance captured by the 1^{st} principal component would drop and the secondary principal components would contribute a higher percentage of the total proportion of variance. This highlights the importance of restricting the length of the ion current window for AFR identification so as not to acquire unrelated and unnecessary information.

The separate principal components are displayed in fig. 6.10.

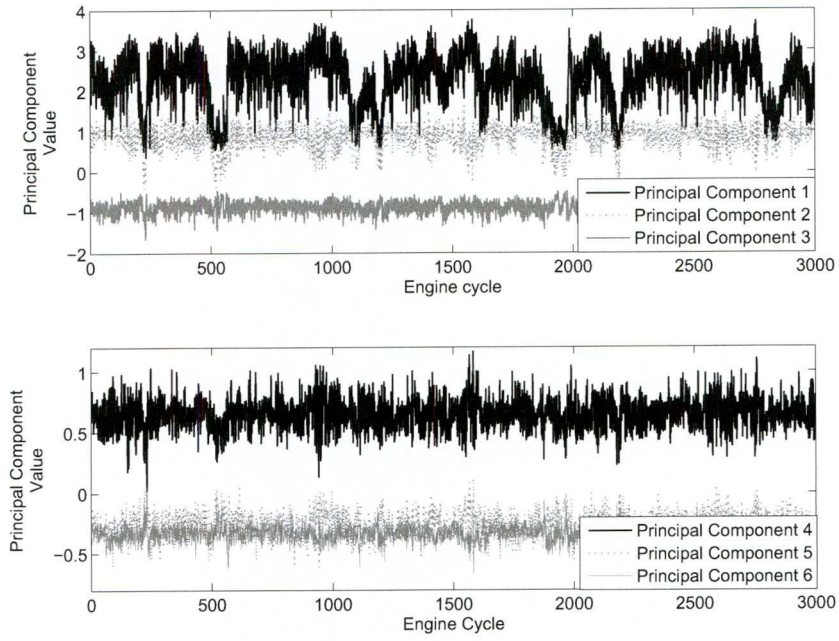

Figure 6.10: 1000 Cycles of 6 Principal Components of the Identification Data

Table 6.5 is the correlation coefficient matrix between the principal components and the AFR. The correlation between principal components themselves is not included since it is unimportant in this work. Interestingly, principal component 4 has a higher correlation to the AFR than principal component 3. Principal component 1 has a higher correlation to the AFR than air bleed valve (ABV), engine speed (N) and fuel pulse width (FPW) from looking at table 6.2.

Table 6.5: Correlation Coefficient Matrix between PCA and AFR

-	AFR	PCA1	PCA2	PCA3	PCA4	PCA5	PCA6
AFR	1	0.339	0.232	-0.050	0.230	0.128	0.036

6.7 Neural Networks Employed for AFR Estimation

Figure 6.11 shows the chosen 2 layer NARX network which is very similar in structure to that used in chapter 4. The input layer weight matrix is denoted IW and other layer weight matrices are denoted LW. The activation function f_1 is a tansigmoid functions while f_2 is a pure linear activation function. Layer 1 contains 10 neurons whilst layer 2 only contains 1 neuron since the predicted λ output of the network is a single value per cycle. The network has a single feedback loop from final layer output $y(t)$ to the first layer through a tapped delay line (TDL) to implement delays in the data and obtain $y(t-1), y(t-2)$. The 9 inputs pass through an additional TDL to instigate the delays: $u(t), u(t-1), u(t-2), u(t-3), u(t-4)$, the input signal and the input signal delayed up to 4 sample times. It is these TDL blocks that differentiate this network from the network chosen in chapter 4 and are as such to reflect the dynamic delays inherent in the data sets. The bias values for each layer are here denoted b_1 and b_2. The input to the NN, shown in fig. 6.11, is a vector of order $R = 9$.

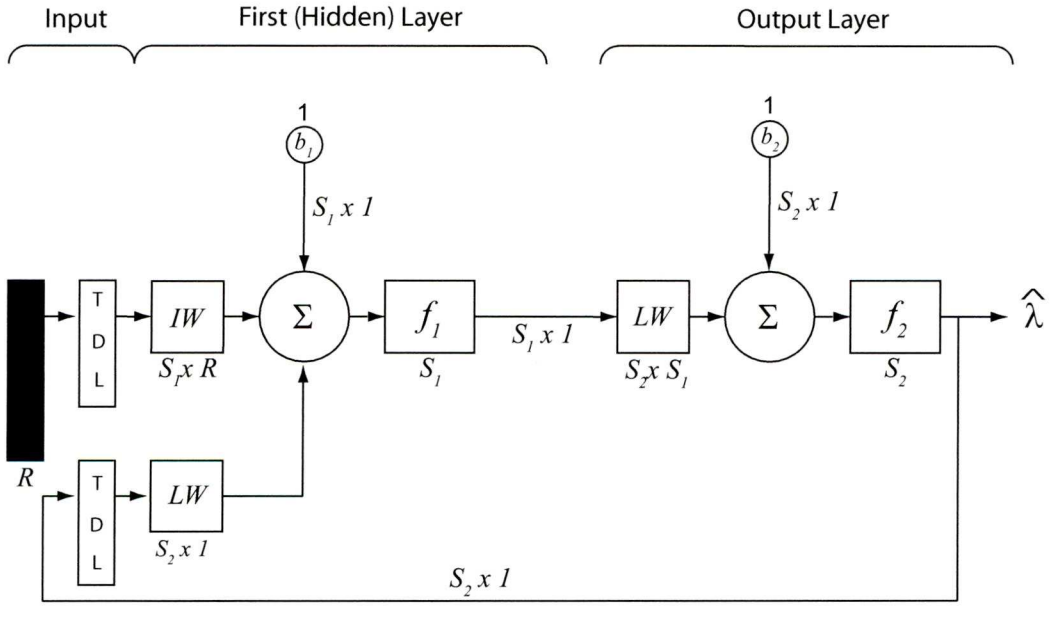

Figure 6.11: Schematic of Three Layer NARX Network

The defining equation of this NARX network is the difference equation

$$y(t) = f(y(t-1), y(t-2), u(t), u(t-1), u(t-3), u(t-4))$$

The training uses these 9 input data sets and 1 target data set. The network is trained using 'Bayesian-Regularisation backpropagation with early stopping' to prevent over training. The validation dataset of 1000 combustion cycles is presented to the network after each training epoch and when the mean squared error of the validation dataset begins to increase, the optimal training epoch for that network has been reached and early stopping occurs.

All datasets have mean values removed and are normalised so that they have maximum and minimum values of 1 and -1 as per chapter 4. Scaling the inputs in this manner results in the NN output also being scaled between 1 and -1. For the output of the NN output (predicted λ) to represent realistic values of λ, it is upscaled in a reverse procedure to that the target data (measured λ) was downscaled.

6.8 Offline Neural Network Proving

After this offline training, the 1000 cycles of hold-out data is used to prove the network is predicting λ accurately. A sample of the comparison of measured λ to predicted λ over 700 cycles is shown in fig. 6.12. It can be seen that the NN is predicting λ accurately within its operating range of from 0.8 up to 1.1, that is within the limits of the training data.

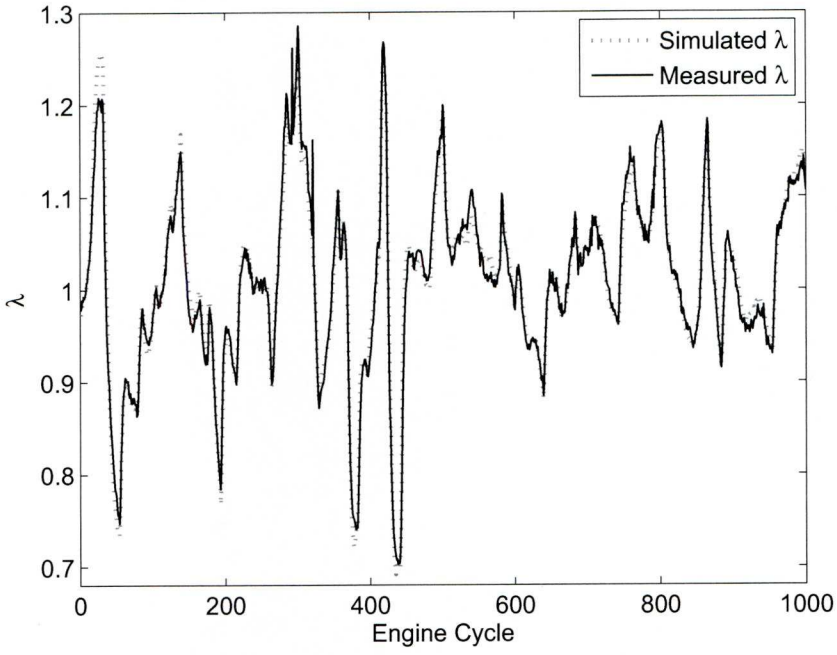

Figure 6.12: Predicted-λ and Measured-λ Over 700 Cycles

The correlation of the predicted λ and measured λ over the 700 cycles of hold-out data can be seen in fig. 6.13.

To quantify the accuracy of the neural network predictions on this hold-out dataset which is the coefficient of determination, R^2, is used:

$$R^2 = 1 - \frac{\sigma_\epsilon^2}{\sigma_y^2}$$

where σ_ϵ^2 indicates the variance of the model residuals and σ_y^2 is the variance of the system

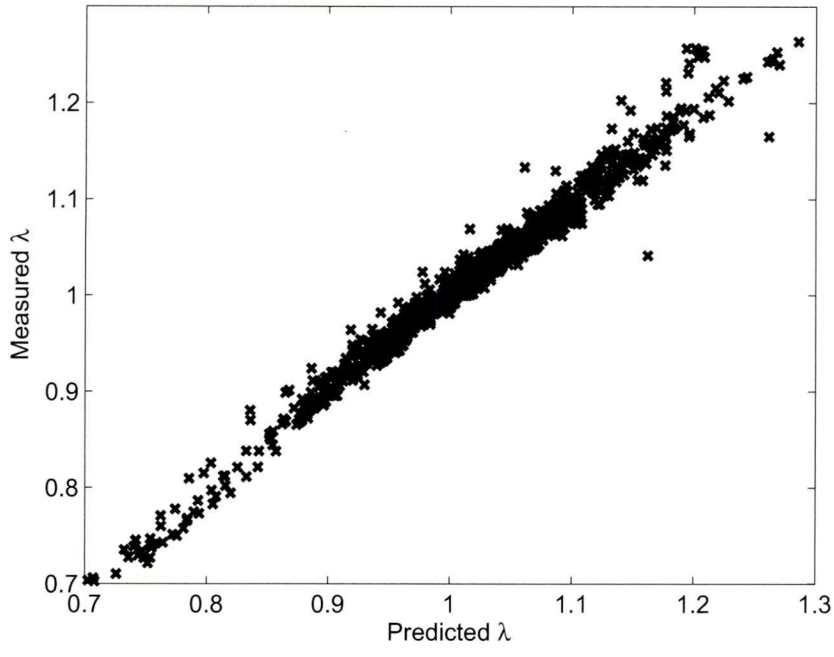

Figure 6.13: Correlation of Predicted-λ and Measured-λ Over 700 Cycles

output. For the 1000 cycles of hold-out data it was found that

$$R^2 = 0.8937 ,$$

indicating that just under 90% of the variance in the AFR is explained by the estimated AFR from the NN output.

6.9 Online Neural Network Proving

This correlation of hold-out data implied good accuracy of the neural network at predicting λ (equivalently AFR). Confidence in the NN then allowed engine implementation with SIMULINK and Real-Time Workshop. Step changes in ABV, load and FPW were made with these engine variables maintained in the ranges used for identification data acquisition. For online PCA computation, the ion current signal window of 38 sample vectors per cycle is projected in real time onto the stored 38×6 'featurevector' matrix to produce the 6 PCA scores per cycle. These can then be used as the NN inputs along with N, integrated MAP and FPW. The proving of the NN occurred on the same day as identification data acquisition to limit the difference in atmospheric conditions as this can affect the low frequency dynamics of the NN output.

The directly measured λ and estimated λ signals plotted during transients in N, MAP and fuel are presented in the figs. 6.14, 6.15 and 6.16. N, integrated MAP, FPW and the

6 PCA score samples have mean values removed and are normalised using values obtained during offline training of the network. These are input to the neural network and a predicted λ value is output that is upscaled using values obtained in network training. As step tests are undertaken for a particular variable, other engine variables are held at their mean value of the identification range. Good correlation of estimated λ to measured λ is achieved when engine variables are within the the ranges of the identification data. In fig. 6.15 the measured λ signal approaches a value of 1.3 where the output of the NN, estimated λ, has a value of 1.2. During these load step tests, ABV and fuel were fixed at mean values which induces an unrealistic lean operation of the engine at higher loads. A combination of these engine variables at these combustion events falls outside of the parameters experienced during identification data acquisition and thus the prediction accuracy falls.

A similar lower prediction accuracy is experienced in fig. 6.16 where measured λ approaches 1.4 between plotted engine cycles 200 to 300. During these events, the FPW could be considered too short for the fixed, mean engine speed and load at that time. This produced an unrealistic lean operation of the engine almost causing engine stall.

To demonstrate the technique successfully over the full range of identification data operating parameters, the lower frequency base fuel signal was set to follow a base MAP signal as per the identification data acquisition so as to avoid these lean, stall operating regions. Higher frequency perturbations in load and fuel are initiated to diverge λ from stoichiometry. A typical window of 1000 engine cycles showing the predicted λ in the presence of the simultaneously perturbed load, ABV and fuel signals plotted against the measured λ is shown in fig. 6.17.

Taking the error as the difference between the predicted λ and the measured λ, fig. 6.18 shows the percentage of all predicted λ data items with an absolute error less than a specific maximum.

It is emphasised that the results are for inputs to the engine which are changing dynamically and the good fit shown is from measurements during this transient behaviour. The figure shows that the predicted signal is within 8% of the measured signal in 100% of the data and is within 0.01 in over 70% of the data. It should be noted that the results presented from the NN proving were obtained on the same day as identification data acquisition to limit the effect of atmospheric conditions, which can offset the NN output low frequency dynamics by a fractional percentage. Also of note is that the aim of the work in the chapter was to replicate the filtered output signal from the UEGO sensor. No attempt was taken to remove the time delays present within the system due to transport time of the exhaust gas to the UEGO location (see section 7.2.1). Using the ion current system which measures combustion properties during the combsution itself, the exhaust gas transport delays can be removed,

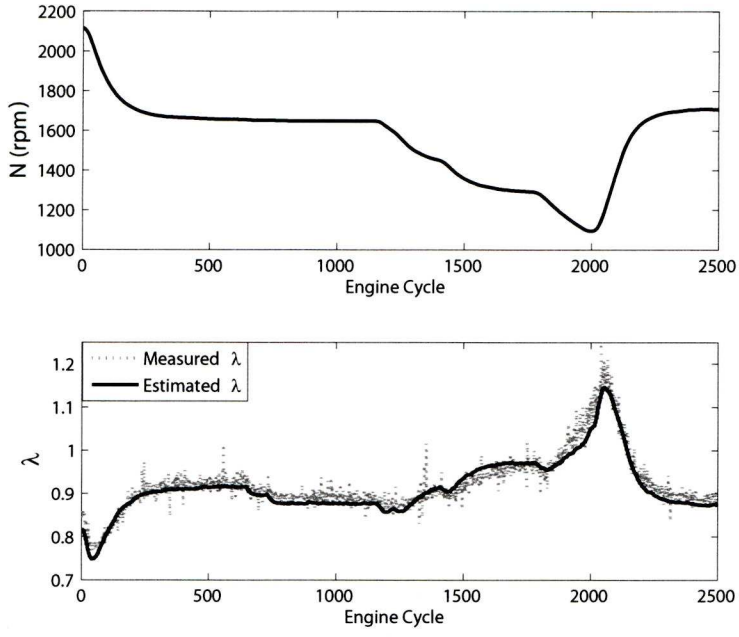

Figure 6.14: Correlation of Measured-λ over 2500 Cycles in Speed Transient Conditions

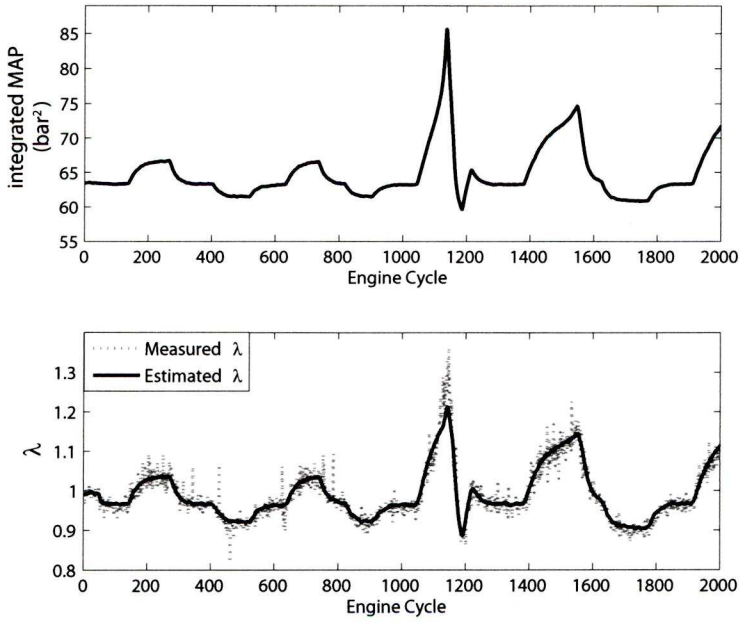

Figure 6.15: Correlation of Measured-λ over 2000 Cycles in Load Transient Conditions

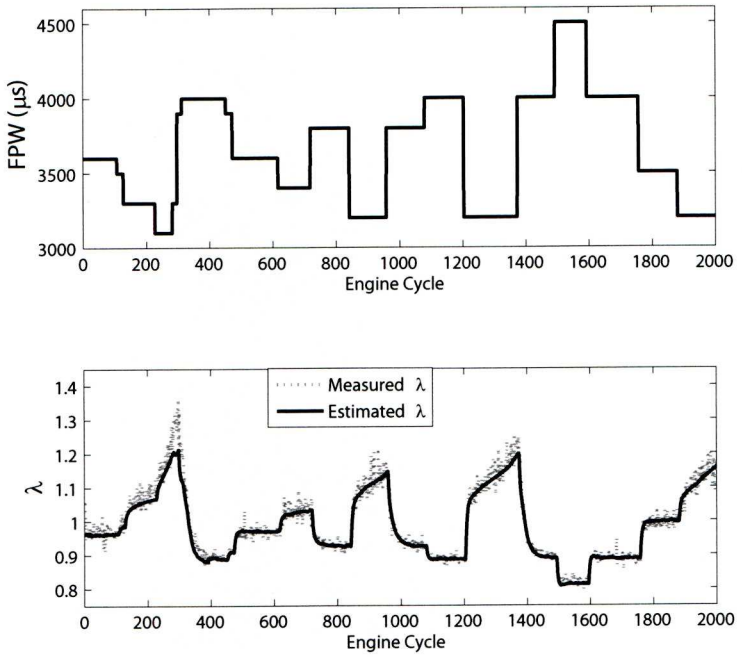

Figure 6.16: Correlation of Measured-λ over 2000 Cycles in FPW Transient Conditions

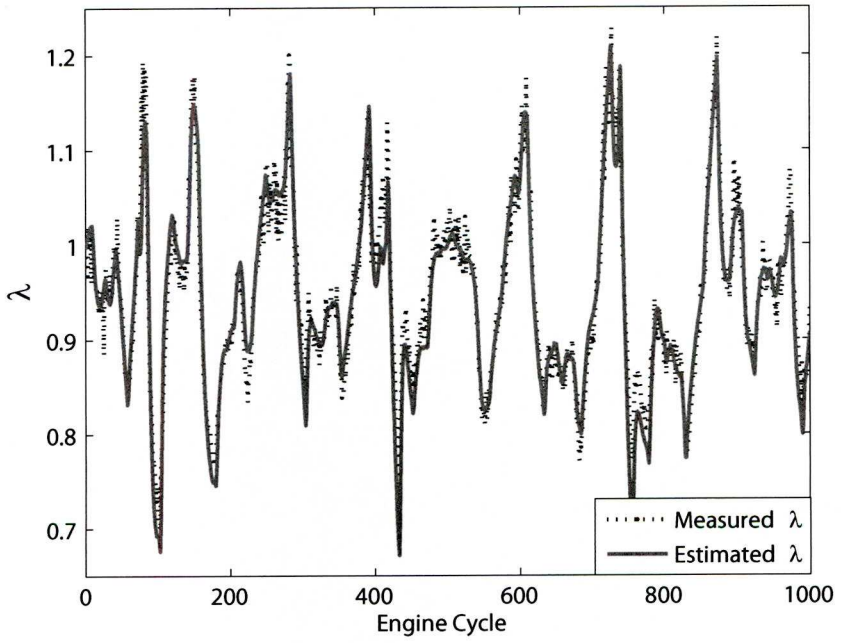

Figure 6.17: Measured-λ and Predicted-λ

which is discussed in chapter 7.

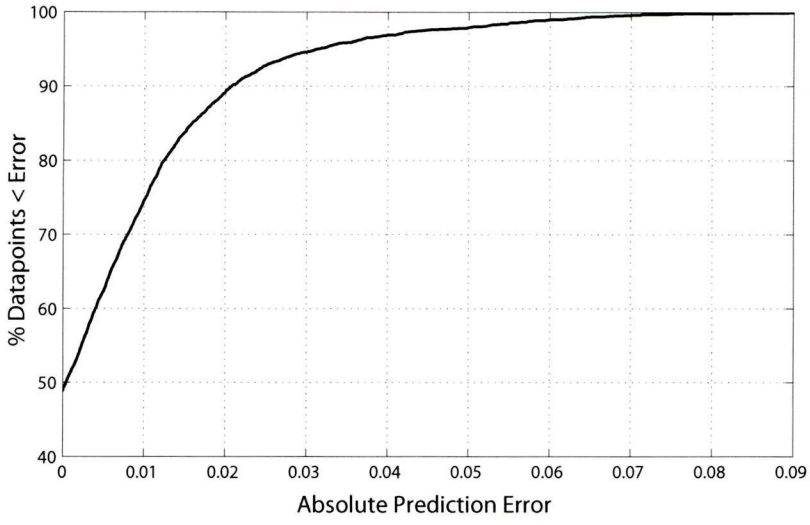

Figure 6.18: Percentage λ-Predictions Less Than an Absolute Error

6.10 Average Torque Estimation

An interesting extension of the network used in λ estimation is that this MISO network can easily be extended to a multiple input, multiple output (MIMO) network by the addition of third layer. Average torque has been recorded simultaneously with the identification data used in section 6.3.2 and this dataset can be presented as a second target set of data in a MIMO network. This would mean that the new MIMO network would be able to predict both λ and average torque with little additional effort.

Average torque is the torque output across all four cylinders averaged across a single combustion cycle or 720° or crank angle. This is not to be confused with instantaneous torque estimation, which is the torque estimated in real time per crank angle degree for each cylinder.

Since the MISO network is currently using available engine signals plus the ionization current principal components, these will be also used in the MIMO network. Torque is usually estimated from engine speed variation or crank angle acceleration. Rizzoni *et al* have worked on such an idea [135, 136]. Kaisheng *et al* [137] presented a feedforward neural network method of estimating the average torque using the FPW, SA, MAP, throttle position and N as inputs. Good estimation results obtained in real time are presented.

Andersson [138] developed a torque estimation model from an existing ionization calibration. Dong *et al* used the ionization current to estimate the torque [139], though the

ionization signal was required to be averaged over twenty combustion cycles.

In this work, available signals are being used to estimate average torque and although the PCA values are inputs, these are measured from a single cylinder whereas average torque is averaged across all four cylinders. It is expected the correlation of inputs to torque output will exist from the non PCA inputs.

6.10.1 MIMO Neural Network

Figure 6.19 illustrates the extended MIMO network. A third layer has been placed parallel to the second layer with a single neuron. This layer takes identical data from the output of the first layer, simultaneously to the second layer. The output of the second layer is a prediction of λ, the output of the third layer is an estimation of average torque.

The input layer weight matrix is denoted IW and other layer weight matrices are denoted LW. The activation function f_1 is a tansigmoid functions while f_2 and f_3 is a pure linear activation function. Layer 1 contains 10 neurons whilst layer 2 and 3 contain 1 neuron each. The network has feedback loops from each of the two final layers to the first layer through a tapped delay line (TDL) to implement delays in the data. The 9 inputs pass through an additional TDL to instigate the delays: $u(t), u(t-1), u(t-2), u(t-3), u(t-4)$, the input signal and the input signal delayed up to 4 sample times. The bias values for each layer are here denoted b_1 to b_3. The input to the NN is a vector of order $R = 9$.

6.10.2 Identification Data for the MIMO Network

The data used in this MIMO identification is generated in an identical manner to that used in section 6.3.2 with the additional measurement of average torque. 1000 cycles are used for estimation training, 1000 cycles are used for validation training and 1000 cycles are used as a hold-out dataset. Figure 6.20 displays the identification data used. The six principal component values have been separated into two plots for clarity.

The training uses these 9 input data sets and 2 target data sets. The network is trained using 'Bayesian-Regularisation backpropagation with early stopping' to prevent over training. The validation dataset of 1000 combustion cycles is presented to the network after each training epoch and when the mean squared error of the validation dataset begins to increase, the optimal training epoch for that network has been reached and early stopping occurs.

All datasets have mean values removed and are normalised so that they have maximum and minimum values of 1 and -1. Scaling the inputs in this manner results in the NN output also being scaled between 1 and -1.

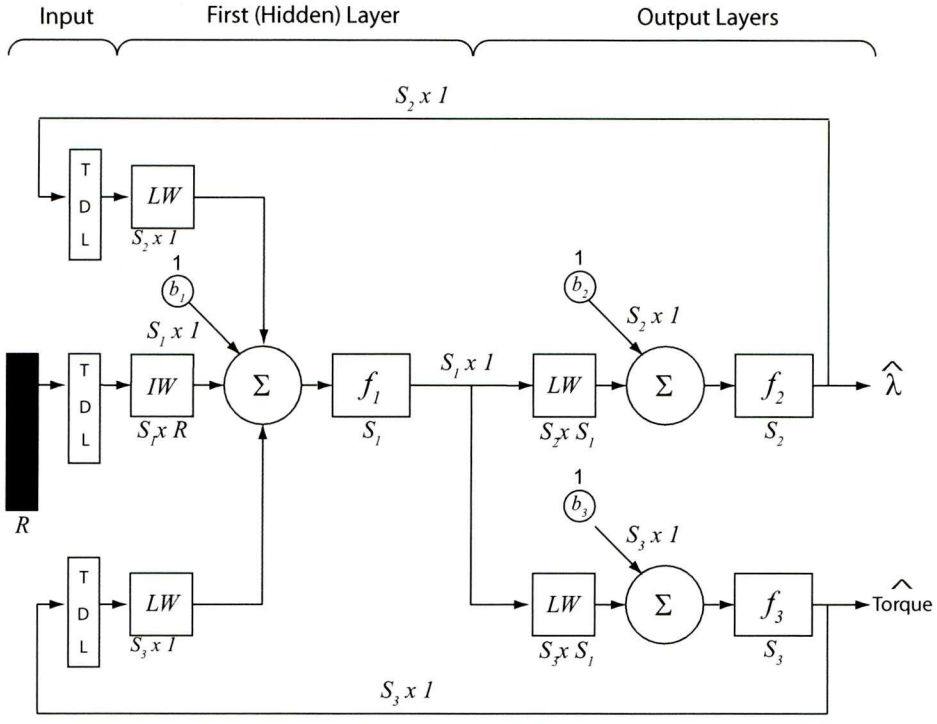

Figure 6.19: A MIMO Neural Network to Predict λ and Average Torque

6.10.3 MIMO Network Results

Figure 6.21 displays the offline network performance of both λ and average torque estimation on a hold out dataset. These results are the raw output of the neural network before any rescaling has occurred, they are still mapped between -1 and 1.

To quantify the accuracy of the neural network predictions on the hold-out dataset, the coefficient of determination, R^2, is used:

$$R^2 = 1 - \frac{\sigma_\epsilon^2}{\sigma_y^2}$$

For the 1000 cycles of hold-out data it was found that:

$$R_\lambda^2 \;=\; 0.8923\ ,$$

indicating that just under 90% of the variance in the λ signal is explained by the estimated λ signal from the first NN output and:

$$R^2_{AverageTorque} \;=\; 0.9219\ ,$$

indicating that just over 90% of the variance in the average torque signal is explained by the estimated average torque from the second NN output.

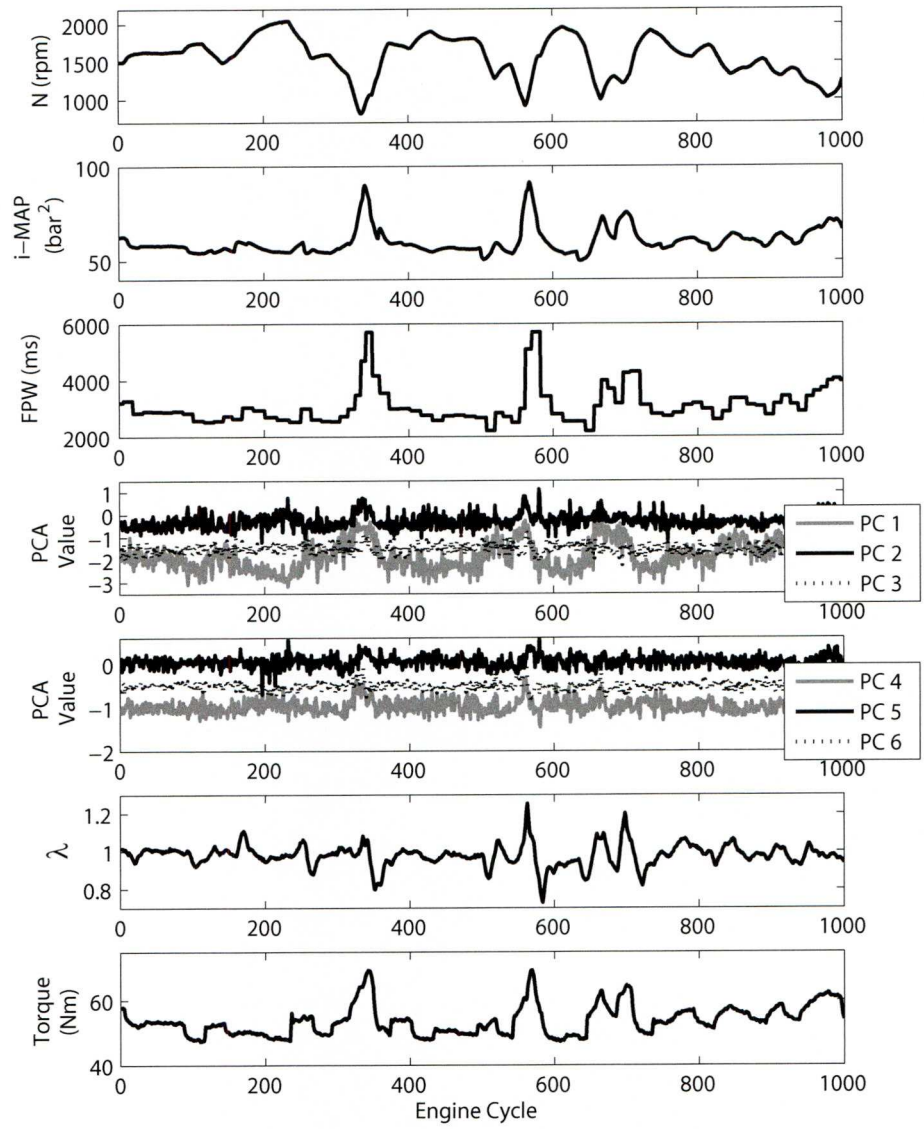

Figure 6.20: Identification Data for a MIMO Network

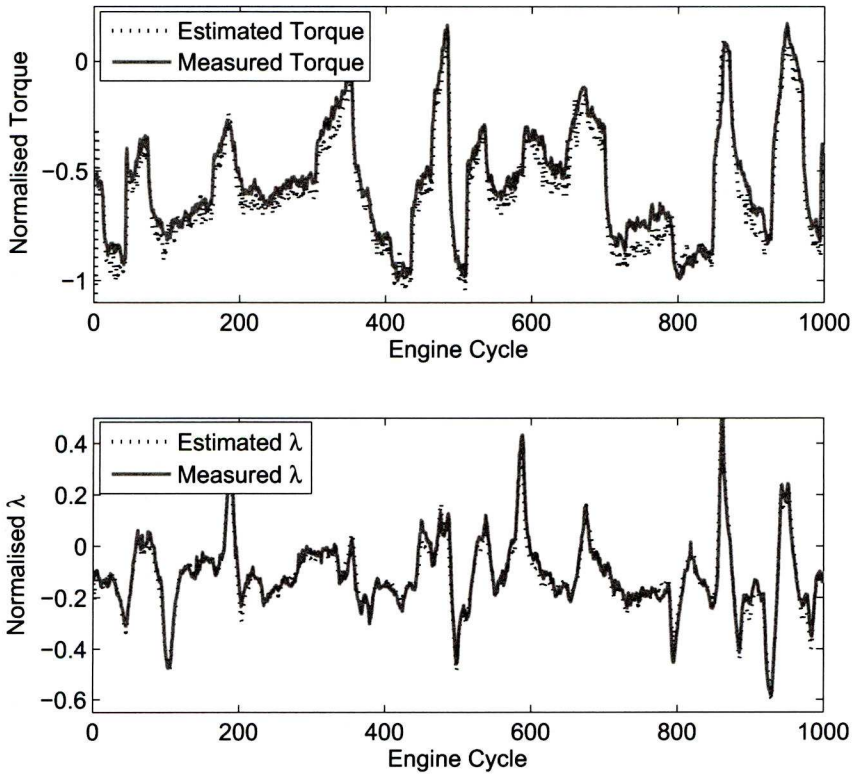

Figure 6.21: Dual Estimation Output of the MIMO Neural Network

This would indicate that not only is average torque being predicted at a good accuracy, but there is no degradation in ability of the network to predict λ.

6.11 Conclusions

Prediction of AFR has been demonstrated using an ion current sensing method with a neural network on one cylinder of a four cylinder IC engine. Dynamically varied input signals were used to excite λ which was measured by a closed coupled wideband UEGO sensor across a range of engine loads and speeds. The PCA technique was used for feature extraction and data reduction of the ion current signal. The resulting 6 principal components were combined with fuel pulse width, MAP and engine speed for identification of a NARX neural network model. This NN was experimentally validated over the identified range and was proven to offer high online accuracy, although there was no attempt to remove the inherent delays present within the UEGO system at this stage. In an extension to the application, average torque has been estimated at a high accuracy 'for free'. Little additional effort is need to extend the two layer neural network to a double final layer neural network to simultaneously predict average torque and λ. The dataset used for this MIMO network is identical with the addition of measured average torque used as a second target dataset.

Chapter 7

Single Cylinder Air-Fuel Ratio Control

7.1 Introduction

A change in λ of 0.1% around $\lambda = 1$ would double the emissions rate although across transients of engine speed and torque, deviations of 2 to 3% around $\lambda = 1$ over short periods of time are acceptable [4].

The amount of fuel that enters an individual cylinder is determined by the length of time that an injector sprays fuel toward the inlet port for each cycle. This injection time is known as the fuel pulse width (FPW) and is in the order of 1×10^3 to $8 \times 10^3 \mu s$. Look-up tables are used in standard production engines for determining the appropriate FPW with an air pressure or air mass flow reading from the manifold absolute pressure (MAP) or manifold air flow (MAF) sensors. The effort to produce the look-up table maps is extensive and must cover possible engine loads and speeds. The capital cost of a single universal exhaust gas oxygen (UEGO) sensor may be currently similar to the ionization current equipment used in this work but the latter has the ability to work on 4 cylinders simultaneously; four UEGO sensors would be too expensive for realistic implementation in production engines.

The AFR can be determined from both FPW and MAP (or MAF) since knowledge of these constituents would imply knowledge of the AFR. The previous chapter 6 illustrates that using the FPW, MAP, N and the ionization current to estimate AFR is feasible but feedback is required for fast control of the AFR to within a desired accuracy across transients. In this chapter, the UEGO λ signal is initially used as a feedback signal in section 7.3 and proves to be accurate although it has inherent delay characteristics due to the sensor location down stream of the exhaust port. The logical step is to use a feedback signal from a λ predicting neural network from chapter 6 that can initially replace the UEGO signal. The ultimate aim

would be to remove these inherent transport delays; this would be the advantage of using the ionization current signal method. Not only does the ion current possess AFR information but it measures combustion information during the combustion process rather than in the exhaust gases indicating no inherent transport delays. The UEGO feedback signal will therefore be substituted for an estimated λ signal generated from the processed ion current. In this manner, feedback control across transients is achieved with similar performance to the UEGO sensor but with less discrete time delay.

The steps undertaken in this chapter to illustrate the benefits of the ion current for AFR control are as follows:

1. A feed forward fuelling controller using available engine signals is created, section 7.2
2. A feedback signal from the UEGO sensor is then incorporated to improve performance, section 7.3
3. The UEGO sensor λ signal is substituted for an estimated λ signal from the ion current, section 7.4

It should be noted that all tests are performed within a short time frame so as to minimise the effect of changing ambient conditions.

7.2 Feed-forward Fuel Control

A fuelling feed-forward prediction controller is generated for illustrative purposes using available engine signals. This type of controller was developed for automotive mass market engines initially from work by Aquino [140]. The air-fuel ratio of a combustion event is obviously dependent on a measure of the air constituent and a measure of the fuel constituent of the cylinder 'charge' for that combustion event, hence the use of MAP, FPW and measured λ in this controller. In the preceding chapter FPW, N, MAP and the ion current signal were used in a neural network (NN) identification to predict the AFR, or λ. Since these signals are causal, an identified model can be inverted using a desired λ of 1, N and MAP to control the FPW. This is then termed the 'inverse' identification whereby the FPW, as an output of the 'inverse' identified model (Λ), in turn fuels the engine to keep the resulting measured λ to within 0.1% of the optimal value.

Figure 7.1 illustrates an identified NN model for λ prediction from available engine signals: N, FPW and integrated MAP.

Figure 7.2 then illustrates how the same identification data can be used to construct the inverse model Λ, also an identified NN, for FPW prediction to fuel the engine or plant, G.

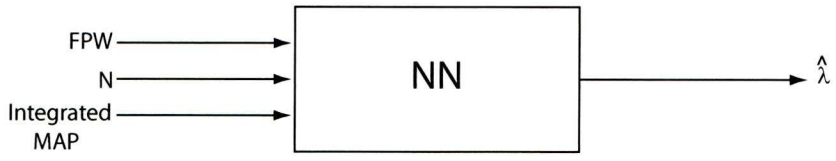

Figure 7.1: Forward Neural Network Identification of λ

The desired λ ratio input, λ_D, is set to 1 after identification so that Λ predicts the necessary fuel pulse width, $F\hat{P}W$ for this condition. The plant/engine, G, uses the $F\hat{P}W$ and the resultant λ value is measured.

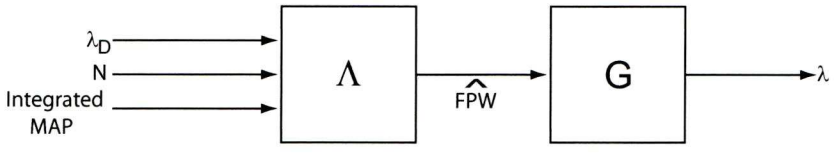

Figure 7.2: Inverse of Causal Signals for Identification of FPW

7.2.1 Inherent Delays

Creating the inverse model requires manipulation of the identification data to produce causal data. This can only be done accurately with prior knowledge of the system dynamics, specifically the pure delays present between engine input and output samples. A particular causal output response from the engine is experienced by a sensor a definite delay period after perturbation of the engine input signal from an actuator. A single delay period in this work can be thought of as one combustion cycle event or 720° of crank angle (for a four stroke engine) since although data is sampled every crank angle degree, the NN is trained using one sample per combustion cycle.

There have been numerous detailed models of the dynamics between fuelling actuation to the response experienced at the lambda sensors [14, 4, 141, 142]. The models detail various delays along the fuel-air path that should be accounted for when determining appropriate control.

Delays are present between the fuel injection spray from the injector and the resulting AFR or λ signal measured at the UEGO sensor in the exhaust stream. In a series of papers, Wang and Detwiler performed dynamic studies of the individual steps of the delay [143, 144, 145] concluding that the wall wetting effect of the fuel delivery is the most important source for the transient air-fuel ratio excursions [141], which refers to the puddle or film of fuel that accumulates as the injector sprays towards the closed inlet valve. The next most significant delay is the transport delay of the exhaust gas from the exhaust valve to the UEGO sensor. Conventionally a gas oxygen sensor is located downstream at a confluence point and so there

would be a discrete time lag of a few combustion cycles as each gas exhaust charge pushes the preceding charge further along the exhaust; this discrete time lag determined by the volume of the exhaust plenum. In simplified terms, this overall delay, t_{total} is composed of:

1. t_{IPS}, Induction to power stroke: the time from the fuel demand, the wall wetting, the inlet valve opening, the combustion to the exhaust valve opening.
2. $t_{transport}$, the time taken for the exhaust gas to travel from the exhaust port to the UEGO sensor.
3. t_{UEGO}, the reaction time of the UEGO sensor to report the experienced AFR.

$$t_{total} = t_{IPS} + t_{transport} + t_{UEGO}$$

Figure 7.3 displays a simplified block diagram of the dynamic delays involved between the fuel command being issued to the injector to the UEGO sensor reporting it.

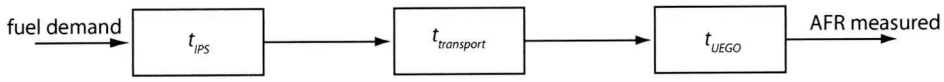

Figure 7.3: Block Diagram Showing Delays From Injector to UEGO Sensor

For the application presented here, between fuel injection and the UEGO sensor at the outlet exhaust port, $t_{total} = 2$, i.e. a delay of two combustion cycles is experienced. This was found during work occurring in chapter 6.

Figure 7.4 illustrates the crank domain timing of events that occur in cylinder 4, including the crank angle that signals are sampled at during this work on fuelling. These have been chosen carefully so that all sampled signals are synchronised to a relative combustion event and delays are not introduced.

Taking this illustrated 720° of crank angle to be the current combustion cycle (n): Between 0° and 25° ATDC relative to cylinder 4, combustion is occurring from a previous fuel and air charge $(n-1)$. At this crank angle, at the UEGO sensor near the exhaust port is the exhaust gas from an even earlier combustion $(n-2)$. Therefore to ensure unnecessary delays are not introduced, the AFR (or λ) is sampled after the exhaust valve has closed (around 400° ATDC. This would mean the exhaust gas at UEGO is from the previous combustion cycle $(n-1)$, whereby the FPW for that combustion charge is sampled 1000° previous. Fuel is sampled when the injector signal is given for the present combustion cycle, 120° ATDC, along with integrated MAP (since the inlet valves have not yet opened). Since the resolution of the discrete sampling is once per 720°, this implies that there are 2 delays experienced , as already stated.

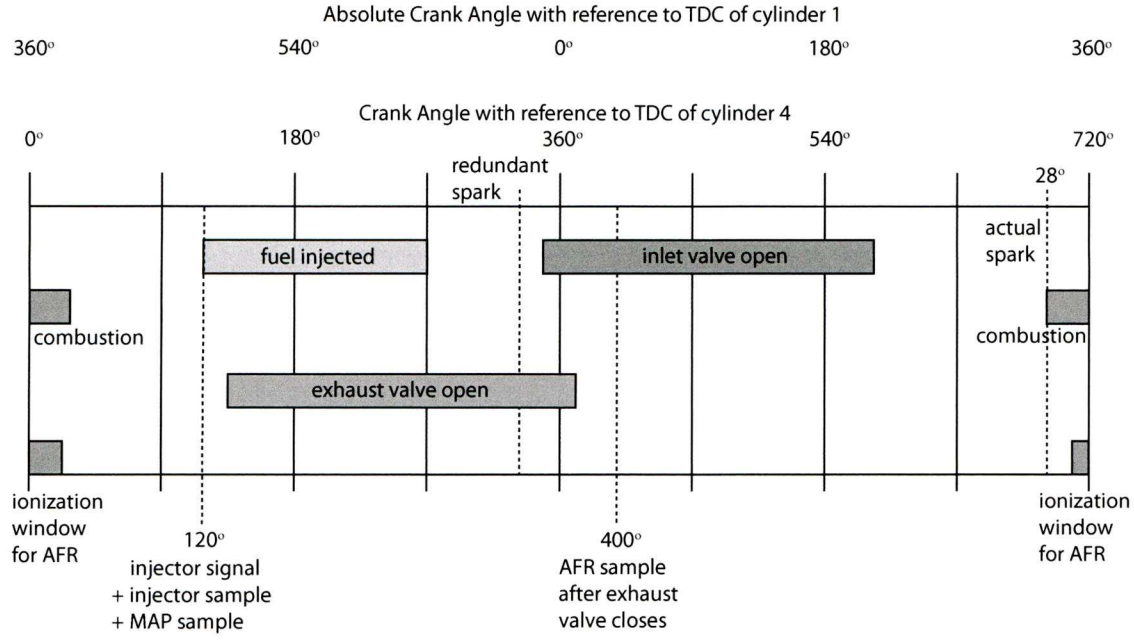

Figure 7.4: Crank Angle Domain Cylinder 4 Events

The ionization window used to measure the AFR data is sampled between 7° and 45° after the spark event, this implies that for the current combustion cycle (n), the ionization window occurs between 699° and 737° ATDC since the spark advance is fixed at 28° BTDC.

Figure 7.5 illustrates these delays between the fuel pulse width and the resulting UEGO λ signal in both the raw data sampled every crank angle degree (a and b) and the processed data sampled once per combustion cycle (c and d). The figures show a traverse of the FPW from a longer to a shorter duration, the resulting λ signals are shown, whereby a corresponding reaction from a richer to a leaner AFR is experienced. From the raw data sampled at every crank angle, there is a delay of around 1600 crank angles, this equates to just over 2 combustion cycles. This is confirmed by the processed data sampled once per combustion cycle. The step in fuel from a larger to a smaller FPW commences at 18 combustion cycle and the corresponding reaction in λ is seen to be experienced at 20 combustion cycles.

7.2.2 Engine Signals for Identification

The dynamometer load applied to the crankshaft of the engine is perturbed, to vary the MAP, simultaneously with the FPW to excite dynamics of the AFR in exactly the same manner as per chapter 6 with a FPW mapped to the resultant MAP signal. There are also minor FPW perturbations applied to deviate the AFR from stoichiometry. The following table 7.1 shows the perturbed signal ranges used in the forward identification for the resulting measured λ value.

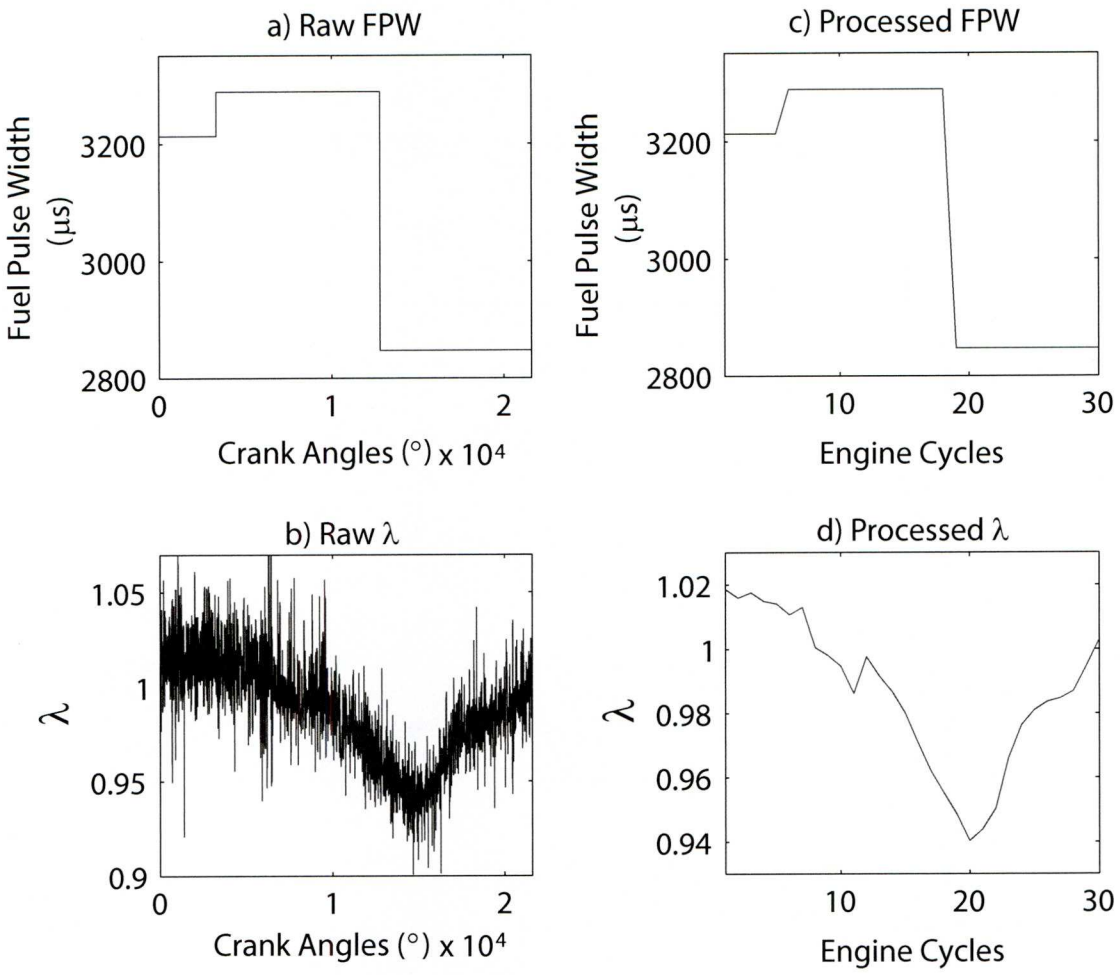

Figure 7.5: Traversing FPW and Corresponding λ

Table 7.1: Perturbed Signals for AFR Feed-forward Identification

Signal	Range	Perturbation Period
ABV [$\%_{duty}$]	40 to 53	1.2 seconds
Load (V)	-0.01 to -0.09	2 seconds
FPW [μs]	2200 to 8000	1.5 seconds

Table 7.2: Resulting Signals for AFR Feed-forward Identification

Signal	Obtained Range
Speed $[rpm]$	900 to 2000
Integrated MAP $[bar^2]$	50 to 120
FPW $[\mu s]$	2200 to 8000
λ	0.7 to 1.4

These perturbed signals result in the obtained signal ranges detailed in table 7.2.

3000 cycles of the identification data are obtained. Although the data is sampled every degree online through dSPACE, further data processing offline for NN training requires samples once per combustion cycle, i.e. every 720°; 1000 cycles are illustrated in fig. 7.6.

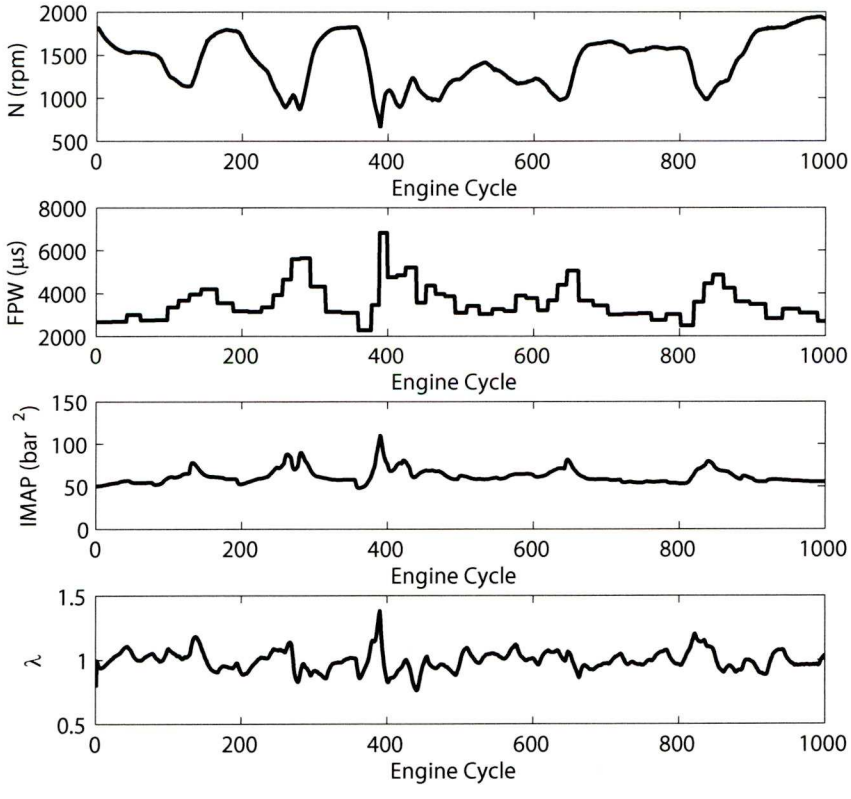

Figure 7.6: 1000 Cycles of Obtained Identification Data

7.2.3 Inverse of the Identification Data

There are a number of issues associated with the inversion of any plant and the ability of the inverted plant to achieve good tracking will depend very much on the accuracy of the initial model; inversion-based feedforward inputs can adversely affect the output tracking performance in the presence of large modelling errors [146]. Non-minimum phase systems or systems with time delays are especially difficult to invert. The inputs on such an inverted system would be non-causal unless the inputs are changed before the output is modified [147]. More fundamentally, non-minimum phase models by nature have zeros outside of the unit circle. Upon an inversion process these roots can become poles of the system still outside of the unit circle hence creating an unstable system unless great care is taken. Also for non-minimum phase systems inversion methods with unbounded inputs can lead to ustable inverse systems and so cannot be easily applied. For the following method, the inverted system is generated in a black-box identification directly from input/output data rather than inverting an already identified model. Great care is still taken in making the inverted inputs causal.

For FPW estimation, we require model input signals to be N, integrated MAP and λ (effectively becoming λ_D; the model output signal is FPW. This would create an inverted MISO system from the obtained identification data. As discussed in 7.2.1, there are delays present in the data between the input and output signals; AFR experiences a delayed response to changes in the integrated MAP, FPW and N. In order to invert this data for FPW estimation, these delays should be taken into account to produce causal identification data. This would involve 'shifting' of datasets by a number of combustion cycles to synchronise inputs to outputs.

The diagram, fig. 7.7, illustrates the inherent delays in the identification data and the procedure for inverting the data for FPW identification. 7.7a shows the system in the original non-inverted state, where by N, integrated MAP and FPW were used as input signals to the plant G to obtain a measured λ signal. There are 2 measured combustion cycles or time delays between a change in the FPW and a measured influence on the UEGO sensor. Similarly, there is only one delay between a change in N or the integrated MAP before being experienced at the UEGO sensor. This also implies a single time delay between the input FPW and the other two inputs, N and integrated MAP.

To invert this system to predict FPW and use λ as an effective input, λ and FPW are switched with the time delays between all signals remaining intact, as per fig. 7.7b. This figure is not physically realiseable; FPW is now predicted 2 sample delays as an output before the new input λ_D and this is not causal. There is still 1 time delay between FPW and the other existing inputs ,N and integrated MAP, but again, not in a causal manner.

7.7c displays the system that has been made causal; the input data has been shifted by

the required 2 time delays to create the correct inverse model Λ. If the final control achieves good regulation of λ, then λ_D is effectively constant [148].

7.2.4 Neural Network for Feed-forward fuelling Control

3000 cycles of causal inverted identification data is now used in a Neural Network training algorithm. 1000 cycles are used for estimation, 1000 cycles are used for validation and 1000 cycles are used as a 'hold-out' dataset for offline proving before engine implementation occurs [101].

To choose a specific network, the input and output training data must be taken into consideration. There is no feedback in the identification, a MISO network which will be able, after training, to predict an estimated FPW, from λ_D, N and integrated MAP.

Network sizes are tested and performances obtained, starting with a larger network continuing with a systematic network size reduction. A two layer network structure which has a compromise between model prediction accuracy, complexity and computational processing speed is chosen.

Figure 7.8 shows the chosen 2 layer feed-forward multilayer perceptron neural network where the input layer weight matrix is denoted IW and output layer weight matrices are denoted LW. f_1 activation functions is a tansigmoid function while f_2 is a pure linear activation function. Layers 1 contains 10 neurons whilst layer 2 contains 1 neuron (since the output of the network is a single value, FPW. TDL denotes a tapped delay line. The input are passed through a tapped delay line to instigate the delays present in the data. In this actual Network, the 3 inputs pass through a specific tapped delay line where the output is a vector made up of the input signal at the current time and the previous input signal.

The defining equation of this network is as equation 7.1.

$$y_2(t) = f(u(t), u(t-1), u(t-2)) \tag{7.1}$$

The network is trained using 'Bayesian-Regularisation backpropagation with early stopping', which prevents over-training. The validation dataset of 1000 cycles is employed here after each training epoch through being presented to the network. Early stopping occurs when the mean squared error of the validation dataset begins to increase indicating the optimal training epoch for that network has been reached.

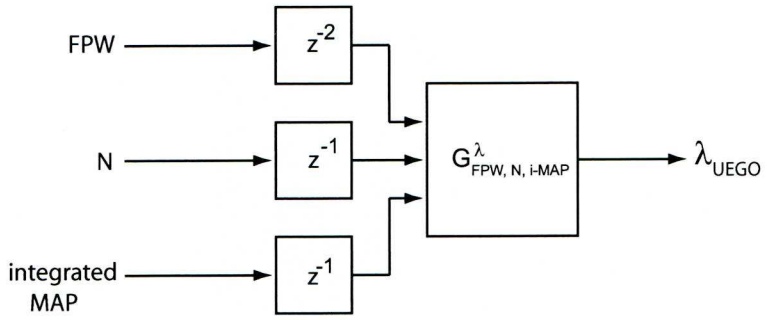

a) Forward Identification Data Illustrating Present Delays

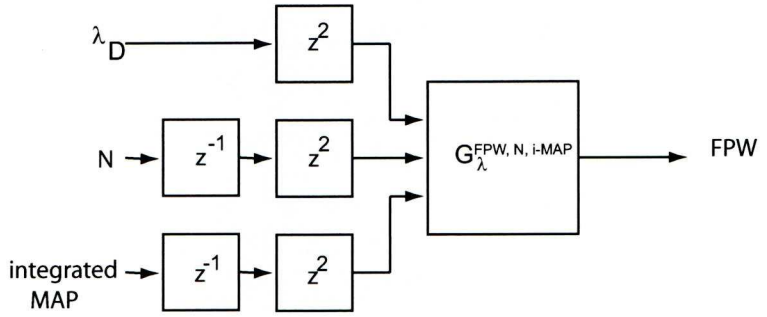

b) Inverted Identification Data (Partial Inverse Model)

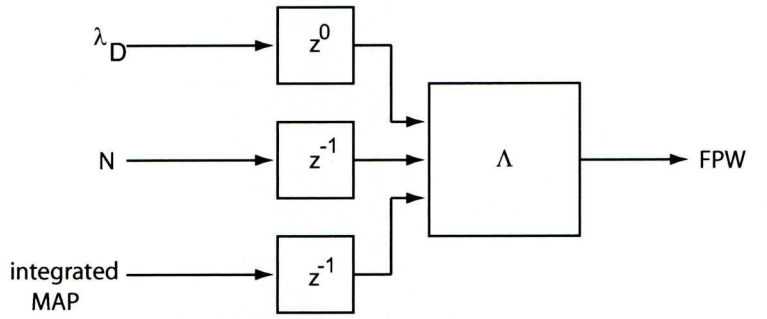

c) Inverted Identification Data with Synchronised Data (Inverse Model)

Figure 7.7: Inverting the Identification data with Delays

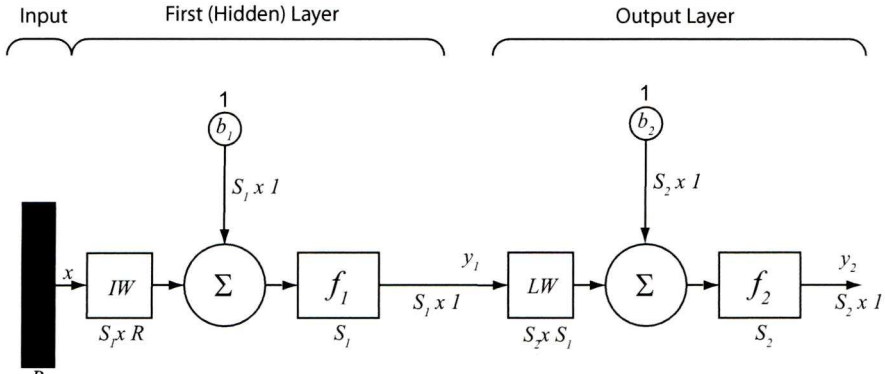

Figure 7.8: Schematic of a Two Layer Feed-forward Network

Offline Feed-forward Network Proving

After this offline training, the 1000 cycles of hold-out data is used to prove the network is predicting FPW adequately enough. A sample of the comparison of measured FPW to predicted FPW over 1000 cycles is shown in fig. 7.9. It can be seen that the feed-forward NN is predicting FPW within the limits of the training data to a reasonable accuracy although FPW is a square edge stepped signal.

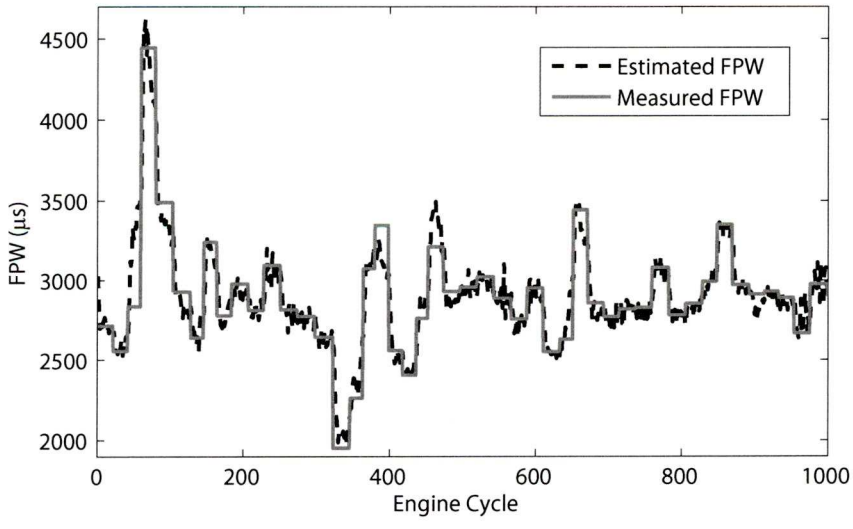

Figure 7.9: Predicted FPW and Measured FPW Over 1000 Cycles

To quantify the accuracy of the neural network predictions on this hold-out dataset which is the coefficient of determination, R^2, is used:

$$R^2 = 1 - \frac{\sigma_\epsilon^2}{\sigma_y^2}$$

where σ_ϵ^2 indicates the variance of the model residuals and σ_y^2 is the variance of the system

output. For the 1000 cycles of hold-out data it was found that

$$R^2 = 85.87 ,$$

indicating that just over 85% of the variance in the FPW is explained by the estimated FPW from the feed-forward NN output.

Online Feed-forward Network Proving

Good correlation of identification output data, FPW, to the predicted FPW offline instills enough confidence to implement the network onto the engine for online proving. Online network proving involves predicting FPW in real time as the engine is running with input signals streaming into the network. With reference to fig. 7.2, the input λ_D is set to 1. This would cause the output of the NN to predict the FPW necessary for a λ at stoichiometry.

To emulate the offline simulation online, all signal processing that was done offline has to be undertaken online on the engine/dynamometer. This is done with SIMULINK and Real Time Workshop and the advantages of simplifying the offline computation becomes apparent. For proving, the fuelling is now decoupled from the MAP signal, as the FPW is now provided as an output from the NN.

Whilst the engine is running, the following must be occurring:

- $\lambda_D = 1$, N and integrated MAP are to be sampled once per 720° at a specific crank angle, matching the angle chosen for offline computation.
- $\lambda_D = 1$, N and integrated MAP samples are input to the neural network and a $\hat{FPW}$ value is output.
- The engine uses the $\hat{FPW}$ from the output of the neural network for combustion.
- The combustion AFR is read by the UEGO sensor near the cylinder exhaust port.

Engine variables (load and ABV ranges) were brought in line with the ranges used for identification data acquisition (a must) and λ_D was step-changed to illustrate robustness of the network at predicting FPW to keep λ tracking to a desired λ value.

The resulting measured λ signal and the step changed input signal λ_D is presented in fig. 7.10. It can be seen that although transient behaviour is present, the required λ bias levels when not at stoichiometry are not achieved. This is not the purpose of the feed-forward controller, it is designed to maintain stoichiometry whilst rejecting disturbance inputs; not track to alternative λ values. Hence disturbance rejection was examined using step changes in the speed and load.

The resulting measured λ signal and the step changed input signals, ABV (and thus N) are presented in fig. 7.11. When step changes in ABV are present causing the speed to traverse a small range, the λ diverges from stoichiometry. Step changes in load (and thus integrated MAP), the resulting FPW and the resulting measured λ signal are presented in fig. 7.12. Small step changes in the load cause an error in λ away from stoichiometry. It should be noted that upon a step change away from the average values of N and load used in the identification, the λ value does not eventually return to stoichiometry but maintains and excursion from $\lambda = 1$ until the value of N and load return to the average value. Although the shortcomings of the feed-forward controller can be seen in this simple test, the controller is able to restrict λ to within $0.95 < \lambda > 1.05$ when $\lambda_D = 1$.

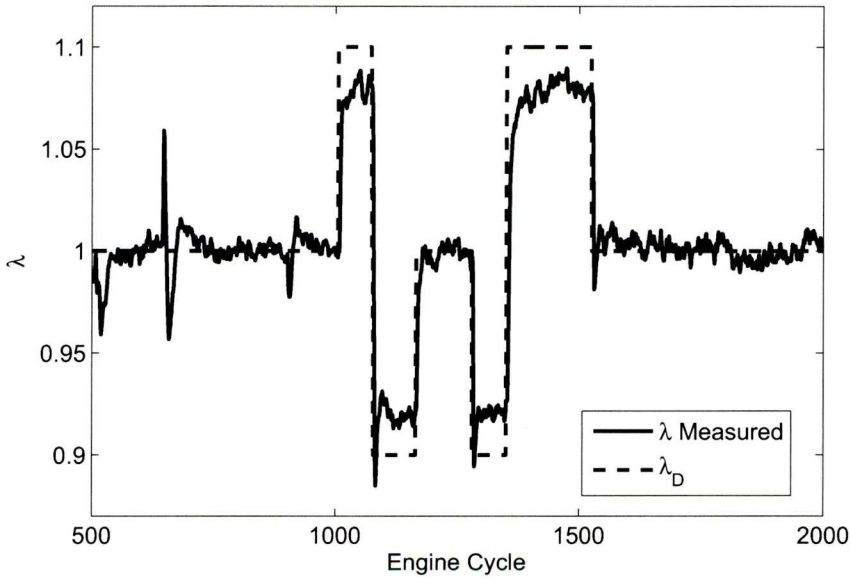

Figure 7.10: Validation Data Showing Measured λ with λ_D

A fuelling feed-forward controller created in this manner is generated quicker than for a series of static mappings. Only one set of identification data is required to generate both the forward identification model and the inverse identification model. A static mapping within an EMS determines fuelling duty from speed and load variables whereas this feed-forward technique also determines fuelling from speed and load variables but with the added benefit of including dynamic characteristics of the conditions. Transient behaviour of the system is captured in the model due to the perturbed engine signals and therefore is intrinsic to the controller. The excursions from stoichiometry upon step changes in load and ABV, in addition to the controller's inability to track accurately to λ settings away from 1 proves the necessity for an appropriate feedback control scheme.

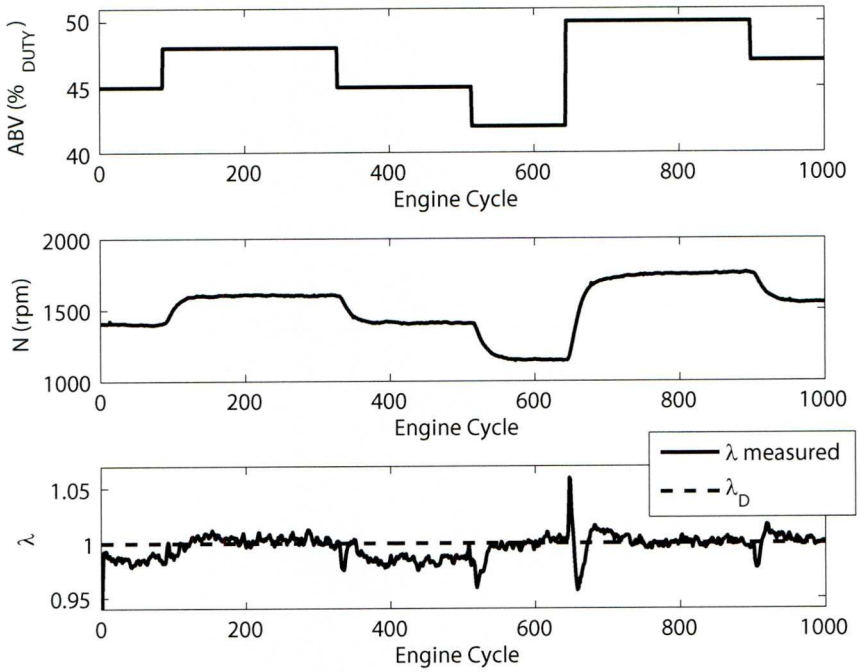

Figure 7.11: Validation Data Showing Measured λ with Step Changes in Speed

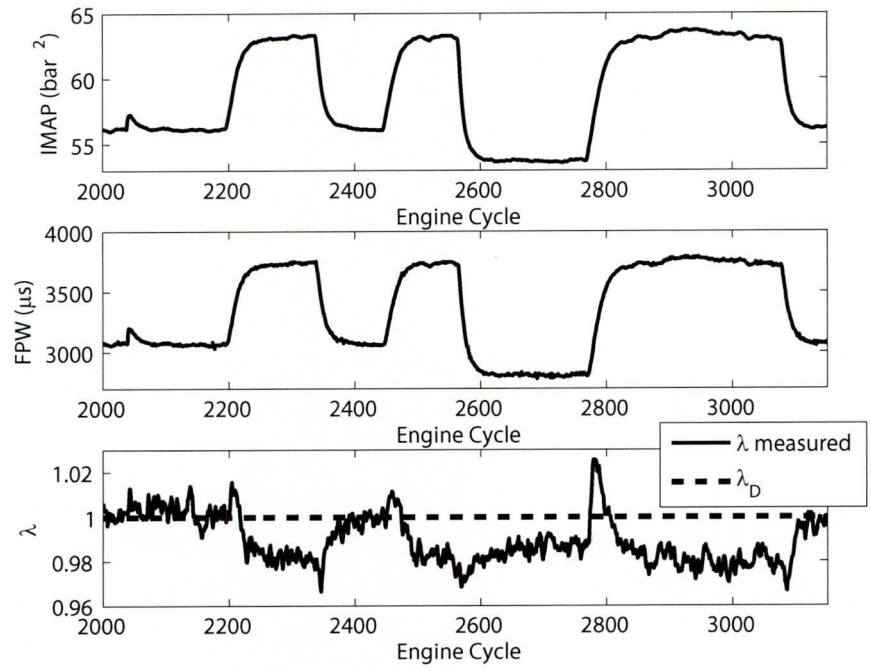

Figure 7.12: Validation Data Showing Measured λ with Step Changes in Load

7.3 Feedback Control using the UEGO sensor

A fuelling feed-forward controller has been established. This predicts the FPW, $F\hat{P}W$ for stoichiometry from the available engine signals, N, integrated MAP and λ_D. The engine or plant, G, uses $F\hat{P}W$ for combustion and the combustion AFR is measured with a UEGO sensor.

A feedback signal can be integrated into the feed-forward fuelling controller to give higher accuracy. This can be done initially using the measured λ from the UEGO sensor placed near the exhaust port of the cylinder as in fig. 7.13. K represents the control implemented in the feedback loop.

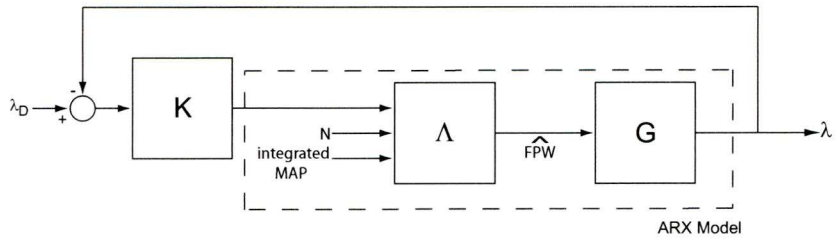

Figure 7.13: UEGO Signal Feedback Incorporated into the Feed-forward Control

To generate a controller, a model of the system that is to be controlled will be identified. The actual measured λ signal is to be controlled to meet stoichiometry across steady state and transient engine behaviour with rapid response to step changes with little overshoot. The basic principle is to perturb the λ_D input signal to excite the system dynamics, measure the resulting λ output signal from the UEGO sensor and then identify the relationship between these input and output signals to give a model.

7.3.1 Engine Signals for Identification

The previously identified feed-forward NN that produces $F\hat{P}W$ as an output uses N, integrated MAP and λ_D as input signals. A SISO linear Auto Regressive with eXogenous inputs (ARX) model of the system will be generated from the λ_D input signal to the measured λ output signal encompassing the dashed box in fig. 7.13. In this manner the identified ARX model will give a relationship between λ_D and λ, but the system will still be able to account for changes in load and speed for correct fuelling due to the 'interior' NN. The signals used to generate the ARX model are as table 7.3. Load and ABV were set at a steady state mid point of the NN Identification.

Input and output data is collected over 3000 combustion cycles from the engine/dynamometer set-up. All signals are sampled online once per degree and so over 3000 combustion cycles

Table 7.3: Used Signals for Identification

Signal	Range	Perturbation Period
λ_D	0.9 to 1.1	2 seconds
ABV [$\%_{duty}$]	46	N/A
Load [V]	−0.06	N/A

would give 2160000 samples per signal channel. This resolution of information is unnecessary in identifying this model; only one sample is required per combustion cycle. Hence 3000 samples each for 3000 combustion cycles are used in the identification process. Figure 7.14 shows identification data used to obtain the ARX model of λ_D to measured λ.

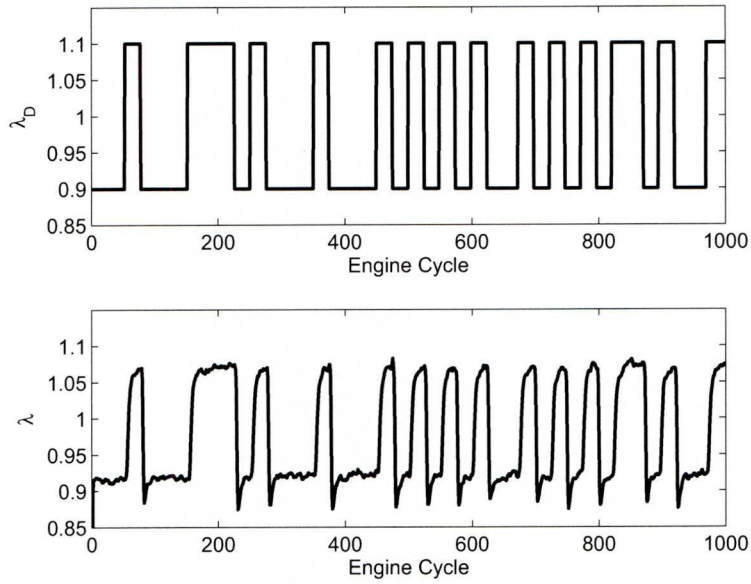

Figure 7.14: λ_D and measured λ used for Identification

7.3.2 Obtained ARX Model

The ARX model structure was chosen for its simplicity. It is already established that the feed-forward neural network will have 1 inherent time delay from λ_D to estimate the FPW. But there are also a further 2 delays from the FPW to the actual λ signal experienced at the UEGO sensor.

Therefore 3 is chosen as the time delay, n_k, for the chosen structure.

The ARX model may be represented as

$$y(z) = \frac{B(z)}{A(z)}u(z) + e(z) \tag{7.2}$$

where A, B , and C are polynomials of the form

$$\begin{aligned} A(z) &= 1 + a_1 z^{-1} + \ldots + a_{na} z^{-na} \\ B(z) &= b_1 z^{-1} + \ldots + b_{nb} z^{-nb+1} \end{aligned}$$

In this case the model orders n_a, n_b and the discrete time delay order, n_k were found to be 3, 2, 3 respectively.

The identified polynomials lead to the following ARX model:

$$y(z) = \frac{0.1862z - 0.08704}{z^4 - 1.697z^3 + 1.17z^2 - 0.339z}u(z) + e(z) \tag{7.3}$$

A pole-zero plot, fig. 7.15, of the ARX model shows the stability, whilst magnitude and phase of the frequency response is shown in a bode plot, fig. 7.16. Using this information, loop shaping control can be implemented in the feedback loop.

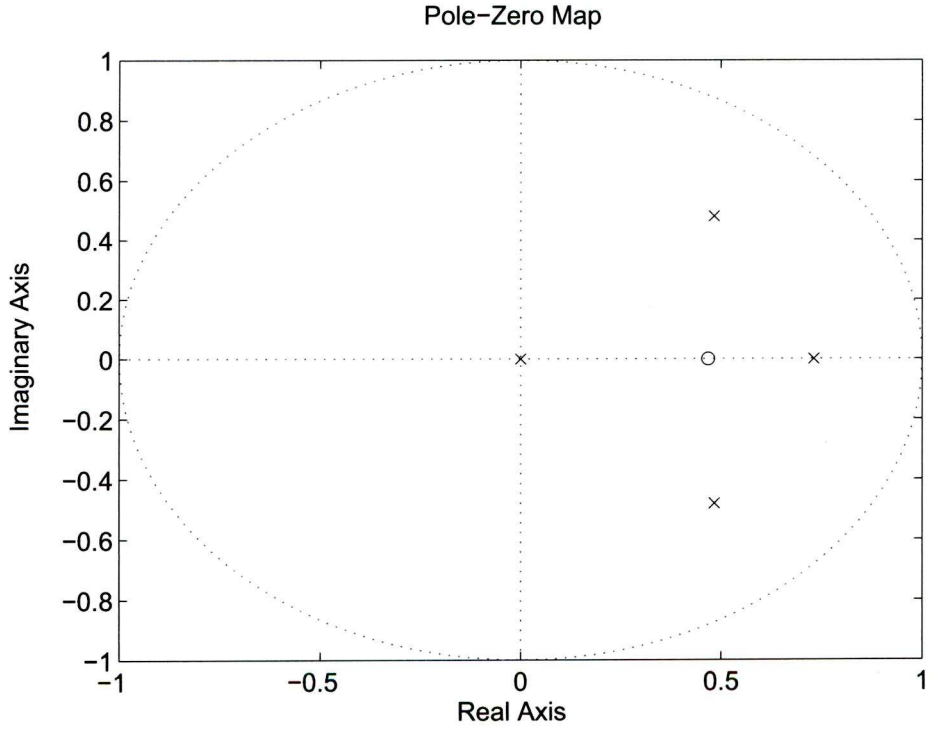

Figure 7.15: Pole-Zero Plot of the Identified ARX model

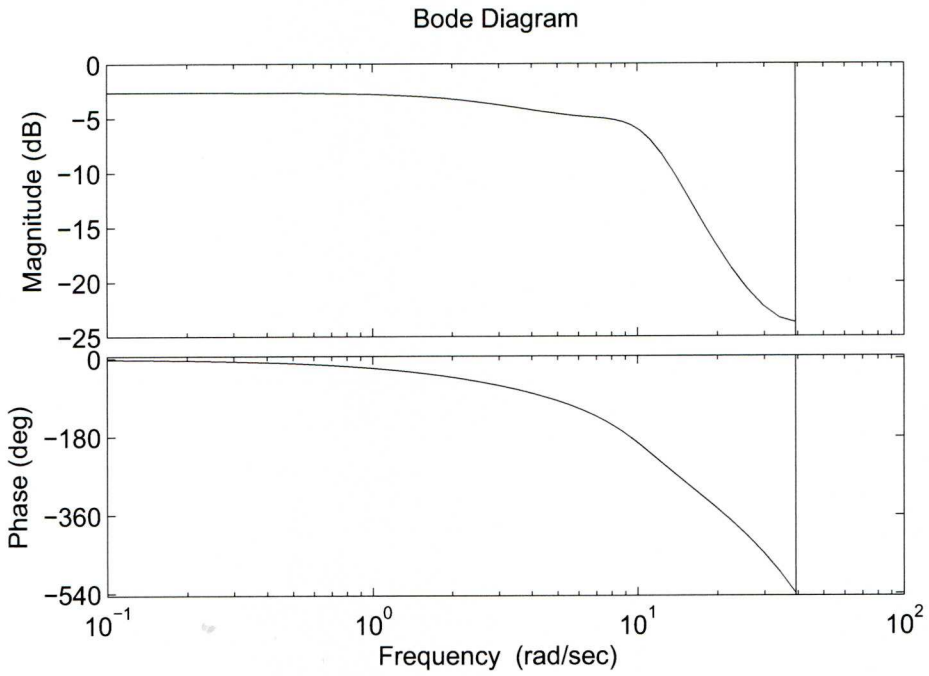

Figure 7.16: Bode Plot of the Identified ARX model

7.3.3 Loop Shaping Control

Loop shaping control techniques use closed loop objectives in terms of requirements of open loop singular values to shape the open loop system $L = GK$ where K is the controller. The nominal plant singular values give desired open loop properties at frequencies of high and low loop gain [114]. The control in loop shaping techniques can be designed for performance, robustness or a trade off of both to achieve robust performance. Typical design trade offs are [113]:

- For stability robustness: $|L(j\omega)| < 1$. The target loop should have low gain (as small as possible) at high frequencies where typically the plant model is poor.

- For performance: $|L(j\omega)| > 1$. The target loop should have high gain (as great as possible) at frequencies where the model is good, in order to ensure good control accuracy and good disturbance attenuation.

- Crossover and Roll-Off: The desired loop shape should have its 0 dB crossover frequency between the above two frequency ranges. Below the crossover frequency ω_c the loop should roll off with a negative slope of between -20 and -40 dB/decade, which helps to keep phase lag to less than $-180°$ inside the control loop bandwidth ($0 < \omega < \omega_c$).

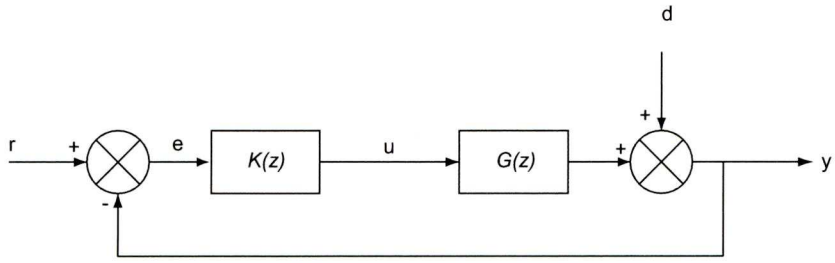

Figure 7.17: Multivariable Feedback Control System

The singular values of the open loop transfer function matrix L are important because L determines the closed loop matrices S and T. Closed loop transfer functions, S (the sensitivity transfer function) and T (the complimentary sensitivity transfer function) are defined as:

The transfer function of an exogenous input r to tracking error e is:

$$S = \frac{1}{(1+GK)} = \frac{1}{(1+L)} \tag{7.4}$$

The transfer function of an exogenous input r to output y is:

$$T = \frac{GK}{(1+GK)} = \frac{L}{(1+L)} \tag{7.5}$$

The singular values of $S(j\omega)$ determine the disturbance attenuation, because $S(s)$ is in fact the closed-loop transfer function from disturbance to plant output as seen in fig. 7.17. Thus a disturbance attenuation performance specification can be written as:

$$\bar{\sigma}(S(j\omega)) \leq \left|W_1^{-1}(j\omega)\right| \tag{7.6}$$

where $\left|W_1^{-1}(j\omega)\right|$ is the desired disturbance attenuation factor.

The robustness stability design requirements can be written:

$$\bar{\sigma}(T(j\omega)) \leq \left|W_3^{-1}(j\omega)\right| \tag{7.7}$$

where $\left|W_3^{-1}(j\omega)\right|$ largest anticipated multiplicative plant perturbation. In essence, $|W_1(j\omega)|$ and $\left|W_3^{-1}(j\omega)\right|$ describe the performance and robustness bounds respectively and loop shaping synthesis can be undertaken, in practice, by describing these boundaries, though it is also acceptable to describe the open loop shape based on knowledge of the system. From the open loop shape, the singular values $\frac{1}{\bar{\sigma}(S)}$ and $\bar{\sigma}(T)$ of the closed loop transfer function matrices S and T can be calculated.

For the identified ARX model in equation 7.3, the required control loop should possess the following properties:

- The control loop should be rapid, with minimum overshoot.
- Control effort or action should be realistic.
- For stability robustness: $|L(j\omega)| < 1$. The target loop should have low gain at higher frequencies above 10 rad/sec.
- For performance: $|L(j\omega)| > 1$. The target loop should have high gain at lower frequencies below 1 rad/sec.
- Crossover and Roll-Off. The desired loop shape should have its 0 dB crossover frequency, (ω_c), between the above two frequency ranges, 1 rad/sec $< \omega_c >$ 10 rad/sec. Below ω_c the loop should roll off with a negative slope of between -20 and -40 dB/decade.

The open loop shape chosen, $G_d(z)$, is discrete since the identified ARX model 7.3 is discrete. Converting to a continuous sampled model introduces phase changes and the model becomes non-minimum phase. This arises since the discrete model has inherent pure time delays shown as two orders of poles greater than zeros. The loop shape is iteratively chosen, based on the above restrictions.

$$G_d(z) = \frac{0.1z + 0.05}{z - 1} \tag{7.8}$$

This desired loopshape is displayed graphically in fig. 7.18. The desired crossover frequency, ω_c, occurs at $10^{0.087}$ rad/sec. The accuracy that can be achieved is represented by $\gamma = +/- 1.6914$ where 1 would be a perfect fit. This translates to 4.5649 db accuracy. The achieved loopshape, L, is also plotted.

Figure 7.19 displays the performance and robustness from the singular values of the closed loop transfer function .

The loop shape controller is generated in MATLAB software [113] with the LOOPSYN command using the desired open loop shape in equation 7.8. This initially generates an 8^{th} order controller. Using MATLAB controller model reduction techniques in the same toolbox, this model order will be reduced to simplify the controller without any degradation in performance.

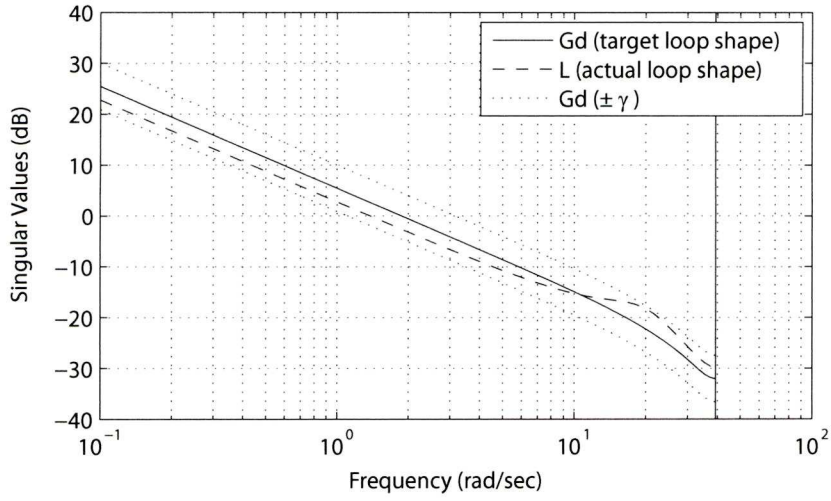

Figure 7.18: Frequency Response of the Target Loop Shape $G_d(z)$

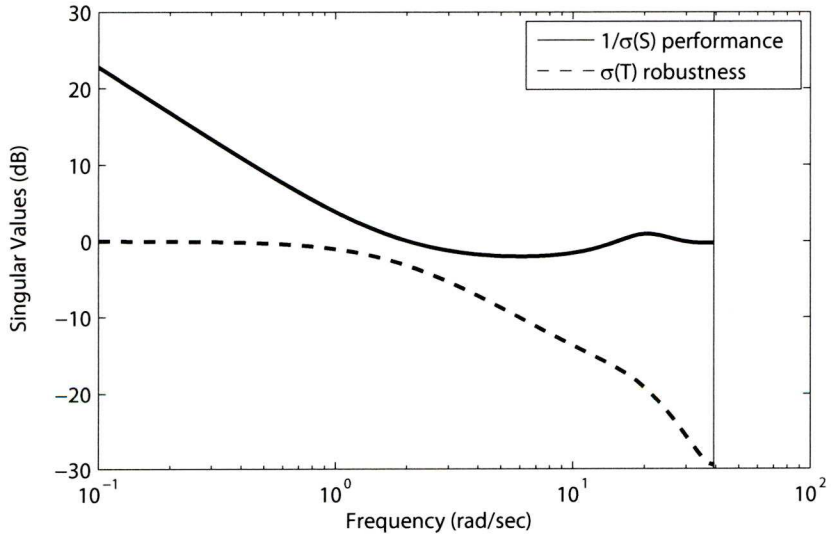

Figure 7.19: Performance and Robustness of the Closed Loop System $G_d(z)$

7.3.4 Controller Model Reduction

From plotting the Hankel singular values of the controller, fig. 7.20, it can be seen that the 8^{th} order contributes relatively less than the first 7 orders, therefore this order can be removed to create a 7^{th} order controller.

When the controller is implemented, a constant of 1 will be removed from the λ signal because the controller was designed for a zero mean ARX model. The output of the controller will have a constant of 1 added back on so that the input to the feed-forward NN represents

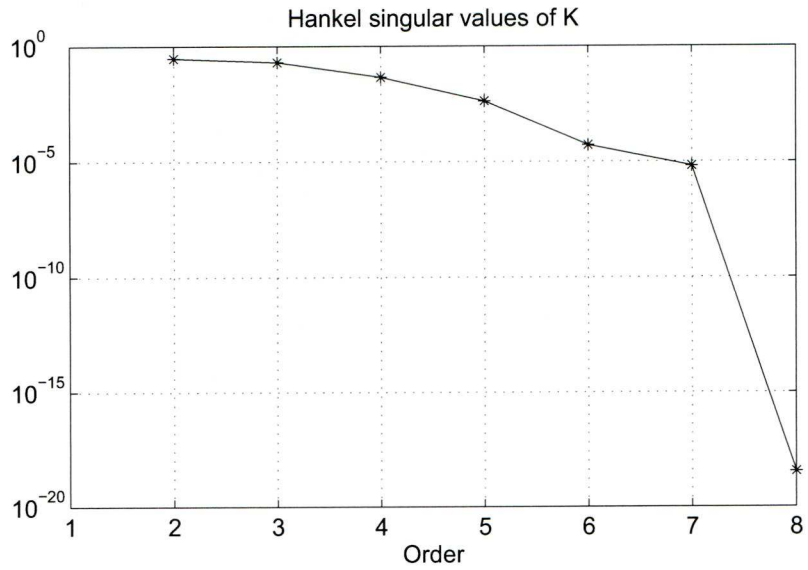

Figure 7.20: Hankel Singular Values of the Controller

a non zero mean λ_D.

The reduced acquired controller can be displayed in the following transfer function:

$$K =$$

$$\frac{0.636z^7 - 0.7597z^6 + 0.2062z^5 + 0.1551z^4 - 0.1093z^3 + 0.001459z^2 - 3.23 \times 10^6 z - 0.0004337}{z^7 - 1.2z^6 + 0.3502z^5 - 0.1846z^4 - 0.009157z^3 + 0.04383z^2 + 7.314 \times 10^{-15} z - 5.415 \times 10^{-15}}$$

7.3.5 UEGO Feedback fuelling Results

Again, to demonstrate the ability of the NN fuelling control with incorporated UEGO signal feedback, it was implemented on to the engine/dynamometer. Engine variables (load and ABV ranges) were brought in line with the ranges used for identification data acquisition and these were step-changed individually, along with λ_D, to illustrate robustness of the network at keeping λ close to λ_D.

The resulting measured λ signal and the step changed input signal λ_D is presented in fig. 7.21. Now the feedback from the UEGO signal is incorporated, the system is able to output more accurate levels of λ to follow λ_D as opposed to the feed-forward controller implemented without feedback in fig. 7.10 where by the DC bias levels of λ could not achieve accuracy at $\lambda_D = 0.9$ or $\lambda_D = 1.1$.

The resulting measured λ signal and the step changed input signals, ABV (and thus N) are presented in fig. 7.22. Step changes in load (and thus integrated MAP), the resulting

FPW and the resulting measured λ signal are presented in 7.23. It should be noted that the feedback control system is able to restrict the measured λ signal to within 0.05 of λ_D across all transient step changes.

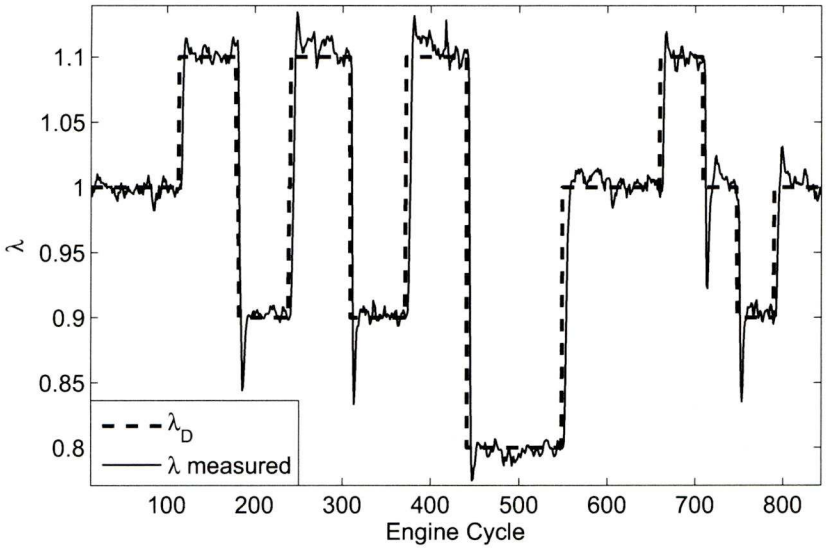

Figure 7.21: Comparison of λ_D and measured λ

Although adequate in accuracy and performance, the feedback controller using the measured λ signal from the UEGO sensor has a significant disadvantage. The placement of the UEGO sensor for this demonstration is near to the exhaust port of the cylinder giving rapid λ response from limited transfer delays. In production vehicles the UEGO sensor is fitted further downstream of the exhaust, usually at the confluence point of the exhaust gases from all cylinders. This would lead to even longer transport delays of the exhaust gases from exhaust port to sensor and ultimately give a slower control response. Figure 7.24 shows the a single λ step response compared to the step demand, λ_D taken from the same data to produce fig. 7.21. 3 delays are clearly present.

7.4 Feedback Control using the Ion Current

The ability to determine and control the AFR without the use of a UEGO sensor for an individual cylinder would be desirable due to cost. The traditional location of the UEGO sensor at the exhaust stream confluence point introduces transport delays into the AFR measurement inherently. In the previous section, these exhaust gas delays were minimised due to the UEGO sensor being located close to the exhaust post. Measuring the AFR during the current combustion event and using this determined value for a feedback signal would remove inherent delays from when using a UEGO sensor for the feedback signal.

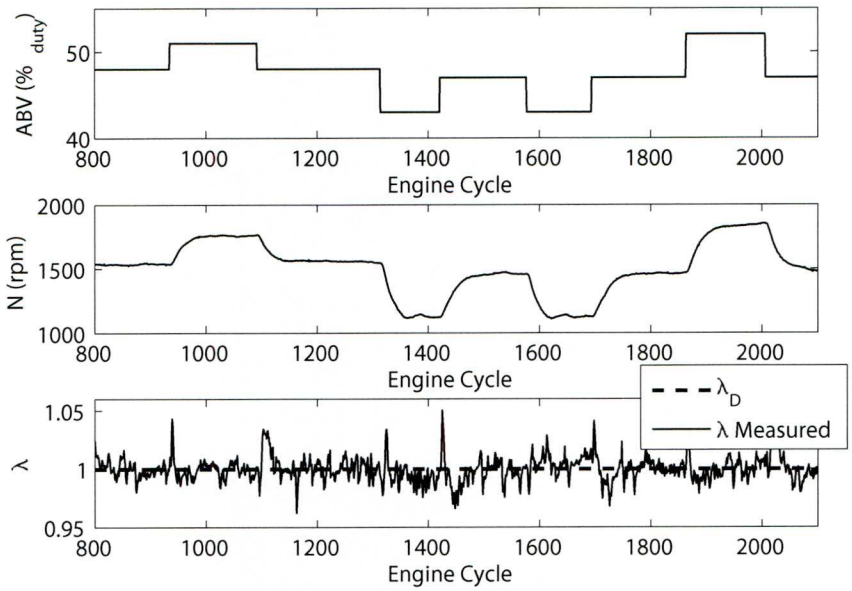

Figure 7.22: Validation Data Showing Measured λ with Step Changes in Speed

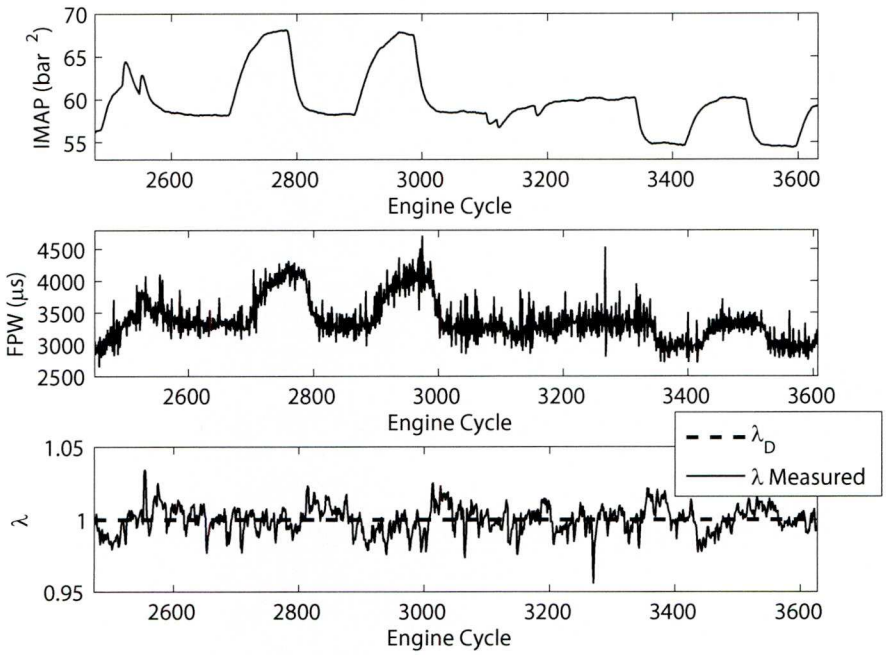

Figure 7.23: Validation Data Showing Measured λ with Step Changes in Load

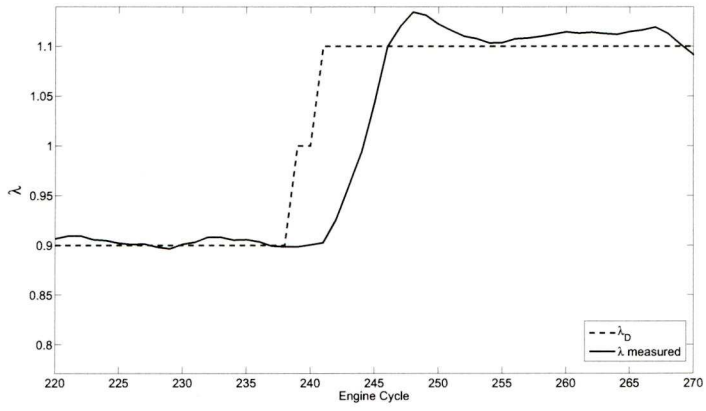

Figure 7.24: Step response comparison of λ_D and measured λ

The ion current sensing method provides the solution. The $\hat{\lambda}$ ratio can be determined from the ion current signal which occurs during the combustion stroke. A feed-forward fuelling controller was developed previously in this section and feedback control applied with the use of the UEGO sensor signal. In this current section, measured λ from the UEGO sensor is substituted for an estimated $\hat{\lambda}$, which is an output from a NN similar to chapter 6. The accuracy achieved with the UEGO feedback system in the previous section is a benchmark for the accuracy aimed to be achieved with the ionization current feedback system.

Because two neural networks are incorporated into this system they shall be denoted as follows: 'Λ NN' describes the feed-forward NN for estimating the FPW and 'NARX NN' refers to the recurrent NN used to estimate λ. Figure 7.25 illustrates the system concept using the feed-forward NN controller, Λ NN, to predict the fuel necessary to give $\lambda = 1$ at the output of the plant G, the NARX NN used to estimate λ and a loop shaping feedback control, K. This is fundamentally the same concept as when using the UEGO sensor signal as feedback but the UEGO feedback signal is replaced with an estimated lambda signal, $\hat{\lambda}$.

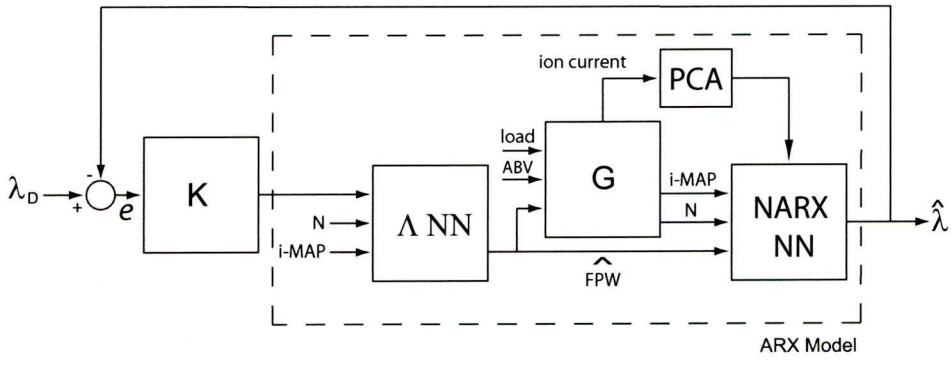

Figure 7.25: Ion Current NN Signal Feedback Incorporated into the feed-forward Control

7.4.1 Engine Signals for Identification

To produce Λ NN and NARX NN, the same identification data set is used; Λ NN uses an inverse identification to achieve FPW estimation. The dataset that was collected in section 7.2.2 is used again and although there are different delays in the system, the inverse procedure results in the same feed-forward compensator. Measured λ is recorded so that Λ NN can be initially created, before being substituted for estimated $\hat{\lambda}$.

Inverse of the Identification Data for Λ NN

As before for FPW estimation, we require model input signals to be N, integrated MAP and λ; the model output signal is FPW. This would create an inverted MISO system from the obtained identification data. The delays present in the data now using the ionization current method instead of the UEGO signal are estimated to be lower between the input and output signals; This is because the UEGO sensor is placed in the exhaust port of the cylinder, whilst the ionization current is measured during combustion. In this manner, one delay can be removed from the input signals to the output signal; The FPW has an effect on the combustion after one discrete delay (combustions cycles), whilst the effects of the speed, N, and the integrated MAP occur during the present combustion cycle. It should be remembered that N and integrated MAP result from the actuation of ABV and load.

In order to invert this data for FPW estimation, these delays should be taken into account to produce causal identification data. This would involve 'shifting' of datasets by a number of combustion cycles to synchronise inputs to outputs.

The diagram in fig. 7.26 illustrates the inherent delays in the identification data and the procedure for inverting the data for FPW identification with the ionization current method. 7.26a shows the system in the original non-inverted state, where by N, integrated MAP and FPW were used as input signals to the plant G to obtain an estimated λ signal from the NARX NN. There is 1 measured combustion cycle or time delay between a change in the FPW and a measured influence at the ionization current sensing spark plug. There is no delay between a change in N or the integrated MAP before being experienced at the ionization current sensing spark plug. This implies that the combustion occurring at any instant is affected by or will affect the engine speed N and the integrated MAP during that specific combustion cycle.

To invert this system to predict FPW and use estimated λ as an effective input, estimated λ and FPW are switched with the time delays between all signals remaining intact, as per fig. 7.26b. Again, This figure is not physically realiseable; FPW is now predicted 1 sample delay as an output before the new input λ_D and this is not causal. There is still 1 time delay between FPW and the other existing inputs ,N and integrated MAP, but again, not in

a causal manner.

7.26c displays the system that has been made causal; the input data has been shifted by the required 1 time delay to create the correct inverse model Λ. Again, there are no time delays between the used λ input signal and the other two inputs, N and integrated MAP.

Using this inverse identification data Λ NN is created to predict the FPW necessary for stoichiometry. The network structure of Λ NN is the same as in section 7.2.4 and trained in the same manner using 3000 cycles of the inverted data; 1000 cycles for estimation, 1000 cycles for training and 1000 cycles for a hold out dataset.

Figure 7.27 displays the fit of the estimated FPW as an output of Λ NN with the measured FPW training target data.

To quantify the accuracy of Λ NN predictions on the hold-out dataset R^2 is used:

$$R^2 = 1 - \frac{\sigma_\epsilon^2}{\sigma_y^2}$$

where σ_ϵ^2 indicates the variance of the model residuals and σ_y^2 is the variance of the system output. For the 1000 cycles of hold-out data it was found that

$$R^2 \;=\; 0.7938\;,$$

indicating that just under 80% of the variance in the FPW is explained by the estimated FPW from the Λ NN output.

Manipulation of Identification Data for NARX NN

As in chapter 6 a NN model is trained for estimating $\hat{\lambda}$. In this section, the prediction of $\hat{\lambda}$ is required 1 discrete sample time before λ is measured with a UEGO signal. This is because $\hat{\lambda}$ is estimated using ionization current information measured during the combustion process whereas λ is measured using the UEGO sensor located in the exhaust port.

To train the NARX NN to account for this removed sample time, the identification data has to be manipulated. The identification data to train the NARX NN consists of 9 inputs per combustion cycle: 6 PCA scores, integrated MAP, N and FPW. The output or target data set is λ.

This whole measured λ output dataset is shifted by one discrete sample (one combustion cycle) backwards in time. This results in a training set whereby the NARX NN is trained to 'see' the UEGO λ signal one discrete sample period before it was actually measured. Hence, when implemented, the trained NARX NN output will be an estimated $\hat{\lambda}$ occurring one discrete sample time before the measured λ used for comparison. 3000 cycles of the

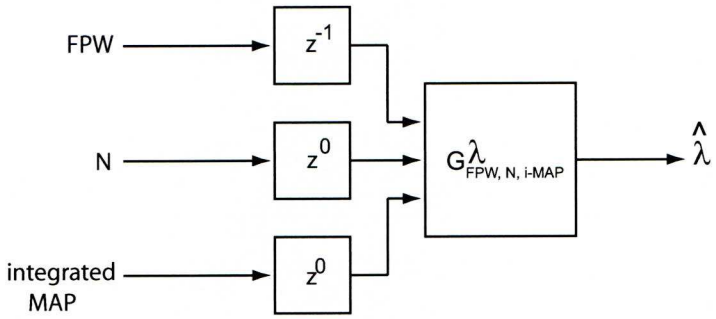

a) Forward Identification Data Illustrating Present Delays Using Ionization Current Method

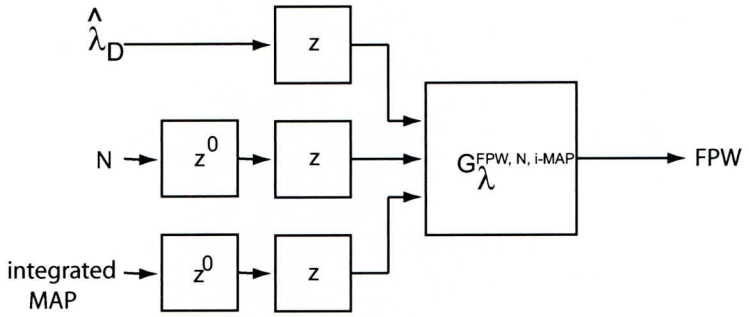

b) Inverted Identification Data (Partial Inverse Model)

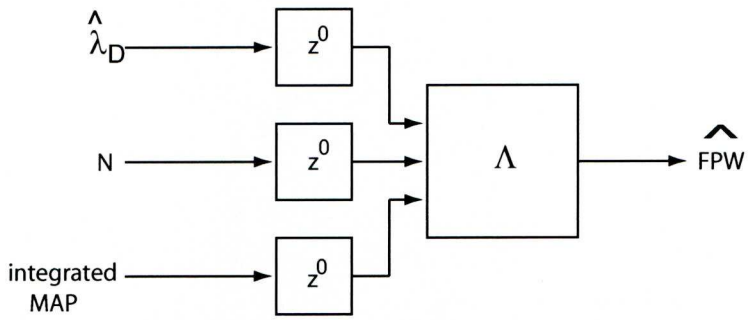

c) Inverted Identification Data with Synchronised Data (Inverse Model)

Figure 7.26: Inverting the Identification data with Delays using the Ionization Current

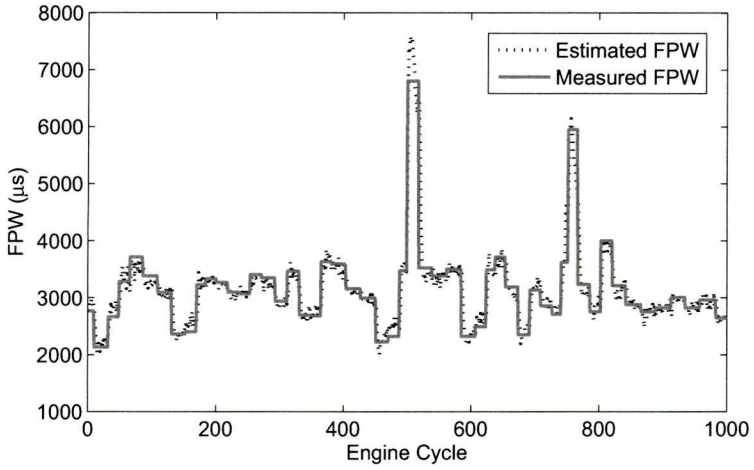

Figure 7.27: Estimated FPW as an output of Λ NN

manipulated training dataset are used; 1000 cycles for estimation, 1000 cycles for validation and 1000 cycles as a hold-out dataset.

The plot 7.28 shows the use of a holdout dataset implemented offline that shows the NARX NN output prediction of $\hat{\lambda}$ compared to the measured λ UEGO signal output. The holdout dataset is a 500 combustion cycle portion of that collected in section 7.2.2 and used to train both Λ NN and NARX NN.

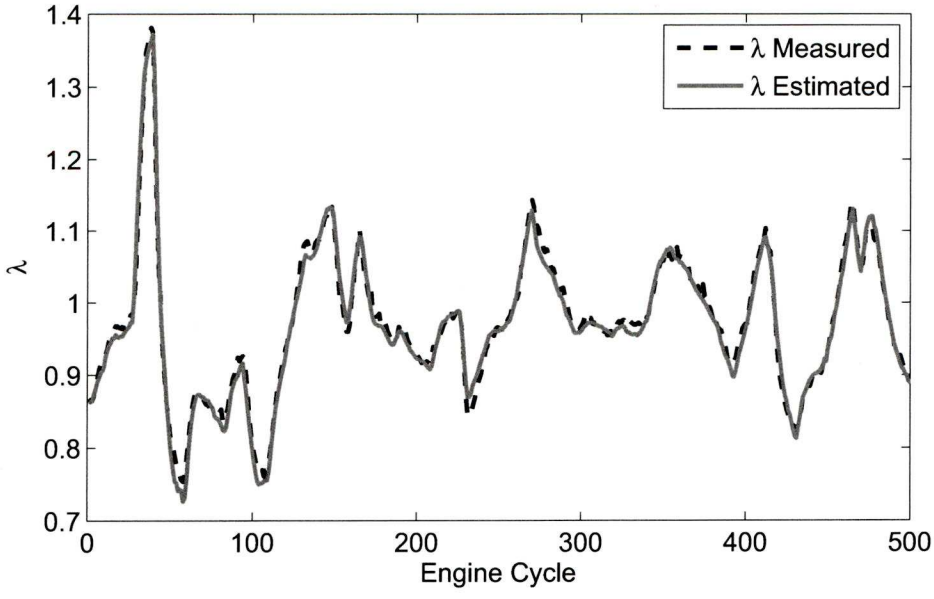

Figure 7.28: NARX NN output prediction of $\hat{\lambda}$ compared to the measured λ UEGO signal output with a holdout dataset

To quantify the accuracy of the NARX NN predictions on the hold-out dataset R^2, is

Table 7.4: Used Signals for Identification

Signal	Range	Perturbation Period
λ_D	0.8 to 1.2	2 seconds
ABV [$\%_{duty}$]	45	N/A
Load [V]	−0.05	N/A

used again. For the 1000 cycles of hold-out data it was found that

$$R^2 = 0.9328 ,$$

indicating that just over 90% of the variance in the FPW is explained by the estimated FPW from the Λ NN output.

7.4.2 Creating the ARX model around both Neural Networks

An ARX identification is done that defines the relationship between the desired lambda input signal, λ_D, and the estimated lambda output signal, $\hat{\lambda}$, encompassing the dashed box in fig. 7.25. In this manner the identified ARX model will give a relationship between λ_D and $\hat{\lambda}$, but the system will still be able to account for changes in load and speed for correct fuelling due to the 'interior' feed-forward NN. The signals used to generate the ARX model are as table 7.4. Load and ABV were set at a steady state mid point of the NN identification.

Input and output data is collected over 3000 combustion cycles from the engine/dynamometer set-up, downsampled at only one sample per combustion cycle. Figure 7.29 shows 1000 cycles of identification data used to obtain the ARX model of λ_D to $\hat{\lambda}$. Measured λ from the UEGO sensor is also illustrated in this plot to show the accuracy of the NARX NN at estimating λ. The NARX NN output,$\hat{\lambda}$, and the measured UEGO signal, λ, do not match λ_D at the extremes of the traversed range since these outputs are still results of a feed-forward Λ NN with no feedback.

7.4.3 Obtained ARX Model

In section 7.3.2, the ARX model was chosen to represent the 3 time delays. This was due to the use of the UEGO sensor that inherently introduced time delays. Because the system is now being identified to the NARX NN output, instead of the UEGO sensor output, 2 is chosen as the time delay, n_k, for the chosen structure; 1 delay from the NARX NN and 1 delay from the feed-forward Λ NN.

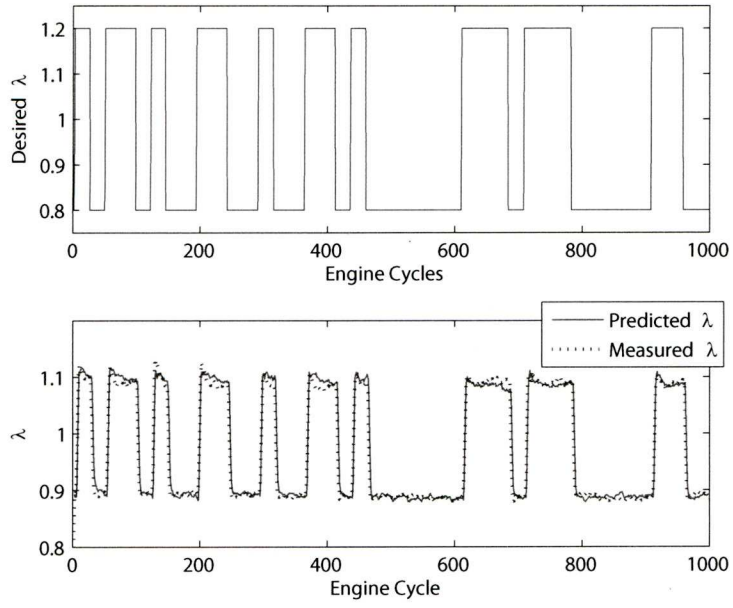

Figure 7.29: λ_D and measured λ used for Identification

The following ARX model is identified:

$$y(z) = \frac{0.1322z - 0.006031}{z^3 - 1.148z^2 + 0.3796z - 0.02613}u(z) + e(z) \tag{7.9}$$

A pole-zero plot 7.30 of the ARX model shows the stability, whilst magnitude and phase of the frequency response is shown in a bode plot 7.31. Using this information, loop shaping control can be implemented in the feedback loop.

7.4.4 Loop Shaping Control using the Ion Current

As before loop shaping is chosen as an appropriate form of control. The open loop shape chosen, $G_d(z)$, is discrete since the identified ARX model 7.9 is discrete. Converting to a continuous sampled model introduces phase changes and the model becomes non-minimum phase. This arises since the discrete model has inherent pure time delays shown as two orders of poles greater than zeros. The loop shape is iteratively chosen as before based on the below restrictions:

- The control loop should be rapid, with minimum overshoot.
- Control effort or action should be realistic.
- For stability robustness: $|L(j\omega)| < 1$. The target loop should have low gain at higher frequencies above 10 rad/sec.

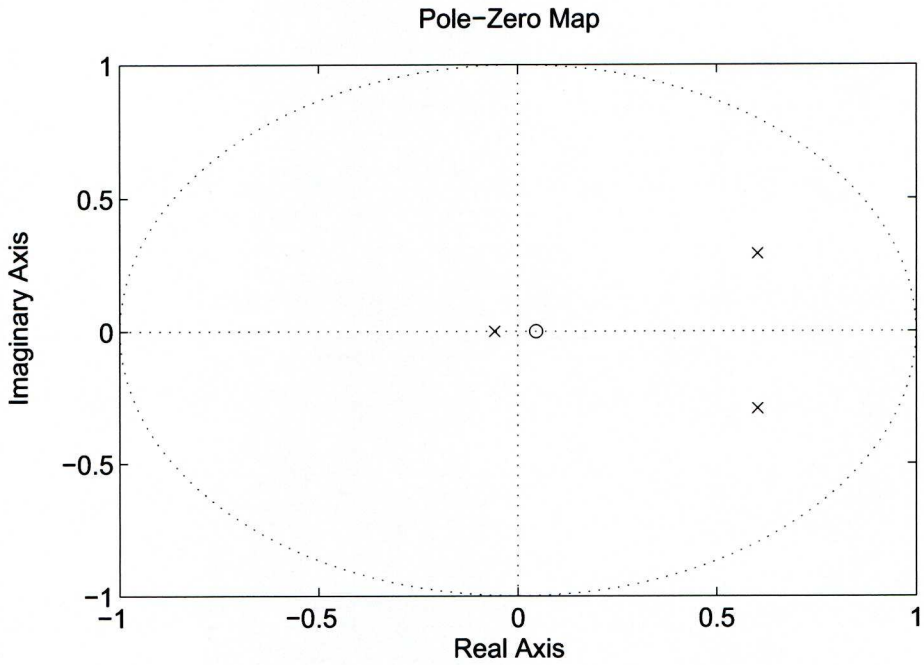

Figure 7.30: Pole-Zero Plot of the Identified ARX model

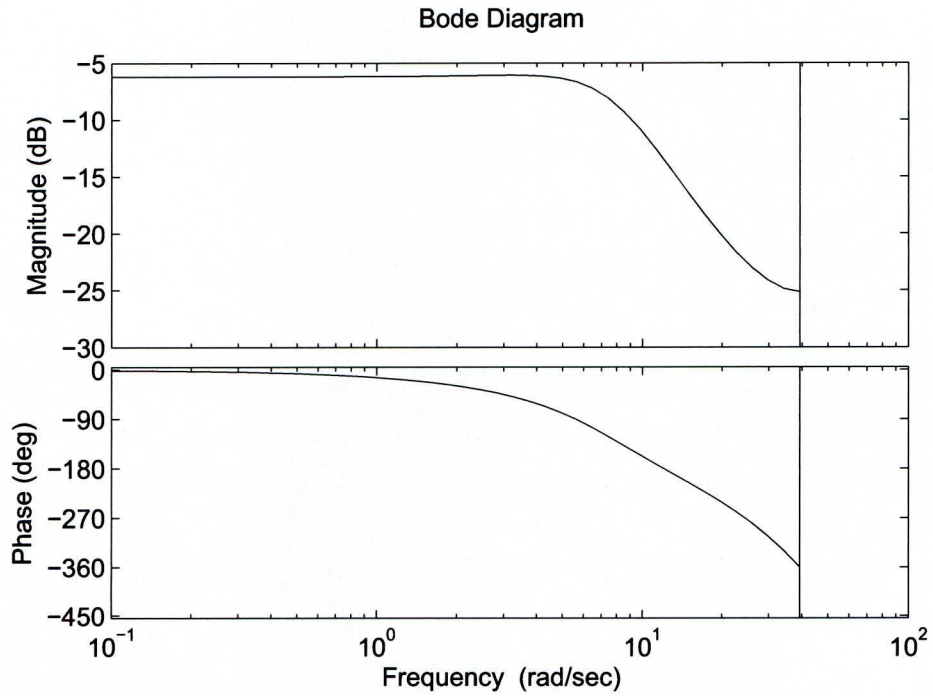

Figure 7.31: Bode Plot of the Identified ARX model

- For performance: $|L(j\omega)| > 1$. The target loop should have high gain at lower frequencies below 1 rad/sec.
- Crossover and Roll-Off. The desired loop shape should have its 0 dB crossover frequency, (ω_c), between the above two frequency ranges, 1 rad/sec $< \omega_c >$ 10 rad/sec. Below ω_c the loop should roll off with a negative slope of between -20 and -40 dB/decade.

An identical controller could have been used to that in section 7.3.3. Faster performance was attempted which lead to an open loop shape of:

$$G_d(z) = \frac{0.25z + 0.10}{z - 1} \tag{7.10}$$

This is displayed graphically in fig. 7.32. The crossover frequency, ω_c, occurs at $10^{0.64}$ rad/sec. The accuracy that can be achieved is represented by $\gamma = +/-1.8256$ where 1 would be a perfect fit. This translates to 5.2281 db accuracy. The achieved loopshape, L, is also plotted.

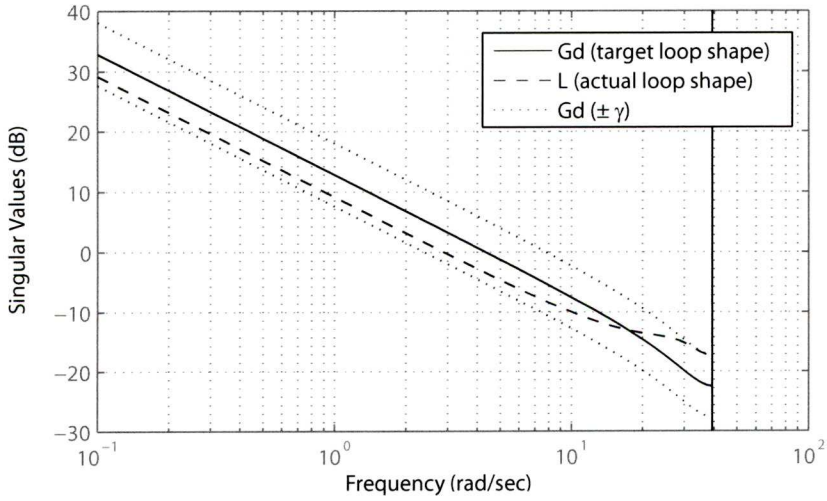

Figure 7.32: Frequency Response of the Target Loop Shape $G_d(z)$

Figure 7.33 displays the performance and robustness from the singular values of the closed loop transfer function .

Again, the loop shape controller is generated in MATLAB software [113] with the LOOPSYN command using the desired open loop shape in equation 7.10. This initially generates an 6^{th} order controller. Using MATLAB controller model reduction techniques in the same toolbox, this model order will be reduced to simplify the controller without any degradation in performance.

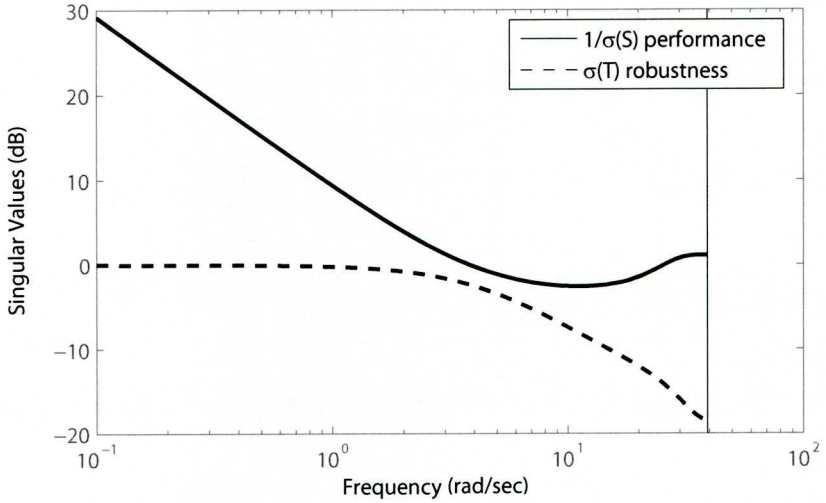

Figure 7.33: Performance and Robustness of the Closed Loop System $G_d(z)$

7.4.5 Controller Model Reduction

From plotting the Hankel singular values of the controller, fig. 7.34 it can be seen that the 5^{th} and 6^{th} orders contribute relatively less than the first 4 orders, therefore this order can be removed to create a 4^{th} order controller.

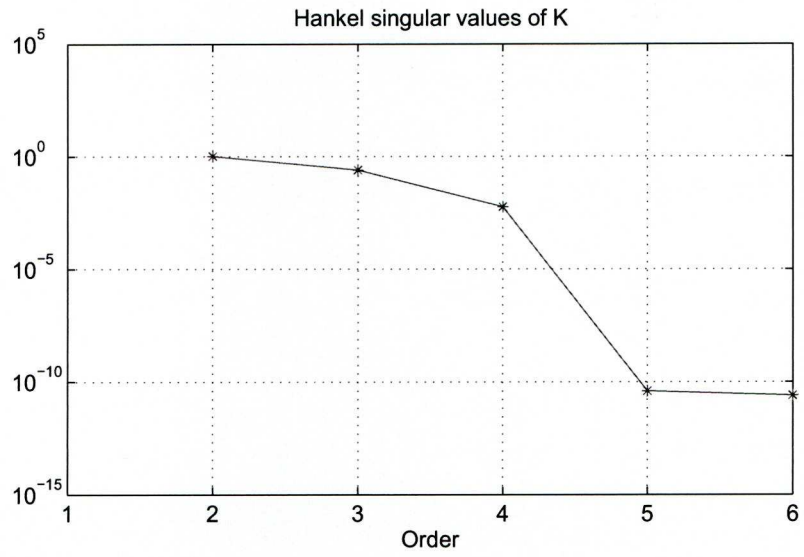

Figure 7.34: Hankel Singular Values of the Controller

The reduced acquired controller can be displayed in the following transfer function:

$$K =$$

$$\frac{2.105z^4 - 1.575z^3 - 0.1678z^2 + 0.3746z + 0.022}{z^4 - 0.5033z^3 - 0.3642z^2 - 0.1397z + 0.007178}$$

Again, when implemented, a constant of 1 will be removed from the $\hat{\lambda}$ signal because the controller was designed for a zero mean ARX model. The output of the controller will have a constant of 1 added back on so that the input to the feed-forward NN represents a non zero mean λ_D.

7.4.6 Ion Current Feedback fuelling Results

Again, to demonstrate the ability of the NN fuelling control with incorporated $\hat{\lambda}$ signal feedback, it was implemented on to the engine/dynamometer. Engine variables (load and ABV ranges) were brought in line with the ranges used for identification data acquisition and these were step-changed individually, along with λ_D, to illustrate robustness of the network at keeping $\hat{\lambda}$ and λ close to λ_D.

The resulting measured λ signal and the step changed input signal λ_D is presented in fig. 7.35.

The $\hat{\lambda}$ feedback signal from the NARX NN is incorporated and the system is able to output acceptable levels of λ to follow λ_D as opposed to when no feedback was incorporated as shown in fig. 7.10 where the DC bias levels of λ could not achieve accuracy at $\lambda_D = 0.9$ or $\lambda_D = 1.1$.

The resulting measured λ signal and the step changed input signals, ABV (and thus N) are presented in fig. 7.36. Step changes in load (and thus integrated MAP), the resulting FPW and the resulting measured λ signal are presented in fig. 7.37.

It should be noted that the feedback control system is able to restrict the measured λ signal to within 0.05 of λ_D across all transient step changes, which is comparable to the UEGO feedback results in section 7.3.5, but the ionization current method delivers a faster response due to the removal of a delay of a single combustion cycle .

Three fuelling techniques have been created:

1. Pure feed-forward with no feedback.
2. Feed-forward with UEGO signal used for feedback
3. Feed-forward with a predicted λ signal using the ionization current technique used for feedback

The three techniques were tested under identical disturbance tests in speed and load.

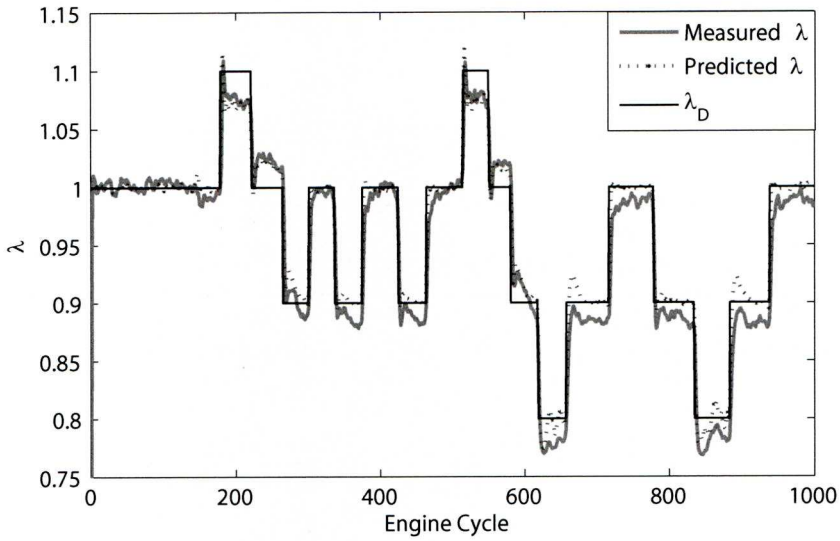

Figure 7.35: Comparison of λ_D and measured λ

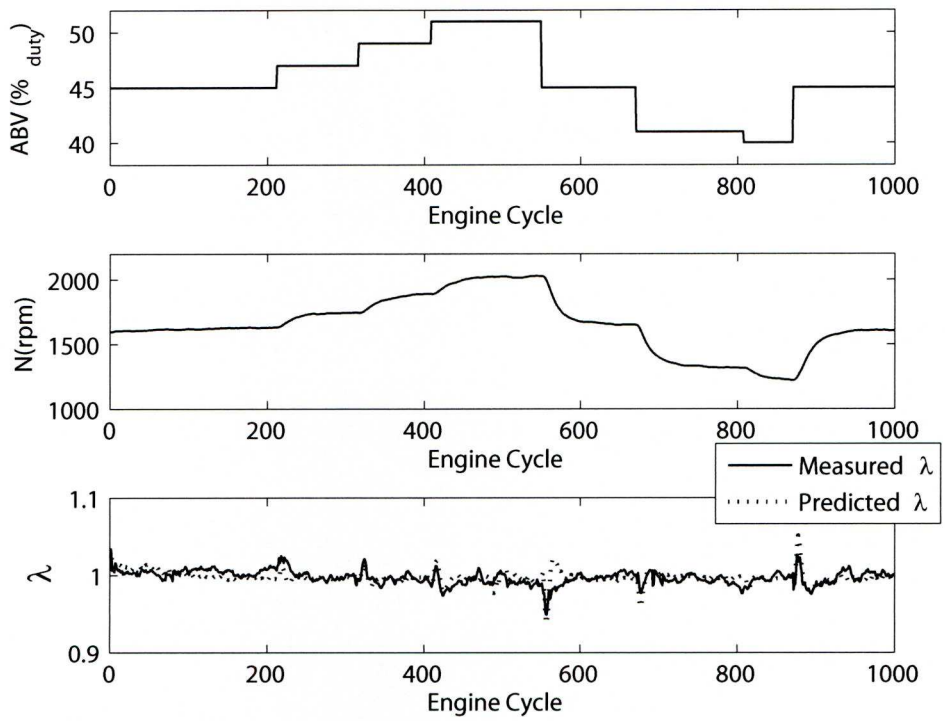

Figure 7.36: Validation Data Showing Measured λ with Step Changes in Speed

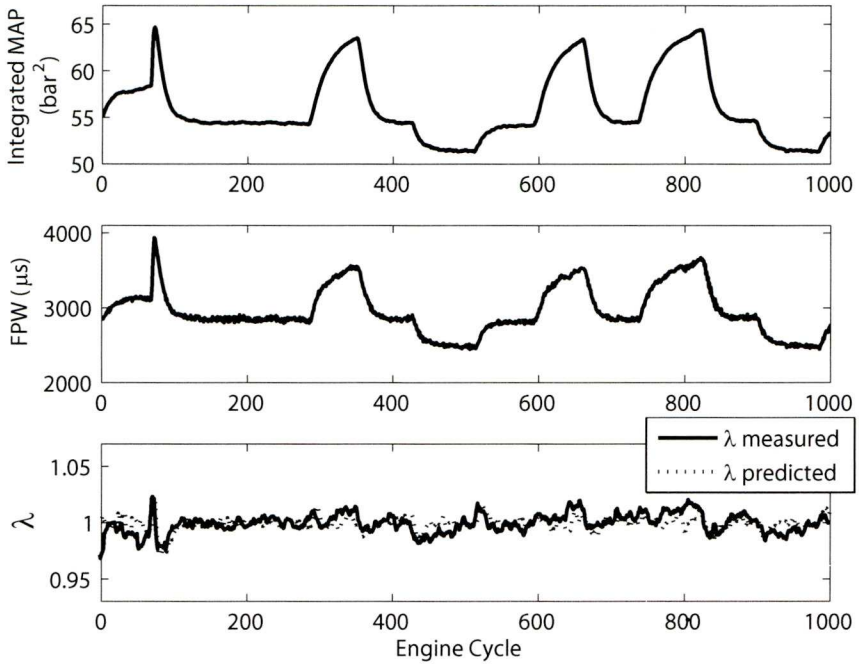

Figure 7.37: Validation Data Showing Measured λ with Step Changes in Load

Firstly engine signals were taken to average values and ABV was step changed to provide a disturbance in speed. This identical test was executed once for each of the three techniques and the responses have been overlayed and plotted in fig. 7.38.

Secondly engine signals were taken to average values and the load was step changed to provide a disturbance in integrated MAP and speed. This identical test was executed once for each of the three techniques and the responses have been overlayed and plotted in fig. 7.39.

The response of the resulting λ signal for all three techniques is of interest in these plots. Only one plot of ABV is required to be shown since the step is identical for all three technique tests. The UEGO feedback technique and the ionization current technique display comparable performance. The response in λ of the ionization technique during the ABV step test does appear to occur before the UEGO feedback technique response. The ability to reject the disturbance in magnitude of deviation from stoichiometry by the UEGO and ionization feedback techniques can be seen to be similar.

Similarly for the load step test response, three integrated MAP signals from each technique response test are plotted since integrated MAP is a signal that results from a load step, and would not be absolutely identical for each test. Again, The UEGO feedback technique and the ionization current technique display comparable performance. The response in λ of

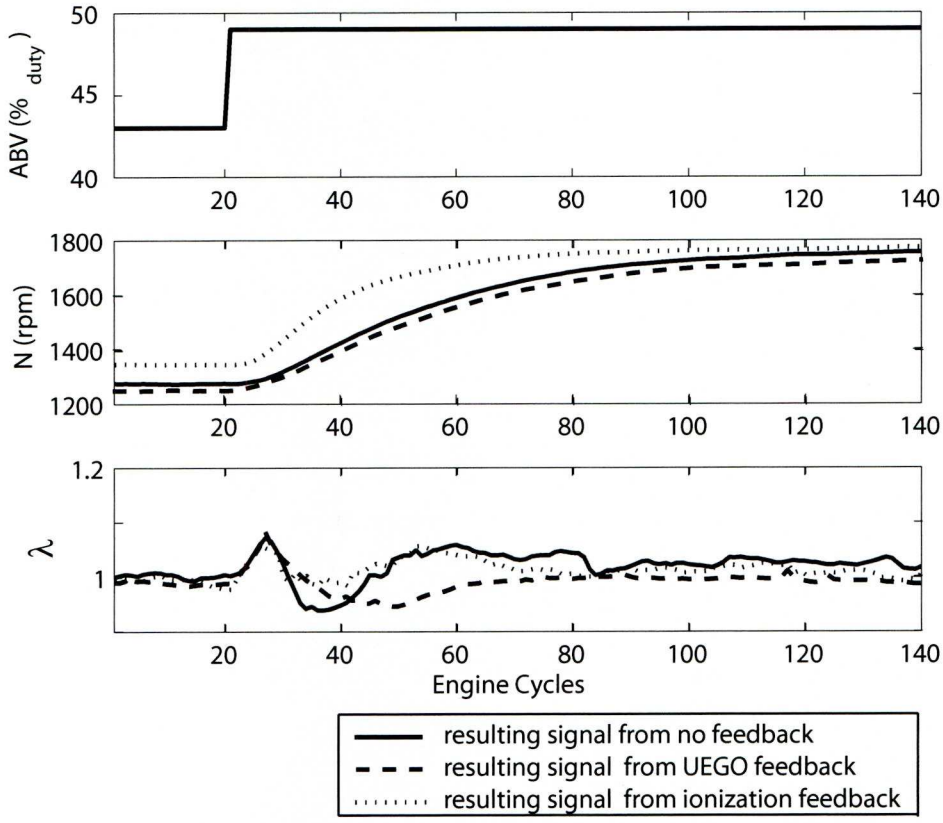

Figure 7.38: All Three Techniques Showing a Response to an ABV Step Demand

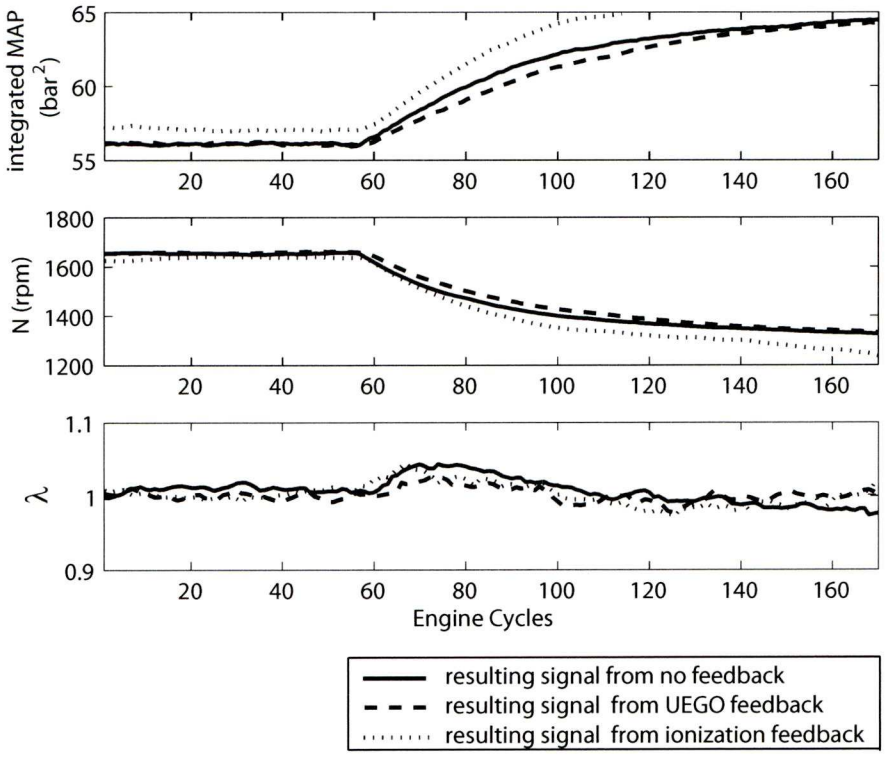

Figure 7.39: All Three Techniques Showing a Response to a Load Step Demand

the ionization technique during the load step test does appear to occur before the UEGO feedback technique response. Again, the ability to reject the disturbance in magnitude of deviation from stoichiometry by the UEGO and ionization feedback techniques can be seen to be similar. Interestingly, the pure feed-forward controller displays adequate disturbance rejection from stoichiometry in this plot but it should be noted that at the extremes of the speed identification range ($1000rpm$ or $2000rpm$), the resulting λ from the feed-forward controller deviates from stoichiometry by an unacceptable amount (> 0.1 from stoichiometry).

7.5 HEGO Incorporation

The preceding work has the disadvantage that atmospheric conditions affect the ionization in the cylinder causing a DC bias offset of the NARX NN output, λ. To overcome this problem elegantly, a correctional factor for the atmospheric conditions could be incorporated to account for these changes, or an extra input related to atmospheric conditions could be used in the NARX NN, whereby any change in atmospheric conditions could be accounted for by this correctional factor or extra input and the NARX NN would predict λ correctly irrespectively. Unfortunately, this is unavailable as the equipment used in the work does not have ability to measure these atmospheric conditions.

Another approach would be the occasional recalibration of the NARX NN output, which would involve using a HEGO sensor. Justification for using this cheap sensor in addition to the ionization technique would still be the removal of the expensive UEGO sensor from the system, but still achieving a performance advantage over the more expensive UEGO system. The HEGO sensor is by nature a switching sensor around stoichiometry. It has been simulated in software at the exhaust port by using the existing UEGO signal at the exhaust port to produce a switching HEGO voltage output, i.e. a high voltage if the exhaust gas in rich of stoichiometry and a low voltage if the exhaust gas is lean of stoichiometry.

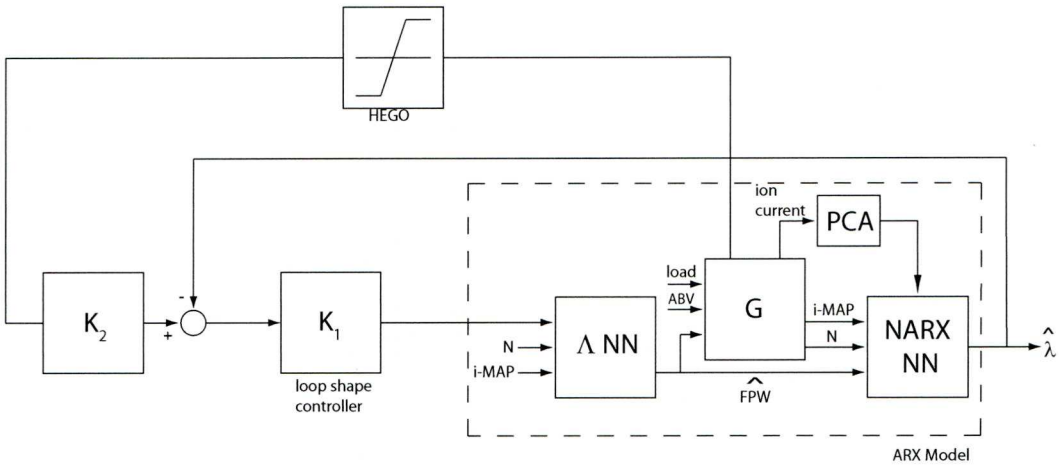

Figure 7.40: Incorporating a HEGO Sensor to Prevent Sensor Drift

Figure 7.40 illustrates this incorporation of the HEGO with a controller implemented as K_2 to ensure λ is at stoichiometry. λ_D that will now be the input to Λ NN will be fixed at stoichiometry; $\lambda_D = 1$, and K_2 would simply be a slow integral controller that calibrates the system to ensure stoichiometry is attained whilst the original ionization technique controller ensures rapid disturbance rejection.

The output of the HEGO sensor has a mean of 1 removed before being presented to the controller. K_2, as stated, is a simple integral controller, $\frac{z}{z-1}$, to track to a zero mean target with a gain that reduces the integral action. A mean of 1 is added to the controller output. In this manner, the system can track to stoichiometry regardless of atmospheric conditions whilst the fast acting controller, K_1, rejects disturbances to load and speed.

Robustness to load and speed disturbances to maintain stoichiometry are undertaken and results are displayed in figs. 7.41 and 7.42.

The figures illustrate that the ionization system performs as in section 7.4.6 and is still able to reject disturbances. The difference now is that the system is not susceptible to changes in humidity because the temporary HEGO calibration circuit ensures sensor drift is corrected.

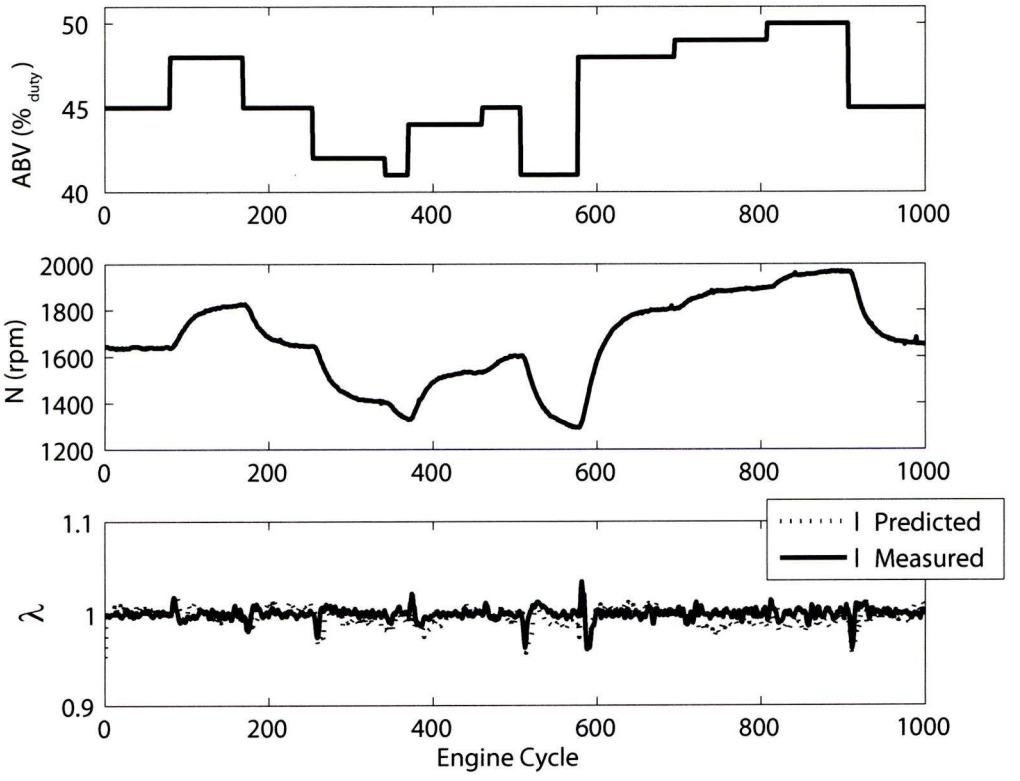

Figure 7.41: Stoichiometry Speed Disturbance Rejection with Additional HEGO Control

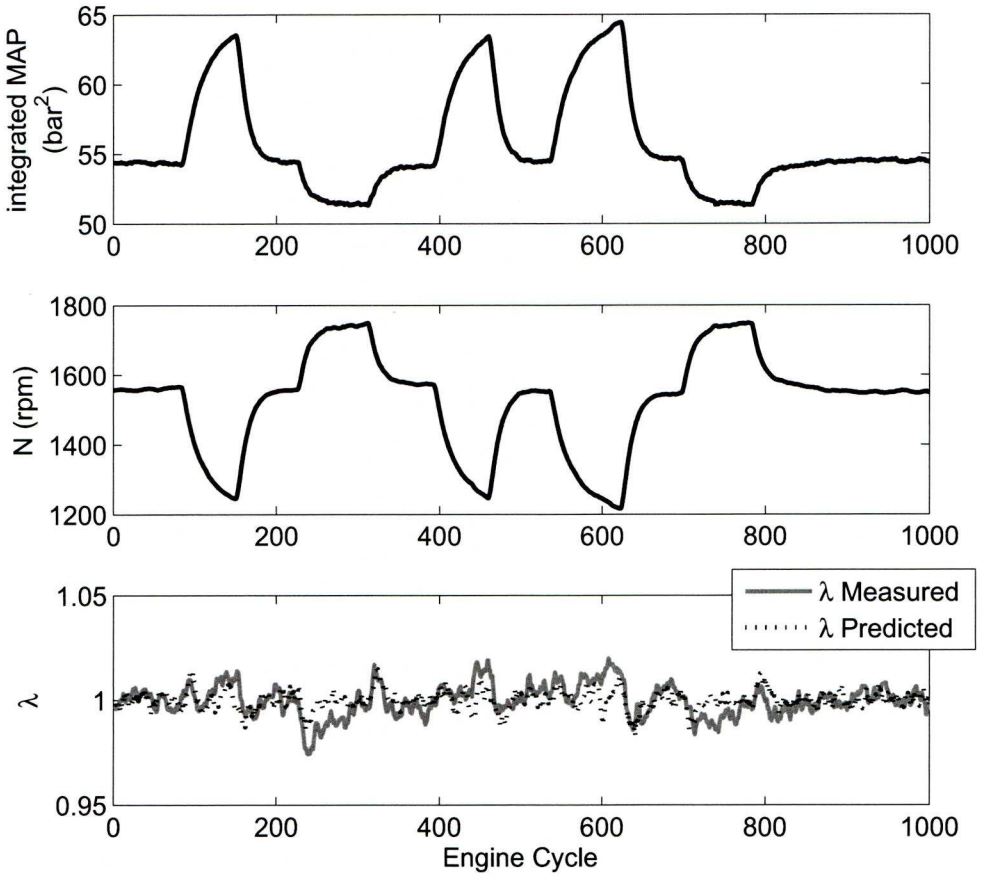

Figure 7.42: Stoichiometry Load Disturbance Rejection with Additional HEGO Control

This chapter 6 has detailed the work undertaken to control the air-fuel ratio at the exhaust of a single cylinder to a desired λ value using the ion current signal technique. This work could be expanded to encompass all four cylinders of the engine. The ion current technique would be used on each cylinder simultaneously, neural network models would be created for each cylinder and fuelling for each injector is controlled individually. This would enable the λ from each cylinder to be set individually leading to cylinder balancing in terms of air-fuel ratio. For the issue of the installation on the HEGO sensor, it would be reasonable to assume that the atmospheric conditions would affect the ionization on all four cylinders by an identical amount and therefore the HEGO calibration would be required only on a single cylinder with the calibration effect being applied to all four cylinders.

7.6 Conclusions

Firstly, a feed forward neural network was developed to provide a fuel pulse width that regulated the engine air-fuel ratio to stoichiometry. The identification signals were again generated using randomly perturbing signals to capture the dynamics of the identified system. The feed-forward controller was unable to track to a λ demand in excursions from stoichiometry and did not resist disturbances in load or ABV. This highlighted the need for feedback control which was initially done with a signal from the UEGO sensor. Loop shaping control was designed using performance criteria and the resulting feedback system was able to maintain stoichiometry during ABV and load disturbances, and also track to a desired λ ratio.

There are pure time delays inherent to the fuelling between the injector command to the response received from the UEGO sensor. During this work, the UEGO sensor was located in the exhaust manifold, close to the exhaust port and two combustion cycle delays were experienced. In production vehicles, the UEGO sensor is located at a confluence point of the exhaust manifold, further downstream, where delays of four or five combustion cycles would be experienced. Using the ionization current method, AFR information is sensed during combustion, hence the transport delays of the exhaust gas have been removed.

Building on feedback from the UEGO sensor, the ionization current was used to predict λ as an output of a neural network, and it was this signal that has been incorporated into the feedback control loop. Loop shaping was again used as control which was shown to provide similar controlled accuracy for both the UEGO output signal and ionization current method output signal, the distinct advantage of the ionization current being that time delays were removed.

Chapter 8

Conclusions and Further Recommendations

This thesis concentrates on the use of the ionization current method for use in applications for automotive control, specifically peak pressure position and air-fuel ratio.

8.1 Conclusions

In chapter 4, a technique for on-line prediction of PPP from the ionization current signal is presented. The proposed method uses a NN scheme applied to dynamically changing data output from an on-line principal-component filter. Experimental results demonstrate that the network accurately predicts the PPP measured by a piezoelectric in-cylinder pressure sensor using charge amplifiers on-line across varying operating engine parameters. A constrained-variance, robust, low control-effort method for PPP regulation and tracking with near minimum variance control is described. It is shown experimentally on an engine dynamometer that with the proposed techniques the PPP in a single cylinder of a production four-cylinder PFI gasoline engine can be accurately controlled over the range of an identified model. The experimentally implemented control system is demonstrated to be robust to step disturbances of load and speed and to successfully track to a desired PPP setting.

In chapter 5, four cylinder closed-loop feedback control of PPP has been demonstrated using an ion current technique. Estimation of PPP on each cylinder is achieved using the ion current signal and engine signals currently available to a production standard EMS. The signals are processed through NARX neural networks which are trained individually using pseudo binary random test signal data that gives network prediction accuracy, not only in steady state but across transient ranges. An ARMAX model is identified around the neural network as a SA to PPP relationship, by again using randomly perturbed test signals.

Accurate prediction of PPP on all cylinders has been demonstrated using the technique. The ARMAX models allow PID control to be applied. A form of robust minimum variance control was chosen as an appropriate control technique due to the stochastic nature of the PPP through combustion. The recently developed constrained variance controller design technique was applied. The resulting feedback control was shown to reduce the variance in the PPP whilst regulating it to a demanded value on each individual cylinder. Subject to the use of an appropriate PPP demand signal, MBT can thereby be achieved on each cylinder independently through the feedback scheme. The fundamental success in applying the technique is very much dependent on the use of the appropriate test signals used in training the neural networks and in identifying the ARMAX models. The technique can only reliably predict and control within the boundaries of the identification test data used.

In chapter 6, prediction of AFR has been demonstrated using an ion current sensing method with a neural network on one cylinder of a four cylinder IC engine. Dynamically varied input signals were used to excite λ which was measured by a closed coupled wideband UEGO sensor across a range of engine loads and speeds. The PCA technique was used for feature extraction and data reduction of the ion current signal. The resulting 6 principal components were combined with fuel pulse width, MAP and engine speed for identification of a NARX neural network model. This NN was experimentally validated over the identified range and was proven to offer high online accuracy.

The accuracy was maintained even during rapid transients and was robust to changes in engine speed, fuel pulse width and load. This range is restricted by stall conditions and speed limitations when perturbing the variables randomly simultaneously. During control of λ in the following chapter, a method is introduced that allows a larger speed range to be traversed by manipulating the FPW signal with the applied load.

In an extension to the application, average torque has been estimated at a high accuracy 'for free'. Little additional effort is need to extend the two layer neural network to a double final layer neural network to simultaneously predict average torque and λ. The dataset used for this MIMO network is identical with the addition of measured average torque used as a second target dataset.

In chapter 7, a progression of fueling controllers was implemented on to the engine to regulate the λ ratio to stoichiometry. Firstly, a feed forward neural network was developed to provide a fuel pulse width that regulated the engine air-fuel ratio to stoichiometry. The experimentally demonstrated feed-forward controller was unable to track to a λ demand in excursions from stoichiometry and did not resist disturbances in load or ABV. This highlighted the need for feedback control which was initially done with a signal from the UEGO sensor. Loopshaping control was designed using performance criteria and the resulting feed-

back system was demonstrated experimentally able to maintain stoichiometry during ABV and load disturbances, and also track to a desired λ ratio.

There are pure time delays inherent to the fueling between the injector command to the response received from the UEGO sensor. During this work, the UEGO sensor was located in the exhaust manifold, close to the exhaust port and two combustion cycle delays were experienced. In production vehicles, the UEGO sensor is located at a confluence point of the exhaust manifold, further downstream, where delays of four or five combustion cycles would be experienced. Using the ionization current method, AFR information is sensed during combustion, hence the transport delays of the exhaust gas have been removed.

Building on feedback from the UEGO sensor, the ionization current was used to predict λ as an output of a neural network, and it was this signal that has been incorporated into the feedback control loop. Loopshaping was again used as control which was experimentally shown to provide similar controlled accuracy for both the UEGO output signal and ionization current method output signal, the distinct advantage of the ionization current being that time delays have been removed.

8.2 Recommendations for Further Work

It is accepted that the work undertaken in this thesis does not cover a full engine operating range of parameters, such as speed or load. The neural networks developed for estimating the peak pressure position and air-fuel ratio only work within the ranges used for identification; this is a limitation on the signals used rather than the technique used. Additional work should aim at producing better identification signals that traverse larger ranges of speed, load and fuel pulse widths. The networks can be then be trained as in this thesis.

The ionization current is dependent on atmospheric conditions such as humidity, which affects results for λ prediction by introducing a bias offset at the output of the neural network. In this work, this is overcome by training and validating the neural network on the same day so as to minimize the introduction of changing ambient conditions. To overcome this issue entirely, the neural network would need an additional input of temperature or humidity.

Certainly four cylinder application of the air-fuel ratio control techniques can be undertaken. Achieving air-fuel ratio control on a single cylinder proved challenging but the step to four cylinders would be one of repeating the same procedure for each other cylinder. Indeed this step up to four cylinders would have been undertaken in this work had the equipment for each cylinder worked simultaneously. From experience and frustration, UEGO sensors appear to be lacking in robustness.

The benefits of balancing all four cylinders to stoichiometry individually would be obvious; allowing each cylinder to perform at an optimum for stoichiometry. Investigation into further benefits would require more thought.

It is feasible that the proposed control for air-fuel ratio and peak pressure position techniques could be applied simultaneously on a single cylinder.

Lastly, the topic of torque estimation was touched upon in chapter 6. Although this was average torque estimation and not instantaneous torque estimation, the results proved accurate enough to indicate further work could produce interesting results. Using the ionization current technique from each cylinder applied to a corresponding window of the torque output may provide detailed torque output estimation.

References

[1] *http://www.statistics.gov.uk/census2001/profiles/commentaries/housing.asp.*

[2] U.S. Department of Transportation. National highway traffic safety administration. 1992-2001.

[3] S. H. Cousins, J. Garcia Buenoa, and O. Palomares Coronadoa. Powering or depowering future vehicles to reach low carbon outcomes: The long term view 19302020. *Journal of Cleaner Production*, 15(11-12):1022–1031, 2007.

[4] U. Kiencke and L. Nielsen. *Automotive Control Systems.* Springer, 2005.

[5] M. Hubbard, P. D. Dobson, and J. D. Powell. Closed loop control of spark advance using cylinder pressure sensor. *Journal of Dynamic Systems, Measurement and Control*, pages 414–420, December 1976.

[6] S. D. Carroll. *Control of S.I. Engines Using In-Cylinder Pressure.* PhD Thesis, The University of Liverpool, 2003.

[7] G. Triantos, A. T. Shenton, and S. D. Carroll. Minimum variance control of cylinder peak pressure position. *IFAC AAC04*, 2004.

[8] G. Triantos. *NARMAX Modelling and Control With Powertrain Applications.* 2006.

[9] J. Heywood. *Internal Combustion Engine Fundamentals.* McGraw-Hill, 1988.

[10] L. Guzzella and C. H. Onder. *Introduction to Modeling and Control of Internal Combustion Engines.* Springer, 2004.

[11] S. Karagiorgis, K. Glover, and N. Collings. Control challenges in automotive engine management. *European Journal of Control*, 13:92–104, 2007.

[12] Bosch. *Gasoline Engine Management.* SAE International, 1999.

[13] J. W. Grizzle, K. L. Dobbins, and J. A. Cook. Individual cylinder air-fuel ratio control with a single EGO sensor. *IEEE transactions on Vehicular Technology*, (1), February 1997.

[14] J. L. Kainz and J. C. Smith. Individual cylinder fuel control with a switching oxygen sensor. *SAE Technical Paper*, (1999-01-0546), 1999.

[15] P. Tunestål, M. Wilcutts, A. Lee, and J. Hedrick. In-cylinder measurement for engine cold-start control. *Proceedings of the 1999 IEEE International Conference on Control Applications*, 1999.

[16] K. W. Randall and J. D. Powell. A cylinder pressure sensor for spark advance control and knock detection. *SAE Technical Paper*, 1979.

[17] R. J. Hosey and J. D. Powell. Closed loop, knock adaptive spark timing control based on cylinder pressure. *ASME Journal of Dynamic Systems, Measurement and Control*, Mar:64–70, 1979.

[18] I. Glaser and J. D. Powell. Optimal closed loop spark control of an automotive engine. *SAE Technical Paper*, (810058), 1981.

[19] J. D. Powell. Engine ocntrol using cylinder pressure: Past, present and future. *ASME Journal of Dynamic Systems, Measurement and Control*, 115:343–350, 1993.

[20] M. C. Sellnau, F. A. Matekunas, P. A. Battison, C. Chang, and D. R. Lancaster. Cylinder-pressure-based engine control using pressure-ratio-management and low-cost non-intrusive cylinder pressure sensors. *SAE Technical Paper*, (2000-01-0932), 2000.

[21] S. D. Walters, M. M. De Zoysa, and R. J. Howlett. Monitoring the air-fuel ratio of internal combustion engines using a neural network. *Measurement Science and Technology*, 17:2773–2782, 2006.

[22] H. Zhao and N. Ladommatos. Engine performance monitoring using spark plug voltage analysis. *Proceedings of the IMechE: Part D, Journal of automobile engineering*, 211:499–509, 1997.

[23] M. M. de Zoysa, R. J. Howlett, and S. D. Walters. Effect of varying engine block temperature on spark voltage characterization for the measurement of air-fuel ratio in internal combustion engines. *IEEE Fourth International Conference on Knowledge-Based Intelligent Systems and Allied Technology*, pages 545–548, 2000.

[24] R. J. Howlett, S. D. Walters, P. A. Howson, and I. Park. Air-fuel ratio measurement in an internal combustion engine using a neural network. *Conference on Advances in Vehicle Control and Safety*, July 1998.

[25] L. Eriksson, L. Nielsen, and J. Nytomt. Ignition control by ionization current interpretation. *SAE Technical Paper*, (960045), 1996.

[26] H. F. Calcote. Mechanism for the formation of ions in flames. *Combustion and Flame*, 1(4):385–403, 1957.

[27] K. Schnauffer. Engine cylinder flame propagation studies by new methods. *SAE Technical Paper*, (340074), 1934.

[28] G. M. Rassweiler and L. Withrow. Motion picture of engine flames correlated with pressure cards. *SAE Technical Paper*, pages 185–204, 1938.

[29] W. G. Rado and W. J. Johnson. Monitoring the combustion quality in internal combustion engines using the spark plug as a plasma probe. *IEEE Transactions on Vehicular Technology*, VT-24(2):17–21, May 1975.

[30] K. Terada and S. Suzuki. Measuring ignition and combustion by detecting ionization current. *Internal Combustion Engines*, 17, 1978.

[31] A. Saitzkoff, R. Reinmann, F. Mauss, and M. Glavmo. In-cylinder pressure measurements using the spark plug as an ionization sensor. *SAE Technical Paper*, (979857), 1997.

[32] A. Saitzkoff, R. Reinmann, T Beglind, and M. Glavmo. An ionization equilibrium analysis of the spark plug as an ionization sensor. *SAE Technical Paper*, (960337), 1996.

[33] S. Miyata, Y. Ito, and Y. Shimasaki. Flame ion density measurement using spark plug voltage analysis. *SAE Technical Paper*, (930462), 1993.

[34] L. Peron, A. Charlet, P. Higelin, B. Moreau, and J. F Burq. Limitations of ionization current sensors and comparison with cylinder pressure sensors. *SAE Technical Paper*, (2000-01-2830), 2000.

[35] L. Eriksson and L. Nielsen. Ionization current interpretation for ignition control in internal combustion engines. *Control Engineering Practice*, 5(8):1107–1113, 1997.

[36] L. Eriksson and L. Neilsen. Closed loop ignition control by ionization current interpretation. *SAE Technical Paper*, (970854), 1997.

[37] F. An, D. Upadhyay, and G. Rizzoni. Combustion diagnostics in methane-fueled SI engines using the spark plug as an ionization probe. *SAE Technical Paper*, (970033), 1997.

[38] H. Klövmark, P. Rask, and U. Forsell. Estimating the air/fuel ratio from gaussian parameterizations of the ionization currents in internal combustion si engines. *SAE Technical Paper*, (2000-01-1245), 2000.

[39] B. Lee, Y. G. Guezennec, and G. Rizzoni. Estimation of cycle-resolved in-cylinder pressure and air-fuel ratio using spark plug ionization current sensing. *International Journal of Engine Research*, 2(4):263–276, 2001.

[40] G. G. Zhu, C. F. Daniels, and J. Winkelman. Mbt timing detection and its closed-loop control using in-cylinder ionization signal. *SAE Technical Paper*, (2004-01-2976), 2004.

[41] M. Asano, T. Kuma, M. Kajitani, and M. Takeuchi. Development of new ion current combustion control system. *SAE Technical Paper*, (980162), 1998.

[42] L. Neilsen and L. Eriksson. An ion-sense engine fine-tuner. *IEEE Control Systems Magazine*, 18(5):43–52, 1998.

[43] M. Hellring, T. Munther, T. Rognvaldsson, N. Wickstrom, C. Carlsson, M. Larsson, and J. Nytomt. Robust afr estimation using the ion current and neural networks. *SAE Technical Paper*, (1999-01-1161), 1999.

[44] M. Hellring, T. Munther, T. Rognvaldsson, T. Wickstrom, C. Carlsson, and J. Nytomt M. Larsson. Spark advance control using the ion current and neural soft sensors. *SAE Technical Paper*, (1999-01-1162), 1999.

[45] M. Hellring and U. Holmberg. A comparison of ion current based algorithms for peak pressure position control. *SAE Technical Paper*, (2001-01-1920), 2001.

[46] U. Holmberg and M. Hellring. A simple virtual sensor for combustion timing. *Journal of Dynamics, Measurement and Control*, 125, 2003.

[47] C. F. Daniels. The comparison of mass fraction burned obtained from the cylinder pressure signal and spark plug ion signal. *SAE Technical Paper*, (980140), 1998.

[48] Y. Ohashi, W. Fukui, F. Tanabe, and A. Ueda. The application of ionic current detection system for the combustion limit control. *SAE Technical Paper*, (980171), 1998.

[49] N. Wickström, M. Taveniku, A. Linde, M. Larsson, and B. Svensson. Estimating pressure peak position and air-fuel ratio using the ionization current and artificial neural networks. *IEEE Conference on Intelligent Transportation Systems*, (0-7803-4269-0):972–977, 1998.

[50] J. Förster, A. Günther, M. Ketterer, and K-J. Wald. Fuel and additive influence on the ion current. *SAE Technical Paper*, (1999-01-0204), 1998.

[51] Y. Moudden, A-K. Seghouane, and O. Boubal. Extraction of peak pressure position information from the spark-plug ionization signal. *IEEE Internation Workshop on Intelligent Data Aquisition and Advanced Computer Systems*, pages 170–173, 2001.

[52] C. F. Daniels, G. G. Zhu, and J. Winkelman. Inaudible knock and partial-burn detection using in-cylinder ionization signal. *SAE Technical Paper*, (2003-01-3149), 2003.

[53] G. W. Malaczynski and M. E. Baker. Real-time digital signal processing of ionization current for engine diagnostic control. *SAE Technical Paper*, (2003-01-0119), 2003.

[54] G. G. Zhu, I. Haskara, and J. Winkelman. Stochastic limit control and its application to knock limit control using ionization feedback. *SAE Technical Paper*, (2005-01-0018), 2005.

[55] G. G. Zhu, I. Haskara, and J. Winkelman. Stochastic limit control and its application to knock limit control using ionization feedback. *American Control Conference*, pages 5027–5034, 2005.

[56] I. Haskara, G. G. Zhu, C. Daniels, and J. Winkelman. Closed loop maximum dilution limit control using in-cylinder ionization signal. *SAE Technical Paper*, (2005-01-3751), 2005.

[57] A. Gazis, D. Panousakis, R. Chen, and W-H. Chen. Computationally inexpensive methods of ion current signal manipulation for predicting the characteristics of engine in-cylinder pressure. *IMechE, Journal of Engine Research*, 7:271–282, 2006.

[58] M. Kinoshita, A. Saito, K. Mogi, and K. Nakata. Study on ion current and pressure behavior with knocking in engine cylinder. *JSAE Review*, (21):483–488, 2000.

[59] A. Vressner, P. Strandh, A. Hultqvist, P. Tunestål, and B. Johansson. Multiple point current diagnostics in an HCCI engine. *SAE Technical Paper*, (2004-01-0934), 2004.

[60] Y. Wang and L. Zhou. Investigation of the detection of knock and misfire of a spark ignition engine with the ionic current method. *IMechE*, 271(D:J):617–621, 2003.

[61] Y. Huang. Effects of engine operating conditions on in-cylinder air/fuel ratio detection using a production ion-sensing device. *SAE Technical Paper*, (2004-01-0515), 2004.

[62] G. G. Zhu, D. L. S. Hung, and J. Winkelman. Combustion characteristics detection for low pressure direct injection engines using ionization signal. *SAE Technical Paper*, (2006-01-3317), 2006.

[63] H. Zhao and T. Ma. Engine performance monitoring by means of the spark plug. *Proceedings of the IMechE: Part D, Journal of Automobile Engineering*, 209(D2):143–146, 1995.

[64] A. G. Gadyon and H. G. Wolfhard. *Flames, Their Structure, Radiation, and Temperature.* Chapman and Hall, London, 1979.

[65] Y. Shimasaki, M. Kanehiro, S. Baba, S. Maruyama, T. Hisaki, and S. Miyata. Spark plug voltage analysis for monitoring combustion in an internal combustion engine. *SAE Technical Paper*, (930461), 1993.

[66] R. Reinmann, A. Saitzkoff, B. Lassesson, and P. Strandh. Fuel and additive influence on the ion current. *SAE Technical Paper*, (980161), 1998.

[67] L. Eriksson. Spark advance control by ion-sensing and interpretation, 1998. www.fs.isy.liu.se/ larer/Projects/main.html.

[68] P. Attard and J. Micallef. Ion current combustion technology for controlled auto-ignition gasoline engines. *IMechE, International Journal of Engine Research*, (5):429–437, 2007.

[69] G. G. Zhu, C. F. Daniels, and J. Winkelman. Mbt timing detection and its closed-loop control using in-cylinder pressure signal. *SAE Technical Paper*, (2003-01-3266), 2003.

[70] N. Collings and T. Ma. Knock detection alternatives for production vehicles. *IMechE*, 199(D4):301–307, 1985.

[71] A. Linde, M. Taveniku, and B. Svensson. Using neural networks for air-to-fuel ratio estimation in two-stroke combustion engines. *International Conference on Engineering Applications of Neural Networks EANN '95)*, pages 327–334, August 95.

[72] S. Park, P. Yoon, and M. Sunwoo. Feedback error learning neural networks for spark advance control using cylinder pressure. *IMechE Part D: Journal of Automotive Engineering*, 215:625–636, 2001.

[73] R. A. Johnson and D. W. Wichern. *Applied Multivariate Statistical Analysis.* Prentice-Hall, 1982.

[74] M. Hellring and U. Holmberg. An ion current-based, peak-finding algorithm for pressure peak position estimation. *SAE Technical Paper*, (2000-01-2829), 2000.

[75] I. Haskara, G. G. Zhu, and J. Winkelman. Ic engine retard ignition timing limit detection and control using in-cylinder ionization signal. *SAE Technical Paper*, (2004-01-2977), 2004.

[76] A. H. Shamekhi and A. Ghaffari. Fuzzy control of spark advance by ion current sensing. *IMechE Part D: Journal of Automotive Engineering*, 221:335–342, 2007.

[77] R. Reinmann, A. Saitzkoff, and F. Mauss. Local air-fuel ratio measurements using the spark plug as an ionization sensor. *SAE Technical Paper*, (970856), 1997.

[78] E. N. Balles, E. A. VanDyne, and A. M. Wahl. In-cylinder air/fuel ratio approximation using spark gap ionization sensing. *SAE Technical Paper*, (980166), 1998.

[79] D. Upadhyay and G. Rizzoni. Afr control on a single cylinder engine using the ionization current. *SAE Technical Paper*, (890203), 1998.

[80] R. J. Howlett, P. A. Howson, and S. D. Walters. Determination of air fuel ratio in automotive ignition system using neural networks. *ISATA*, June 1996.

[81] I. Arsie, C. Pianese, and M. Sorrentino. A procedure to enhance identification of recurrent neural networks for simulating air-fuel ratio dynamics in SI engines. *Engineering applications of artificial intelligence*, 19:65–77, 2006.

[82] N. Collings and J. Willey. Cyclically resolved HC emissions from a spark ignition engine. *SAE Technical Paper*, (871691), 1987.

[83] J. Lawton and F. J. Weinberg. *Electrical Aspects of Combustion.* Clarendon Press, Oxford, 1969.

[84] V. Naoumov, A. Demin, and A. Sokolov. Modelling of combustion and non-equilibrium ionization in spark ignition engines. *SAE Technical Paper*, (2002-01-0009), 2002.

[85] V. Naoumov and A. Demin. Numerical study and analysis of pollutant production and emission control using ion current prediction in the si engine. *SAE Technical Paper*, (2003-01-0724), 2003.

[86] M. Glavmo, P. Spadafora, and R. Bosch. Closed loop start of combustion control utilizing ionization sensing in a diesel engine. *SAE Technical Paper*, (1999-01-0549), 1999.

[87] S. Byttener, T. Rogenvaldsson, and N. Wickström. Estimation of combustion variability using in-cylinder ionization measurements. *SAE Technical Paper*, (2001-01-3485), 2001.

[88] M. Misiti, Y. Misiti, G. Oppenheim, and J-M. Poggi. *Matlab Wavelet Toolbox 4, Users Guide.* The MathWorks, Inc., 2007.

[89] S. J. Liu and A. K. Chan. *Wavelet Toolware: Software for Wavelet Training.* Academic Press, 1998.

[90] Y. Tan and M. Saif. Nonlinear dynamic modelling of automotive engines using neural networks. *Proceedings of the IEEE International OCntrol Conference on Control Applications*, pages 408–410, 1997.

[91] E. L. Hanzevack, T. W. Long, C. M. Atkinson, and M. L. Traver. Virtual sensors for spark ignition engines using neural networks. *Proceedings of the American Control Conference*, pages 669–673, 1997.

[92] M. L. Traver, R. J. Atkinson, and C. M. Atkinson. Neural network-based diesel engine emissions prediction using in-cylinder combustion pressure. *SAE Technical Paper*, (1999-01-01532), 1999.

[93] S. W. Wang, D. L. Zu, J. B. Gomm, G. F. Page, and S. S. Douglas. Adaptive neural network model based predictive control for air-fuel ratio of si engines. *Engineering Applications of Artificial Intelligence*, 19:189–200, 2006.

[94] Z. Hou, Q. Sen, and Y. WU. Air-fuel ratio identification of gasoline engine during transient conditions based on elman neural networks. *IEEE International Conference on Intelligent Systems and Design Applications*, (0-7695-2528-8/06), 2006.

[95] Y. Zhang, L. Xi, and J. Liu. Transient air-fuel ratio estimations in spark ignition engine using recurrent neural networks. *KES 2007/WIRN 2007, Part II*, pages 240–246, 2007.

[96] I. Arsie, C. Pianese, and M. Sorrentino. Development and real-time implementation of recurrent neural networks for AFR prediction and control. *SAE Technical Paper*, (2008-01-0993), 2008.

[97] I. Arsie, C. Pianese, and M. Sorrentino. Nonlinear recurrent neural networks for air fuel ratio control in SI engines. *SAE Technical Paper*, (2004-01-1364), 2004.

[98] I. Arsie, M. M. Marotta, C. Pianese, and M. Sorrentino. Experimental validation of a recurrent neural network for air-fuel ratio dynamic simulation in SI IC engines. *Proceedings of the ASME Dynamic Systems and Control Division*, 73(1, Part A):127–136, 2004.

[99] I. Arsie, M. M. Marotta, C. Pianese, and M. Sorrentino. Experimental validation of a neural network A/F virtual sensor for SI engine control. *SAE Technical Paper*, (2006-01-1351), 2006.

[100] H. Demuth, M. Beale, and M. Hagan. *Matlab Neural Network Toolbox User's Guide Version 5*. The Mathworks Inc, 2006.

[101] S. Haykin. *Neural Networks, A Comprehensive Foundation*. Prentice-Hall, 1999.

[102] J. E. Dennis and R. B. Schnabel. *Numerical Methods for Unconstrained Optimization and Nonlinear Equations*. Prentice-Hall, Englewood Cliffs, 1983.

[103] D. W. Marquardt. An algorithm for the least-squares estimation of nonlinear parameters. *J. Soc. Indust. Appli. Math*, 11(2):431–441, 1963.

[104] M. T. Hagan and M. B. Menhaj. Training feedforward networks with the marquardt algorithm. *IEEE Transactions on Neural Networks*, 5(6), 1994.

[105] J. C. Principe, N. R. Euliano, and W. C. Lefebvre. *Neural and adaptive systems: fundamentals through simulations.* J. Wiley and sons, 2000.

[106] F. D. Foresee and M. T. Hagan. Gauss-newton approximation to bayesian regularization. *Proceedings of the 1997 International Joint Conference on Neural Networks*, pages 1930–1945, 1997.

[107] J.C. Maxwell. On governors. *Proceedings of the Royal Society*, (100), 1868.

[108] B. Friedland. *Control System Design: An Introduction to State-Space Methods.* McGraw-Hill, New York, 1986.

[109] D. Hrovat and J. Sun. Models and control methodologies for ic engine idle speed control design. *Control Engineering Practice*, 5(8), 1997.

[110] K. A. Astrom. *Introduction to Stochastic Control Theory.* Academic Press, 1970.

[111] P. E. Wellstead and M. B. Zarrop. *Self-Tuning Systems.* Wiley, 1991.

[112] P. B. Dickinson. *Robust Low-Order Control Techniques with Powertrain Applications.* PhD Thesis, The University of Liverpool, 2007.

[113] A. Packard, G. Balas, R. Chiang, and M. Safonov. *Robust Control Toolbox 3, User's Guide.* The Mathworks Inc, 2006.

[114] D. Mcfarlane and K. Glover. A loop shaping design technique procedure using h_∞ synthesis. *IEEE Transactions on Automatic Control*, 37(6):759–769, 1992.

[115] A. Bemporad, M. Morari, and N. L. Ricker. *Model Predictive Control Toolbox 3, User's Guide.* The Mathworks Inc, 2009.

[116] H. J. Ferreau, G. Lorini, and M. Diehl. Fast nonlinear model predictive control of gasoline engines. *IEEE International Conference on Control Applications*, pages 2754–2759, October 2006.

[117] S. Hashimoto, H. Okuda, Y. Okada, S. Adachi, S. Niwa, and M. Kajitani. An engine control systems design for low emission vehicles by generalized predictive control based on identified model. *Proceedings of the IEEE International Conference on Control Applications*, pages 2411–2416, October 2006.

[118] D. Neary. Four cylinder ion current sensing circuit, MEE10044-1, 2008.

[119] J. S. Rigden. *Macmillan Encyclopedia of Physics.* Simon and Schuster, 1996.

[120] L. Ljung. *System Identification, Theory for the User.* Prentice Hall, 1987.

[121] The Mathworks Inc. *Matlab 7, Data Analysis.* The Mathworks Inc, 2008.

[122] J. Miles and M. Shevlin. *Applying Regression and Correlation; A Guide to Students and Researchers.* SAGE Publications Ltd, 2000.

[123] T. Söderstrom and P. Stoica. *System Identification.* Prentice Hall, 1989.

[124] P. Li, K. Suzuki, and T. Shen. A case study of cyclic balancing control for SI engines. *SICE Annual Conference*, pages 1727–1733, 2007.

[125] P. Li, T. Shen, and Y. Oguri. Experimental analysis and control-oriented modeling for cyclic variation of cylinder pressure in ic engines. *Proceedings of the 26th Chinese Control Conference*, pages 613–617, 2007.

[126] D. P. Lindorff. *Theory of Sampled-Data Control Systems.* Wiley, 1965.

[127] P. B. Dickinson and A. T. Shenton. A parameter space approach to constrained variance PID controller design. *Automatica*, 2008.

[128] M. J. van Nieuwstadt and I. Kolmanovsky. Cylinder balancing of direct injection engines. *Proceedings of the American Control Conference*, (0-7803-4990-6/99):202–206, 1999.

[129] P. E. Moraal, J. A. Cook, and J. W. Grizzle. Single sensor individual cylinder airfuel ratio control of an eight cylinder engine with exhaust gas mixing. *Proceedings of the American control conference*, 1993.

[130] K. J. Bush, N. J. Adams, S. Dua, and C. R. Markyvech. Automatic control of cylinder by cylinder airfuel mixture using a proportional exhaust gas sensor. *SAE Technical Paper*, (940149), 1994.

[131] L. Benvenutia, M. D. Di Benedettob, S. Di Gennarob, and A. Sangiovanni-Vincentellic. Individual cylinder characteristic estimation for a spark injection engine. *Automatica*, 39:1157–1169, 2003.

[132] P. Li, K. Liu, T. Shen, and J. Kako. Torque balancing control in ignition event based scale for multi-cylinder SI engines. *International Journal of Advanced Mechatronic Systems*, 1(2):137–145, 2008.

[133] M. F. J. Brunt and C. R. Pond. Evaluation of techniques for absolute cylinder pressure correction. *SAE Technical Paper*, (970036), 1997.

[134] D. R. Lancaster, R. B. Krieger, and J. H. Lienesch. Measurement and analysis of engine pressure data. *SAE Technical Paper*, (750026), 1975.

[135] G. Rizzoni. *A Dynamic Model for the Intenral Combustion Engine.* PhD Thesis, The University of Michigan, 1986.

[136] G. Rizzoni, Y-Y. Wang, and S. Drakunov. Estimation of engine torque using nonlinear observers in the crank angle domain. *ASME, Journal of Dynamic Systems and Control*, (980161):189–193, 1995.

[137] H. Kaisheng, W. Shuaiyu, J. Zhenhua, and J. Dinan. Feedforward method of engine torque estimation. *IEEE, ICVES*, pages 246–249, 2006.

[138] I. Andersson. Ion current and torque modeling for combustion engine control. *Doktorsavhandlingar vid Chalmers Tekniska Hogskola*, (2388):1–68, 2005.

[139] G. Dong, L. Li, S. Yu, and X. Zhang. A method of torque estimation utilizing ionization sensing technology in internal combustion si engines. *IEEE International Conference on Vehicular Electronics and Safety*, pages 32–36, 2006.

[140] C. F. Aquino. Transient a/f control characteristics of the 5 liter central fuel injection engine. *SAE Technical Paper*, (810494), 1981.

[141] D. Y. Wang and E. Detwiler. Exhaust oxygen sensor dynamic study. *Sensors and Actuators B*, 120(1):200–206, 2006.

[142] Y. Yildiz, A. Annaswamy, D. Yanakiev, and I. Kolmanovsky. Adaptive air fuel ratio control for internal combustion engines. *2008 American Control Conference*, pages 2058–2063, 2008.

[143] D. Y. Wang, E. Detwiler, and S. Nelson. Dynamic study of louvre shield and exhaust pipe for exhaust gas oxygen sensors. *Delphi Internal Report*, 2001.

[144] D. Y. Wang and E. Detwiler. Electrode dynamic study of exhaust gas oxygen sensors. *Sensors and Actuators B*, 99(2-3):571–578, 2004.

[145] D. Y. Wang and E. Detwiler. Dynamic study of porous coating layers of exhaust oxygen sensors. *Sensors and Actuators B*, 106(1):229–233, 2005.

[146] S. Devasia. Should model-based inverse inputs be used as feedforward under plant uncertainty? *IEEE Transactions on Automatic Control*, 47(11):1865–1871, 2002.

[147] *http://faculty.washington.edu/devasia/Research/Broad_Research_Areas/Inversion.htm.*

[148] A. T. Shenton. New research directions in gasoline powertrain control. *UK Automatic Control Conference*, September 2008.